

Strong Spin-Orbit Coupling in Low Dimensional Systems Investigated by Static and Time-Resolved ARPES

THÈSE N° 5602 (2013)

PRÉSENTÉE LE 31 JANVIER 2013

À LA FACULTÉ DES SCIENCES DE BASE

LABORATOIRE DE SCIENCE À L'ÉCHELLE NANOMÉTRIQUE

PROGRAMME DOCTORAL EN PHYSIQUE

ÉCOLE POLYTECHNIQUE FÉDÉRALE DE LAUSANNE

POUR L'OBTENTION DU GRADE DE DOCTEUR ÈS SCIENCES

PAR

Alberto CREPALDI

acceptée sur proposition du jury:

Prof. G. Meylan, président du jury
Prof. K. Kern, Prof. M. Grioni, directeurs de thèse
Dr C. R. Ast, rapporteur
Prof. F. Carbone, rapporteur
Dr J. H. Dil, rapporteur



ÉCOLE POLYTECHNIQUE
FÉDÉRALE DE LAUSANNE

Suisse
2013

Acknowledgments

I would like to express my deep gratitude to Prof. Marco Grioni and Prof. Klaus Kern for the great opportunity they have offered me four years ago, and for all their precious advises and teachings. But I am especially grateful to them for the freedom they granted me: I had the possibility to develop my own ideas, to fail (very often) and learn from my own faults. When I arrived I was only a young student, and they have been two important examples of scientist. I hope to have gained a fraction of their skills and of their wide knowledge.

I acknowledge Prof. Fulvio Parmigiani, despite all my past wrong decisions, he has been always present for me and he offered me his help. I thank him for the possibility he gave me to work on the tr-ARPES project. He knows more than any other how this project is important for me. I am keen of working with him in Trieste: there are so many open-questions and fascinating problems to face and hopefully to solve!

Any scientist is "an *Ulysse*" and before reaching *Ithaca* a long and exciting journey is waiting for him. Since the journey is the most important thing, clearly the travelling companions are fundamental persons. Arriving at the EPFL I brought with me a piece of my previous life in Trieste: Sergio, Alberto and Davide are good friends, the kind of friends who are always present and ready to help. Now we separate for a while, but I am sure soon or later we will meet again. During these years I met new friends and some of them have already left: Luca, Tony, Joy, Miguel and Marco. Among them, Stéphane and Emmanouil have been particularly important for my scientific growth, they have strongly contributed to my PhD and I have a special gratitude for them.

I must confess I would like to start my PhD again tomorrow, because I am sure that with Simon, Cedric, Jens and Afsoon I would spend beautiful days, discussing about physics (and everything else). During my PhD I have often worked alone, but I thank all them because in the last year they taught me again how to appreciate the pleasure to share my ideas with other people. I hope a long friendship will link all us in the future. The ICMP is like a small (Italian) family and I want to thank all the other friends: Fabian, Fabio, Giulia, Luca, Quentin and Simon.

During these years we have developed several projects in collaboration with other groups and I want in particular to acknowledge Prof. Harald Brune, Dr. Stefano Rusponi, Dr. François Patthey, Dr. Marina Pivetta, Dr. Helmuth Berger, Dr. Philippe Bugnon, Dr. Arnaud Magrez, Prof. Oleg Yazyev, Dr. Gabriel Autés, Dr. Alessandro Baraldi, Dr. Rong Rong Zhan, Dr. Carlo Carbone, Dr. Marco Papagno, Dr. Daniela Pacilé, Dr. Polina Sheverdyaeva, Dr. Paolo Moras and Dr. Cephice Cacho.

Among the collaborations, a special place is occupied by the T-ReX group and in particular I am grateful to Dr. Barbara Ressel, Dr. Cesare Grazioli and Dr. Michele Zacchigna. They developed the tr-ARPES setup, they dedicated themselves to this project for several years and any result would have been impossible without their fundamental help. They are great scientists and good friends. Recently Federico joined the group: it took time to convince him about the superiority of ARPES against optics, and I am sure we will have great fun working together.

I thank all the members of the jury, Prof. Georges Meylan, Prof. Fabrizio Carbone, Dr. Jan Hugo Dil and Dr. Christian Ast for having gone through this long manuscript and for

their advices and suggestions on how to improve it.

Life is all but science. Unfortunately I recognize that in the last months I have dedicated too much time to my job, and not enough to myself and to my family and friends and especially not enough to the most important person of my life: my beloved Costanza. No words are enough to describe my love for you. These four years have been long and lonely so far from you, but we overcome this great difficulty, and soon we will be together again. Even if we were separated you have always helped me, giving me the strength to keep going on. You have been my confidant when things were going wrong and we shared together all the most beautiful moments of these four years in Lausanne.

I am grateful to Ardea and Giorgio for being always so kind with me, for their generosity and all their help and support during the difficult periods in Trieste when everything seemed not work.

During the PhD period I had the possibility to entangle my life again with the one of Alessandra, David, Elisa, Franco, Luca, Marco and all my friends in Verbania. I discovered that the true friendship, as the true love, is strong and robust against distance in space and time. I thank all them for infinite reasons.

Finally I want to thank my parents, Daniela and Paolo, my sister Giulia (and also Bea, a special member of the family). They have always believed in me and they encouraged me in the adversities, they have been always present to hear my numerous and continuous complains, giving me (often) good advises. I thank also Zio Carlo and Zia Luigina for all the beautiful moments during the numerous week-end spent together in Padova, during the PhD but also previously at the University. Finally a special tribute to Nonna Pina, Nonno Ernesto, Nonna Nini: also thank to their love I grew up and I have reached this important goal.

I congratulate myself for having survived! (Never give up!)

Abstract

The effect of strong spin-orbit coupling (SOC) on the valence and conduction bands of solids can often be considered as a minor perturbation. Recently, however, SOC has been shown to lead, in special circumstances, to large and measurable qualitative effects on the electronic structure. High resolution angle-resolved photoemission spectroscopy (ARPES) reported the existence of spin polarized conduction channels localized at surfaces and interfaces. The attention of the condensed matter community was strongly attracted firstly by the discovery of giant spin splitting in surface alloys, grown on metallic substrates and successively also on semiconductors, and secondarily by the breakthrough of topological insulators and bismuth tellurohalides, the latter characterized by *bulk* spin split states. These spin polarized states are interesting both for fundamental and practical reasons, in the perspective of spintronics applications.

This work is an experimental investigation, mainly by ARPES, of several systems, both bulk materials and complex interfaces formed by high Z elements (Bi and Pb) on various substrates. We have studied the electronic band structure and the effect of spin-orbit coupling in systems with different dimensionality, ranging from one-dimensional Bi and Pb chains, to two-dimensional dense Pb monolayer up to the novel three-dimensional bulk Rashba compound BiTeI. The experimental findings have been confirmed by first-principle calculations, and other experimental techniques, namely scanning tunnelling microscopy (STM) and X-ray photoelectron diffraction (XPD), have been used to characterize the surface structures of the interfaces.

A parallel project of this thesis was the development and characterization of a novel time-resolved ARPES setup, based on ultrashort laser pulses. I have exploited it to investigate the out-of-equilibrium electronic properties of the topological insulator Bi₂Se₃. This study shows an ultrafast chemical shift of the conduction band due to photo-doping. I developed a model, based on the modification of the effective thermal distribution, to interpret the relaxation dynamics of the photo-excited electronic population.

The thesis is organized as follow: after a brief description of the ARPES technique (chapter 1) I summarize the most important theoretical and experimental investigations of spin-split surface states (chapter 2). Chapter 3 reports the investigation of the gap structure in the complex tri-layer BiAg₂-Ag/ Si(111). In Chapter 4 I compare the electronic properties of the incommensurate and commensurate Pb monolayer grown respectively on Au(111) and on Ag(100). Chapter 5 reports the study of the one-dimensional spin split surface states of the Bi chain grown on Cu(110). There, the role played by the adsorbate in defining the magnitude of the splitting is explored by substituting Bi with Pb. Chapter 6 contains an investigation of the electronic properties of the novel bismuth tellurohalide BiTeI. Finally chapter 7 gives a short introduction of the time-resolved ARPES technique, and reports the investigation of the out-of-equilibrium electronic properties of Bi₂Se₃.

Keywords:

Angle- and time-resolved photoemission spectroscopy; spin orbit coupling; surface states; topological insulators; bismuth tellurohalide; reduced dimensionality.

Sommario

L'accoppiamento spin-orbita è stato a lungo trattato solo come un termine perturbativo nella struttura a bande dei solidi. Di recente, tuttavia, diversi studi hanno evidenziato come l'interazione spin-orbita sia responsabile di modifiche sostanziali delle proprietà elettroniche della materia. L'avvento della spettroscopia di foto-emissione ad alta risoluzione ha permesso di osservare l'esistenza di stati di superficie polarizzati in spin. Dapprima l'interesse della comunità scientifica si è focalizzato sullo studio di leghe metalliche di superficie, in cui la separazione energetica tra i canali di spin è diversi ordini di grandezza maggiore che nelle superfici dei singoli substrati. Le possibili applicazioni nel campo della spintronica hanno motivato studi volti a trasferire questi canali di spin alle superfici di semiconduttori. In questo senso, un importante passo avanti è rappresentato dalla scoperta degli isolanti topologici e dallo studio dei bismuto tellururo-alidi. In particolare, quest'ultima famiglia di semiconduttori costituisce il primo esempio di stati elettronici di volume polarizzati in spin.

Questo lavoro di tesi consiste nello studio, mediante spettroscopia di foto-emissione risolta in angolo, delle proprietà elettroniche di diversi sistemi, sia cristalli singoli sia interfacce preparate *in situ* mediante evaporazione di metalli pesanti (Bi e Pb) su vari substrati. Ho studiato le modifiche indotte dall'interazione di spin-orbita nella struttura a bande di catene unidimensionali di Pb e Bi, di sistemi bidimensionali formati da strati monoatomici di Pb ed infine di cristalli singoli con proprietà elettroniche tridimensionali, quali BiTeI. I risultati sperimentali sono stati supportati, quando possibile, da modelli teorici e calcoli della struttura a bande. Nel corso della tesi ho potuto utilizzare tecniche complementari, volte a determinare la struttura cristallina delle interfacce, tra queste in particolare la spettroscopia ad effetto tunnel e la diffrazione di foto-elettroni.

In parallelo, nel corso della tesi, ho collaborato al progetto di sviluppo e caratterizzazione di un nuovo apparato sperimentale per foto-emissione risolta in angolo e in tempo. Questa tecnica ci ha permesso di investigare la struttura elettronica fuori equilibrio di un isolante topologico, Bi₂Se₃. Questo studio mostra come, in seguito al foto-drogaggio della banda di conduzione, il potenziale chimico si sposti a più alte energie. La dinamica di rilassamento delle popolazioni elettroniche fuori equilibrio è stata modellizzata a partire dalla modifica della distribuzione termica degli elettroni.

La tesi è organizzata come segue: il primo capitolo contiene una breve introduzione alla tecnica sperimentale. Il secondo capitolo riassume i principali risultati sperimentali e teorici della fisica degli stati di superficie polarizzati in spin. Nel terzo capitolo sono discussi i risultati del nostro studio sulla simmetria della struttura a bande del sistema BiAg₂-Ag/Si(111). Nel quarto capitolo viene confrontata la struttura a bande di due strati monoatomici di atomi di Pb, il primo non-commensurabile al substrato ove è cresciuto (Au(111)), il secondo invece commensurabile (Ag(100)). Il quinto capitolo riporta lo studio delle proprietà elettroniche di catene di Bi cresciute su Cu(110), e l'effetto indotto dalla sostituzione di Bi con Pb. Il sesto capitolo è dedicato alle proprietà elettroniche di BiTeI. Infine, il settimo capitolo contiene una breve introduzione alla tecnica di foto-emissione risolta in tempo e i risultati dello studio di Bi₂Se₃.

Parole chiave:

Spettroscopia di foto-emissione risolta in angolo e in tempo; accoppiamento spin-orbita; stati di superficie; isolanti topologici; bismuto tellururo-alidimensionalità ridotta.

Contents

1	Experimental Method and Principles	1
1.1	Photoemission spectroscopy	1
1.1.1	Historical introduction	1
1.1.2	General formulation	2
1.1.3	1- Versus 3-step models	3
1.1.4	Kinematic of Angle-Resolved Photoemission Spectroscopy	5
1.1.5	One particle spectral function formulation	7
1.1.6	EDC and MDC lineshapes of the quasiparticle peak	8
1.1.7	Direct and indirect transitions	10
2	Spin Orbit Interaction at Surfaces	13
2.1	Surface states in metals	13
2.1.1	The origin of surface states	13
2.1.2	Spin splitting in the Au(111) surface state	16
2.1.3	Spin-split surface states in different material surfaces	25
2.2	Giant spin splitting at surfaces and interfaces	31
2.2.1	Metallic surface alloys	31
2.2.2	Exporting the Rashba-Bychkov effect in semiconductors	39
2.2.3	Spin splitting in confined quantum well systems	43
3	The Gaps Structure of BiAg₂-Ag/ Si(111)	47
3.1	Conductance properties of a Rashba system	47
3.1.1	Tunneling conductance	48
3.1.2	Magnetoconductance	48
3.2	Anisotropic spin gaps in BiAg ₂ – Ag/ Si(111)	51
3.2.1	I. Introduction	51
3.2.2	II. Methods and system description	51
3.2.3	III. Results and discussion	54
3.2.4	IV. Conclusion	58
3.2.5	Appendix	59
3.3	BiAg ₂ – Ag/Si(111) a parallel ARPES study	60
4	Symmetry-Dependent Hybridization in Supported Pb Monolayers	63
4.1	ARPES studies of a Pb monolayer on a metallic substrate	63
4.2	Combined ARPES and STM study of Pb/Au(111) moiré: one overlayer two symmetries	66
4.2.1	I. Introduction	66
4.2.2	II. Experiment	67
4.2.3	III. Results	69
4.2.4	IV. Discussion	71

4.2.5	V. Conclusions	74
4.2.6	Appendix	74
4.3	Combined ARPES and XPD study of the Pb/Ag(100) $c(6 \times 2)$ interface . .	75
4.3.1	Structural determination by means of XPD	76
4.3.2	Electronic properties of Pb/Ag(100)	79
4.3.3	Discussion and comparison between the Pb/Au(111) and Pb/Ag(100) results	80
5	Large Spin Splitting in One-Dimensional Surface Alloys	83
5.1	One dimensional surface states at stepped Si(111) surface	84
5.2	One dimensional spin-split states at the Cu(110) surface	87
5.2.1	Surface characterization of the Bi/Cu(110) interface	87
5.2.2	Spin-split surface states with one-dimensional character in the Bi/Cu(110) $p(4 \times 1)$ surface alloy	88
5.2.3	Surface characterization of the Pb/Cu(110) interface	93
5.2.4	Evolution of the spin splitting in Pb/Cu(110) $p(5 \times 1)$ and in the mixed alloy	94
6	Large Dresselhaus and Rashba Spin Splitting at BiTeI Surfaces	99
6.1	The Crystal structure of Bismuth Tellurohalide BiTeI	100
6.2	Giant Rashba-type spin splitting in bulk BiTeI	101
6.3	Giant Ambipolar Rashba Effect in the Semiconductor BiTeI	103
6.4	Supplemental Material: Giant Ambipolar Rashba Effect in the Semiconductor BiTeI	109
6.4.1	Surface Terminations	109
6.4.2	Bulk conduction and valence bands	111
6.4.3	Surface potential manipulation by K dosing	112
6.4.4	Spin resolved constant energy contours	113
6.5	Two independent XARPES studies of the three-dimensional band dispersion of BiTeI	115
7	Time- and Angle-Resolved Photoemission Study of the Topological Insulators Bi₂Se₃	119
7.1	Time- and angle-resolved photoemission	120
7.1.1	Introduction	120
7.1.2	The time dependent spectral function and Fermi-Dirac distribution .	122
7.1.3	Hot electrons and time dependent Fermi-Dirac distribution	123
7.1.4	Two-temperatures model and its extension	125
7.2	Tr-ARPES investigation of the topological insulator state	127
7.2.1	The role of topological invariants in solid state physics: the rise of topological insulators	127
7.2.2	The ground state electronic properties of bismuth chalcogenides Bi ₂ X ₃ X = Te, Se	130
7.2.3	Previous tr-ARPES investigation of p doped Bi ₂ Se ₃	132

7.2.4	Previous tr-ARPES investigation of Bi_2Te_3	133
7.3	Ultrafast photo-doping and effective Fermi-Dirac distribution of the Dirac particles in Bi_2Se_3	135
7.4	Supplemental Material: Ultrafast photo-doping and effective Fermi-Dirac distribution of the Dirac particles in Bi_2Se_3	141
7.4.1	1. Extracting the Fermi-Dirac distribution term from the EDC fit . .	141
Concluding Remarks		143
Bibliography		145
Curriculum Vitae		I

Experimental Method and Principles

Contents

1.1 Photoemission spectroscopy	1
1.1.1 Historical introduction	1
1.1.2 General formulation	2
1.1.3 1- Versus 3-step models	3
1.1.4 Kinematic of Angle-Resolved Photoemission Spectroscopy	5
1.1.5 One particle spectral function formulation	7
1.1.6 EDC and MDC lineshapes of the quasiparticle peak	8
1.1.7 Direct and indirect transitions	10

1.1 Photoemission spectroscopy

1.1.1 Historical introduction

Photoemission spectroscopy (PES), or photoelectron spectroscopy, is an extremely effective and straightforward method to study the electronic structure of atoms, molecules, solids and adsorbates [1]. The term photoemission spectroscopy generally refers to a wide set of experimental techniques based on the application of the photoelectric effect. The first evidence of the photoelectric effect is ascribed to the work of Hertz, in 1887: the electric discharge yielded between two electrodes increases when the cathode is illuminated by ultraviolet (UV) light. After the discovery of the electron by Thompson, different works have shown this phenomenon to be due to electrons emitted from the cathode following the stimulation of the impinging UV light [2, 3]. The accurate study of the dependence between the current and the velocity of the emitted electron and the intensity and frequency of the light [3] clearly demonstrated that the velocity (energy) of the electron is independent on the light intensity, whereas their number is proportional to the light intensity. This observation appeared to be in conflict with the Maxwell description of light as an electromagnetic wave.

This apparent paradox was solved by Einstein in 1905. Einstein's description of the photoelectric effect is based on the assumption that the incident light is constituted by energy quanta, now called photons. This discovery, together with the work of Planck, represented the starting point for the development of Quantum Mechanics, and for his paper "On a Heuristic Viewpoint Concerning the Production and Transformation of Light" Einstein was awarded the Noble Prize in Physics in 1921.

In parallel with the theoretical investigation, from the 60's, the photoelectric effect found experimental applications in the study of solid state electronic structures. This development was possible thanks to the improvements in ultra-high-vacuum (UHV) techniques, and the progresses in UV and x-ray radiation sources. The advent of compact x-ray sources opened the way to the development of Electron Spectroscopy for Chemical Analysis (ESCA), thanks to Siegbahn's work, which led to the Noble Prize for Physics in 1981.

A major step forward in the study of the electronic band structure of solids is attributable to the working out of hemispherical analyzers, with parallel detection of angle and energy dispersion of the photo-emitted electrons [4]. Recently, the requirement for ultra-high energy and angular resolution led to the development of laser-based photoemission spectroscopy [5]. Among lasers, the Ti:Sapphire is capable to produce pulses on the femtosecond timescale (50 - 200 fs). It offers thereby the possibility to study the out-of-equilibrium electronic properties and the relaxation dynamics in solids via time-resolved photoemission spectroscopy in pump-probe experiments [6].

1.1.2 General formulation

Photoemission spectroscopy is a "photon-in" \rightarrow "electron-out" technique. Figure 1.1 illustrates schematically the relation between the electronic structure of a sample and the resulting PES spectrum. A monochromatic light beam illuminates the sample, which may be in solid, liquid or gaseous form. Photons are adsorbed by the electrons of the material and, when the energy transferred is sufficiently high, an electron can be emitted as a photoelectron. From the energy conservation law, one has direct access to the energy distribution of electrons in the ground state of the system:

$$E = h\nu - \Phi - E_B \quad (1.1)$$

where E_B is the binding energy of the electron and Φ is the work function of the sample. The latter represents the minimum energy necessary to remove one electron from the material, i.e. the energy barrier given by the difference in energy between the Fermi level (E_F) (or chemical potential, μ) and the vacuum level (E^{vac}).

If the one-electron approximation is valid, and one can express the initial and final state of the photoemission process as single Slater determinants for the N particles and $N-1$ particles systems, hence the binding energy is proportional to the Hartree-fock orbital energy following the relation [7]:

$$E_B = -\varepsilon_k. \quad (1.2)$$

In the one-electron approximation the PES spectrum can be expressed as

$$I(E_B) \propto \sum_k \delta(E_B + \varepsilon_k) \propto N(-E_B). \quad (1.3)$$

Thus, the PES spectrum is proportional to the density of the occupied electronic states $N(E)$.

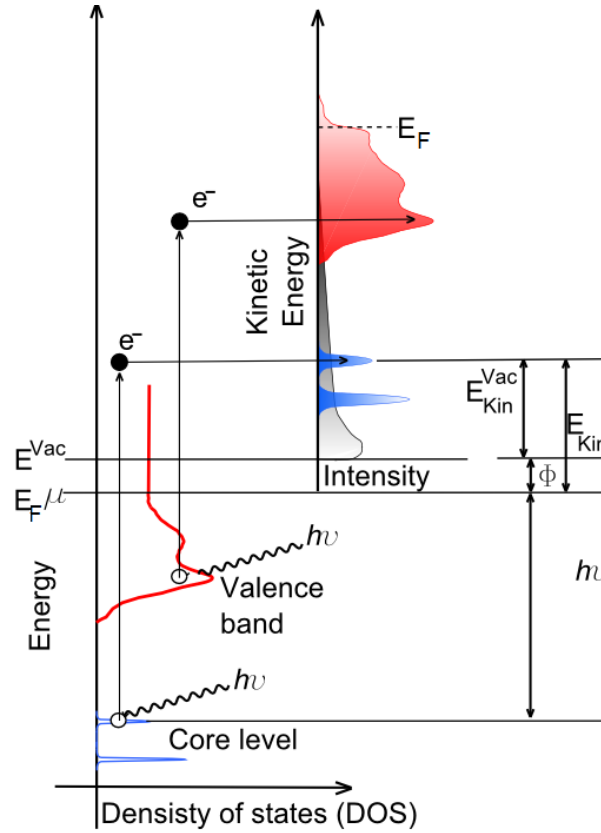


Figure 1.1: Schematic diagram of the principle of photoemission spectroscopy (PES). This shows the relation between the energy levels (core levels and valence band) in a solid and the electron energy distribution produced by photons of energy $h\nu$ [1].

1.1.3 1- Versus 3-step models

One-step is the term commonly used to indicate the description of the photoemission process as a continuous single event. The process results in a photo-excited electron going into a final state in the vacuum, obeying appropriate continuity conditions at the surface of the solid.

It results *formally* easier to discuss the photoemission in terms of three independent events [8, 9]: (1) electron optical excitation, (2) electron transport through the solid, (3) electron escape from the surface.

In the first step the photoexcitation induces an optical transition between the initial and final *bulk* states. In the second step the excited electron travels to the surface, interacting with the lattice and the surrounding electrons and eventual impurities. During this process, a large amount of electrons lose part of their kinetic energy due to scattering events. Therefore, it is impossible to use the energy conservation law of eq. 1.1 to extract their binding energies. For this reason all the electrons which undergo an inelastic scattering process are called secondary electrons, to be distinguished from the primary electrons. The secondary

electrons constitute an unstructured background whose intensity increases at low kinetic energy (the black area of the spectra in Fig. 1.1).

A second important consequence of the electron-electron and electron-phonon interactions is the existence of an electron mean free path λ . It is defined as the length that an electron can travel in the sample with a probability equal to e^{-1} of not undergoing any scattering event. The mean free path defines the escape depth, the thickness of the sample which contributes to the primary signal. Interestingly, even though λ^{-1} is proportional to the dielectric function of the material [1] (which is specific of the material), the mean free path as a function of the kinetic energy yields a roughly "universal" curve (reported in Figure 1.2). For UV light sources based on He discharge (with an intense emission line at 21.22 eV) the primary photoemitted electrons are originated from the very few topmost atomic layers of the surface. The surface sensitivity of the "conventional" photoemission spectroscopy represents a powerful advantage for exploring the electronic properties at the surface: the Shockley surface states [10] and the topologically protected surface states of the newly discovered topological insulators [11] represent some of the nowadays hottest topics in condensed matter physics.

The drawback of the surface sensitivity is the requirement for atomically clean surfaces, and the necessity for ultra-high-vacuum conditions (below 10^{-9} mbar). The aim to overcome the restriction to the study of surfaces has pointed towards two different directions, as one could infer from the behavior of the mean free path. The first consists in the use of very high photon energies (keV), provided by the new generation of synchrotron sources, while the second consists in the use of very low photon energies, which can be generated by table-top laser sources (5-7 eV) [12].

During the process of escape from the sample surface, in the third step of the three-step model, the photoelectron overcomes the surface barrier potential and it loses an energy equal to the work function of the material.

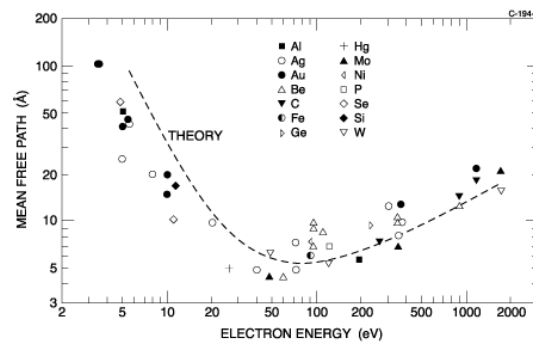


Figure 1.2: Universal curve describing the mean free path of photoemitted electron in a material. The curve has a minimum in the UV range, and it explains the surface sensitivity of UV photoemission spectroscopy.

1.1.4 Kinematic of Angle-Resolved Photoemission Spectroscopy

Photoemission spectroscopy has been discussed in the previous paragraphs only in terms of the energy conservation law. One of the most important advantages of PES is the possibility to analyze not only the energy distribution of the photoemitted electrons, but also their distribution as a function of the photoemission angles (θ , ϕ), in the so called Angle Resolved Photoemission Spectroscopy (ARPES). In this way, the wave-vector (or momentum, $\bar{K} = \bar{p} / \hbar$) of the photoemitted electron in the *vacuum* is completely determined, along with its kinetic energy E_{kin} . While the modulus of the momentum is given by $K = \sqrt{2mE_{kin}} / \hbar$, the three distinct cartesian components depend on the azimuthal (ϕ) and polar (θ) angles, defined by the experimental geometry (see Fig. 1.3)):

$$K_x = \frac{1}{\hbar} \sqrt{2m_e E_{kin}} \sin\theta \cos\phi \quad (1.4)$$

$$K_y = \frac{1}{\hbar} \sqrt{2m_e E_{kin}} \sin\theta \sin\phi \quad (1.5)$$

$$K_z = \frac{1}{\hbar} \sqrt{2m_e E_{kin}} \cos\theta \quad (1.6)$$

with m_e the free electron mass.

At this stage, it is necessary to find a relation between the kinetic energy and the wave-vector of the photoemitted electron in the vacuum and the electronic dispersion $E(\bar{k})$ in the solid. One could start from the energy conservation law (eq 1.1) and the momentum conservation law

$$\bar{k}_i - \bar{k}_f = \bar{k}_{h\nu} \quad (1.7)$$

where the indexes i and f refer to the initial and final states in the *bulk*. $\bar{k}_{h\nu}$ is the momentum of the incoming photon, which is negligible for the UV and soft x-ray photons. For this reason in the first step of the three-step model, any photon absorption is equivalent to a "vertical" transition in the electronic band structure. Such transition is possible for an electron described by a quadratic energy dispersion (free-electron like) only if the periodic crystal potential is taken into account and the band structure is depicted in the so-called reduced-zone scheme [8, 9].

While the binding energy E_B of the electron in the initial state is directly obtained from eq 1.1, recovering the crystal electronic momentum (\bar{k}_i) from the measured wave-vector of the photoemitted electron (\bar{K}_f) is more complex and it requires to take into account carefully the effect of the surface. The broken translation symmetry along the direction orthogonal to the surface (z) makes the wave-vector k_z not-a-good quantum number, whose conservation is not protected when the optically-excited electron leaves the sample surface. The value of k_z is modified by the potential barrier, the so-called inner potential (V_0). The two in-plane components of the crystal momentum are conserved. A simple schematization of the escape condition is shown in Fig. 1.3, where the index f is omitted for all the vectors and suffixes *int* and *ext* indicate the wave-vector inside the crystal and in the vacuum. The set of fundamental relationships at the base of ARPES band mapping are:

$$K_{fx} = k_{fx} = k_{ix} = \frac{1}{\hbar} \sqrt{2m_e (\hbar\nu - \phi - E_B)} \sin\theta \cos\phi \quad (1.8)$$

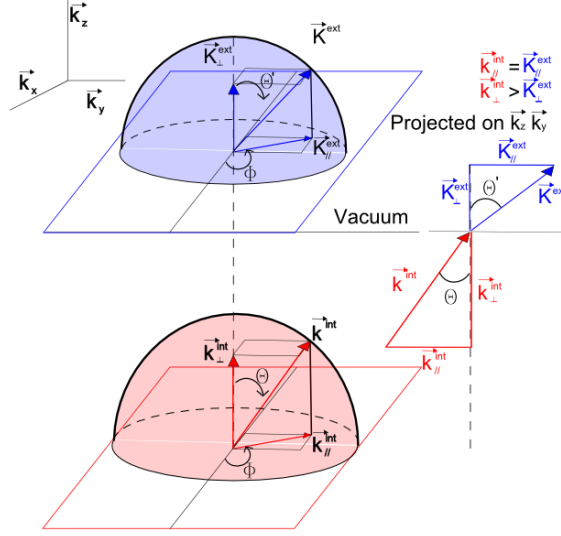


Figure 1.3: Schematic diagram of the emission of an electron from a solid to vacuum through the atomically flat single-crystal surface. The red and blue hemispheres show the external and internal regions, respectively. The right of the image shows the same but projected on the k_{yz} plane. A refraction takes place at the crystal-vacuum interface where only the in-plane k components are conserved.

$$K_{fy} = k_{fy} = k_{iy} = \frac{1}{\hbar} \sqrt{2m_e(\hbar\nu - \phi - E_B)} \sin\theta \sin\phi \quad (1.9)$$

For what concerns the missing information relative to k_z one could start from the calculated band structure, or from simple free-electron model for the final Bloch states:

$$E_f(k) = \frac{\hbar^2 k^2}{2m_e} - |E_0| = \frac{\hbar^2 (k_{\parallel}^2 + k_{\perp}^2)}{2m_e} - |E_0| \quad (1.10)$$

where E_0 corresponds to the bottom of the valence band. Because $(\hbar^2 k_{\parallel}^2)/2m_e = E_{kin} \sin^2\theta$ one obtains

$$k_{\perp} = \frac{1}{\hbar} \sqrt{2m_e(E_{kin} \cos^2\theta + V_0)} \quad (1.11)$$

with $V_0 = |E_0| + \phi$. Different strategies are used in order to determine V_0 , recovering the three-dimensional band structure of a solid [8, 9]. The most convenient is to infer V_0 from the periodicity of the band dispersion along k_z , $E(k_z)$, which is experimentally obtained by varying the incident photon energy.

ARPES has become particularly popular for the study of layered compounds (cuprate and pnictide high temperature superconductors HTSC), and more generally for strongly two-dimensional systems, for which the uncertainty in k_z is less important. Most of the systems subject of investigation in this thesis belong to the family of materials with reduced dimensionality, for which the band mapping is achieved by ARPES at fixed excitation energy.

1.1.5 One particle spectral function formulation

The derivation of eq. 1.3 requires the use of the one-electron approximation, but in order to discuss more realistically ARPES spectra, in particular in the presence of electronic correlation, it is necessary to go beyond this simple model.

In the sudden approximation limit, it is possible to express the complete N particles wave-function describing the final state Ψ_f^N as a properly antisymmetrized product of two contributions: the photoelectron wave-function ϕ_f^k and the final state wave-function Ψ_f^{N-1} describing the N-1 particles system after sudden removal of one electron,. The latter can be projected on the excited states of the N-1 particles system with eigenfunctions $\Psi_{f,s}^{N-1}$ and eigenenergy E_s^{N-1}

$$\Psi_f^N = A\phi_f^k \cdot \sum_s \Psi_{f,s}^{N-1}. \quad (1.12)$$

For the initial state it is commonly assumed that the wave-function can be written as a single Slater determinant product of an one-electron part ϕ_i^k and a (N-1) particles term

$$\Psi_i^N = A\phi_i^k \Psi_i^{N-1} \quad (1.13)$$

where, however, Ψ_i^{N-1} is not an eigenstate of the N-1 particles Hamiltonian. In a second quantization formulation the Ψ_i^{N-1} function is expressed as $\Psi_i^{N-1} = c_k \Psi_i^N$, where c_k is the annihilation operator for an electron with momentum \bar{k} .

By substituting the two given expressions for the initial and final states in the Fermi golden rule, to calculate the total photoemission intensity as a function of E_{kin} at a momentum \bar{k} , one obtains:

$$I(\bar{k}, E_{kin}) = \sum_{f,i} |M_{f,i}^k|^2 \sum_s | \langle \Psi_{f,s}^{N-1} | c_k | \Psi_i^N \rangle |^2 \quad (1.14)$$

where the expression has been formally simplified disregarding all the Dirac δ functions describing mathematically the energy and momentum conservation (total and in-plane component).

The expression for the photocurrent can be rewritten by introducing the one-particle spectral function $A^-(\bar{k}, \hbar\omega) = \sum_s | \langle \Psi_{f,s}^{N-1} | c_k | \Psi_i^N \rangle |^2 \delta(\hbar\omega - E_{f,s}^{N-1} - E_i^N)$ where $\hbar\omega$ is the electron energy with respect to the Fermi level

$$I(\bar{k}, \hbar\omega) = I_0(\bar{k}, \nu, A) A^-(\bar{k}, \hbar\omega) f(\hbar\omega) \quad (1.15)$$

where the Fermi-Dirac distribution function $f(\hbar\omega)$ is introduced to take properly into account the fact that photoemission probes only the occupied electronic states. The term $I_0(\bar{k}, \nu, A)$ is proportional to the dipole matrix element and it depends therefore on the momentum \bar{k} , the photon energy and the polarization of the light.

The next step in the many-body treatment of the photoemission intensity consists in introducing the time ordered one-electron Green's function (or propagator), which describes the evolution in time of a state in which an electron is removed from the system in a given \bar{k} state at time zero. The real space propagator is easily expressed in the energy-momentum

space by applying a Fourier transform

$$G^-(\bar{k}, \hbar\omega) = \sum_s \frac{|\langle \Psi_{f,s}^{N-1} | c_k | \Psi_i^N \rangle|^2}{\hbar\omega - E_s^{N-1} - E_i^N + i\eta} \quad (1.16)$$

where η is a positive infinitesimal. In the limit $\eta \rightarrow 0^+$ the identity $(x + i\eta)^{-1} = P(1/x) - i\pi\delta(x)$ is valid, where P stands for the principal value. By using this identity it is possible to rewrite the Green's function as

$$G^-(\bar{k}, \hbar\omega) = \sum_s (|\langle \Psi_{f,s}^{N-1} | c_k | \Psi_i^N \rangle|^2) (P(\frac{1}{\hbar\omega - E_s^{N-1} - E_i^N}) - i\pi\delta(\hbar\omega - E_s^{N-1} - E_i^N)). \quad (1.17)$$

Hence, a simple relation connecting the Green's function to the one-particle spectral function exists

$$A(\bar{k}, \hbar\omega) = -\frac{1}{\pi} \text{Im } G(\bar{k}, \hbar\omega). \quad (1.18)$$

Initially, one can consider the simplest case in which electrons are not interacting. Hence, the Green's function is given by

$$G^0(\bar{k}, \hbar\omega) = \frac{1}{E - E^0(k) - i\eta} \quad (1.19)$$

Equation 1.19 is particularly important because the Green's function can be properly modified in presence of many-body interaction, and the formalism is now naturally transferred to the ARPES photoemission intensity via the one-particle spectral function.

If one expresses the electron proper self energy as $\Sigma(\bar{k}, \hbar\omega) = \Sigma'(\bar{k}, \hbar\omega) + i\Sigma''(\bar{k}, \hbar\omega)$ the Green's function, the one-particle spectral function and the total photoemission intensity can be expressed as

$$G(\bar{k}, \hbar\omega) = \frac{1}{\hbar\omega - \varepsilon_k - \Sigma(\bar{k}, \hbar\omega)}, \quad (1.20)$$

$$A(\bar{k}, \hbar\omega) = -\frac{1}{\pi} \frac{\Sigma''(\bar{k}, \hbar\omega)}{[\hbar\omega - \varepsilon_k - \Sigma'(\bar{k}, \hbar\omega)]^2 + [\Sigma''(\bar{k}, \hbar\omega)]^2}, \quad (1.21)$$

$$I(\bar{k}, \hbar\omega) = -\frac{1}{\pi} I_0(\bar{k}, \nu, A) f(\hbar\omega) \frac{\Sigma''(\bar{k}, \hbar\omega)}{[\hbar\omega - \varepsilon_k - \Sigma'(\bar{k}, \hbar\omega)]^2 + [\Sigma''(\bar{k}, \hbar\omega)]^2}, \quad (1.22)$$

where ε_k is the single particle electron band energy, and the real and imaginary part of the self energy contain all the information relative respectively to the energy renormalization and to the intrinsic lifetime of the photo-induced hole. In particular the latter results equal to the FWHM of the lorentzian distribution, hence equal to $2\Sigma''(\bar{k}, \hbar\omega)$.

1.1.6 EDC and MDC lineshapes of the quasiparticle peak

ARPES spectra are characterized by different possible levels of interpretation, depending on the theoretical assumptions and knowledge *a priori* on the system investigated. ARPES

is one of the few techniques with a direct insight in the band structure of a material. Electronic effective mass m^* and Fermi velocity v_f can be extracted and compared to *ab initio* calculations.

The formalism introduced in the previous paragraph opens a deeper level of description, based on the analysis of the spectral lineshape. Given the experimental $I(\bar{k}, \hbar\omega)$ (where \bar{k} describes now the two-dimensional in-plane photoelectron momentum) two main strategies are possible. The first consists in analyzing at a fixed momentum \bar{k}^* the so called Energy Distribution Curve (EDC) $I(\bar{k}^*, \hbar\omega)$. The second instead consists in fixing the binding energy $\hbar\omega^*$, thus analyzing the evolution of the Momentum Displacement Curve (MDC) $I(\bar{k}, \hbar\omega^*)$.

The expression of the one-particle spectral function eq. 1.21 can be further modified by adopting suitable approximations to describe the electron-electron and electron-phonon interaction in the material. Different theoretical models have been developed, and in the following a very simple example will be given for the case of the Fermi liquid (FL) model [8, 9, 1, 13].

In proximity of the Fermi level ($\varepsilon_F - \hbar\omega \gg \Sigma''$), the interacting electron system can be mapped one-to-one in an interacting fermions system whose particles are called *quasiparticles*. Physically the quasiparticle is interpreted as an electron "dressed" with virtual excitations which move coherently with it. Formally the quasiparticle spectral function is expressed as the sum of two terms which describe the coherent and incoherent parts. The latter is experimentally difficult to be defined and interpreted rigorously, even though some models were proposed [14]. The former term contains all the low energy excitations and is equal to

$$A(\bar{k}, \hbar\omega) = \frac{1}{\pi} \frac{(Z_{k_F} b)(\hbar\omega)^2}{[\hbar\omega - Z_{k_F} \varepsilon_k]^2 + (Z_{k_F} b)^2 (\hbar\omega)^4} \quad (1.23)$$

where the self energy expression for the FL system $\Sigma(\bar{k}, \hbar\omega) = a\hbar\omega + ib(\hbar\omega)^2$ has been used, and the renormalization constant $Z_{k_F} = (1 - \partial\Sigma'/\partial\omega)^{-1} = \frac{1}{1-a}$ has been introduced, as well [15, 16].

The k -dependence of the self energy is neglected and this explains the difference in the MDC and EDC analysis. At fixed energy the spectrum is characterized by a simple analytical form and an MDC is described by a lorentzian centered at $\bar{k} = \bar{k}_f + [\hbar\omega(1-a)]/v_f^0$ with FWHM $\Delta E_{FWHM} = 2b(\hbar\omega)^2/v_f^0$, where v_f^0 is the bare Fermi velocity normal to the Fermi surface $\varepsilon_k \simeq v_f^0(\bar{k} - \bar{k}_f)$. The behavior of an EDC reflects the strong dependence of $\Sigma(\bar{k}, \hbar\omega)$ on the energy. In the FL system the quasiparticle peak sharpens up approaching the Fermi level, where the lifetime of the quasiparticle is infinite.

Deviations from this behavior are interesting as fingerprint of the breakdown of the FL model. Such effects may arise from different ingredients such as reduced dimension (the one-dimensional case with the Luttinger liquid [17], Luttinger-Tomonaga liquid [18]), disorder and interaction with impurities [19], or very strong correlations which deplete intensity at the Fermi level, by transferring spectral weight from the coherent to the incoherent part of the spectral function [20] (as in the case of electron phonon coupling and strong polaron formation [14], Peierls instability [18] and Charge Density Wave [21]).

When facing the problem of extracting the self energy from the the experimental line

width one should be aware of the fact that the intrinsic physical information is convolved with experimental effects. In an ARPES spectrum, in fact, the measured lifetime is given by $\frac{1}{\tau} = \frac{1}{\tau_{el}} + \frac{1}{\tau_h}$. Hence, it results from the combination of the photo-electron lifetime τ_{el} and the hole lifetime τ_h . For particular experimental conditions (photoemitted electron at grazing incidence) the line width results even smaller than the inverse of the photo-hole lifetime [22]. Nevertheless, it results that for two-dimensional systems the latter term is negligible and the hole lifetime can be extracted by the ARPES spectra [23].

1.1.7 Direct and indirect transitions

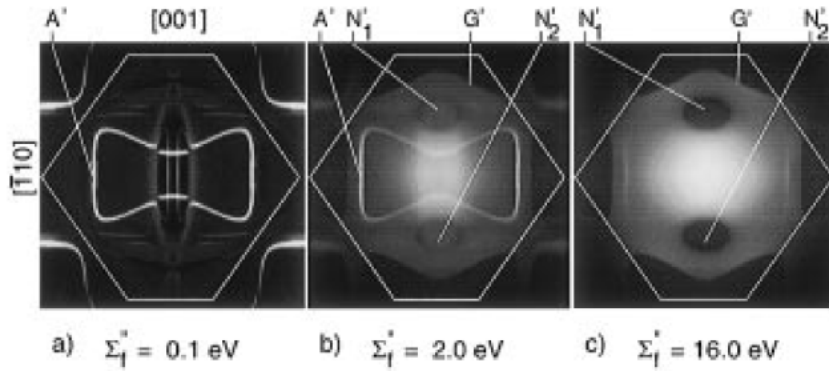


Figure 1.4: Theoretical Fermi Surface spectra from Cu(110) for 21.2 eV unpolarized light using three different values of the final state damping. (a) and (c) refer to artificially low (0.1 eV) and high (16 eV) values of damping, respectively; the damping (2 eV) in (b) is representative of the physical situation. Letters A' , G' and N' denote various spectral features discussed in the text. Whites denote regions of high spectral intensity [24].

This thesis is concerned with ARPES studies of metal-metal interfaces. The escape depth of the photoemitted electrons is of the order of few monolayer (MLs), therefore larger than the surface region itself. Hence, a non negligible fraction of the photoelectrons are originated from the substrate. Different substrates have been used, but they are all metals with a partially filled three-dimensional conduction band. While a simple qualitative analysis of the band structure and of the symmetry of the band contours is straightforward also in the presence of this "parasite" extra signal, a more quantitative analysis (such as a description of the EDC/MDC lineshapes) requires some more considerations.

From the kinematic analysis it results that, at fixed excitation energy, only one particular k_z component of the overall three-dimensional band structure is probed. Unfortunately, this appears experimentally to be valid if only direct transitions are taken into account in the optical absorption step. In the study of interfaces it is necessary to disentangle the signal from a continuous unstructured background observed for all the different $k_{//}$ values. A non negligible intensity and a clear Fermi Edge are normally observed even for k values where momentum conservation (eq. 1.7) is not fulfilled. Lindroos and Bansil have already treated this intriguing problem, in order to address the origin of extra features in the constant initial

energy, angle scanned spectrum [24]. The additional photointensity is found proportional to the k_z integrated density of states (DOS), and it originates from indirect transitions in the optical absorption. Computational analysis was performed in the frame of one-step model taking into account multiple scattering effect in the initial and final electronic states. The calculations were performed with three different values of the imaginary part of the final state self energy Σ_f'' (0.1 eV, 2 eV and 16eV respectively). This physical quantity is found to be connected to the mean free path of the photoemitted electron λ_f via the relation

$$\lambda_f = \frac{\sqrt{2E}}{2\Sigma_f''}. \quad (1.24)$$

The three studied cases correspond respectively to a very long mean free path (200 Å), a more physical representative situation and finally to a very small value of λ_f with all the photoemitted electrons essentially emanate from the very topmost layer. Figure 1.4 displays the results of the calculation for the Cu(110) surface. In panel **a** for the large value of λ_f the spectral feature, labelled A' arises from direct transition. With increasing Σ_f'' the state become more diffuse and DOS related feature (G') gain intensity. For the (110) surface the neck of the complete three-dimensional band structure is projected into two dark areas (N'_1 and N'_2) which intersect G' . Figure 1.4 **b** shows clearly that in the case of Σ_f'' values close to reality one should expect the simultaneous presence of features derived both from direct transition and from the k_z integrated one-dimensional DOS.

Spin Orbit Interaction at Surfaces

Contents

2.1	Surface states in metals	13
2.1.1	The origin of surface states	13
2.1.2	Spin splitting in the Au(111) surface state	16
2.1.3	Spin-split surface states in different material surfaces	25
2.2	Giant spin splitting at surfaces and interfaces	31
2.2.1	Metallic surface alloys	31
2.2.2	Exporting the Rashba-Bychkov effect in semiconductors	39
2.2.3	Spin splitting in confined quantum well systems	43

2.1 Surface states in metals

2.1.1 The origin of surface states

Electrons in a solid are described as waves solutions of the Schrödinger equation under a periodic potential. The problem is simplified by introducing periodic boundary conditions and by considering an infinite crystal [25, 26]. These approximations represent strong *ansatz* on the character of the solutions which describe waves penetrating into the bulk and periodic over the entire crystal. The infinite crystal approximation disregards all the possible solutions which are strongly localized at the surface of the crystal, the *surface states*. More detailed review of the origin of the surface states and their experimental investigation can be found in ref. [27] and ref. [28].

The general electronic properties of a crystal surface were derived for the first time in the 1930s [29, 30, 31, 32]. In the case of a finite crystal two main consequences are found: any "bulk" solution of the Schrödinger equation decays exponentially in the vacuum in order to match the solution outside. Secondly, besides the penetrating solutions, new eigenfunctions are possible with an exponential decaying behavior also *inside* the crystal. The corresponding states are therefore localized at the surface.

The mechanism of localization was described in different theoretical models. In all the cases the damping of the wave-function in the direction orthogonal to the surface is formally accounted for by introducing an imaginary part of the wave-vector in that direction. In the first model, developed by I.E. Tamm [29], the surface atoms are not equivalent to the bulk ones, because of the missing neighbors. This asymmetry is reflected in the crystal

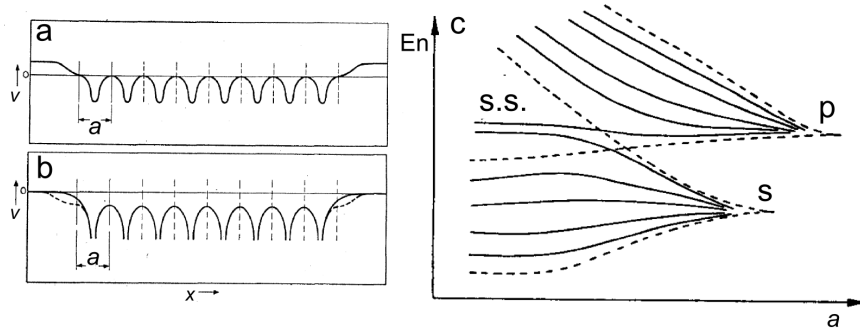


Figure 2.1: Crystal potentials modelled to describe the formation of surface states. **a** is a potential periodic around the center of each atom, as the one introduced by Shockley. **b** is the potential corresponding to Goodwin's "tight binding" approximation developed on the basis of the Tamm model. **c** shows schematically the formation of Shockley surface states in the inverted band gap when the s and p bands cross [32].

potential, whose periodicity is broken at the outer edges of the end crystal cells. In a tight binding (TB) picture [31, 33] there is a difference between the on-site energy at bulk and surface sites, and this difference term (ϵ) competes with the hopping energy term (γ). This competition results in the possibility to localize states at the surface sites, where the bulk band states have nearly no amplitude.

A second mechanism for localization of a state at the surface was developed in a nearly free-electron model (NFE) by Shockley [32] following the pioneer work of Maue [30]. In this model the (one-dimensional) crystal is described by a periodic potential in which every atom is represented by a potential well symmetric around the nuclei, as shown in Figure 2.1 **a**. Figure 2.1 **b** shows instead the potential modelled by Goodwin, on the basis of the Tamm model, with a difference in the potential associated to the termination atom. The so-called Shockley states are possible in the presence of an inverted band gap. Band gaps can be described as the result of destructive interference between bulk standing waves. When two states with s and p characters mix, for suitable coupling potential, the p state may lie below the s state, leading to an inverted band gap. In the resulting forbidden energy window a surface state with complex k can connect the two sides of the gap. Figure 2.1 **c** shows the evolution of the s p bands as a function of the atomic distance a : when the bands ordering inverts, a surface state is formed [33]. The Tamm and Shockley models are basis for further recent theoretical studies in the frame of tight-binding, nearly free-electron models, multiple reflection approach and ab-initio calculation with pseudo-potential [34, 35, 36, 37].

The first experimental evidence of the existence of surface states is attributed to optical absorption experiments on semiconductors [38, 39], but the surface character makes this research topic especially attractive for ARPES and for scanning tunnelling microscopy/spectroscopy (STM/STS). One of the most famous results obtained by the latter technique is the observation of quantum interference between the surface wave-functions scattered

by atomic defects, or step edges, or by an artificial quantum corral. STS succeeded also in providing a numerical evaluation of the photo-hole lifetime Γ_h for Shockley surface states in the inverted L gap of noble metals (Cu, Ag, Au) [40, 41]. Nevertheless, only ARPES offers the possibility of direct insight in the band dispersion $E(\vec{k})$ of the surface states, which is the focus of the next section.

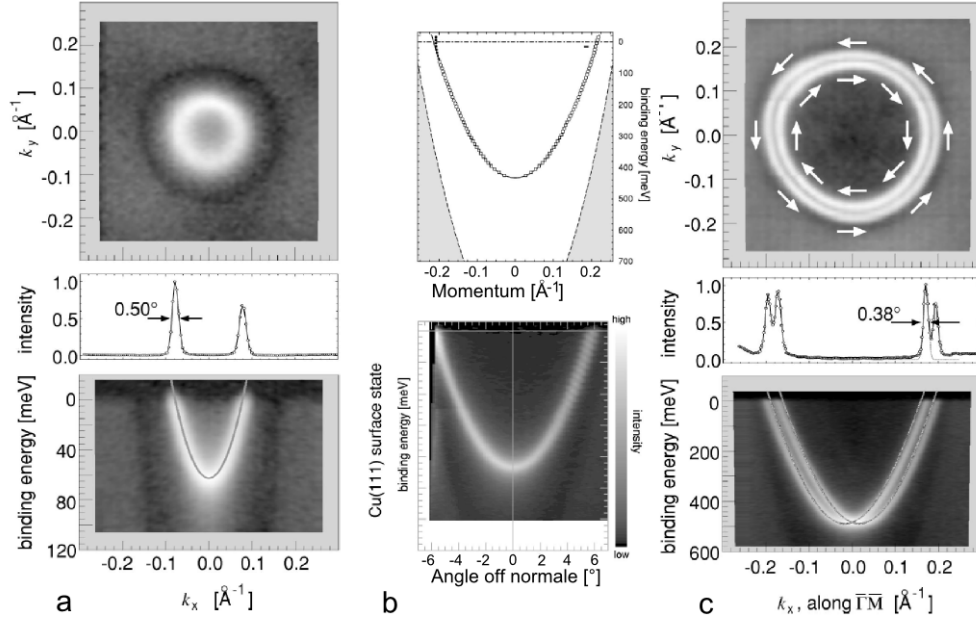


Figure 2.2: **a-c** two dimensional ARPES images of the Shockley surface states in the L gap of Ag(111), Cu(111) and Au(111) respectively (**a** and **c** from [42] and **b** from [43]). For Ag(111) and Au(111) the Fermi Surface is also reported in the upper panels. For the latter the spin splitting is clearly resolved.

2.1.2 Spin splitting in the Au(111) surface state

The advent of ARPES with high energy and angular resolution opened the way to the study of surface states in the L-gap of noble metals. The L-gap results from the projection of the three-dimensional bulk Fermi surface neck onto the (111) crystal surface. The very high momentum resolution achieved for the first time by LaShell *et al.*, with the use of ArI line at $h\nu = 11.83\text{eV}$, enabled them to clearly distinguish a doubling of the surface state of Au(111) [10]. Afterwards, Reinert *et al.* performed a detailed study by comparing the surface state of the Au(111) and Ag(111) surfaces [42], and their results are shown in Figure 2.2, along with similar results for Cu(111) [43]. Interestingly, a clear signature of the L gap is also visible in all the ARPES images, as a low intensity area surrounding the surface state.

The doubling of the Au(111) surface state was correctly interpreted by LaShell as the result of strong spin-orbit (SO) interaction, which lifts the spin degeneracy of the bands at the surface. A formal description of the effect was later proposed by Petersen and Hedegård [44] in a tight binding approach, while the case for a free electron model had already been described by Rashba and Bychkov several years before the work of LaShell [45].

In a relativistic description, an electron travelling at the surface in an electric field \vec{E} with velocity \vec{v} , experiences an effective magnetic field \vec{B} , which in its rest frame is equal to $B = 1/c^2 \cdot \vec{v} \times \vec{E}$. This effective field is coupled to the electron spin via a Zeeman like term. In a non relativistic description, the Schrödinger equation is corrected starting from the Dirac equation by expanding it to the lowest order in v^2/c^2 . In this way, the perturbation hamiltonian takes the form $H_{SOC} = \frac{\hbar^2}{4im^2c^2} (\vec{\nabla}V \times \vec{p}) \cdot \sigma$, where V is the potential at the surface where the electron moves.

In the case of surface states, the electrons form a quasi two-dimensional free electron gas at the surface, hence $\vec{\nabla}V = dV/dz\vec{e}_z$ where \vec{e}_z indicates the unit vector orthogonal to the sample surface. The resulting spin-orbit Hamiltonian assumes the so-called Rashba Bychkov form [45]

$$H_{SOC} = \alpha_R(\vec{e}_z \times \vec{p}) \cdot \sigma, \quad (2.1)$$

with strength parameter α_R proportional to the out-of-plane potential gradient. The effect of this perturbation Hamiltonian, when it is applied to a free electron gas with parabolic dispersion, is the lifting of the spin degeneracy: the original parabolic dispersion is split in two branches with energies

$$E = \frac{k^2}{2m} \pm \alpha_R k. \quad (2.2)$$

The degeneracy of the eigenstates of a given Hamiltonian is related to the symmetry of the problem. The spin degeneracy results as a combined effect of time reversal (TR) symmetry and inversion symmetry (I), which introduce respectively the two following conditions

$$E(\vec{k}, \uparrow) = E(-\vec{k}, \downarrow), \quad (2.3)$$

$$E(\vec{k}, \uparrow) = E(-\vec{k}, \uparrow). \quad (2.4)$$

Only in the case of broken inversion symmetry the resulting Kramers degeneracy relation $E(\vec{k}, \uparrow) = E(\vec{k}, \downarrow)$ can be violated. Even though it remains strictly valid at all the time

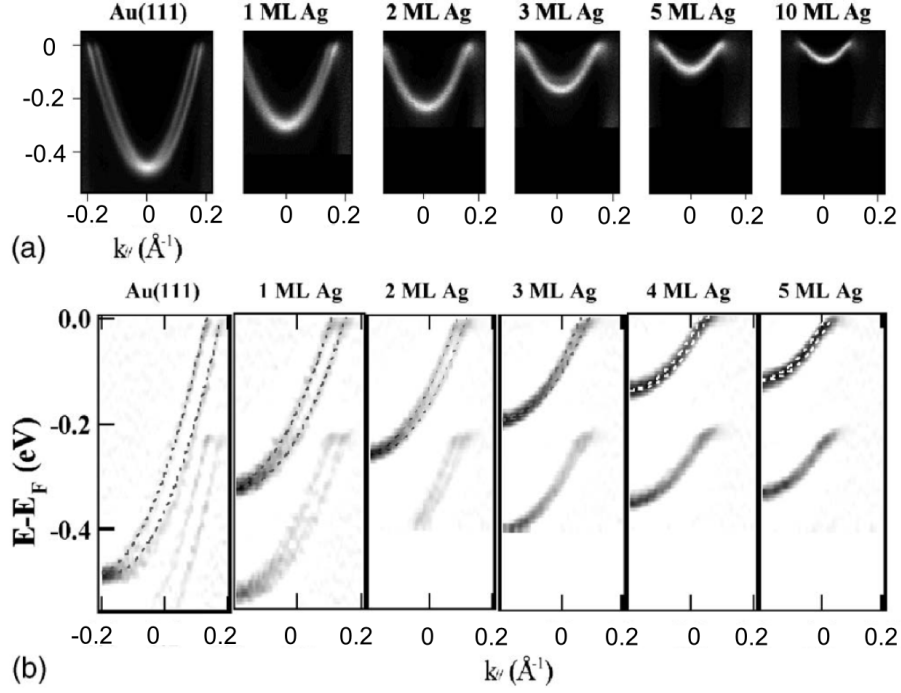


Figure 2.3: ARPES study of the Ag/Au(111) coverage dependence: **a** obtained with He-I line; **b** row data and second derivative of similar coverage dependent study with Ar-I excitation [49, 50, 51].

invariant high symmetry points of the Brillouin zone (*e.g.* $\bar{\Gamma}$ and \bar{M} in the hexagonal lattice). The lifting of the spin degeneracy was proposed for the first time in the case of non-centrosymmetric bulk crystals, where the effect takes respectively the name of Rashba or Dresselhaus splitting, depending on the crystal structure (respectively wurtzite [46] and zinc-blend [47]). Only very recently, ARPES and spin resolved ARPES reported the existence of spin split states in the polar BiTeI compound, which lacks inversion symmetry in the bulk [48].

In general, the Kramers degeneracy can be broken at the surface of any material, since it lacks inversion symmetry. This sets the bases for the Rashba-Bychkov (RB) model, which describes qualitatively the nature of the splitting of the surface states of Au(111). Unfortunately the theory fails in providing a quantitative value for such energy splitting. LaShell *et al.* also recognized the fact that in a nearly free electron model the RB term yields a splitting of 10^{-3} meV, 4 orders of magnitude smaller than the experimental value (2 meV at the Fermi level) [10]. This is an artificial effect of the RB model, and a consequence of the small value of the gradient potential at the surface. The $6p$ states of Au are characterized by a larger spin-orbit coupling (0.4 eV), resulting from the larger gradient potential in proximity of the nuclei. Both the terms should be taken correctly into account for quantitative comparison.

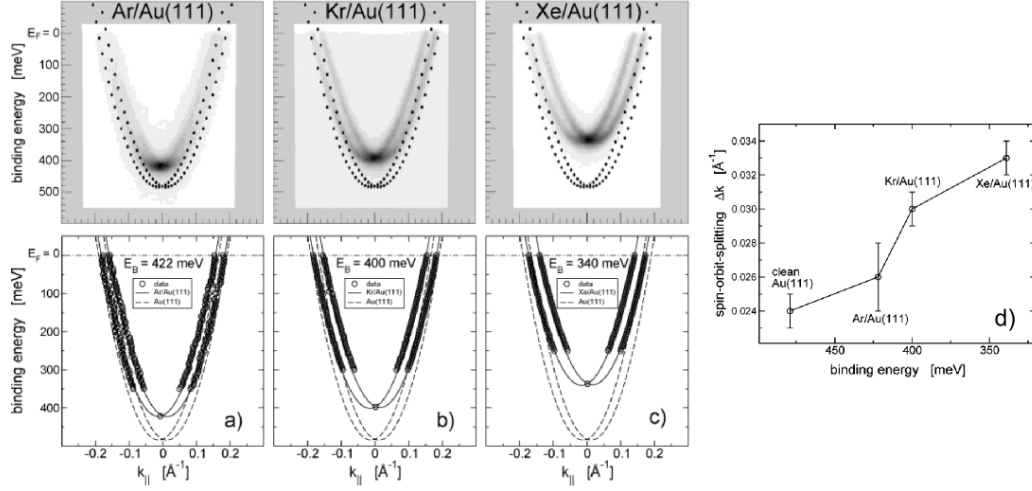


Figure 2.4: **a-c** ARPES intensity map of the band dispersion of the Au(111) spin-split surface states after absorption of approximately 1ML of various rare gases (respectively Ar, Kr and Xe). The dispersion for the clean substrates is reported as well for a direct comparison. Two effects are visible, a decrease of the binding energy and an increase of the splitting. The latter is more clearly shown in **d** where the $\Delta k_{||}$ values for the clean and the three investigated surfaces are reported [53].

Such refined Rashba-Bychkov model was investigated by Cercellier *et al.* [27, 49, 50, 51]. Ag thin films were deposited on the surface of an atomically clean Au(111) substrate, with precise control of the layer thickness. Figure 2.3 shows an example of the evolution of the surface states as a function of the Ag thickness. The binding energies, the effective mass, k_F and the energy splitting scale linearly with the coverage, reaching the nominal Ag(111) values for a coverage of approximately 10 ML. This trend is interpreted as a consequence of the fact that smaller Ag thickness implies higher amount of heavier Au atoms, whose stronger atomic SOC is experienced by the surface wave-function. This experiment clearly shows the importance of the atomic SOC, and it also provides an experimental value for the penetration depth of the surface state in the bulk. Interestingly the L-gap Shockley states are not completely localized at the very topmost atomic layer, but they extend ~ 10 layers.

The magnitude of the spin splitting in the Au(111) surface states results from a complex interplay between different ingredients. Even if atomic SOC plays an important role, it cannot explain alone the difference in spin splitting between Au(111) and Ag(111). The ratio between the Au 6*p* and the Ag 5*p* spin parameter is 1/4, which translates in a theoretical Ag $\delta k \sim 0.003 \text{\AA}^{-1}$. This value is compatible with the angular resolution of state of the art ARPES set-up. Nonetheless this splitting has never been experimentally resolved. Only the recent advent of ultra-high momentum resolution, by exploiting low photon energy laser source, seems to open the way to the experimental measurement of the spin splitting of Cu(111) [52].

Another indication of the fact that the atomic spin-orbit interaction is not the only factor to be taken into account is the enhancement of the spin splitting, achieved by adsorption of rare gases [53, 54]. Figure 2.4 shows the modification of the spin splitting by varying the rare gas (Ar, Kr, Xe) dosed on the Au(111) surface. Such enhancement points in the direction of a model in which the wave-functions involved in the formation of the surface states are deformed by the presence of the surface potential. The contribution of the wave-function asymmetry to the spin splitting was proposed by Petersen and Hedegård [44]. In their tight-binding picture the in-plane p_{xy} states are coupled with the out-of-plane component p_z owing to the presence of the surface potential $V(z)$, which breaks the symmetry of the system. The transfer integral between these two orbital symmetries $\gamma = \langle p_z(\bar{R}) | V | p_{x/y}(\bar{R} + \bar{x}) \rangle$ is a measure of the potential gradient, but it contains also the information on the atomic spin orbit coupling of the p states.

A major step forward in the description of the spin splitting was obtained by *ab initio* calculations which yield quantitative agreement with the experimental findings. Slab calculations in the frame of the fully linearized augmented plane wave (LAPW) were performed initially for Au(111) and Ag(111) [42]. Nagano et al. confirmed, with similar calculations, at a quantitative level the hypothesis of Peterson and Hedegård. They showed, in fact, that the asymmetry of the squared modulus of the wave-function $|\psi(z)|^2$ along the surface normal is crucial for the spin splitting, and this asymmetry results from the coupling of orbitals with different symmetry. The overall splitting arises from the combination of the asymmetric $|\psi(z)|^2$ and the surface potential gradient [55].

The asymmetry of the wave-function represents a key concept for unveiling the origin of the spin orbit splitting, and a similar result was obtained in different *ab initio* calculations, developed within the Korringa-Kohn-Rostoker (KKR) method in a semi-infinite system, avoiding the slab geometry [56]. In this case the asymmetry of the wave-function is introduced by considering the peculiar surface reconstruction of Au(111) (herringbone reconstruction) and the associated outward relaxation of the surface atoms (4% of the bulk interlayer distance). The authors proposed that this structural asymmetry does not reflect directly in the mixing of the orbital components but it introduces an asymmetry in the surface potential: an in-plane potential gradient is added to the Rashba-like out-of-plane component.

The new surface potential term is also responsible for a non-zero polarization orthogonal to the surface, P_z . Spin resolved ARPES, based on spin dependent Mott scattering of the photo-emitted electron, strongly improved in the last two decades in parallel with the increasing interest in spin splitting surface states. The measurement of the out-of-plane component of the spin polarization of the Au(111) surface states represented a challenging task, due to the small spin polarization, comparable to the detection limit of the experimental set-up [58, 59, 57, 60]. Figure 2.5 shows the results of calculations of the different spin polarization components, along with experimental data [57].

The importance of the wave-function asymmetry was confirmed by other *ab initio* calculations within the LAPW method [61]. The authors separated the relativistic correction to the Schrödinger Hamiltonian in a Darwin term and a spin-orbit term. In particular, the latter is important only close to the core of the nuclei, and it is taken into account only in a small sphere around the atom. The potential is expanded in spherical harmonics and only

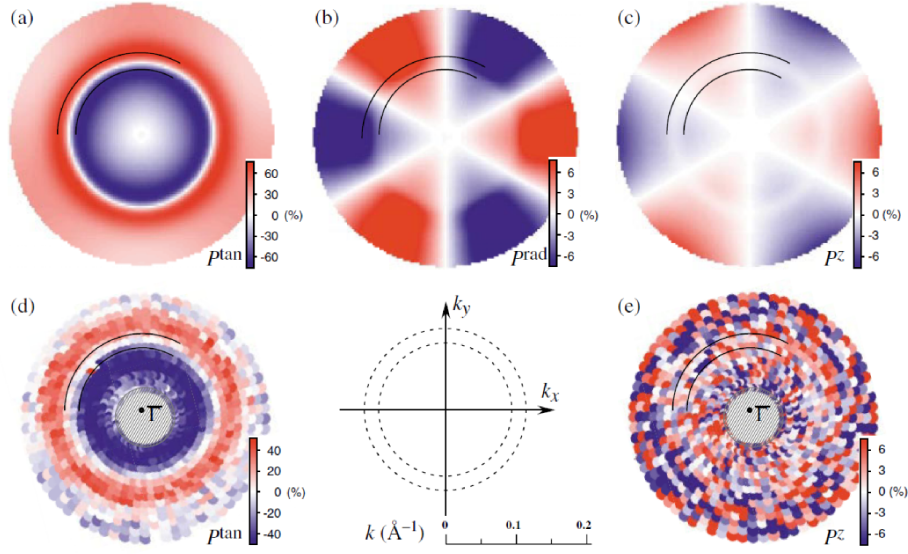


Figure 2.5: **a-c** theoretical spin polarization of the constant energy map at -0.17 eV. The calculated polarization is decomposed respectively into tangential P^{tan} , radial P^{rad} and surface normal components P^z . The position of the surface states is displayed with two black circular arcs. **d** and **e** show the measured tangential and normal component [57].

the $l = 0$ term is conserved, the resulting Hamiltonian is $H_{SOC} = \frac{\hbar^2}{4im^2c^2} \frac{\partial V}{r \partial r} (\vec{r} \times \vec{p}) \cdot \vec{\sigma}$ where V is the spherical symmetric potential. The calculations enabled to distinguish the contribution of each layer of the slab to the overall spin splitting. Figure 2.6 shows that surprisingly almost 40% of the splitting comes from the subsurface layers, where the surface gradient potential should be screened and negligible. This finding proves that the spin splitting arises from the lack of inversion symmetry of the wave-function, and more precisely from the gradient of the surface state wave-function near the position of the atomic nuclei. This also implies that, for a given atom, a pure p -like state, with an $l = 1$ spherical harmonic component, should show no Rashba splitting. Only the hybridization of states with l and $l \pm 1$ characters creates an effective gradient. This is not necessarily true when the orbital hybridization between neighboring atoms is taken into account. Recently, Ast *et al.* proposed, in fact, that the Rashba strength parameters is the results of two terms: an on-site contribution coupling orbitals of the same atom and a nearest-neighbor contribution [62].

In the model developed by Bihlmayer *et al.* the hybridization of p and d states has two different consequences on the spin splitting: on one side the asymmetry of the wave-function is increased by the higher l term, but on the other side the atomic potential gradient is particularly important in proximity of the nuclei and a p state should feel it more strongly than a d state. This result suggests that different spin splitting of the Ag(111) and Au(111) surface states is due to their different p - d ratio (9.5 for Ag and 3.3 for Au). Moreover, also the p - s ratio of Ag suggests a more pronounced p character of its surface state.

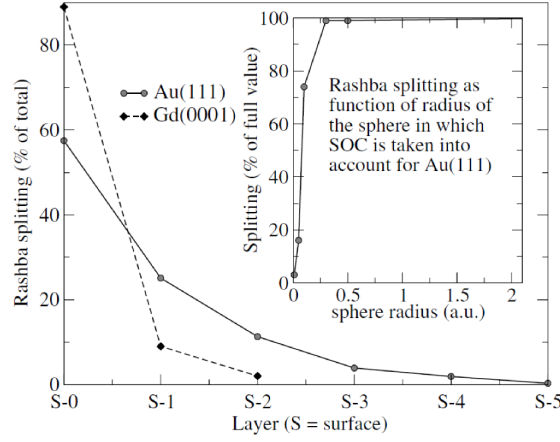


Figure 2.6: Contribution to the Rashba splitting in Au(111) and Gd(0001) arising from the individual layers of a film. The surface layer is denoted by S, deeper layers by S - 1, S - 2. The inset shows the contribution to the Rashba splitting coming from a sphere around the surface atom of Au(111) as function of the sphere radius [61].

Large efforts have resulted in the improvement of the original Rashba-Bychkov model, with the extensions proposed by the tight-binding calculations of Petersen *et al.* [44] and by first-principle calculations [56, 61]. Nonetheless, a microscopic description of the underlying physical mechanism is substantially missing. An attempt to fill this gap was proposed by Ryong Park *et al.*, who developed a novel model to explain the connection between large atomic SOC, the potential gradient at the surface and the asymmetry of the wave-function [63].

The most important aspect of this theory is the assumption of a nonzero of a local Orbital Angular Momentum (OAM). Generally, in the case of a periodic crystal, such OAM is quenched by the crystal field. This is not the case when large atomic SOC is taken into account. SOC makes the description of the eigenstates in term of (l, m_l) states, *e.g.* pure p states, not valid. The solutions of the Hamiltonian are eigenstates of the total angular momentum \vec{J} . This nonzero local OAM yields an asymmetric charge distribution, *i.e.* an electric dipole at the surface. This process is formally described by building suitable Bloch states as superposition of $J = 1/2$ states characterized by the quantum numbers (\vec{k}, \hat{n}) . The first is the wave-vector of the delocalized state, while the second described the orientation of the total angular momentum.

Figure 2.7 a shows a schematization of one of these states, with \hat{n} (\vec{L}) oriented along the x direction. The density of states depends both on \vec{k} and \hat{n} , and Figure 2.7 b and c show cuts in the x -integrated charge density for two wave-vectors, for a given \vec{J} . Clearly the electron distribution is larger (smaller) for negative (positive) z values. The asymmetry is reduced for smaller \vec{k} (panel a). Such asymmetry stems from the superposition of free electron and local OAM states. When the phase velocity of the electron and the OAM are aligned there is a constructive interference (for $z < 0$) and a higher charge density.

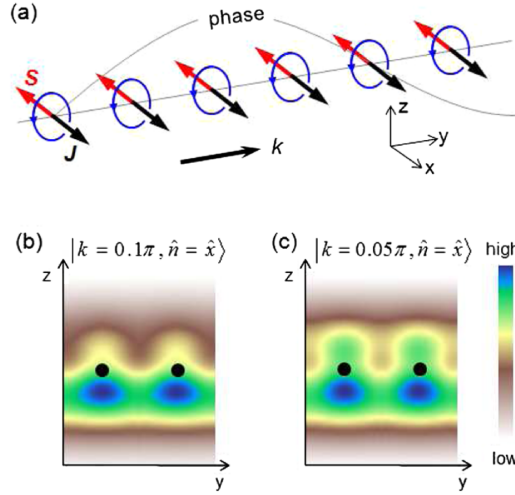


Figure 2.7: **a** shows a tight-binding state built with $J_{1/2}$ states, centered at different atomic positions. The phase of the resulting wave-function is defined by the grey sine function. **b** and **c** show two electron density distributions for different wave-vectors \bar{k} . In both the cases the electron distribution is mainly found in the negative z space, but for smaller \bar{k} the anisotropy is reduced. This suggests the formation of an electric dipole at the surface [63].

The broken symmetry at the surface is still a mandatory ingredient of the model, because it is responsible for the electric field \overline{E}_S at the surface, which couples with this electric dipole. The latter is proportional to $\overline{L} \times \bar{k}$, hence the maximum coupling with the field is achieved for $\overline{L} \times \bar{z}$ parallel or antiparallel to the wave-vector. This locks the dipole orientation, *i.e.* $\overline{J}(\overline{L})$, to the wave-vector, originating a chiral local OAM. The alignment of \overline{E}_S , \bar{k} and \overline{L} is shown in Figure Figure 2.8 **a**. Owing to the strong SOC, \overline{S} is anti-aligned to \overline{L} , resulting in a chiral Spin Angular Momentum (SAM). Figure 2.8 **b** reports the SAM and OAM structures. Interestingly, the model predicts an opposite direction for the spin patterns with respect to the Rashba model, and experimental results for Au(111) are apparently consistent with this new description, as it is schematized in Figure 2.8 **c** [63].

Circular dichroism in ARPES experiment was proposed to give a direct insight in the chiral local OAM structure [64, 65]. Kim *et al.* compared the spin degenerate Cu(111) surface state with Au(111). Figure 2.9 **a-g** show the result for the Au(111) case. Panel **a** and **b** show the Fermi surface and the band dispersion along the $k_x = 0$ direction for right circular polarized light (RCP), while **c** and **d** show the similar results for left circular polarized light (LCP). Panel **e** and **f** display the circular dichroic (CD) signal. The band splitting is well resolved in the dispersion, and it is visible in the CD data, where the signal is negative (positive) in the $k_y > 0$ (< 0) region. Figure 2.9 **g** shows the averaged CD signal for the inner and outer branches as a function of the azimuthal θ angle, for different binding energies. A sine function is fit to the data, with magnitude linearly proportional to k . The CD signal in the case of Au is three times larger than for Cu (not shown), suggesting

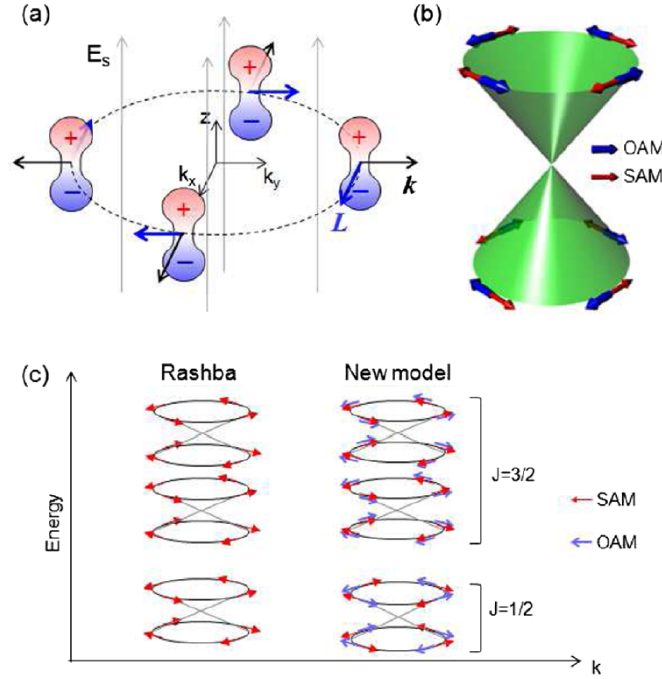


Figure 2.8: **a** shows the interaction of the electric dipole with the surface electric field \overline{E}_s . The dipole is proportional to $\overline{L} \times \overline{k}$, hence the direction of \overline{L} is constrained to be orthogonal to the wave-vector and to \overline{E}_s . This OAM chiral pattern is transformed in a chiral SAM pattern by strong spin-orbit coupling (**b**). The latter is opposite to the prediction of the Rashba model (see **c**) and the result of this model is consistent with the experimental results for the Au(111) surface states [63].

a stronger OAM for the former. Moreover, in the case of Au(111) the inner branch carries 35% larger OAM than the external branch.

In order to elucidate the chiral OAM and SAM structures, the authors performed also first-principle DFT calculations on Au(111). Both the the calculated orbital momentum, and the associated spin chirality, are consistent with the experimental results, except for the difference in OAM between the two spin branches. This was addressed by an analysis of the orbital contribution to the OAM. Both the $5d$ and $6p$ orbitals of Au determine the magnitude and direction of the orbital momentum. The most relevant findings are that the d band contribution dominates, with equal orientation for both the inner and outer branches. On the contrary, the p component has different sign in the two. The final OAM is the same but since it is differently built by the p and d orbitals the resulting CD signal is different.

Finally, the authors developed an effective tight-binding like Hamiltonian, in order to show how the chiral OAM and SAM evolve as a function of the atomic SOC α . Figure 2.10 **a** shows that for small α the outer branch displays always opposite OAM and SAM, while the two are aligned in the inner band. When α increase, the outer branch retains the same anti-alignment, but the inner branch instead shows a peculiar evolution from parallel to

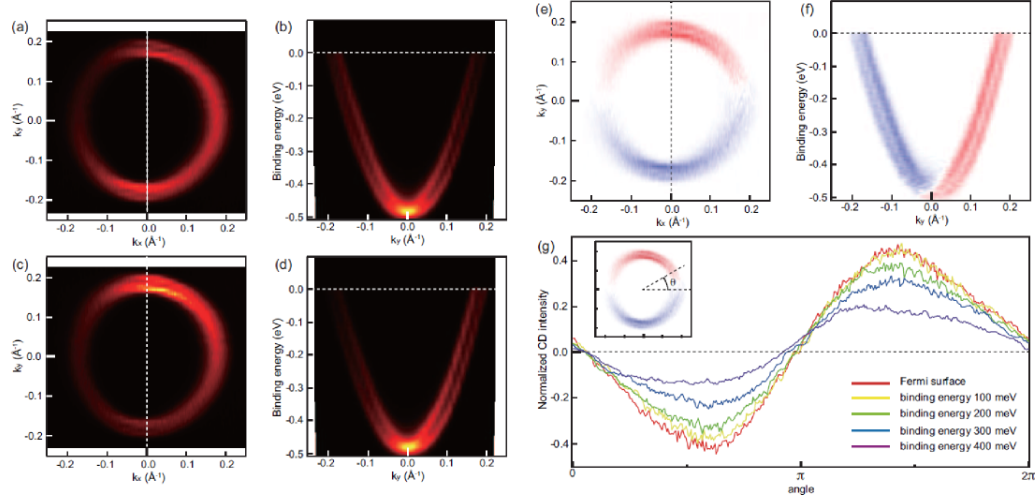


Figure 2.9: ARPES results for the Au(111) surface states. **a** and **b** shows respectively the Fermi surface and the band dispersion along the direction $k_x = 0$ line (dashed line in panel **e**) taken with right circular polarized light. **c** and **d** show the same for left circular polarization. **e** and **f** show the RCP - LCP data. (g) circular dichroic (CD) as a function of the azimuthal angle θ . Data from the inner and outer branches of the surface states are summed in this estimation to have averaged CD [64].

anti-parallel for decreasing \bar{k} values. This effect arises from the competition of the atomic SOC term of the tight-binding Hamiltonian (\bar{k} -independent) with the term describing the interaction between the surface electric field and the surface dipole (\bar{k} -dependent).

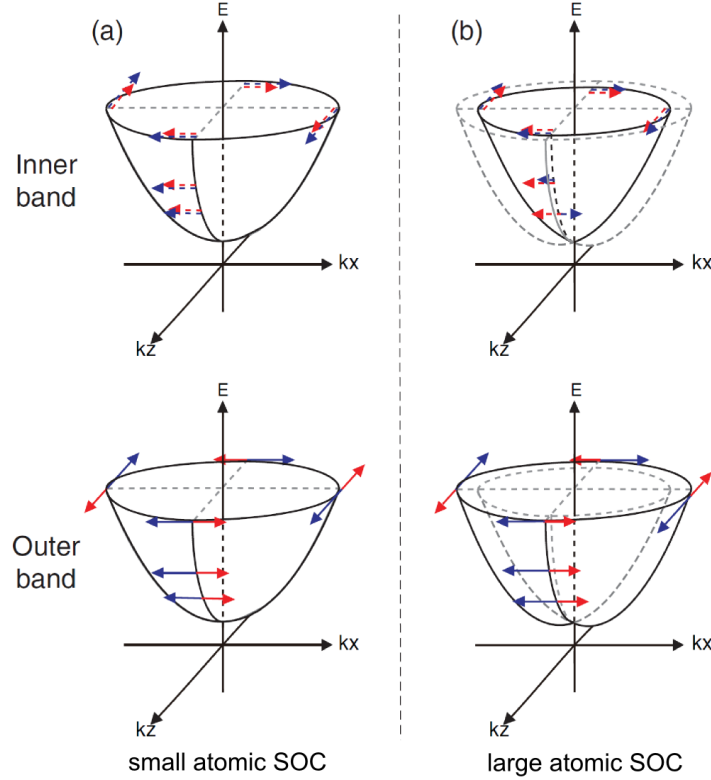


Figure 2.10: **a** and **b** show the SAM and OAM structures calculated respectively for small and large SOC parameter α , for the inner band (top) and the outer band (bottom). The red and blue arrows represent SAM and OAM, respectively [64].

2.1.3 Spin-split surface states in different material surfaces

The goal of unveiling the origin of the spin orbit splitting in the Au(111) surface states has fuelled the development of new theoretical models and motivated fast technical progresses both in ARPES and especially in spin resolved ARPES. Nevertheless, the (111)-terminated surface of noble metals is not the only system hosting Shockley surface states, and the existence of spin split bands was reported at several different surfaces, after the seminal work of LaShell [10].

Transition metals with large Z and large atomic SOC represent the best candidates for giant spin splitting. The surfaces of W(110) and Mo(110) are characterized by a couple of surface states, lying close to the border of the projected bulk band gap, whose splitting was interpreted as arising from a Rashba-like interaction [67, 58]. The splitting was artificially manipulated by evaporation of alkali metal (Li), and it was found to increase by more than a factor 2 (from less than 0.2 eV to more than 0.5 eV). Such effect was interpreted as arising from the modification of the surface potential gradient. A similar experiment was performed by evaporating Au and Ag on top of W(110) and Mo(110) [68]. In this case new extra states appear, but their splitting does not depend on the atomic spin-orbit coupling of

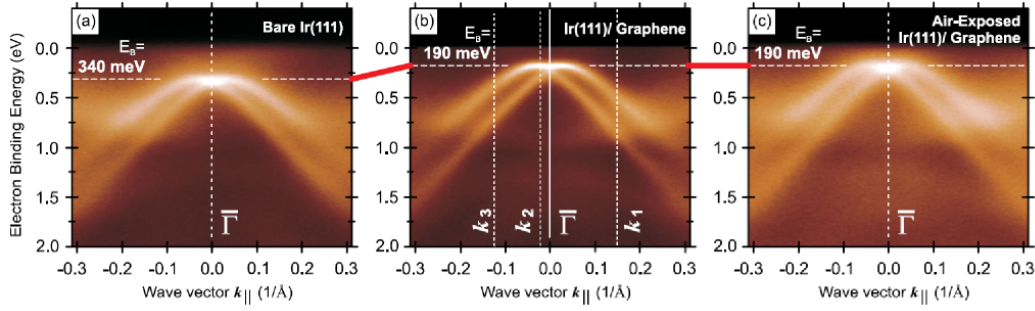


Figure 2.11: **a** displays the dispersion of spin split surface states on bare Ir(111) and **b** under graphene grown on Ir(111). **c** shows the dispersion of the surface state under graphene on Ir(111) after exposure to ambient atmosphere for 15 min [66].

the extra ad-atoms, because the two noble metal yield splitting of similar magnitudes. The origin of such effect is attributed to the substrate SOC, and the surface potential gradient is discarded due to the very different electronegativity of Au and Ag with respect to the Li atoms. In the case of transition metals the density of states close to the Fermi level can exhibit a strong *d*-like character, and the higher *l* is supposed to explain the larger spin splitting observed for W(110) [68].

A pair of spin split surface states was recently observed at the Ir(111) surface. This system was investigated by combined ARPES, spin resolved ARPES and *ab initio* calculations in a 15-atomic-layer-thick slab of Ir [66]. Figure 2.11 **a** shows the spin split surface states, characterized by a negative effective mass (opposite to the case of Au(111)) with a Rashba parameter $\alpha = 1.3 \times 10^{-10} \text{ eV m}$, more than four times the corresponding value of Au(111). The calculations show that the spin split states arise from the hybridization of p_z and d_{xy} states, thus confirming the existence of a $l/l+1$ mixing. The novelty of this system is represented by the possibility to protect the surface states by growing graphene on top of Ir(111). The presence of a carbon ML on the surface of the sample does not affect the splitting, but only shifts the band towards smaller binding energy (see Figure 2.11**b**). A strong influence of the surface potential on the splitting can then be discarded. The very low reactivity of graphene, with respect to a metallic surface, explains the persistence of the surface states after exposure to air (see Figure 2.11**c**). The stability of the spin splitting at ambient pressure is a promising achievement in the perspective of technological application in spintronics.

ARPES investigations of the Shockley states are restricted to the populated part of the bands, below the Fermi level. Some metals, such as Pd(111) and Pt(111), exhibit surface states in the unoccupied density of states, whose existence was reported by inverse photoemission and STS experiments [71, 72]. Deposition of Ag on the surface of Pt(111) was proven to transform the surface state in a surface resonance, by increasing its binding energy out of the projected band gap. For an Ag coverage equal to 2 or 3 ML the bottom of the Shockley state lies below E_F and two independent ARPES experiments reported this band [73, 74]. Detailed *ab initio* calculations confirmed the spin splitting of this surface

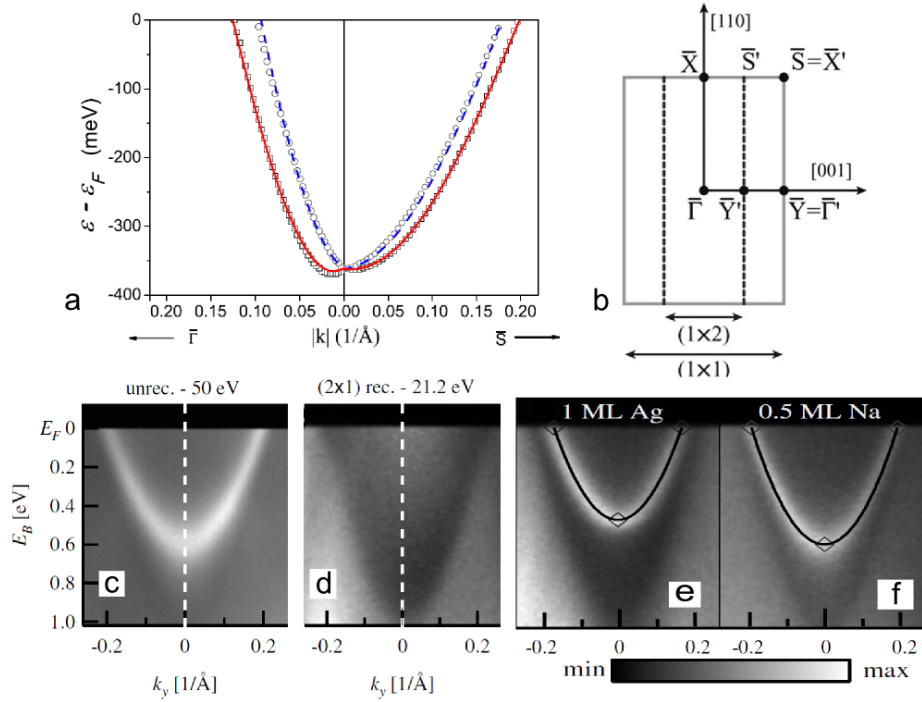


Figure 2.12: **a** displays the theoretical band dispersion of the surface states for the unreconstructed Au(110) surface along two high symmetry directions $\bar{Y}\bar{\Gamma}$ and $\bar{Y}\bar{S}$ [69]. **b** schematic view of the surface Brillouin zone with the high symmetry points. **c-f** band dispersion along $\bar{Y}\bar{S}$ respectively for unreconstructed (**c**), the 2×1 reconstruction (**d**), after deposition of 1 ML of Ag (**e**) or 0.5 ML of Na (**f**) [70].

state, even though the intrinsic broadening of the surface resonance prevented a direct experimental observation of the splitting [73].

It is important to point out that the Shockley surface states of noble metals are not a peculiarity of the (111) face of the *fcc* crystals. Some of the experiments of this thesis work deal with metallic substrates with reduced symmetry (Cu(110) and Au(110)) and also these surfaces host Shockley states in the projected band gap at the \bar{Y} high symmetry point [75, 76]. In the case of Au(110) the combination of a large atomic spin-orbit coupling and the anisotropy of the lattice were proposed to yield an anisotropic Rashba splitting with magnitude in the range accessible to state of the art ARPES set-up [69]. Figure 2.12 **a** shows the calculated band dispersion of the surface states of the unreconstructed Au(110) surface along two high symmetry directions. Two distinct Rashba strength parameters are found $\alpha_x = 0.8 \times 10^{-10} \text{ eV m}$ and $\alpha_y = 0.17 \times 10^{-10} \text{ eV m}$, thus supporting a picture in which the perturbation Hamiltonian is anisotropic. Similarly to Au(111), also the Au(110) surface undergoes a reconstruction, leading in this case to a 2×1 super-periodicity. Experimentally, such reconstruction influences the binding energy of the Shockley state, which is moved above the Fermi level [70]. It is experimentally possible to prepare an unreconstructed Au(110), but only with a large density of defects. The surface state strongly feels

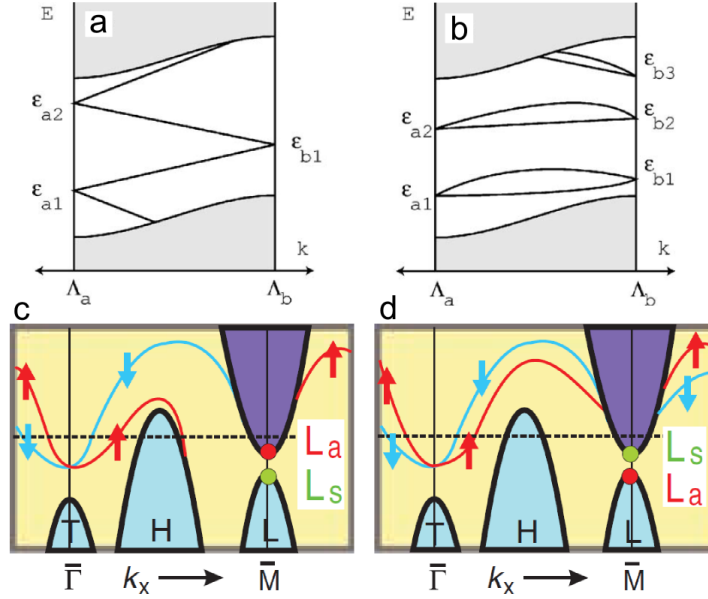


Figure 2.13: **b** explains schematically the concept of *band partner switching* in topological insulator, compared to the trivial topology shown in **a**. In the former case, while moving from the first time-reversal invariant point (Λ_a) to the second (Λ_b) the composition of the spin-split pair, degenerate at the Kramers point, changes. In the latter case the same two states are degenerate at both the TRI-points [77, 78]. **c** and **d** show the same in the case respectively of the band structure of Sb(111) (non-trivial) and Au(111) (trivial) [79].

this disorder, and the splitting is masked by the broadening of the state. Figure 2.12 **b** reports a schematization of the surface Brillouin zone of Au(110) with the high symmetry points of the native surface and of the reconstructed one. Figure 2.12 **c** and **d** show the band dispersion along the $\bar{S} - \bar{Y} - \bar{S}$ direction respectively for the unreconstructed system and for the 2×1 reconstruction, acquired at two photon energies (50 eV and 21.2 eV). The possibility of manipulating the binding energies of this state has been explored. Figure 2.12 **e** and **f** show the effect of evaporation of Na and Ag. Similarly to the case of Pt(111) 1ML of Ag (0.5 ML of Na) increases the binding energy of the Shockley state, but it also increases the disorder at the surface, preventing the experimental observation of the spin splitting.

The study of strongly spin-orbit coupled systems has attracted a huge interest since the recent discover of a new class of spin-split surface states, the so-called topological insulators (TI). The number of experimental and theoretical investigation of these systems has rapidly increased, and several reviews have already been published [80]. A formal treatment of this subject is outside the scope of this section, and a more detailed description is given in chapter 7. As mentioned in section 2.1.2 the broken inversion symmetry at the surface lifts the Kramers degeneracy at all the points of the reciprocal space except the so-called *time reversal invariant* (TRI) high symmetry points ($\bar{\Gamma}$ and \bar{M} in the case of hexagonal (111) face). At the TRI-points the surface states of opposite spins must be

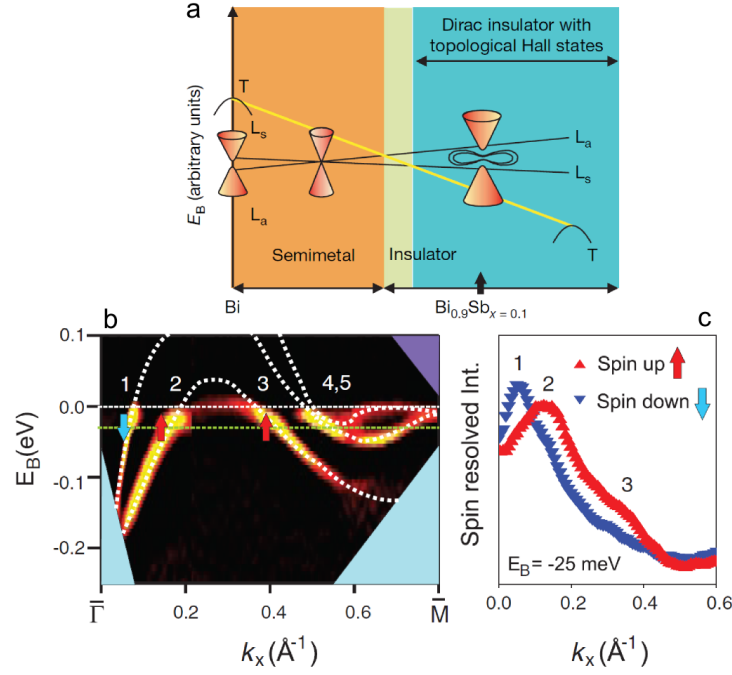


Figure 2.14: **a** displays a schematization of the evolution of the band gap of the alloy $\text{Bi}_{1-x}\text{Sb}_x$ as a function of the Sb concentration x . For $x > 0.07$ the band gap is inverted and the anti-symmetric states lie above the symmetric one. **b** shows the experimental band dispersion for the compound with $x = 0.1$, five distinct bands cross the Fermi level, but only three are surface states. The new topological nature of the system is clarified by the spin resolved ARPES (**c**) revealing an odd number of spin-polarized bands crossing E_F , fingerprint of a non-trivial spin topology [79].

degenerate. Two situations are possible. In the case of trivial surface states the pair of states is conserved when moving from $\bar{\Gamma}$ to \bar{M} . On the contrary, in the case of a topological insulator at any TRI-point the pair is formed by a different combination of bands: this effect is called *band partner switching*. Figure 2.13 **a** and **b** show the two different topologies [78]. At any energy in the non-trivial case, a constant energy cut (for example the Fermi surface) intercepts only one, or in general, an odd number, of spin components. Since scattering on non-magnetic impurity flips \vec{k} , but cannot modify the spin, back-scattering is forbidden in this special materials.

The concept of topological insulator was introduced by Fu and Kane [77, 78] who also proposed special rules to evaluate *formally* the topological character of a given material. They also proposed a simple criterion to search for possible candidates: semiconductors with a small inverted band gap, in which symmetric and anti-symmetric states reverse their ordering in the presence of strong spin-orbit coupling could manifest a non-trivial spin topology. The best candidate is bismuth, a semi-metal with large atomic SOC. The valence and conduction bands are derived from antisymmetric and symmetric p orbitals. Its (111), (110) and (100) surfaces are characterized by surface states with complex disper-

sion, whose spin splitting was first proposed [81], and successively verified by means of spin-resolved ARPES [82]. The Bi(111) surface states are strongly anisotropic, forming lobes elongated along the $\overline{\Gamma M}$ direction and an electron pocket around $\overline{\Gamma}$, characterized by a pronounced hexagonal warping. Sb(111) also exhibits a similar band structure [83]. Antimony is also a semi-metal with the same electronic configuration of the outer shell, with chemical and physical properties similar to the ones of Bi, but for the atomic radius. Bi(111) has a normal gap, but substitution with Sb was found to change the band structure as shown in Figure 2.14 a. At a Sb concentration in the range 4%-7% the VB and CB state cross. For larger Sb concentration the gap is inverted. The BiSb bulk alloy represented the first experimental evidence of topological insulator [11]. Figure 2.14 b shows the band dispersion along $\overline{\Gamma M}$, whose description is complicated by the presence of bulk and surface states. Spin resolved ARPES helped to address the origin of the five bands crossing the Fermi level along the high symmetry direction connecting the two TRI-points [79]. Figure 2.14 c shows that an odd number of spin polarized bands cross the Fermi level. This is the fingerprint of a non-trivial spin topology. Figure 2.13 c shows schematically the band partner switching in Sb(111), while panel d reports the trivial band structure of the Au(111) surface states. The complete evolution of the band structure from the trivial insulator to the topological insulator phase was studied for the *tunable* compound $\text{BiTl}(\text{S}_{1-\delta}\text{Se}_\delta)_2$ as a function of the Se concentration δ [84].

2.2 Giant spin splitting at surfaces and interfaces

2.2.1 Metallic surface alloys

Before the discovery of topological insulators in Bi-based materials, the observation of an unexpectedly large spin splitting in silver surface alloys represented a major breakthrough in the field of strongly coupled spin-orbit systems, and it contributed to raise the interest of the scientific community.

Evaporation of a heavy element (Pb, Bi) with a nominal coverage of $1/3$ ML on the surface of Ag(111) results in the formation of a surface alloy with $\sqrt{3} \times \sqrt{3} R30^\circ$ periodicity, hereafter indicated simply by BiAg₂, where the large Z atoms occupy substitutional sites in the top-most layer [85, 86]. Figure 2.15 **a** and **b** display the results of first principle DFT calculations, within the KRR method, along with the experimental band structure of BiAg₂ [87]. Two sets of spin split bands appear in the occupied DOS, labelled respectively Bi1 and Bi2. The calculation in **a** attributed to the former band mainly sp_z orbital character. Bi1 lies entirely below the Fermi level and it disperses with a negative effective mass ($-0.35 m_e$) in the bulk L-gap reaching the maximum of its dispersion at $k = \pm k_0 = \pm 0.13 \text{ \AA}^{-1}$, where k_0 hence indicates the momentum offset equal to half of the momentum spin splitting. The resulting Rashba strength parameter α is equal to $3.05 \times 10^{-10} \text{ eVm}$. The Rashba Energy E_R , defined as the energy distance between the top of the parabola and the crossing of the spin split branches, is two order of magnitude larger than the equivalent E_R of Au(111) (200 meV against 2.1 meV). The second pair of spin split states crosses the Fermi level (four arrows indicate their k_F) with smaller momentum separation. The calculation reported in panel **a** fails in reproducing quantitatively the value of the splitting, but it indicates the orbital origin of this second pair of bands, which is ascribed mainly to the p_{xy} states.

The striking novelty of this system is that a simple Rashba model cannot explain this large splitting. Quantitatively, the atomic spin-orbit coupling should be proportional to the number of heavy atoms probed by the surface state wave-function [49, 50, 51]. Hence, a sub-monolayer coverage of Bi is expected to show reduced spin splitting with respect to the Bi(111) surface. But that is not the case, and in the surface alloy α_R is one order of magnitude larger than for Bi(111). The origin of the giant spin splitting was theoretically investigated from two distinct points of view, which had been already proposed in their incipient forms for Au(111). The first model, developed by Premper *et al.* [56] and successively refined by Henk *et al.* [87], is based on the existence of an additional in-plane potential gradient, which is large in the case of surface alloy owing to the substitutional sites occupied by the Bi atoms. The combination of the threefold rotational symmetry of the *fcc* substrate, and the presence of six light Ag atoms surrounding the heavy ad-atoms, results in an in-plane gradient potential which is enhanced by the broken inversion symmetry in the $\langle xy \rangle$ surface plane. One of the most important ingredient of this model is the outward relaxation of the Bi atoms with respect to the substrate ones, which contributes to the origin of the in-plane gradient potential.

The electronic band structure of the BiAg₂ alloy is characterized by a strong hexagonal warping of the spin split states. Figure 2.15 **c** and **d** show an experimental constant

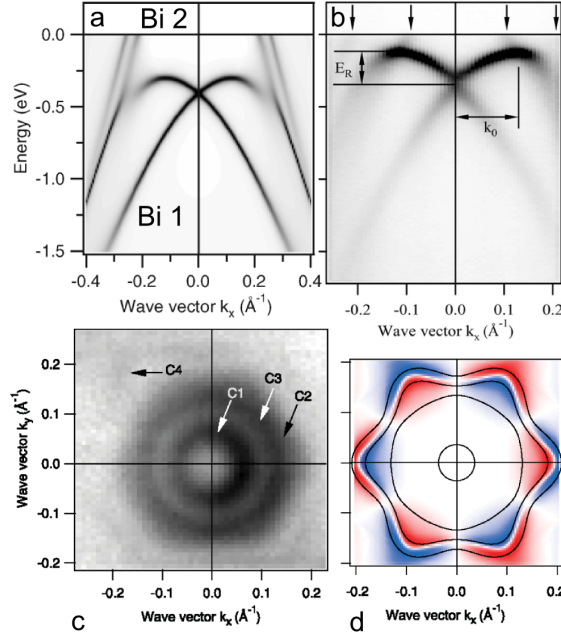


Figure 2.15: **a** and **b** shows the calculated and measured band structure of the Bi/Ag(111) $\sqrt{3} \times \sqrt{3} R30^\circ$ surface alloy. Two sets of spin-split states are observed, labelled with Bi1 (mainly sp_z orbital character) and Bi2 (with p_{xy} orbital character) in **a**. The latter crosses E_f and arrows points to the four k_F in **b**. **c** displays a constant energy cut at -0.55, the contours C1-C2 are associated to Bi1, while C3-C4 to Bi2. The contours associated to the external branches *i.e.* C4 and C2 have clear hexagonal symmetry. **d** is the spin polarization component orthogonal to the surface. The contours of the bands are shown with black line. The hexagonal warping is reproduced along with the Giant spin splitting if an in-plane gradient potential is adequately taken into account. This new extra potential term introduces also a non zero P_z value [87].

energy cut at -0.55 eV, along with the associated calculation of the spin polarization projected along the surface orthogonal. The outer contour (C4, associated to Bi2) reveals an hexagonal shape, which is well reproduced by introducing the in-plane gradient potential [56]. Spin resolved ARPES was performed on this system and Figure 2.16 **a** reports the three Cartesian components of the spin polarization as obtained from an MDC along the $\overline{\Gamma K}$ direction at -0.9 eV. The p_{xy} derived surface states feel strongly the in-plane gradient potential and they are characterized by the rotation of the spin polarization vector and by a non-negligible P_z component along the $\overline{\Gamma K}$ direction. The spin polarization P_z displays a sine-like behavior as a function of the azimuthal angle, *i.e.* P_z is maximum along $\overline{\Gamma K}$ but it vanishes along $\overline{\Gamma M}$. This observation is in agreement with the calculation of Figure 2.15 **d** and it points towards the presence of strong in-plane gradient potential [88].

Bihlmayer *et al.* proposed an alternative description of the physical mechanism at the origin of the giant spin splitting. They attributed the key-role to the asymmetry of the surface state wave-functions in the region of the (sub-)surface nuclei [89]. In the case of

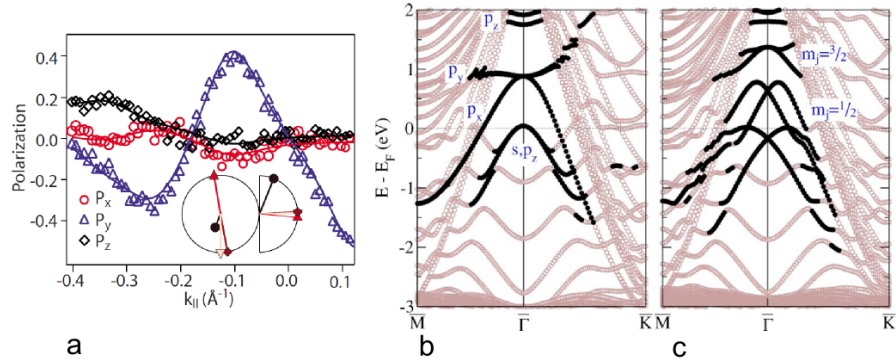


Figure 2.16: **a** shows the result of spin resolved ARPES on BiAg₂. The three components of the spin polarization vector are shown as extracted from an MDC at -0.9 eV. A non-zero P_z value is observed, mainly due to the p_{xy} derived surface states [88]. The P_z sine-like behavior (not shown) confirms the calculations of ref [87] and the validity of the additional in-plane asymmetry in the potential. **b** and **c** show the results of calculations of the band structure of BiAg₂ obtained in a LAPW scheme. The magnitude of the spin splitting of the surface states is well reproduced both for the Bi1 and Bi2 bands. The origin of the large splitting is ascribed to the mixing of orbital character in the surface states wave-function and to the resulting asymmetry in the wave-function [89].

a flat Bi/Ag(111) layer, the Bi1 surface states would have only sp_z character, with an $s:p$ ratio of 4:1. In the calculations this leads to a strong reduction of the spin splitting, which becomes comparable to the one of Bi(111). Only by *switching on* the buckling of the heavy atoms this ratio is modified and the p contribution gets larger (2:1). Moreover the structural relaxation induces the mixing of the sp_z and p_{xy} states and only when this condition is achieved a correct numerical estimation of the splitting is obtained. Figure 2.16 **b** and **c** show the results of the calculations, performed within the LAPW method, for the BiAg₂ alloy without and including the spin-orbit interaction, for the case when the relaxation of the Bi atoms is taken into account [89].

In both theoretical models the structure of the surface alloy plays an important role, along with the atomic SOC of the substrate and of the ad-atoms. In order to disentangle these contributions, similar alloys were grown by varying alternatively the heavy atom adsorbed or the substrate. The complete substitution of Bi with Pb gives origin to a *pure* PbAg₂ alloy, and the very similar atomic radii of Bi and Pb enable the formation of mixed Bi_xPb_{1-x}Ag₂ surface alloys, as well. Both these systems were subject of ARPES experiments [90, 91], and a summary of the results is shown in Figure 2.17. Pb has one electron less than Bi ($[Xe]4f^{14}5d^{10}6s^26p^2$ vs $[Xe]4f^{14}5d^{10}6s^26p^3$), and this explains in a simple rigid band shift the position of the top of the sp_z band above the Fermi level (Figure 2.17 **a** for $x = 0$). Mixing with Bi introduces a broadening of the states, due to disorder, and a continuous shift of the surface states towards higher binding energies (Figure 2.17 **b** for $x = 0.5$ and **c** for $x = 1$). The Rashba parameter α evolves from the one of PbAg₂ to the one of BiAg₂, as shown in Figure 2.17 **d**. These results reinforce the idea that atomic spin

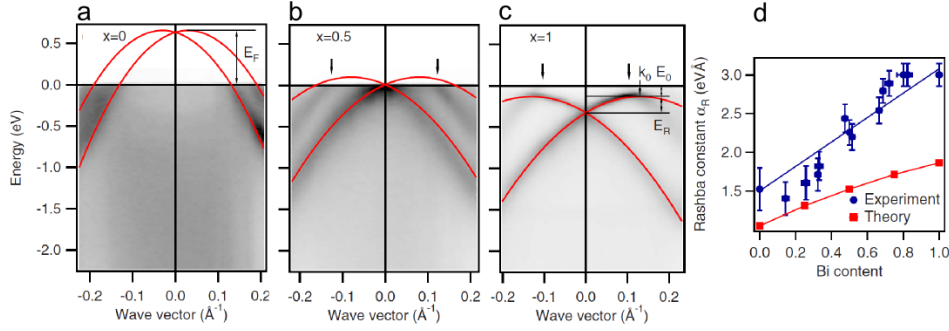


Figure 2.17: **a-c** show the measured band dispersion along the $\Gamma\bar{K}$ high symmetry direction for the $\text{Bi}_x\text{Pb}_{1-x}\text{Ag}_2$ mixed alloy, respectively for $x = 0$; 0.5 ; 1 . The first case represents the pristine PbAg_2 system. The sp_z derived band crossing lies above E_F , the splitting is reduced by a factor four with respect to the BiAg_2 (panel **c**). In the mixed alloy the bands evolve continuously from the one of pure Pb to pure Bi. All the Rashba parameters evolve with the Bi concentration, and panel **d** shows the behavior of the Rashba strength parameter α [90].

orbit coupling alone cannot account for the magnitude of giant spin splitting in the surface alloy, because Pb and Bi have very similar Z values (respectively 82 and 83) and similar $6p$ atomic spin orbit coupling (respectively 0.91 eV and 1.25 eV), and they should display comparable splitting, while there is factor four between them.

An interesting property of the Rashba spin split surface states not yet mentioned, is a variation of the density of states in the energy window between the top of the parabolic dispersion (bottom in case of positive mass dispersion, as in $\text{Au}(111)$) and the crossing point of the spin-split bands. In such region the DOS deviates from the constant value characteristic of a two-dimensional system, and it acquires a $1/\sqrt{E}$ behavior typical of one-dimensional systems. Therefore, the DOS presents a singularity at the band extremum, which was proposed to have dramatic consequences on the electronic properties of the system when the singularity lies close to the Fermi level. An enhancement of the superconducting critical temperature (T_C) [92, 93] was proposed along with a strong variation of the electron-phonon coupling with consequent lattice instability and polaron formation [94]. The singularity in the DOS was experimentally resolved, even though convolved with the experimental resolution, in STS experiments for both the BiAg_2 and PbAg_2 surface alloys [95].

The mixed alloy offers the unique possibility to tune in a controlled way the DOS-singularity across the Fermi level. High resolution ARPES experiments at liquid He temperature have been performed on this system at the early stage of this PhD work, but none of these exotic scenarios could be confirmed. On the other hand, spin resolved ARPES experiments performed on the $\text{Bi}_x\text{Pb}_{1-x}\text{Ag}_2$ mixed alloy reported the existence of an unconventional spin texture of the surface states when x changes between $x = 0.5$ and $x = 0.6$ (*i.e.* when the singularity is shift below E_F). In the former case the inner and outer branches of the surface states at E_F have anti-parallel spin polarization vectors while

in the latter case the two vectors are parallel. Figure 2.18 **a** and **b** show the spin resolved ARPES data for $x = 0.5$ and $x = 0.6$. The spin resolved intensity of the MDC extracted at -50meV shows the change in the spin texture, which translates in a different helicity of the inner and outer branches for the two Bi contents [91].

The first experiments performed on the BiAg₂ and PbAg₂ surface alloys revealed the complex interplay between several parameters, whose singular role was studied thoroughly by L. Moreschini [96]. The contribution of the atomic spin orbit coupling of the ad-atom was investigated by substituting Bi with Sb [97]. Sb shares the same electronic configuration of the outer shell of Bi (s^2p^3) and it is characterized by a smaller atomic radius, which reflects in the smaller outward relaxation of the adsorbed atoms in the substitutional site (10% instead of the 15% for Bi) as obtained by *ab initio* calculation within the KRR method. The calculations show a similar degree of sp_z and p_{xy} orbital hybridization for both the Sb and the Bi alloys. The combination of a similar structural relaxation and a similar admixture of different orbital characters was predicted to generate a strong in-plane gradient potential, comparable to the one reported for Bi/Ag(111). The existence of such in plane gradient potential was confirmed experimentally by the presence of a strong hexagonal warping of the Sb derived surface states.

The striking difference between the Sb and Bi alloys is that in the former system the spin splitting is much smaller, and it is observable only for the p_{xy} states at high binding energy (-0.55 eV). Moreschini et al. ascribed this difference in the spin splitting to the difference between the Bi $6p$ atomic spin orbit coupling (1.25 eV) and the Sb $5p$ value (0.4 eV) [97]. The authors concluded that the in-plane gradient potential alone is ineffective in producing the spin splitting, and it has to be supported by a strong atomic spin-orbit coupling. Interestingly, spin resolved ARPES experiments revealed an unusual modulation of the three cartesian components of the spin polarization. The measurement was repeated by varying the experimental conditions (sample alignment, photon energy and light polarization) in order to distinguish final state from initial state effects. The authors assigned their experimental results to the coherent superposition of two different spinors, which is possible in SbAg₂ because the energy splitting is comparable with the intrinsic line-width of the surface states [98]. The possibility to tune almost independently the Rashba strength parameter α and the binding energies of the surface states was proposed and successively experimentally verified in the Bi_xSb_yPb_{1-x-y}Ag₂ system [99, 100].

The out-of-plane surface potential gradient was the second important term of the Rashba model to be investigated. Similarly to previous studies of the Au(111) surface states, rare gas (Xe) was adsorbed on the surface of Bi/Ag(111) $\sqrt{3} \times \sqrt{3}R30^\circ$, leading to a new (4×4) super-periodicity. Surprisingly, the surface alloy did not present any variation of the splitting, but only a back-folding of the native bands on the new surface periodicity. This result strongly confirmed the hypothesis that the potential gradient orthogonal to the surface is only weakly contributing to the spin splitting, and the predominant physical mechanism must be found elsewhere [101].

The influence of the substrate on the giant spin splitting in BiCu₂ was explored in three independent works. Moreschini et al. proposed that the reduction of the the spin splitting by a factor four is due to the reduction of the atomic spin-orbit coupling of the substrate (0.03 eV for Cu and 0.11 eV for Ag) [104]. Bentamann et al. instead proposed a different

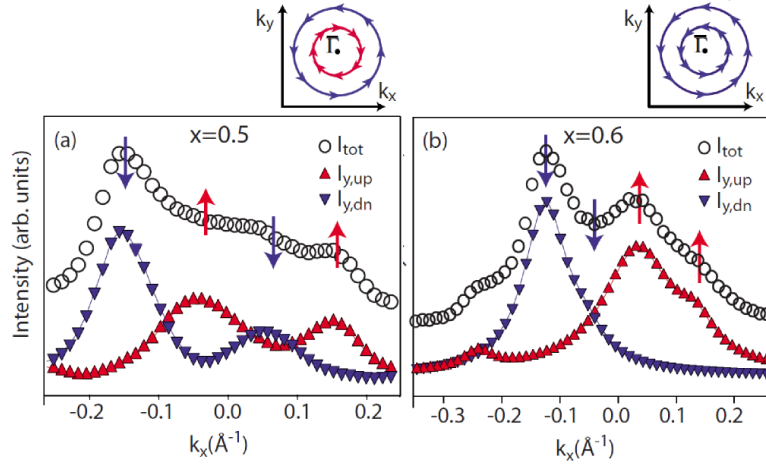


Figure 2.18: **a-b** show spin resolved ARPES data of $\text{Bi}_x\text{Pb}_{1-x}\text{Ag}_2$ respectively for $x = 0.5$ and $x = 0.6$ measured at a binding energy of 50 meV. The figures display the total spin integrated intensity along with the spin-resolved intensity curves projected on the y axis of a MDC along $\bar{\Gamma}\bar{K}$ [91].

picture, which was motivated by *ab initio* calculations: the difference in spin splitting is determined by the different orbital compositions of the surface states. The latter is a direct consequence of the different relaxation of the Bi atoms on the Ag(111) and Cu(111) substrates. The authors stressed the fact that the atomic SOC of the substrate has only little influence on the splitting: in fact, in their *ab initio* calculations, the atomic SOC of Cu was artificially increased to match the one of Ag. Surprisingly the modified value did not affect the spin splitting [102].

Spin resolved ARPES experiments on BiCu_2 were performed by Bentmann et al. [103]. Figure 2.19 **a** and **b** show the experimentally determined spin orientation along with the calculated one. The direction of the spin polarization, combined with the negative effective mass of the surface states, lead to a negative Rashba strength parameter, Au(111) is characterized, for example, by a positive value. In order to understand the physical meaning of this negative value, it is necessary to go back to the definition of α_R as the strength of the potential gradient projected on the surface states wave-functions. The sign depends on where the charge is localized, and the authors noticed an imbalance of charge close to the Bi nucleus with a larger density on the substrate-facing side. Figure 2.19 **c** shows a two-dimensional cut through the charge density, and a larger value is observed in the subsurface region below the Bi atom. Bentmann et al. predict a similar behavior for all surface alloys and interpret the localization of the wave-function as the result of a strong hybridization of the adsorbate sp_z orbitals with the underlying substrates states. This hybridization is affected by the relaxation of the heavy atoms, and the spin splitting certainly bears information on the bonding properties.

The spin polarization of BiCu_2 was also discussed by Mirhosseini et al. emphasizing the unconventional spin textures of the spin-split surface states in the unoccupied DOS

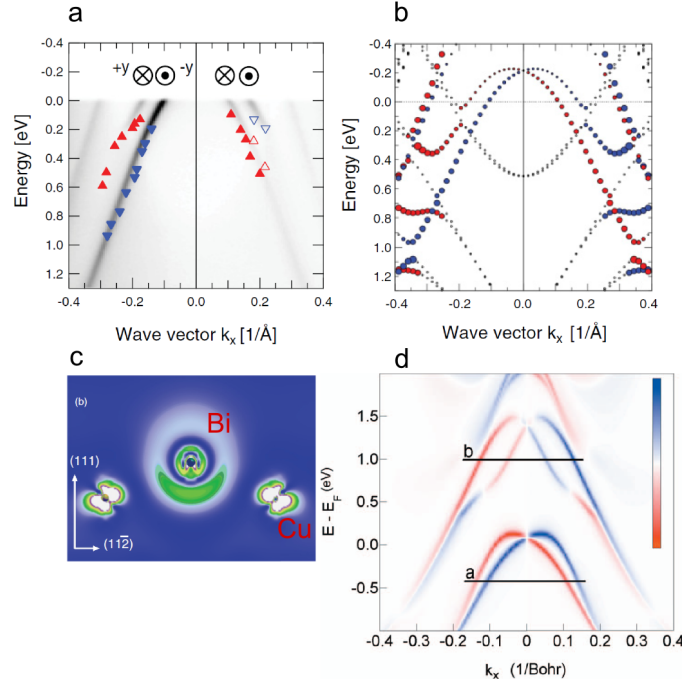


Figure 2.19: **a** displays the measured band dispersion of BiCu_2 along the $\Gamma\bar{K}$ high symmetry direction. Blue and red triangles indicate the band position for the single spin channel as obtained from spin resolved ARPES measurements. The spin topology, combined with the negative effective mass, results in a negative α parameter. The negative sign is proposed to reflect the peculiar asymmetry in the charge distribution around the Bi atoms, with a higher density in the region facing the underlying substrate. This picture is sustained by panel **c**, which shows a two dimensional cut thorough the density of charge in the plane orthogonal to the surface [102]. **d** shows the results of *ab initio* calculations performed in the KKR method for BiCu_2 [103]. The data confirmed the calculation of panel **b**, but they also show a peculiar change in the spin topology for the surface states lying at higher energy (un occupied DOS).

[106]. These states were investigated with the use of 2 photon photoemission (2ppe) and Figure 2.19 **d** shows the results of band calculation within the KRR method. The orientation of the spin-split states below the Fermi energy is anti-parallel for the two spin branches, in agreement with the Rashba model. The pairs of spin-split states above the Fermi level violate the conventional spin topology and the two branches have the same spin helicity. This finding is interpreted as arising from the hybridization of the outer sp_z branch with the inner p_{xy} branch, made possible by the Bi buckling in the surface alloy [106]. We notice an intriguing connection between this finding and the aforementioned transition between conventional and unconventional spin texture in the $\text{Bi}_x\text{Pb}_{1-x}\text{Ag}_2$ mixed alloy [91]. In the latter, the spin polarization is extracted from an MDC at the Fermi level. As the x concentration increases, the p_{xy} derived states shift down in energy. The Fermi level position

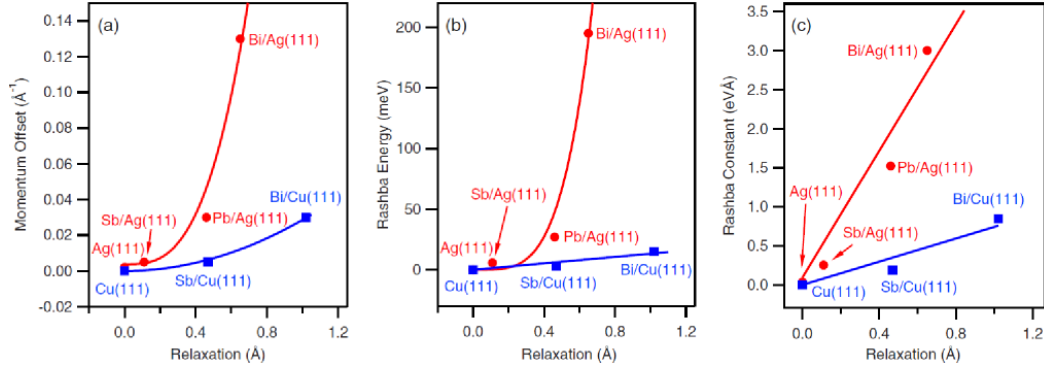


Figure 2.20: Characteristic experimental parameters for a Rashba system, such as **a** momentum offset, **b** Rashba energy, and **c** Rashba constant are shown as a function of the outward relaxation Δz . The lines are drawn as a guide to the eye [105].

approaches the top of the p_{xy} band dispersion where the hybridization is realized and the spin topology is inverted. It would be of interest to study the spin polarization for two different x concentrations but at the same energy distance from the top of the p_{xy} surface states, in order to verify the accordance with the model developed by Mirhosseini *et al.* [106].

Many experimental and theoretical works have pointed out the important role played by the heavy atoms buckling in defining the magnitude of the spin splitting. In order to fully understand the role of the geometry and of the local ordering in the alloys, a complete study of the outward relaxation Δz of the different surface alloys was performed by means of quantitative IV-LEED experiments [105], and the results were compared with the measured spin splitting. Figure 2.20 summarizes this analysis by showing on a same graph, as a function of Δz , respectively the k_0 value (a), the Rashba energy (b) and α (c). For Ag(111) and Cu(111), by considering the two substrates separately, a clear trend is observed: larger relaxation leads to larger spin splitting. The difference between alloys grown on Ag or Cu was proposed to arise from the different orbital composition of the surface states [105].

The giant spin splitting is based on the complex interplay between many parameters which compete with similar strength. To shortly summarize, the spin splitting in surface alloys is almost unaffected by the out-of-plane surface gradient potential because the surface states are localized around the heavy atoms nuclei in the region pointing towards the subsurface layer. The localization arises from the hybridization of the sp_z orbital of the heavy atom with the substrate states. The spin splitting depends on this hybridization and also on the mixing of the sp_z and p_{xy} orbitals of the ad-atoms. Both these hybridizations depend on the surface relaxation of the alloy. The buckling of the heavy atoms also contributes to form an in-plane-gradient potential, which explains the hexagonal warping of the surface states and the existence of a spin polarization orthogonal to the surface. The relation between the anisotropy in the potential and the anisotropy in the wave-function has never been quantitatively explored, but naively the two effects seem to be deeply connected. None of these ingredients is sufficient to produce spin-split states, unless a strong

atomic spin orbit coupling is also present. From a radically different point of view, one may argue that all the aforementioned ingredients are responsible for a chiral local orbital angular momentum (OAM) which is translated in a chiral spin angular momentum (SAM) in the presence of a strong spin orbit coupling.

2.2.2 Exporting the Rashba-Bychkov effect in semiconductors

The large spin splitting achieved in the surface state of metallic alloys represents an attractive candidate for the development of spintronics devices. In these systems, however, the spin polarized bands lie in the partial L band gap, and, at the Fermi level, a high density of charge carriers belongs to the spin degenerate substrate conduction band. Metallic spin-split surface states in a bulk semiconductor represent the key ingredient for the creation of a spin field-effect transistor (spin-FET), as the one proposed by Datta and Das already in 1990 [107]. Materials with Dresselhaus spin-split states (as semiconductor heterostructures) were initially proposed for hosting spin polarized current. The spin polarization \overline{P}_S can be manipulated and rotated along a defined precession axis by applying an external magnetic field. Unfortunately intrinsic scattering partially re-orientes the electron momentum \vec{k} and consequently the precession axis, resulting in a spin relaxation, or dephasing. It is therefore necessary to reduce the length required to manipulate externally \overline{P}_S , lowering it below the dephasing length: this can be obtained by exploiting systems with larger spin splitting.

These considerations motivated large efforts for transferring the giant spin splitting of metallic alloys to semiconducting substrates. Silicon in particular was chosen as first template to export "naturally" the new electronic properties to technological devices. Bismuth on Si(111) yields two different $\sqrt{3} \times \sqrt{3}R30^\circ$ reconstructions, studied by several LEED [108, 109] and X-ray diffraction (XRD) studies [110]. The first is the α phase characterized by a 1/3 ML coverage, in which Bi atoms occupy the so-called T_4 lattice site (hollow site). The second is the β phase in which every Bi atom is replaced by a Bi trimer, centered at the T_4 site, resulting in a 1 ML coverage. Because of the broken inversion symmetry in the surface plane, the trimer phase hosts a strong in-plane asymmetry of the potential gradient, and it was subject of several ARPES and spin resolved ARPES studies [111, 112, 113].

Figure 2.21 a displays the band structure along the $\overline{\Gamma\overline{M}\overline{\Gamma}}$ high symmetry direction. Three distinct states, labelled S1, S2 and S3, are observed. In particular S1 disperses with negative effective mass with a momentum offset of the maximum in proximity of \overline{M} equal to 0.126 \AA^{-1} . This offset is a signature of a large spin splitting. This hypothesis was confirmed by *ab initio* calculations with the KKR method, and Figure 2.21 b reports the calculated band dispersion along $\overline{\Gamma\overline{M}\overline{\Gamma}}$. The two S1 branches, which cross at the time-invariant point \overline{M} , reveal opposite spin polarization. The spin splitting was ascribed to the in-plane asymmetry of the potential gradient resulting from the breaking of the in-plane inversion symmetry.

Frantzeskakis et al. combined new ARPES results with band calculations based on the nearly free electron model and the tight-binding model [112]. The authors proposed an alternative explanation for the large spin splitting of the S1 state. Figure 2.21 c and d show the comparison between TB calculations without and including spin-orbit interaction.

Already in the former, the maximum of S1 is shifted away from the \bar{M} point. In Bi/Si(111) the large momentum offset is therefore inherent in the characteristic band structure of the system [112].

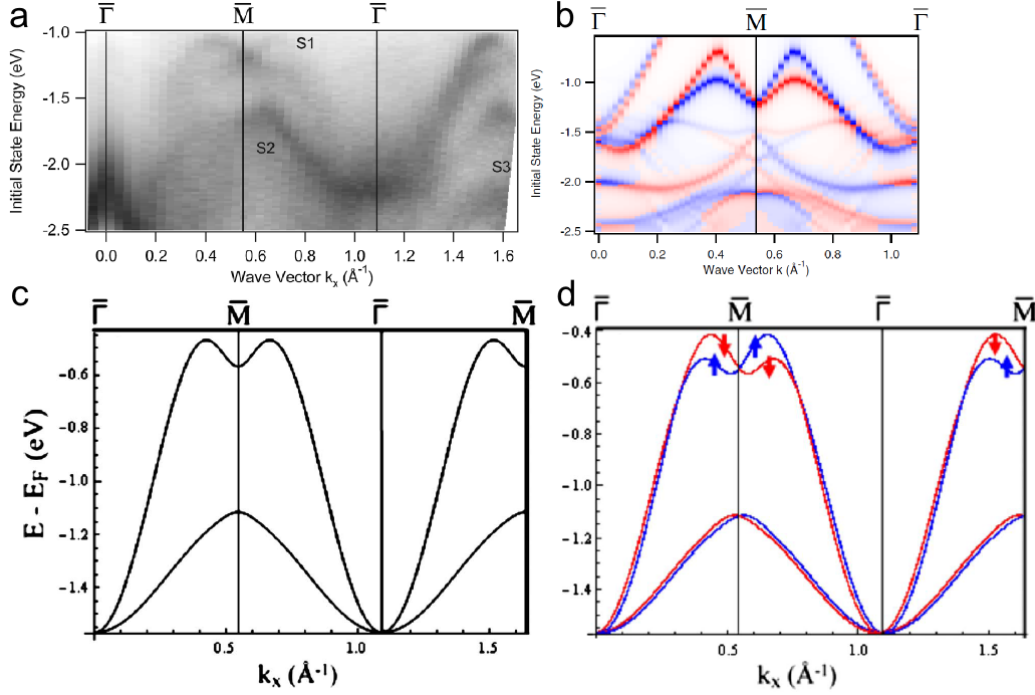


Figure 2.21: **a** and **b** show experimental and calculated band dispersion of Bi/Si(111) $\sqrt{3} \times \sqrt{3}R30^\circ$ β phase along $\bar{\Gamma}\bar{M}\bar{\Gamma}$. Several bands are observed, S1 in particular is constituted by two branches, degenerate at the \bar{M} point. The *ab initio* calculations confirm that the two branches are spin polarized [111]. The origin of the large spin splitting was investigated by means of tight-binding calculation, whose results are reported in **c** and **d**, respectively without and with SOC. In the absence of SOC the S1 state presents already a shift of the maximum from \bar{M} . The large magnitude of the spin splitting of this interface results therefore from an inherent property of band structure of the trimer structure

A complementary point of view of the band structure of the Bi β phase was given by Sakamoto *et al.* in a combined ARPES and spin resolved ARPES study, which confirmed the spin polarization of the Bi induced bands [113]. Moreover the very high quality of the interface revealed the spin degeneracy of the surface states at all the high symmetry points. In the RB model the spin degeneracy is a consequence of the time reversal symmetry, which is not preserved at the \bar{K} point, where the two S1 spin branches are experimentally observed to be degenerate. This was proposed to be a non Rashba-type spin splitting, arising from the peculiar group symmetry. The use of constant energy maps helped in assessing the topology of the spin helicity at the different high symmetry points: a vortical spin arrangement is found at $\bar{\Gamma}$, in agreement with a normal Rashba model, but also at \bar{K} . The two vortical spin structures lead to a non-vortical spin arrangement at \bar{M} , demonstrating

for the first time that time reversal symmetry is not a sufficient condition to yield a vortical spin texture [113].

A peculiar spin splitting at the \bar{K} high symmetry point was reported also for a similar interface, $\text{Ti/Si(111)} \sqrt{3} \times \sqrt{3}R30^\circ$ [114]. Figure 2.22 **a** and **b** show the results of spin resolved ARPES measurements along the $\bar{\Gamma}\bar{K}$ direction ($\bar{\Gamma}$ at $\theta = 0^\circ$ and \bar{K} at $\theta \sim 34^\circ$). In panel **a** the Mott detector was sensitive to the in-plane spin component. The spin branches have equal intensity at $\bar{\Gamma}$, as expected in a Rashba model, but their relative intensity varies with the angle. The magnitude of the spin splitting is small if compared to the Bi/Si(111) system, and in fact spin integrated ARPES failed to detect this splitting. The most intriguing information is provided by the spin resolved EDCs of panel **b**, when the spin polarization \bar{P}_S was measured in the direction orthogonal to the surface. No splitting is observed up to $\theta = 26^\circ$, but then a clear split is detected (large enough to be reported also with conventional ARPES). This result indicates that \bar{P}_S rotates when approaching the \bar{K} point, resulting in a net 100% out-of-plane polarization. This effect is new, and not observed in Bi/Si(111) . Normal vortical spin textures would be expected, as a result of relativistic band calculation, at $\bar{\Gamma}$ and \bar{M} . A clockwise spin helicity is found around the latter point, and conversely anticlockwise at the former high symmetry point. The combination of the

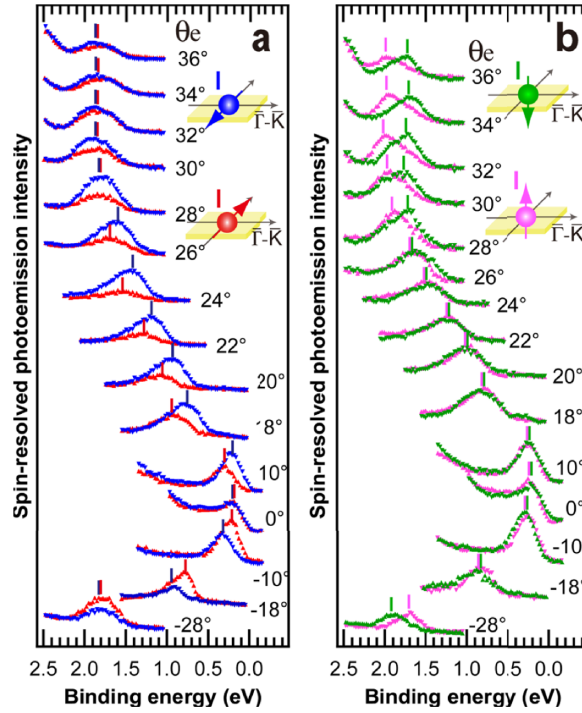


Figure 2.22: **a** and **b** show spin resolved ARPES spectra of $\text{Ti/Si(111)} \sqrt{3} \times \sqrt{3}R30^\circ$. In panel **a** the photoelectrons have \bar{P} parallel to the surface and perpendicular to the $\bar{\Gamma}\bar{K}$ direction, while **b** displays the spectra for \bar{P} perpendicular to the surface. In Ti/Si(111) $\theta = 0^\circ$ corresponds to $\bar{\Gamma}$ and $\theta \sim 32^\circ$ corresponds approximately to \bar{K} . The insets indicate the \bar{P} of the detected electrons [113].

two, in principle, lead to an undefined (in the frame of a simple Rashba-Bychkov model) in-plane \overline{P}_s value at \overline{K} . This experimental finding reveals the existence of an unconventional out-of-plane spin polarization, which might be of interest for manipulating the spin polarization in spintronics devices.

A large spin splitting was also achieved in surface resonances, *i.e.* states mostly localized at the surface but outside the projected band bulk gap induced by adsorption of heavy atoms (Bi and Pb) on Ge(111). Bi/Ge(111) $\sqrt{3} \times \sqrt{3}R30^\circ$ displays split states around \overline{M} , very similarly to the silicon case [115]. *Ab initio* calculations in the LAPW + local orbital scheme confirmed the spin-orbit splitting. This is ascribed to the orbital hybridization of the different Bi p states, which determines a strong anisotropy of the wave-function along z , in a picture that closely resembles the one proposed by Bilhmayer in the case of Au(111) [61] and in the metal alloys [89]. The calculated charge distribution around the Bi nuclei, where the potential gradient plays a stronger role, shows that the p -like orbital is asymmetric and tilted by $\sim 35^\circ$ owing to the $6p_x 6p_z$ hybridization. The charge density map implies that the asymmetry of the wave-function depends on the bonding angle, hence on the local absorption geometry.

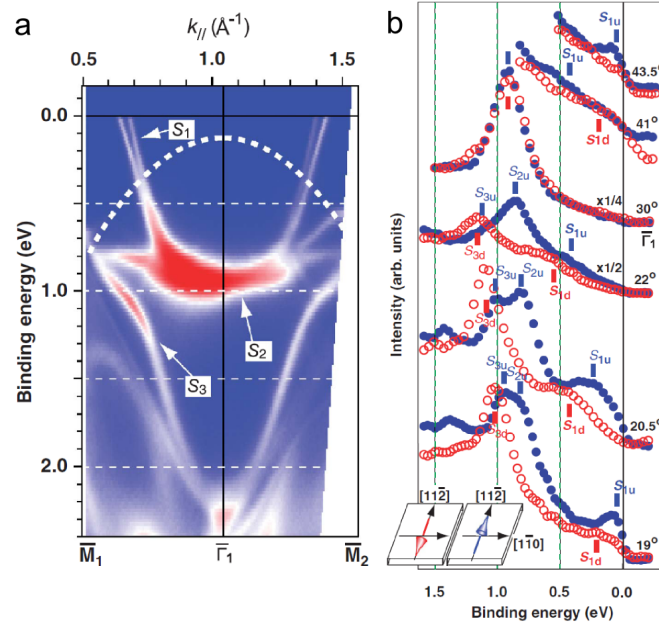


Figure 2.23: **a** shows the band dispersion of Pb/Ge(111) $\sqrt{3} \times \sqrt{3}R30^\circ$ along $\overline{M}\Gamma_1\overline{M}$. Three Pb induced bands are observed (S1, S2 and S3), and most notably S1 crosses the Fermi level and it is split into two. The spin resolved EDCs reported in panel **b** clearly revealed the spin polarized character of the three bands [116].

All these Bi (or Tl)-based interfaces are semiconductors: no spin-split bands contribute to the density of charge at E_F . In the perspective of spintronics application metallic spin polarized states embedded in a semiconducting substrate are desirable. Such a special condition was obtained for the first time in Pb/Ge(111) $\sqrt{3} \times \sqrt{3}R30^\circ$, a Pb dense phase

with a 4/3 ML coverage. ARPES and *ab initio* calculations were performed on this system, and the main results are summarized in Figure 2.23 [116]. Panel **a** shows the measured band dispersion along $\overline{M}\Gamma_1\overline{M}$, and three different Pb induced bands are present, labelled S1, S2 and S3. In particular, S1 crosses the Fermi level with a clear splitting, whose origin was investigated by spin resolved ARPES. A spin polarization is observed for all the bands: Figure 2.23 **b** shows that all the spin up and spin down EDC components are non degenerate, except the one at 30° , corresponding to the center of the second Brillouin zone $\overline{\Gamma}_1$. A fully relativistic calculation confirms the Rashba-type splitting. Pb atoms placed in different adsorption sites carry different contribution to the spin splitting. In particular Pb in the H_3 coordination site displays a strong asymmetry in the wave-function, due to hybridization of p_z and p_{xy} orbitals.

2.2.3 Spin splitting in confined quantum well systems

The drawback of the Pb/Ge(111) interface is the lack of compatibility with the silicon based technology, and this limits its practical exploitation. An alternative strategy was explored to transpose the metallic spin polarized surface states to a silicon substrate: Si(111) is used as a template for the growth of a thin Ag film, which hosts the BiAg₂ alloy. When the thickness of the metallic film is comparable to the electron coherence length, the electronic band structure close to the Fermi level reflects this confinement effect. The electrons are described as Bloch standing waves in the plane parallel to the surface, while the behavior along the surface orthogonal is solution of a quantum well-type problem. The reduced thickness is not the only requirement for the formation of quantum well states (QWS): the confining potential, in fact, is due to the simultaneous presence of a bulk band gap and the vacuum level. The physics of quantum well states has been studied thoroughly in the case of sharp metal-metal interfaces, such as Ag/Au(111) [117]. In this case the difference in energies between the two noble metal L-gaps is sufficient to sustain the quantization along z .

Si(111) was also found to support the formation of QWSs when a sharp interface with a metallic film is formed. Pb/Si(111) represents an interesting example of spin split QWSs, but the magnitude of the splitting is very small ($\alpha \sim 0.04$) and similar to the values of semi-conducting heterostructures [120]. Other systems display large spin split QWSs, namely noble metal or Al films on W(110) [68, 121] but in all these systems the origin of the splitting is ascribed to the interaction of the confined standing waves with the heavy atoms at the substrate interface, and in fact the magnitude of the splitting is inversely proportional to the film thickness.

Thin films of Ag on Si(111) were reported to form QWSs, whose electronic properties have been the subject of several ARPES studies [118, 122]. Figure 2.24 **a** shows an example of the experimental band structure along $\overline{\Gamma}\overline{K}$ for 11 ML Ag coverage. The Ag surface state ($\nu = 0$) and three distinct QW states ($\nu = 1-3$) are observed. When Bi is evaporated, the topmost Ag layer forms the alloy and the electronic band structure results from a complex interplay between the surface states of BiAg₂ and the QWSs of Ag/Si(111). Several experimental works investigated the BiAgSi trilayer system, both with the use of ARPES and spin resolved ARPES [123, 124, 119]. The key findings are well summarized in Fig-

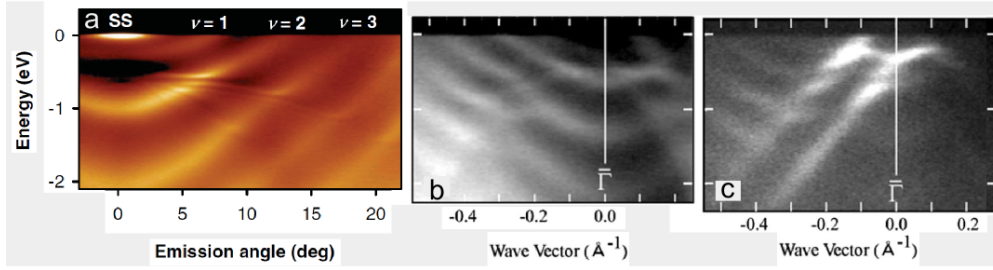


Figure 2.24: **a** displays the band dispersion of Ag/Si(111) for 11 ML Ag coverage, along the $\overline{\Gamma K}$ high symmetry direction. The Ag surface state ($\nu = 0$) and three distinct QW states with ($\nu = 1 - 3$) are observed [118]. **b** and **c** show, at two photon energies ($h\nu = 49.6$ eV and $h\nu = 28.0$ eV) the modification in the band structure after evaporation of 1/3 ML of Bi, in the case of 15 ML Ag coverage. In **b** the quantum well states of the confined Ag are well resolved. At lower photon energy, the cross-section heightens the signal of the surface states of the alloy. Both the features (QWSs and spin split states) are present at the same time. In addition, the two interact and hybridize forming gap [119].

ure 2.24 **b** and **c**, which show the band dispersion for a 15 Ag ML coverage, along the $\overline{\Gamma M}$ direction at two different photon energies (respectively $h\nu = 49.6$ eV and $h\nu = 28.0$ eV). In the former case the cross-section of the photoemission process enhances the signal associated to the QWSs, which are still present after the alloy formation, even though they are shifted downward in energy due to the modification of the confinement conditions induced by the BiAg₂ formation. In **c** the lower photon energy enhances signal from the Bi alloy: the spin split surface states are resolved, with the same characteristic parameters (E_R , k_0 and α) of the alloy formed on the pristine Ag(111) surface [87].

Interestingly, the bands arising from the QWSs and from the Bi induced surface states interact and hybridize, and gaps are opened to avoid the band crossing. No appreciable spin splitting was reported for the QWSs, but similarly to the case of Pb/Si(111) one may infer the existence of such effect, even if the experimental resolution is insufficient to resolve it. This is important to understand the interaction of the Ag QWSs with the spin split surface states. The gap is in fact spin selective due to the spin selective hybridization between one surface state branch and the parallel spin component of the quantum well states. The antiparallel spin component disperses with unchanged free electron-like behavior. These features were independently confirmed by theoretical calculations [124], a surface states-QWS hybridization model [123] and finally by spin resolved measurements [119] whose results are reported in Figure 2.25. The two panels show respectively the spin-up and the spin-down components of the band structure along $\overline{\Gamma M}$. In the region highlighted by a white dashed rectangle, three spin-up bands disperse with parabolic behavior while spin-down states are seen to be dispersion-less.

The almost spin degenerate quantum well states of Ag constitute a transport channel alternative to the spin polarized ones offered by the surface states, similarly to the Ag conduction band in BiAg₂, but the total charge carrier concentration is strongly reduced

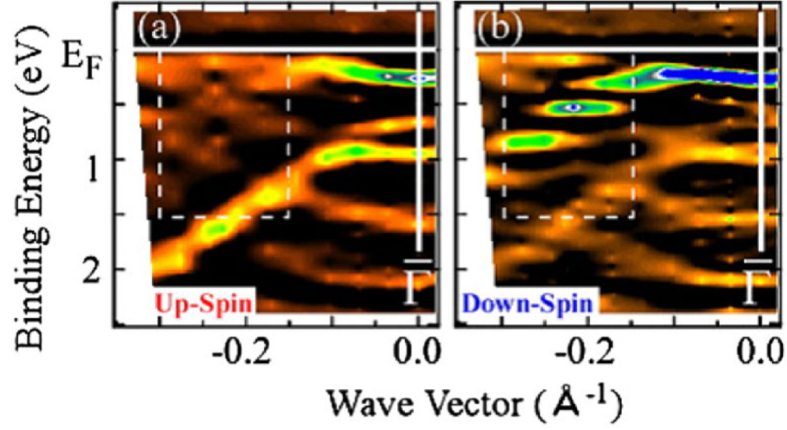


Figure 2.25: **a** and **b** shows second derivative of the spin resolved ARPES spectra along $\overline{\Gamma M}$ in the BiAgSi trilayer system. **a** reports the spin up channel, while **b** the spin down. In the region enclosed by a dashed white rectangle, in the left panel three QWSs disperse with unchanged free electron-like behavior. In the right panel, instead, dispersionless states are observed. This support the scenario of spin polarized gap, arisen from the selective hybridization of the QWSs with the spin split surface states [119].

with respect to the bulk system. For this reason the BiAgSi trilayer system represents a step forward in the direction of spintronics applications. Moreover, the partial gap offers a unique way to tailor the spin transport in this system. This motivated a detailed study of the spin polarized gap, especially focused on its symmetry, along with the investigation of a feasible way to manipulate its energy position. The results of this investigation are described in the next chapter.

The Gaps Structure of BiAg₂-Ag/ Si(111)

Contents

3.1	Conductance properties of a Rashba system	47
3.1.1	Tunneling conductance	48
3.1.2	Magnetoconductance	48
3.2	Anisotropic spin gaps in BiAg₂ – Ag/ Si(111)	51
3.2.1	I. Introduction	51
3.2.2	II. Methods and system description	51
3.2.3	III. Results and discussion	54
3.2.4	IV. Conclusion	58
3.2.5	Appendix	59
3.3	BiAg₂ – Ag/Si(111) a parallel ARPES study	60

3.1 Conductance properties of a Rashba system

The investigation of strongly spin-orbit coupled systems is partly stimulated by the prospect of forthcoming future spintronic applications. The discover of Rashba - Bychkov effect in oxides (KTaO₃ [125]), in semiconductors (BiTeI [48]) or in semiconductor based interfaces [111] represented some of the major steps-forward in this direction. Similarly, the discovery of topological insulators has been another breakthrough [77, 11].

The possibility to interface the BiAg₂ surface alloy with a Si substrate is of particular interest because the growth of metallic films with nanometer thickness constitutes a central topic of spintronics. The confinement along the *c* axis increases the surface-volume ratio and it gives rise to quantum effects. For instance, as noticed in section 2.2.3, Ag films on Si(111) host the formation of quantum well states [126], whose spin and electronic properties can be modified and controlled by the adsorption of specific atoms. In particular, large *Z* atoms (Pb and Bi) induce surface states with giant spin splitting [124, 127], while alkali metals (Na) provide a tool for controlling the position of the Fermi level in the material [128].

3.1.1 Tunneling conductance

Various theoretical and experimental works have addressed the connection between the conductance properties and the electronic band structure. Srisongmuang *et al.* proposed that in-plane tunneling spectroscopy may provide a direct way to measure the Rashba energy E_R [129]. They modelled a junction between a metal and a RB system. Figure 3.1 shows the calculated conductance for two different cases: when the spin-split surface states lie partially below E_F (left) or when the band is totally unoccupied (right). In the former case the current flows from the metal to the RB system when a negative voltage is applied, while on the other hand in the latter case a positive ΔV is necessary. Apart from the sign of the voltage the two results are identical: the conductance is characterized by two regions with respectively parabolic and linear behavior. The conductance increases from the bottom of the spin-polarized band. The slope decreases continuously up to a kink, whose energy position corresponds to the crossing point of the two spin-split branches. Hence, the difference in energy between the rise and the kink (E_λ) is exactly equal to the Rashba energy (E_R). The main difference with similar previous studies [130, 131] is the introduction of an interfacial spin-flip scattering, which results from the presence of magnetic impurities in the substrate or among the adsorbed atoms. In the case of metallic contacts the spin-flip scattering suppresses the conductance, while in the tunneling regime the conductance is increased [129].

3.1.2 Magnetoconductance

Since a giant spin splitting is obtained in the BiAg₂ surface alloy, the electronic and transport properties of the BiAg₂ – Ag/Si(111) system were subject of extensive studies [124, 132, 123, 119, 128, 133].

The vertical confinement of the metallic layer limits the number of bulk conduction

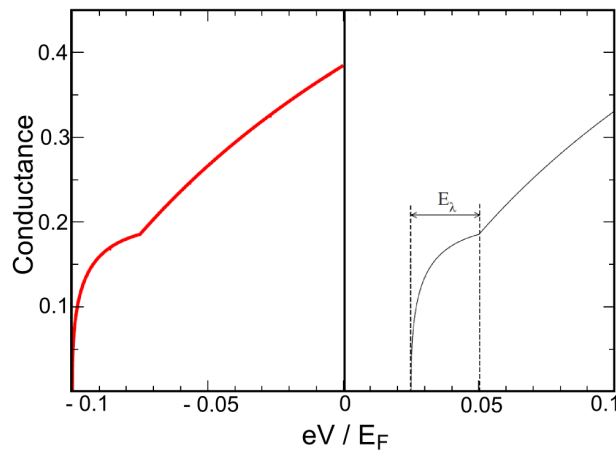


Figure 3.1: Left column shows the conductance spectrum for a RB-metal interface in the case where the energy band of the Rashba system is partly occupied $E_0 = -0.075E_F$. The right panel represent the case where the band is unoccupied $E_0 = 0.05E_F$ [129].

channels, resulting in an enhanced surface contribution. Recently Miyata *et al.* succeeded in measuring the magnetoconductance of bare and Bi-alloy terminated Ag(111) films, by exploiting a micro four point probe (MFPP) [132]. Figure 3.2 **a** shows the schematic drawing of the MFPP experiment and panel **b** displays the results for the Ag(111) film (blue) and for the BiAg₂ alloy (red), in all the case the thickness of the Ag film is equal to 15 monolayer. For both the surface terminations weak anti-localization (decrease of $\Delta\sigma$) and localization (increase of $\Delta\sigma$) effects are observed.

The two quantum effects are interpreted at a quantitative level by the use of the Hikami, Larkin and Nagaoka formula [134], which is characterized by four free parameters with the dimension of an effective magnetic field: B_0 describes the elastic scattering and it is set equal to a constant. B_s takes into account the spin-flip scattering and it is discarded in the analysis since no magnetic impurities are present in the system. B_i and B_{so} describe the inelastic and spin-orbit scattering and they determine respectively the localization and anti-localization phenomena.

What is relevant for our study is the fact that all these effective fields are related to the two-dimensional density of states at the Fermi level (N^{DOS}) and to the specific carrier

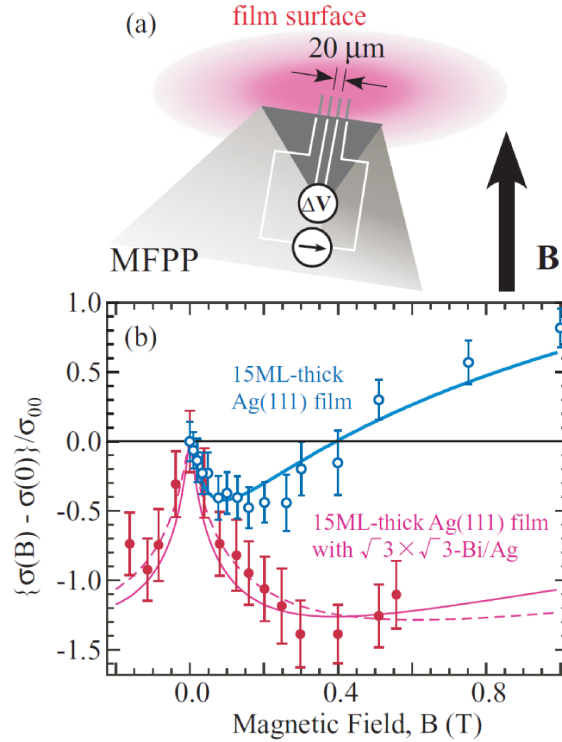


Figure 3.2: **a** shows a schematic drawing of the experimental MFPP geometry. **b** displays the magnetoconductance data for the bare (blue open circles) and Bi/Ag-terminated (purple solid circles) 15-ML Ag(111) film on Si(111). Solid and broken lines are fits to the data according to the Hikami-Larkin-Nagaoka (HLN) formula [132].

relaxation times τ_p (with $p = 0, s, i, so$) by the relation

$$B_p = \frac{e\hbar N^{DOS}}{4\sigma_0\tau_p}. \quad (3.1)$$

In order to access the relaxation times, of interest for the transport properties, it is necessary to know the detail of the two-dimensional density of states and the Fermi velocity of each quantum well state. These can be extracted from ARPES data, as in Figure 3.3. A simple 2D nearly free electron model (NFE) is used to simulate the band structure, in order to infer the Fermi velocity and the N^{DOS} . For the sake of simplicity, in this model the presence of spin gaps at the Fermi level is disregarded. Nevertheless, this hypothesis is not supported by high resolution ARPES experiments. The BiAg₂ surface alloy, in fact, presents two pairs of spin-split bands. One lies entirely below the Fermi level and it does not form gaps at E_F . The second state, on the contrary, crosses E_F and it forms hybridization gaps with the QWSs, whose number depends on the Ag thickness. The manipulation of the spin gaps position with respect to the Fermi level has been already proposed by Frantzeskakis *et al.* [124] by varying the number of Ag ML. This strategy offers only discrete variations in the energy position and the experimental realization of a gap at E_F might be difficult.

The need for an accurate study of the topology of the spin gaps at the Fermi level in the tri-layer BiAg₂ – Ag/Si(111) motivated the work described in the next section, which has been published in Physical Reviews B [135]. Here I demonstrate an alternative mechanism to modify continuously the energy position of the gaps via deposition of small amount of alkali metal (Na).

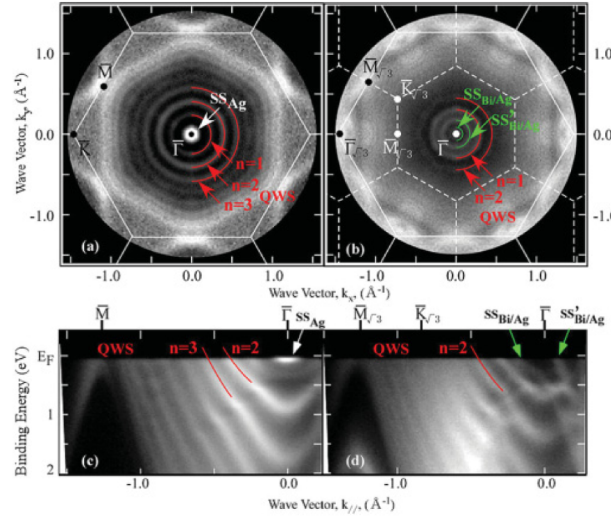


Figure 3.3: In the top row photoemission Fermi surfaces are shown for (a) bare and (b) Bi/Ag-terminated 15-ML Ag(111) film on Si(111) measured at $h\nu = 49.6$ eV. The 1×1 and $\sqrt{3} \times \sqrt{3}R30^\circ$ Brillouin zones are shown with solid and broken lines respectively. The bottom row display the associated band structure measured along the $\bar{\Gamma}\bar{M}$ high symmetry direction [132].

3.2 Anisotropic spin gaps in BiAg₂ – Ag/ Si(111)

We present a detailed analysis of the band structure of the $\sqrt{3} \times \sqrt{3}$ R 30° BiAg₂/Ag/ Si(111) trilayer system by means of high resolution Angle Resolved Photoemission Spectroscopy (ARPES). BiAg₂/Ag/ Si(111) exhibits a complex spin polarized electronic structure due to giant spin-orbit interactions. We show that a complete set of constant energy ARPES maps, supplemented by a modified nearly free electron calculation, provides a unique insight into the structure of the spin polarized bands and spin gaps. We also show that the complex gap structure can be continuously tuned in energy by a controlled deposition of an alkali metal.

3.2.1 I. Introduction

The control over the polarization of the electronic states close to the Fermi energy and the capability to transport spin polarized currents represent two fundamental requirements for spintronic applications [136, 137, 138]. The discovery of a giant Rashba effect in surface alloys has highlighted the potential of spin-split states at surfaces and interfaces [87] to achieve these goals. In these systems, the net polarization of the density of states is null because of time reversal symmetry. Nevertheless, the Rashba interaction introduces a momentum-dependent effective magnetic field which separates the spin density of states in the reciprocal space [45]. Such effective magnetic field and spin separation of the bands are expected to enable the control of spin polarized currents [107, 129]. Recent experiments indicate the fascinating prospect of transferring the spin-split surface states to semiconductor substrates [124, 123, 114, 111, 139, 116, 132], bringing these systems one step closer to future technological applications. In this work, we present a detailed analysis of the band structure properties of the BiAg₂/Ag/ Si(111) trilayer system. We show that constant energy (CE) maps provide a unique source of information on the topology of the spin polarized surface states and gaps. We also show that the energy of the gap structure can be continuously tuned by a controlled deposition of an alkali metal (Na).

3.2.2 II. Methods and system description

A Si(111) crystal (n-doped, resistivity 0.011 Ω cm) was cleaned by repeated cycles of direct current heating, with flashes at 1400K followed by steps at 900K. The sample was slowly cooled across the 7×7 transition temperature during the last preparation cycle. The quality of the 7×7 reconstruction was checked by means of low-energy electron diffraction (LEED). Ag films (thickness > 8 ML) were evaporated from a tungsten basket onto the cold substrate (100K). After a mild post-annealing, Ag 1×1 spots appeared in the LEED pattern. This protocol yields a layer-by-layer growth with a sharp incommensurate interface [126]. The deposition of $1/3$ ML Bi was achieved with an EFM3 Omicron evaporator. After a post-annealing at RT, $\sqrt{3} \times \sqrt{3}$ R 30° extra spots in the LEED pattern indicated the formation of a BiAg₂ surface alloy. Na was evaporated from a commercial dispenser (SAES getter) onto the cold sample (100K).

Angle-resolved photoelectron spectroscopy (ARPES) was performed at 70K with a Phoibos 150 Specs analyzer. The energy resolution was set equal to 10 meV. The partially

polarized UV light (HeI α line at 21.22 eV) was produced by a monochromatized high brightness Gammadata VUV 5000 lamp.

The interplay of a large spin-orbit splitting and of quantum confinement in the BiAg₂/Ag/Si(111) system leads to a complex electronic structure, presented Fig. 3.5(a) and Fig. 3.4 (a) [124, 114, 128, 119]. Its origin can be summarized as follows:

- a. Quantum well states (QWS) develop in the silver layer due to the confinement of the Ag s-states by the vacuum on one side, and by the fundamental energy gap

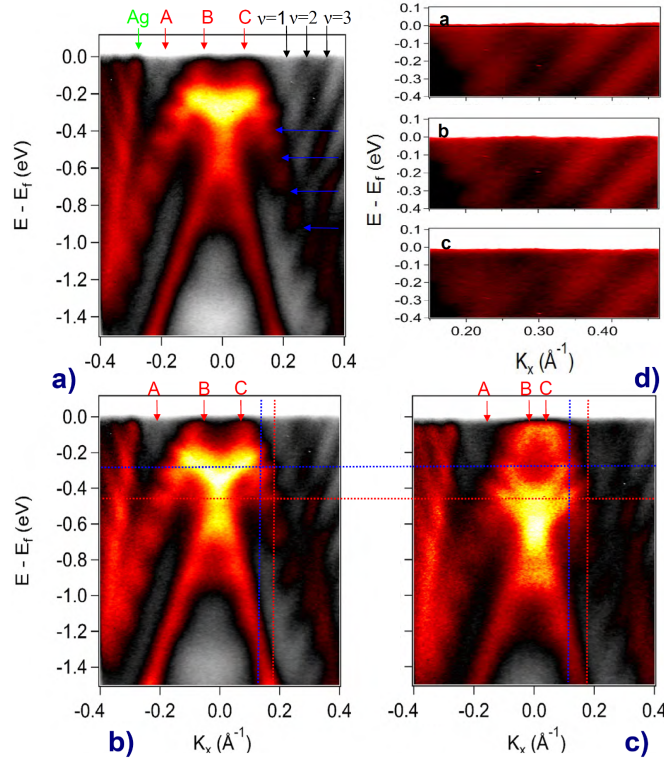


Figure 3.4: a) ARPES intensity map of BiAg₂/Ag/Si(111) for $\theta=19\text{ML}$. The first three silver quantum well states ($\nu = i$ with $i = 1, 2, 3$) are indicated by black vertical arrows. The deposition of $1/3\text{ML}$ of Bi yields fully occupied $|sp_z\rangle$ derived surface states (SS), and $|sp_{xy}\rangle$ derived SS crossing E_F (vertical red arrows A, B, C). Band gaps open at the crossing of the spin-split states with the nearly degenerate QWS. A downward ~ 100 meV energy shift is observed for the Ag QWS after the formation of the surface alloy, consistent with previous reports [127, 124]. The feature marked by the vertical arrow labelled Ag is due to scattering of photoelectrons emitted from a QWS on the periodic potential of the reconstruction. b) and c) were measured after two subsequent Na depositions. Red (blue) dashed lines in (b) cross at the presence (absence) of a spin gap. After reaching the saturation Na coverage, (c), the same crossings are now associated with the absence (presence) of the gap. d) Corresponding close-ups of the QWS dispersion near E_F .

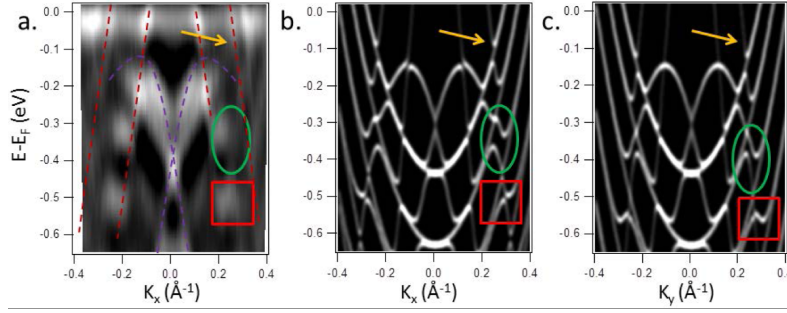


Figure 3.5: a) Derivative of the photoemission intensity along the $\bar{\Gamma}\bar{K}$ direction (k_x) for a silver thickness of 25ML. Dashed lines are guide to the eyes and indicate the surface states. The silver quantum well states are localized in the subsurface planes so they have a low spectral weight with respect to the surface states. b) and c) Calculated band structure around $\bar{\Gamma}$ along the $\bar{\Gamma}\bar{K}$ (a) and $\bar{\Gamma}\bar{M}$ (b) high symmetry directions. The calculation parameters are given in the appendix. The QWS positions agree well with a silver thickness of 25ML. White stands for high intensity. The broadening and the intensity of the calculated bands are the result of an artificial gaussian convolution with an arbitrary width. The arrow and the boxes point out some peculiar patterns described in the text.

on the substrate side [126]. The QWS have a nearly-free electron character, and give rise to a set of parabolic sub-bands with small and positive effective masses around $\bar{\Gamma}$, the center of the Brillouin zone (BZ) Fig. 3.4 (a). The number and energy positions of these sub-bands are determined by the thin film thickness. A standard Rashba mechanism [45] splits the QWS, but the splitting is too small to be directly observable [124, 123].

b. A downward ~ 100 meV energy shift is observed for the Ag QWS after the formation of the surface alloy, consistent with previous reports [127, 124]. Two-dimensional SS with negative effective masses develop in the BiAg₂ surface alloy. They have mainly $|sp_z\rangle$ and, respectively, $|sp_{xy}\rangle$ character. Each band is split into two strongly spin polarized sub-bands as a result of a strong Rashba interaction, similar to what was previously found in BiAg₂/Ag(111) [87]. The $|sp_z\rangle$ states are split in momentum by $\Delta k_{sp_z} = 0.13 \text{ \AA}^{-1}$, and cross at $\bar{\Gamma}$ at a binding energy $E_B^{sp_z} = 350$ meV. The two $|sp_{xy}\rangle$ spin components cross ~ 500 meV above the Fermi level (E_F) [89, 90]. All the SS bands of BiAg₂ deviate from a simple parabolic dispersion and show a hexagonal anisotropy [87, 56].

c. Spin conservation [140] and symmetry considerations determine the hybridization of the spin polarized SS bands with the nearly degenerate quantum well states. As a result the BiAg₂/Ag/Si(111) system exhibits a spin polarized and multi-gapped electronic structure [124, 123, 128, 119].

The ARPES intensity map of Fig. 3.4 (a) illustrates the dispersion of the hybridized $|sp\rangle$ SS and $|s\rangle$ QWS. Spin gaps can already be identified in the image. The high contrast enables a precise analysis of the intensity distribution, namely close to E_F and around

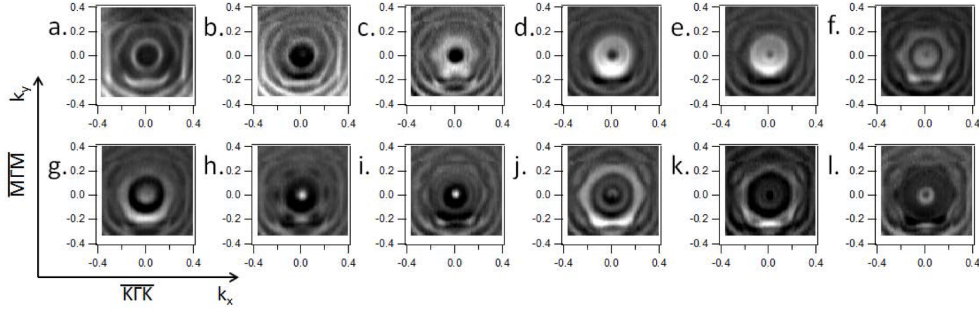


Figure 3.6: Second derivative images of the constant energy ARPES intensity maps close to $\bar{\Gamma}$ for the following binding energies: a. 50meV, b. 100meV, c. 150meV, d. 200meV, e. 250meV, f. 300meV, g. 350meV, h. 400meV, i. 450meV, j. 500meV, k. 550meV, l. 600 meV. k_x and k_y vary from -0.4 to +0.4 \AA^{-1} in each frame. the sample corresponds to a silver thickness of 25ML. White stands for high intensity. The spots at the center of the images are an artifact of the derivative procedure.

the gaps. We show in the following that the hexagonal anisotropy of the SS dispersion generates a peculiar spectral density pattern in this quantum-confined Rashba system.

3.2.3 III. Results and discussion

We restrict our ARPES study to a region of reciprocal space around $\bar{\Gamma}$ covering the first Brillouin Zone of the $\sqrt{3} \times \sqrt{3}$ R 30° reconstruction. Fig. 3.6 presents a set of constant energy cuts through the band structure, for several binding energies between 50 meV and 600 meV. The two contours closest to $\bar{\Gamma}$ in panel (a) correspond to the spin polarized $|sp_{xy}\rangle$ SS of the BiAg₂ alloy [124]. These bands exhibit specific features of the giant Rashba splitting: the inner contour is circular, while the outer one is hexagonal. The hexagonal third contour around $\bar{\Gamma}$ is the backfolded signal of an Ag QWS. It is due to the scattering of the photoelectrons from the $\sqrt{3} \times \sqrt{3}$ R 30° surface potential, and therefore is a final state effect of the ARPES process. This feature partly masks the circular contours of the Ag QWS in Fig. 3.6 (a) and (b). The signatures of the Ag QWS are visible at larger momenta, near the corners of the image. At higher binding energy, in panel (c), the additional hexagonal contour at $\mathbf{k} \approx (0.2, 0.2)\text{\AA}^{-1}$ reflects the top of the spin-orbit split $|sp_z\rangle$ bands of the alloy. With increasing binding energy the contours of the QWS shrink, while those of the SS expand, according to the opposite sign of their effective masses.

A description of the band structure is hampered by the large number of bands and by the hexagonal anisotropy of the multigapped structure. *Ab-initio* calculations of the constant energy contours face the difficulties of a complex interface structure, and of the dense sampling of k space. We chose instead a phenomenological approach, based on an anisotropic nearly free electron (NFE) model, with additional terms describing the hybridization of the surface and quantum wells bands.

Due to the lack of structural inversion symmetry of the (crystal, interface, vacuum) system, both the SS and the QWS are expected to exhibit a Rashba behavior [45] and to be

at least partially polarized. A spin polarization of the QWS, which has been observed e.g. for Pb thin films on Si(111) [120], is a prerequisite for the opening of spin gaps [124, 123]. However, the Rashba coupling is so weak that the splitting cannot be directly observed, and the Ag QWS appear to be degenerate and parabolic. The sixfold symmetry of the SS contours is the result of the threefold rotational symmetry of the alloy structure and time reversal symmetry. The giant SO splitting of the bands has been attributed to i) an anisotropy in the in-plane surface potential [87, 56], ii) the buckling of the Bi alloy layer, contributing to the anisotropy of the SS wave-function along the surface normal [102]; or again iii) the unquenching of the orbital momentum at the surface [63]. Time reversal symmetry requires that the two spin branches of a Rashba system have opposite polarization, so that each branch can be considered separately in discussing their hybridization with other states.

Recently, the snow-flake-like contour of the Fermi surface of Bi₂Te₃ was simulated by adding higher order terms to an effective Hamiltonian [141, 142]. A similar NFE calculation for the Bi/Si(111) interface [112] yields a good agreement with the experiment [143, 144]. We extend that approach to the present case. We used the following spin Hamiltonian with the basis states $|\mathbf{k}, \uparrow\rangle$, $|\mathbf{k}, \downarrow\rangle$, ($\mathbf{k}^2 = k_x^2 + k_y^2$), to describe the spin polarized branches of the $|sp_z\rangle$ and $|sp_{xy}\rangle$ SS:

$$H_{sp}(\mathbf{k}) = \begin{pmatrix} E_0^{sp} + \frac{1}{2}c_{sp}((k_x - ik_y)^3 + (k_x + ik_y)^3) + \frac{\mathbf{k}^2}{2m_{sp}} & \alpha_{sp}(-ik_x - k_y) \\ \alpha_{sp}(ik_x - k_y) & E_0^{sp} + \frac{1}{2}c_{sp}((k_x - ik_y)^3 + (k_x + ik_y)^3) + \frac{\mathbf{k}^2}{2m_{sp}} \end{pmatrix} \quad (3.2)$$

where m_{sp} , E_0^{sp} , α_{sp} are respectively the negative effective mass of the SS, the binding energy of the surface band and the effective Rashba constant, and c_{sp} is an anisotropy parameter. The parameters for the $|sp_z\rangle$ and $|sp_{xy}\rangle$ states are different. Each spin-branch of the QWS is described by a parabolic band of $|s\rangle$ character:

$$H_{QWS,\nu}(\mathbf{k}) = \begin{pmatrix} E_{0,\nu}^{QWS} + \frac{\mathbf{k}^2}{2m_{QWS}} & 0 \\ 0 & E_{0,\nu}^{QWS} + \frac{\mathbf{k}^2}{2m_{QWS}} \end{pmatrix} \quad (3.3)$$

where the effective mass of the QWS, m_{QWS} , is the same whatever the index (ν) of the quantum well band. $E_{0,\nu}^{QWS}$, the binding energy of the ν^{th} quantum well band, follows the standard confinement law along one dimension. $E_{0,\nu}^{QWS}$ and m_{QWS} can be fit to the unperturbed QWS dispersion far from the SS. The parameters V_ν describing the hybridization between the quantum well states $|QWS, \nu, \sigma\rangle$ and the $|sp_z, \sigma'\rangle$ and $|sp_{xy}, \sigma'\rangle$ SS were adapted from [123], and assumed independent of the orbital character of the SS. A full polarization for the QWS is enforced by setting the hybridization to 0 for opposite spin states; i.e.

$$\langle QWS, n, \sigma | H | sp, \sigma' \rangle = V_\nu \text{ if } \sigma = \sigma', \quad (3.4)$$

and

$$\langle QWS, n, \sigma | H | sp, \sigma' \rangle = 0 \text{ if } \sigma \neq \sigma'. \quad (3.5)$$

As suggested by group theory considerations [106, 145] and *ab-initio* calculations [87, 124, 89], we also introduce a weak coupling between the $|sp_z\rangle$ and $|sp_{xy}\rangle$ SS:

$$\langle sp_z | H | sp_{xy} \rangle = V. \quad (3.6)$$

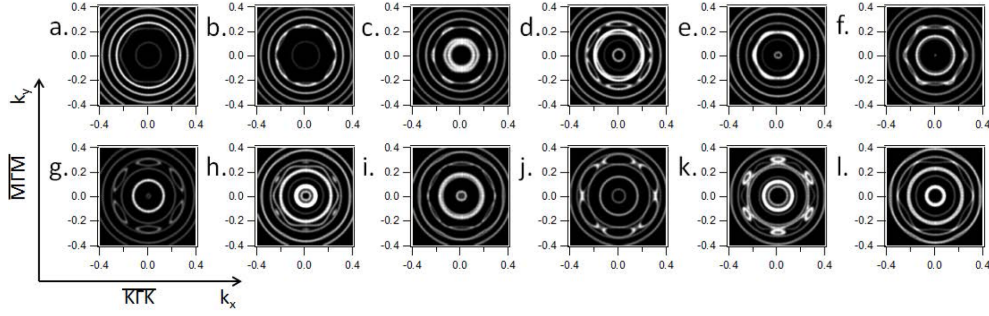


Figure 3.7: Calculated CE contours close to $\bar{\Gamma}$ for the following binding energies: a. 50meV, b. 100meV, c. 150meV, d. 200meV, e. 250meV, f. 300meV, g. 350meV, h. 400meV, i. 450meV, j. 500meV, k. 550meV, l. 600 meV. k_x and k_y vary from -0.4 to $+0.4 \text{ \AA}^{-1}$ in each frame. The calculation parameters are given in the appendix. The QWS positions agree well with a silver thickness of 25ML. White stands for high intensity. The broadening and the intensity of the calculated bands are the result of an artificial gaussian convolution with an arbitrary width.

A weak but nonzero coupling is necessary to achieve a good agreement with the data. This additional term would lead to a contradiction with eq. (3.5) for V large with respect to V_ν , which is not the case here. All parameters (see appendix) were determined from the best fits to the data of Fig. 3.6. The QWS parameters correspond to a thickness of around 25 ML. Despite its simplicity, the model captures the main features of the experimental data. The hexagonal anisotropy of the surfaces states is not perfectly reproduced near the top of the bands. The inner bands are closer to $\bar{\Gamma}$ and more circular than in the experimental maps. The agreement improves further away from $\bar{\Gamma}$. The model does not include the backfolding of the SS.

Fig. 3.5(b) and (c) show the simulated band dispersion in the k_x ($\bar{\Gamma}\bar{K}$) and, respectively, k_y ($\bar{\Gamma}\bar{M}$) directions of the reconstructed BZ (parameters correspond to a thickness of around 25 ML, see appendix). It should be compared to Fig. 3.5a) acquired for the same thickness. The experimental data show a stronger spectral weight for the SS than for the QWS. Indeed, the surface states are strongly localized at the topmost layer whereas the QWS lie deeper in the Ag layer. The z-delocalization of the states is not computed so the balance of intensity between the SS and the QWS cannot be reproduced. The QWS are unperturbed at large k values as in the experimental data. The spin gaps appear here as diamond shapes, e.g. in the (green) oval box. The NFE model predicts that the diamond structures are strongly spin polarized, in agreement with *ab-initio* calculations [124]. Because of the hexagonal symmetry of the SS, the avoided crossings with the QWS – i.e. the gaps – occur at different energies in different directions, e.g. in the (red) rectangular box, and the width of the diamond structures is also different.

A comparison of the simulated constant energy map and the calculated band diagram of Fig. 3.5 yields further insight into the complex gap structure. As expected, only the $|sp_{xy}\rangle$ and the QWS contribute to the spectral intensity near E_F (Fig. 3.7 (a)). In Fig. 3.7 (b) ($E_B=100 \text{ meV}$) the hybridization between the $|sp_{xy}\rangle$ SS and the first QWS induces a

small decrease of spectral intensity at $k_x \approx 0.3 \text{ \AA}^{-1}$ and at the five equivalent wave vectors rotated by 60° from each other. In Fig. 3.7 (c) ($E_B=150 \text{ meV}$; on the other side of the energy gap) the spectral weight is largest at the same BZ locations. Such a contrast inversion is observed whenever the $|sp_{xy}\rangle$ or $|sp_z\rangle$ SS cross a QWS. The arrows in Fig. 3.5 (b) and (c) show that it reflects a hybridization gap in one of the spin polarized component of the QWS. Thus, the QWS acquire a hexagonal anisotropy close to the gaps.

Further from E_F the band structure is more complex, because the sequence of the bands is affected by hybridization. Fig. 3.7 (d) and (e) ($E_B \approx 200 - 250 \text{ meV}$) show an interesting energy range where the outer $|sp_{xy}\rangle$ band hybridizes with the 1^{st} QWS, and the outer $|sp_z\rangle$ band hybridizes with the 2^{nd} QWS. In this window of energy, only one spin branch of each of the two first QWS contributes to the band diagram in the $\bar{\Gamma}\bar{K}$ direction whereas there is no spin gap in the $\bar{\Gamma}\bar{M}$ direction (this is also visible in Fig. 3.5). The resulting band topology yields strongly anisotropic polarization patterns. The two circular signatures close to the center of the image correspond to the top of the $|sp_z\rangle$ bands. In Fig. 3.7 (j) ($E_B=500 \text{ meV}$) closed contours are visible at $k_y \approx 0.3 \text{ \AA}^{-1}$ and at the equivalent wave vectors. They correspond to wiggles in the dispersion, inside the (red) square box of Fig. 3.5, where an NFE model predicts strongly spin polarized states (see e.g. [123]). By contrast, unpolarized states are expected at $k_x \approx 0.3 \text{ \AA}^{-1}$ and at the equivalent wave vectors, where two bands with opposite polarization cross.

The difference in the $\bar{\Gamma}\bar{M}$ and $\bar{\Gamma}\bar{K}$ band structure is expected to introduce a different response for the electrons involved in the conduction properties along two orthogonal directions. The viability of a future device based on a similar Rashba system depends on the possibility of adjusting the energy positions of the spin gaps relative to the Fermi level. We have already shown that the electronic structure of the trilayer can be controlled by varying the thickness of the Ag layer [124]. However, only discrete shifts in the energy position of the quantum well states could be obtained, corresponding to discrete changes of the boundary conditions for the confined $|s\rangle$ Ag states. This falls short of the precise control of the spin gap texture required for spintronics applications. Here we explore a different strategy, and dope the trilayer system by depositing an alkali metal (Na). We show below that this approach enables a fine tuning of the band structure.

The ARPES intensity maps of Fig. 3.4 illustrate the effect of doping. Fig. 3.4 (a) is a reference for the BiAg₂/Ag/Si(111) surface. The initial deposition of a small amount of Na (panel (b)) induces a downward energy shift (-50 meV) of the $|sp_z\rangle$ SS. The energy shift increases with the amount of Na, and eventually saturates (panel (c)) at a coverage $\theta \sim 0.25 \text{ ML}$, estimated by comparison with the case of Na on Bi/Cu(111) [102].

At the saturation, the total energy shift of the two fully occupied $|sp_z\rangle$ SS is $\sim -250 \text{ meV}$, similar to what was observed for BiAg(111) [128]. Besides, at saturation, the total shift (Δk_F) of the inner $|sp_{xy}\rangle$ branches is equal to 0.05 \AA^{-1} . While the inner branches of the $|sp_{xy}\rangle$ derived SS ($k_F = \pm 0.08 \text{ \AA}^{-1}$ before doping, and $k_F = \pm 0.03 \text{ \AA}^{-1}$ at saturation) are clearly resolved (red arrows B and C in Fig. 3.4). The outer branches, which cross E_F at $k_F = \pm 0.21 \text{ \AA}^{-1}$ [87, 128], are much weaker due to ARPES matrix elements, and a Fermi level crossing can be identified only for negative k values (arrow A in Fig. 3.4). Figure 3.4 (d) presents a close-up of the QWS dispersion for positive k values, before (a) and after (b, c) two Na depositions cycles. Contrary to the Bi-derived SS, the energy of the QWS is not

affected by the Na adsorption. Even at saturation there is no change in the corresponding Fermi wave vectors. Clearly, the electrons donated by the Na atoms dope the BiAg₂ SS, which are strongly localized at the surface, rather than the deeper lying QWS. The result is a continuous shift of the SS with respect to the QWS as a function of Na coverage, and a corresponding shift of the gap structure relative to the Fermi level. The partially spin polarized gap structure is so strongly affected by the alkali doping that the position of the gap (indicated by the crossing of the blue dashed lines in Fig. 3.4 (b)) can be swept with the fully un-gapped region (blue lines crossing in Fig. 3.4 (c)) and viceversa (crossing of the red lines in Fig. 3.4 (b) and (c)). Similar effect, even if not experimentally resolved, must affect also the spin gap close to the Fermi level.

3.2.4 IV. Conclusion

In summary, ARPES reveals the topology of the spin-dependent hybridization gaps of the trilayer BiAg₂/Ag/Si(111) system which exhibits a giant Rashba effect. Doping of the surface states by the deposition of controlled amounts of sodium opens the way to a complete control of the energy position of the band structure. The ability of tuning the Fermi level across states with strong and opposite polarization suggests possible future applications in spintronics. We expect that our novel experimental data will stimulate further theoretical work on the spin-dependent transport properties of Rashba surface alloys.

3.2.5 Appendix

NFE calculation parameters	
$E_0^{sp_{xy}}$	500 meV
$m_{sp_{xy}}$	−0.019
$\alpha_{sp_{xy}}$	2.9
$c_{sp_{xy}}$	36
$E_0^{sp_z}$	−350 meV
m_{sp_z}	−0.035
α_{sp_z}	3.1
c_{sp_z}	19
$E_{0,1}^{QWS}$	−430 meV
$E_{0,2}^{QWS}$	−620 meV
$E_{0,3}^{QWS}$	−860 meV
$E_{0,4}^{QWS}$	−1150 meV
$E_{0,5}^{QWS}$	−1400 meV
m_ν	0.092
V	20 meV
V_1	25 meV
V_2	50 meV
V_3	70 meV
V_4	100 meV
V_5	120 meV

3.3 BiAg₂ – Ag/Si(111) a parallel ARPES study

At the same time of our work a similar high resolution study of the spin gaps symmetry in BiAg₂ – Ag/Si(111) was performed by the group of Prof. Matsuda [133]. Figure 3.8 displays experimental CE maps at increasing binding energies (0, 0.26, 0.7, 0.8, 0.9 and 1.36 below E_F). The topmost row shows the electronic properties of the bare 15ML Ag film. The second and third rows show CE maps of the Bi-terminated film at two photon energies (50eV and 28eV), chosen in order to maximize respectively the cross section of the Ag QW states or the Bi derived surface states.

The results obtained by Ogawa *et al.* at the lower photon energy closely resemble our experimental findings (HeI α line at 21.2eV). In panel 3 and 4 of the bottom row, dark pockets with hexagonal symmetry reflect the presence of the hybridization gaps between the QWS and the spin-split surface states. Interestingly, the contours of the QW states of the bare Ag film are also found to deviate from perfect circles. The orientation of the hexagon is found to rotate at different binding energies, for example the QW with $n=2$ between panel 2 and 3. This is interpreted as an effect of the interaction of the Ag states with the Si substrate, and more precisely with the edge of the heavy hole (HH) and light hole (LH) band, which are characterized by hexagonal symmetry.

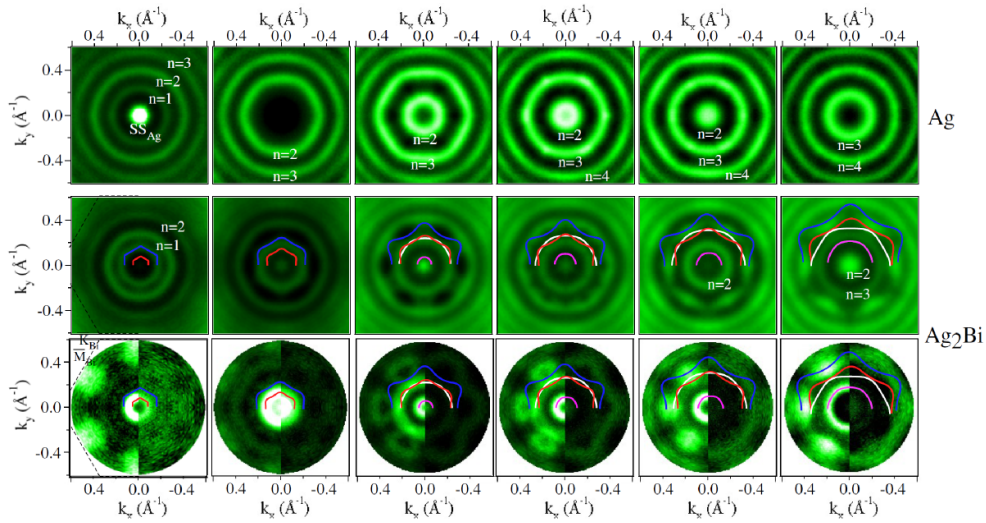


Figure 3.8: CEMs measured at 0, 0.26, 0.70, 0.80, 0.90, and 1.36 eV below E_F (from the first to the sixth column, respectively) for the bare (topmost row) and Bi-covered Ag(111) film. Photon energy is 49.6 eV for the first and second row and 28.0 eV for the bottom row [133].

The ARPES data presented in this chapter have provided important detail on the complex electronic properties of BiAg₂ – Ag/Si(111). We think that the anisotropy of the spin gaps and the possibility to manipulate their position in proximity of the Fermi level might offer a template for the the development of spintronics devices. Moreover, ultrathin metallic films with large spin splitting grown on semiconductor substrates are also good candidates for gate tuning, *i. e.* tuning of E_F by a deposited gate, which also represents an

interesting approach for future spintronics applications.

Symmetry-Dependent Hybridization in Supported Pb Monolayers

Contents

4.1	ARPES studies of a Pb monolayer on a metallic substrate	63
4.2	Combined ARPES and STM study of Pb/Au(111) moiré: one overlayer two symmetries	66
4.2.1	I. Introduction	66
4.2.2	II. Experiment	67
4.2.3	III. Results	69
4.2.4	IV. Discussion	71
4.2.5	V. Conclusions	74
4.2.6	Appendix	74
4.3	Combined ARPES and XPD study of the Pb/Ag(100) $c(6 \times 2)$ interface	75
4.3.1	Structural determination by means of XPD	76
4.3.2	Electronic properties of Pb/Ag(100)	79
4.3.3	Discussion and comparison between the Pb/Au(111) and Pb/Ag(100) results	80

I have investigated the possible existence of spin-split states in the Pb ML grown on Au(111). Even if Pb and Au are characterized by large atomic SOC, we did not observe any signature of Rashba-Bychkov effect. Nonetheless, a peculiar symmetry-dependent hybridization of the Pb states is experimentally resolved. Furthermore, I have examined this effect by growing the Pb ML on Ag(100). Despite the difference in symmetry between the six-fold closed-packed Pb ML and the four-fold substrate, this interface results commensurate with a $c(6 \times 2)$ reconstruction. The atomic positions, with particular attention to the vertical displacement, were investigated by means of X-ray photo-electron diffraction (XPD). The inferred structure helped in clarifying the differences in the band structure of the incommensurate Pb/Au(111) and the commensurate Pb/Ag(100) interfaces.

4.1 ARPES studies of a Pb monolayer on a metallic substrate

Lead monolayer on Cu(111) promotes the layer by layer growth of epitaxial films [146]. The mechanism at the origin of this effect has been investigated by a previous ARPES study [147]. The Pb layer is found to be weakly coupled to the substrate, and it is characterized

by large compressibility: at ~ 1 ML coverage the film results compressed of more than 3% (3.39\AA) with respect to the bulk Pb lattice constant [148]. Owing to the very large lattice mismatch between the ad-layer and the substrate, the Pb ML displays a considerable buckling (0.2 \AA). In addition, quantitative LEED analysis resolved a large inverted corrugation in the Cu underlying lattice [149].

The very low melting temperature of the Pb film made this system a case study for unveiling the evolution of the electronic band structure in a quasi-liquid metal [150]. For the sake of simplicity hereafter, only the ARPES results below the phase transition temperature are shown, in order to provide a reference for our study. Figure 4.3 **a** and **b** report respectively the measured band structure along the $\bar{\Gamma}\bar{K}$ high symmetry direction and the corresponding DFT calculations for the free standing Pb ML. Three bands are present, one with p_z and two with p_{xy} character. Very interestingly, in the experimental band structure the first state is broad and hardly detectable, while the other two clearly interact and a gap opens at the \bar{K} point. The origins of both these effects were not discussed in detail in this work. Figure 4.3 **c** shows the Fermi surface resulting from DFT calculations [147]. Two distinct features are present: electron pockets at the \bar{K} points and a sixfold closed contour around the $\bar{\Gamma}$ point, resulting from the two degenerate p_z and p_{xy} states.

The origin of the large broadening of the p_z derived band was discussed in a second ARPES study, which investigated the electronic properties of the Pb ML growth on Ag(111) [151]. Figure 4.4 shows the experimental band dispersion along the $\bar{\Gamma}\bar{K}_{Pb}$ direction, it closely resembles the one of Pb/Cu(111). Both the gap at the \bar{K} point and the broadening of the p_z state are resolved. In particular, the latter is interpreted as arising from the selective hybridization of the Pb derived states with the Ag continuum. The p_{xy} bands are expected to be localized in the film, weakly interacting with the substrate. On the contrary the p_z state interacts and hybridizes with the Ag s state, acquiring a long penetration depth in the material, and consequently a larger hybridization with the bulk bands.

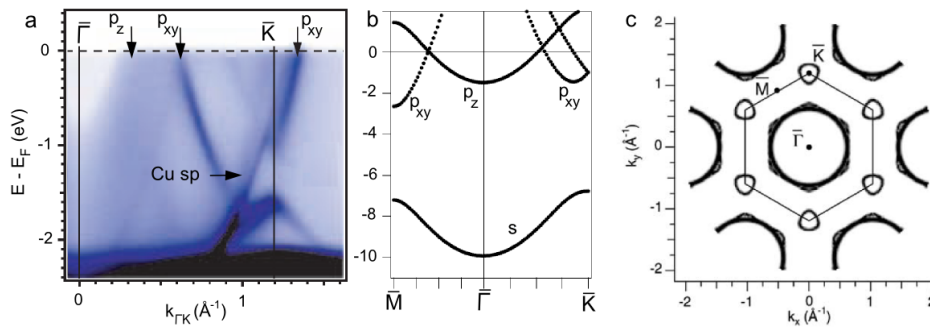


Figure 4.1: **a** shows the experimental band dispersion along $\bar{\Gamma}\bar{K}$ for Pb/Cu(111). The vertical arrows mark the Fermi level crossings of the Pb derived states. Also the dispersion of the substrate sp state is observed. **b** shows DFT calculation of the band structure of a free standing planar Pb layer with an in-plane lattice constant equal to the bulk nearest neighbor distance of 3.5 \AA . The dominant orbital character of the different bands is indicated. **c** displays the Fermi surface, as obtained from DFT calculations [147].

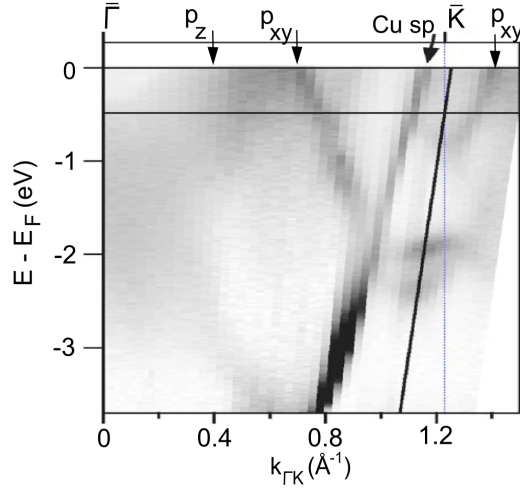


Figure 4.2: Experimental band structure of Pb/Ag(111) measured along $\bar{\Gamma}\bar{K}$. Vertical arrows indicate the Fermi level crossings of the three Pb derived states and the Ag sp band [151].

Our ARPES study of the electronic properties of the Pb ML on Au(111) indicates that also the band gap at the \bar{K} point results from a previously unnoticed hybridization of the *mainly* p_{xy} states with the p_z orbital component. The hybrid states can then interact and partially delocalize in the Au(111) bulk, thus feeling the symmetry of the substrate lattice. This work has been submitted to Physical Review B and it is the subject of the next section.

4.2 Combined ARPES and STM study of Pb/Au(111) moiré: one overlayer two symmetries

The structural and electronic properties of the Pb monolayer (ML) grown on Au(111) are investigated by ARPES and STM. Pb forms two domains rotated by $\pm 5^\circ$ with respect to the substrate. The resulting interface is an incommensurate moiré structure with an approximate unit cell of (5.77×5.77) R21.5°. Several Pb induced bands are observed with distinct orbital characters and different symmetries. The p_{xy} states cannot be described in a freestanding Pb ML picture: one of them clearly displays the two domains symmetry of the adlayer while the second follows the symmetry of the substrate. These are interpreted as arising from different degrees of hybridization of the Pb bands with the Au(111) substrate continuum.

4.2.1 I. Introduction

Angle resolved photoelectron spectroscopy (ARPES) with the advent of parallel high resolution angular detection is a powerful technique for the investigation of novel electronic properties in the band structure of solids [9]. Namely ARPES has been applied for the study of conflicting symmetries and multiple periodicities in the electronic band structure of solids [152]. In particular, systems displaying charge and spin density waves (CDW, SDW), with commensurate or incommensurate wave vectors, have been paradigm cases for the study of band topologies and conflicting periodicities [153, 154, 155]. Recently, complex surface super-periodicities have been observed not only at metal-metal interfaces [151], but also for boron-nitride and graphene grown on metallic substrates [156, 157, 158, 159, 160, 161, 162, 163]. In these cases, ARPES has direct access to the results of the interplay between different symmetries and periodicities.

Pb overlayers have been studied in detail to unravel surfactant effects at the base of homo-epitaxial growth on Cu [147, 164]. Due to its high compressibility, a monolayer (ML) of Pb forms dense moiré superstructures. The corrugation of the adlayer and the expanded atomic distance with respect to the topmost substrate layer, yield a reduced vertical bonding strength with the latter [165]. The use of constant energy maps and quantitative analysis of the single-particle spectral function from ARPES data, has enabled the investigation of the electronic properties and the coherence length of a melting Pb layer on Cu(111) [150]. Recently unexpected superconductivity has been suggested in the 4/3 ML dense phase of Pb on Si(111) by means of scanning tunneling microscopy and spectroscopy (STM/STS) [166, 167].

In the present study of a Pb ML on Au(111), STM topography and LEED evidence an incommensurate moiré structure with an approximate (5.77×5.77) R21.5° unit cell, consisting of two Pb domains rotated by $\pm 5^\circ$ with respect to the Au(111) substrate. In the ARPES spectra three Pb induced bands are observed. The use of constant energy maps (CE maps) and a related tight-binding model calculation reveal that two of the latter states have mainly p_{xy} character, one of which follows the periodicity and symmetry of the substrate, while the other does not. On the other hand, the third Pb derived state, with mainly p_z character, is strongly broadened in energy and momentum. Similar behavior has already

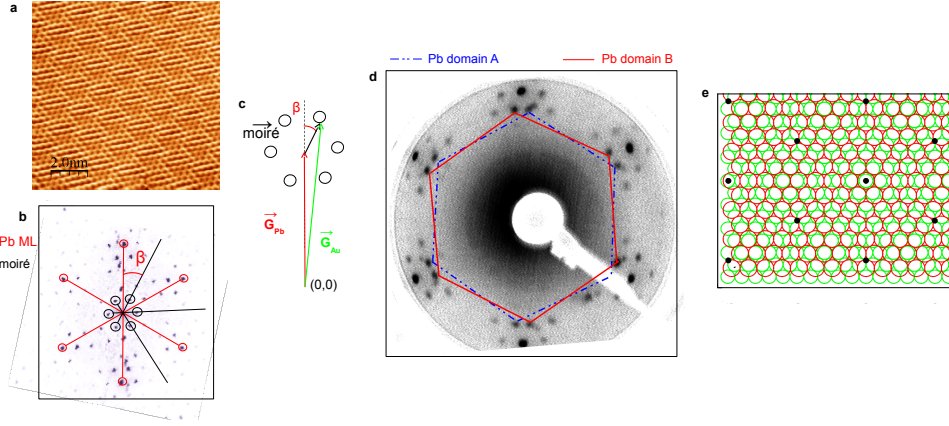


Figure 4.3: **a** Constant current STM image of 1 ML Pb on Au(111), showing one rotational domain of the (5.77×5.77) R21.5° moiré structure ($V_t = 2.0$ V and $I = 0.14$ nA, $T = 4.2$ K). **b** Fourier transform of a larger scale (20×20 nm²) STM data-set: the highest intensity spots enclosed in red circles are associated with the periodicity of the Pb adlayer. The moiré superstructure spots are indicated by black circles. The corresponding unit cell is rotated by $\beta = 26.5^\circ \pm 1^\circ$ and its fundamental vector is 4.74 times smaller than the (1,0) lattice vectors of Pb. The angle of rotation between the Pb ML and Au substrate is equal to $5^\circ \pm 0.2^\circ$. By using the Au substrate as a reference we can infer a structure close to (5.77×5.77) R21.5°. Panel **c** is a cartoon of the reciprocal lattice vectors associated to the Au substrate, to one Pb domain and to the moiré superlattice. **d** LEED image of the moiré: blue and red lines trace the two hexagonal Pb domains. A rotation of $\pm 5^\circ$ is found between the Au substrate and the two rotational domains: the lengths and position of the reciprocal lattice vectors are in agreement with the STM results. **e** Structural model of the Pb monolayer (green circles represent the Au substrate, while red circles correspond to one of the two rotational Pb domains).

been observed for other Pb MLs grown on Ag(111) [151] and on Cu(111) [147]. These peculiar features of the three Pb induced bands are interpreted as arising from their orbital dependent hybridization with the substrate continuum.

4.2.2 II. Experiment

Au(111) has been cleaned by several cycles of sputtering (with Ar⁺ at 300 K, 1keV for 30 minutes) and annealing (800 K for 25 minutes). In ARPES experiments, the cleanliness of the surface was verified by low energy electron diffraction (LEED) and ARPES measurements of the spin-split surface states. Pb was evaporated (at 300 K with a flux of 0.33ML/min) from a calibrated EFM3 Omicron evaporator. The structural quality was improved by post-annealing at 400 K, and it was controlled by means of LEED. ARPES measurements have been performed at room temperature (RT) with a Specs Phoibos 150 analyzer. The experimental energy resolution was set at 10 meV. The UV light source was a monochromatized high brightness GammaData VUV 5000 operating at the HeI α (21.22

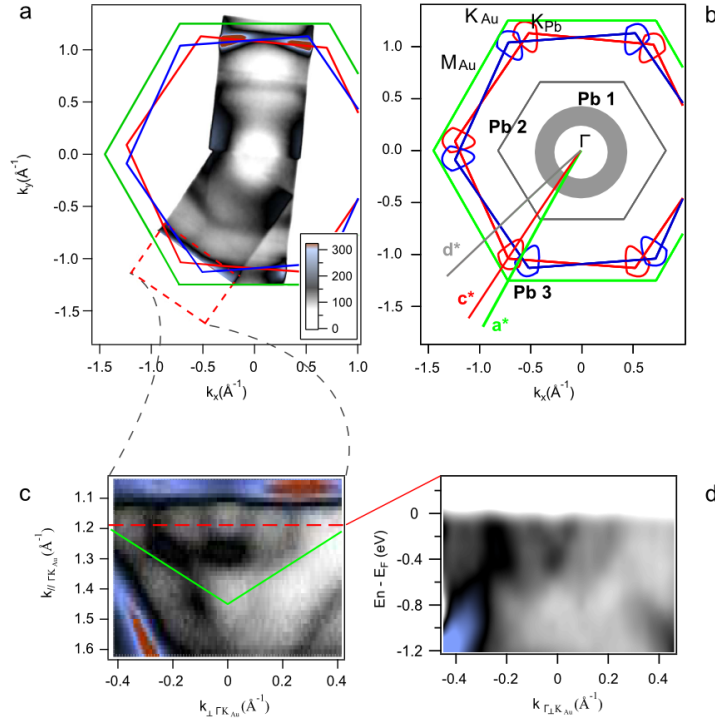


Figure 4.4: **a** Fermi surface map obtained by combining CE maps along the $\overline{\Gamma M}_{\text{Au}}$ and $\overline{\Gamma K}_{\text{Au}}$ directions. The green hexagon follows the Au(111) surface BZ, while the two smaller blue and red hexagons define the two Pb BZs, with a rotation of $\pm 5^\circ$ with respect to the substrate. **b** Cartoon of the Pb derived Fermi surface: three lines with different colors, labelled a^* , c^* and d^* trace the directions of the cuts presented in panels **b-d** of Figure 4.5 (respectively $\overline{\Gamma K}_{\text{Au}}$, $\overline{\Gamma K}_{\text{Pb}}$ and 15° rotated with respect to $\overline{\Gamma K}_{\text{Au}}$). The first state (Pb1) appears in the Fermi surface map as a blurred circle close to the $\overline{\Gamma}$ point. The second one (Pb2) constitutes a well defined hexagon, displaying the substrate symmetry. In panel **a** a red dashed rectangle defines the region of the Fermi surface shown with higher detail in panel **c**. In panel **c** the outer Pb derived state (Pb3) is clearly visible; red and blue lines trace the position of the Pb3 derived pockets at the respective \overline{K} points belonging to the BZs of the two rotational Pb domains. Panel **d** shows the band dispersion along a cut orthogonal to $\overline{\Gamma K}_{\text{Au}}$, traced in **c** with a red dashed line. The two-domain contribution on the Pb3 states is clearly depicted.

eV) line. STM experiments have been performed in a separated UHV system equipped with home-built 0.4 K STM. The sample temperature in the experiments was 4 K, and the indicated bias voltage refers to the sample.

4.2.3 III. Results

STM reveals large terraces of the adlayer with a characteristic periodic modulation. Figure 4.3 a shows a constant-current STM image of the Pb monolayer on Au(111). The STM image presents atomic resolution of the topmost layer and the long-range period created by the moiré pattern. This long periodicity is studied thoroughly in the reciprocal space. Figure 4.3 b shows the Fourier transform map obtained from a larger scale STM image ($20 \times 20 \text{ nm}^2$) [168]. The analysis of the characteristic lengths and angle between the periodicities enables us to classify the Pb/Au(111) moiré as a $(5.77 \times 5.77) \text{ R}21.5^\circ$ with respect to the Au substrate lattice. The rotation between the moiré and the atomic lattices is compatible with a rotation of 5° between the Pb and the Au(111) [169].

Figure 4.3 d reports a LEED image of the Pb/Au(111) interface. The highest intensity spots are the first order diffraction spots of the Au substrate. Each Pb extra spot presents a weak replica, the data suggests the existence of two Pb domains with a rotation of $+5^\circ$ and -5° with respect to the substrate. Blue and red lines delineate the hexagonal unit cells of the two rotational Pb domains. Moreover, the presence of higher order diffraction spots ensures the good crystalline quality of the interfaces subject of the ARPES measurements. Figure 4.3 c shows a cartoon of the characteristic lengths of the reciprocal lattice vectors and the angles between them. Figure 4.3 e shows a geometrical model for the $(5.77 \times 5.77) \text{ R}21.5^\circ$ interface: one single Pb adlayer (red circles) is superimposed to the Au substrate (green circles), with a rotation between the two lattices equal to 5° .

We describe in the following the experimental band structure arising from the interaction of the Pb ML with the Au(111) substrate. The Fermi Surface (FS) of the interface is shown in Fig. 4.4 a. This image is composed of data obtained by measurements along $\overline{\Gamma\text{K}}$ and two inequivalent $\overline{\Gamma\text{M}}$ high symmetry directions. A green hexagon defines the substrate Brillouin zone (BZ) while the smaller red and blue hexagons delimit the two Brillouin zones of Pb monolayers rotated of $\pm 5^\circ$. The highest intensity is related to the bulk Au *sp* valence band state, while all the other features are Pb induced. Figure 4.4 b displays a schematization of the Fermi Surface arising from bands with mainly Pb origin. The high symmetry points and the Pb states are indicated. Previous tight binding calculations performed for dense Pb monolayers on Cu(111) and Ag(111) [151, 147, 150], predict the presence of three Pb derived states with p_z orbital character, hereafter labelled Pb1, and with p_{xy} character, labelled Pb2 and Pb3. The same bands have been experimentally observed and they are depicted in the following. Close to the $\overline{\Gamma}$ point we observe a broad, almost circular state, Pb1. At larger k values we see straight sections, associated to the Pb2 state, which form a hexagon, as schematized in b. In panel a a dashed red rectangle encloses the region of the reciprocal space which is shown in detail in panel c. Close to the $\overline{\text{K}}_{\text{Pb}}$ point of the two rotational Pb domains, one may observe a trigonally distorted pocket related to the Pb3 band (in panel b two distinct colors are used to distinguish the contributions of the two Pb domains). A red dashed line, orthogonal to $\overline{\Gamma\text{K}}_{\text{Au}}$, traces the direction of the cut in the band dispersion shown in panel d. In the latter, the two domains contribution of Pb3 is clearly noticeable.

The behavior of the three Pb derived states is more clearly described by observing the energy dispersion of the bands as reported in Figs. 4.5 a-c-d. The three panels show cuts

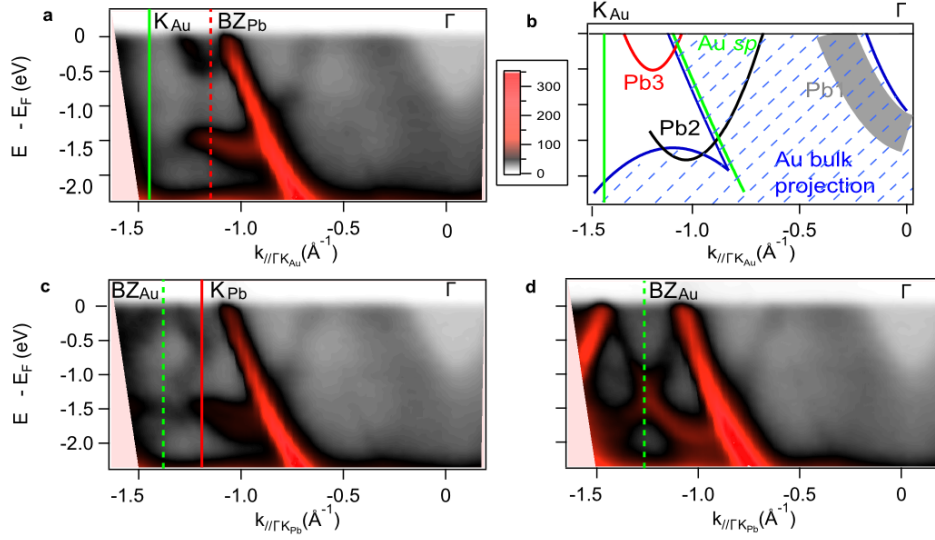


Figure 4.5: **b** Sketch of the band structure along $\overline{\Gamma K_{Au}}$ where the position of the three Pb induced bands is reported. The dispersion of the Au sp state and the projected bulk band gap as reported in Ref. [170] are also reported. Panels **a-c-d** report respectively the band dispersion along $\overline{\Gamma K_{Au}}$, $\overline{\Gamma K_{Au}}$ and 15° rotated with respect to $\overline{\Gamma K_{Au}}$. The positions of $\overline{K_{Au}}$ and $\overline{K_{Pb}}$ are traced with continuous green and red lines respectively. The borders of the Au and Pb BZs are indicated with dashed lines. In panel **b** and **c** a hybridization gap opens due to the interaction between the Pb2 and Pb3 states. The complete (un-gapped) dispersion of Pb2 and its Umklapp replica are visible in **c**.

along $\overline{\Gamma K_{Au}}$, $\overline{\Gamma K_{Pb}}$ and 15° out of $\overline{\Gamma K_{Au}}$ respectively (with $\overline{\Gamma K_{Au}} = 1.45 \text{\AA}^{-1}$ and $\overline{\Gamma K_{Pb}} = 1.19 \text{\AA}^{-1}$). The direction of the cuts is traced in Fig. 4.4 **b** with three lines labelled **a***, **c*** and **d*** respectively. Figure 4.5 **b** displays a sketch of the band structure along $\overline{\Gamma K_{Au}}$: the dispersion of the Au sp state and the projected bulk band gap as reported in [170] are also included. In Figures 4.5 **a-c-d** the highest intensity state is the Au sp bulk valence band. In Figures 4.5 **a** and **c**, with the help of panel **b**, it is possible to identify the three Pb derived bands crossing the Fermi level. The first band, labelled Pb1 with $k_{F1} = -0.35 \text{\AA}^{-1}$, disperses with positive mass reaching its local minimum at the $\overline{\Gamma}$ point and displays strong broadening in energy and momentum, similar to what has been observed on Pb/Ag(111) [151]. This broadening is responsible for the blurring of the resulting circular contour at the Fermi level in Figs. 4.4 **a** and 4.4 **b**.

At larger k values, the Pb2 state crosses the Fermi Level along $\overline{\Gamma K_{Au}}$ at $k_{F2} = -0.67 \text{\AA}^{-1}$. The Pb2 band is sharper than Pb1 but the intensities of the two are comparable. The former crosses the Au sp state at -1.3 eV and $k = -0.89 \text{\AA}^{-1}$ and displays a significantly higher intensity after the crossing. Along $\overline{\Gamma K_{Au}}$ the dispersion of Pb2 shows a gap close to the BZ boundary of a freestanding Pb ML, near the minimum of the dispersion of the third Pb induced state, Pb3. Both the gap and the Pb3 band are absent in the band dispersion presented in Fig. 4.5 **d** (15° off symmetry). This suggests that the gap observed in Fig. 4.5 **a** results from the hybridization between Pb2 and Pb3. In Fig. 4.5 **d** we observe the Umklapp

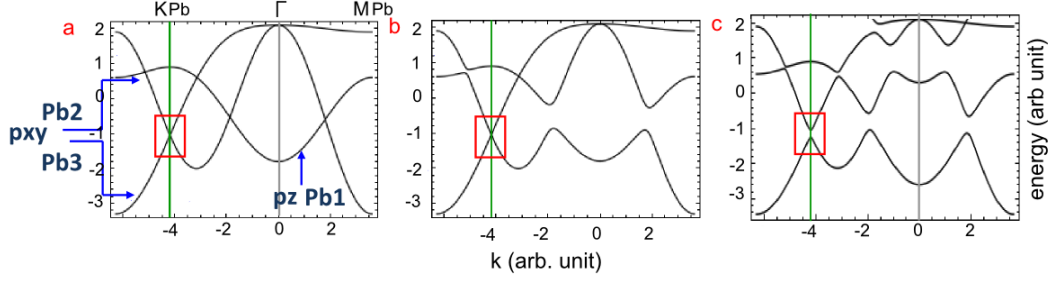


Figure 4.6: **a** Calculated band structure for a tight binding model of p states arranged in a hexagonal 2D lattice as an equivalent to a freestanding Pb ML. Three bands are observed: two of them with p_{xy} orbital character and the third with p_z character, in agreement with previous calculations and our ARPES results [151, 147]. **b** The effect of an asymmetric p_z state, which mimics the presence of the underlying substrate. A gap opens between the p_{xy} and p_z states. **c** One possible way to lift the \bar{K} degeneracy of the two p_{xy} states is to introduce the interaction between the Pb p states and the s state of the substrate, in the case of broken in-plane hexagonal symmetry (see text); a hybridization gap appears between the Pb2 and Pb3 states, similarly to our ARPES experimental results. The parameter values of the tight binding model are summarized in the Appendix.

replica of the Pb2 state, which is degenerate at the Fermi level with the Au sp state. The increase of the Pb2 intensity after the crossing of the Au sp state is even more pronounced in this figure.

The inner branch of the Pb2 state forms the hexagon in the CE map of Fig. 4.4 a. Its outer branch is masked by the strong Au sp intensity. The third Pb induced band, labelled Pb3, has a parabolic dispersion with a positive effective mass. It gives rise to the small trigonally distorted pockets centered at the \bar{K} points of the two Pb rotational domains, more clearly visible in Fig. 4.4 c. As a matter of fact, the Pb3 state follows the symmetry of the two rotational Pb domains. This is in striking contrast with the behavior of the Pb2 band, which displays the substrate symmetry. This symmetry difference, manifested by Pb states with nominally the same p_{xy} orbital character, represents a new finding, not reported in previous studies of a dense Pb ML [151, 147, 150].

In the present system we do not observe moiré-induced replica of the bands. This contrasts with recent findings for graphene grown on a metallic substrate [163, 162], for which the moiré gives rise to band replicas whose intensity reflects the strength of the superlattice potential. Therefore, in line with former observations [151, 147], we conclude that the moiré potential must have a comparatively smaller amplitude in the present case.

4.2.4 IV. Discussion

The moiré periodicity and the interaction between the overlayer and the substrate are responsible for various peculiar features in the band structure of the Pb/Au(111) interface. The opening of a hybridization gap between Pb2 and Pb3 is clearly resolved in Figs. 4.5 a

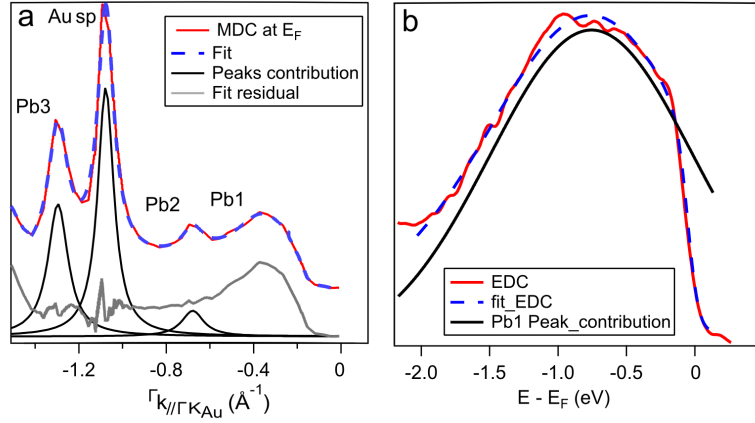


Figure 4.7: **a** Momentum distribution curve (MDC) at the Fermi Level along $\bar{\Gamma}\bar{K}_{Au}$. The fit is composed of three lorentzians with widths: Pb2 0.11 \AA^{-1} , Pb3 0.11 \AA^{-1} and Au sp 0.08 \AA^{-1} . The three lorentzian peaks are displayed under the MDC. The residual (light gray) shows the spectral weight associated to Pb1. **b** Energy distribution curve (EDC) at $k = -0.13 \text{ \AA}^{-1}$ along $\bar{\Gamma}\bar{K}_{Au}$ after the removal of a Shirley background. The Pb1 state is fitted with a gaussian width of $1.75 \pm 0.13 \text{ eV}$.

and **c**. We have performed a model tight-binding calculation in order to elucidate the origin of this gap. Figure 4.6 **a** shows the results of a TB calculations for p states arranged in a hexagonal lattice where the matrix elements are calculated using Slater-Koster energy integrals [171]. The resulting band structure mimics a freestanding Pb ML where p_z and in-plane p_{xy} states do not hybridize. Similar oversimplified tight binding models have been used to analyze experimental results obtained for Pb/Ag(111) and Pb/Cu(111) [151, 147]. As already proposed in the case of Pb/Cu(111) [147], the hybridization may be induced by the presence of the substrate and by the buckling of the Pb layer. Figure 4.6 **b** shows the tight binding calculation in the case of an asymmetric p_z state, following the methodology of Ref. [44]. This z -asymmetry artificially mimics the presence of the underlying substrate, allowing the interaction of p_{xy} and p_z states and the opening of a hybridization gap between them. Nevertheless, the degeneracy of the two p_{xy} states at \bar{K} is insensitive to any value of this z -asymmetry parameter. One possible way to open a gap at the \bar{K} point between the p_{xy} states (i.e. Pb2 and Pb3) is to extend the tight binding model in order to take into account an interaction between the p states and an s state of the substrate. Figure 4.6 **c** shows the effect of this interaction in the case of broken in-plane hexagonal symmetry, i.e. nearest-neighbor substrate and overlayer interactions, where three substrate atoms are arranged on *hollow* sites determined by six overlayer atoms.

In this case, a gap opens between the p_{xy} states at the \bar{K} point, as observed experimentally in our ARPES results. Moreover, the interaction with the substrate breaks naturally the symmetry along the z axis, opening another hybridization gap between the p_{xy} and p_z states (i.e. no need for an artificial z -asymmetry parameter). A similar hybridization gap was previously reported for Pb/Cu(111) [147], but it cannot be observed in the present ARPES results, because the bands cross above the Fermi level. The absence of degeneracy

at \bar{K} is a direct consequence of the broken in-plane symmetry, while a substantial value of sp hybridization is necessary for a non-negligible gap (see parameters in the Appendix). In the case of a cluster with hexagonal in-plane symmetry, there is no p_{xy} gap at \bar{K} for any value of sp hybridization, as we have verified for (a) an atomic arrangement where overlayer atoms sit on *on-top* sites and (b) for *on-site* sp hybridization (data not shown).

We stress the fact that our model tight binding calculation represents an oversimplified picture of the real structure, aiming to a qualitative explanation of the main band structure features. Despite its simplicity it may well identify the interaction between the Pb p states and the substrate s state, and the necessity to break the nearest-neighbor in-plane hexagonal symmetry, as the two important ingredients. The in-plane hexagonal symmetry is actually absent in the real Pb/Au(111) due to the incommensurate character of the interface.

The second characteristic feature of the band structure is the difference between the energy and momentum linewidth of Pb1 and those of the other states. Figure 4.7 quantifies this momentum and energy broadening. Figure 4.7 a shows a momentum distribution curve (MDC) at E_F , along $\bar{\Gamma}\bar{K}_{Au}$ displaying the three Pb peaks and the Au sp band. The curve is fitted by three lorentzians to account for the Au sp state and Pb2 and Pb3 states. The residual is shown in grey and it represent the contribution of Pb1, which is found to be almost three times broader than the other peaks. The EDC at $k = -0.13\text{\AA}^{-1}$ displays the Pb1 peak after background removal. This strong background is probably due to the contribution of an indirect transition; its photointensity is proportional to the one-dimensional density of states of the initial state integrated along k_z [24]. The Pb1 peak is fitted with a gaussian having a width of 1.74 ± 0.13 eV. This value is large and comparable to the one of 1.86 eV reported for a Pb ML on Ag(111) [151].

The effect of the aforementioned moiré periodicity, and the resulting inequivalence of Pb absorption sites in the nearly commensurate superstructure, is equivalent to disorder. But such an effect is not strong enough to explain the energy and momentum broadening of Pb1. As pointed out for a Pb ML on Ag(111) [151], it is necessary to consider a second mechanism: the hybridization of the p_z state with the Au surface state. When hybridized, the Pb band, acquires a longer penetration depth in the substrate and presents a stronger interaction with the bulk continuum. The latter contributes to the spectral weight spreading around the Pb1 band dispersion: this is similar to the case of an impurity interacting with a continuum.

A third unexpected, and previously unreported, feature in the band structure of the Pb ML on Au(111) is the symmetry difference of the CE contours between the two p_{xy} derived bands, illustrated by the CE maps of Fig. 4.4. The Pb3 state becomes apparent as two pockets centered around the respective \bar{K} points of the BZs of the two rotational Pb domains; in Fig. 4.4 b they are traced by red and blue lines. By contrast, the Fermi contour constituted by Pb2, as can be seen in Fig. 4.4 a, is a single hexagon. Therefore the symmetry of Pb2 is that of the substrate and not the one of the overlayer. The symmetry of the Fermi contour attributed to Pb1 state cannot be determined because of the blurring induced by the band broadening.

We interpret the different band symmetry of the p_{xy} derived states as arising from a different degree of hybridization of the Pb2 and Pb3 bands with the Au continuum. We have previously shown that such an interaction between the p_{xy} states and substrate s state

is a key ingredient for explaining the opening of the hybridization gap between Pb2 and Pb3 at the \bar{K} point. Our tight binding model has also evidenced that Pb2 interacts and hybridizes with Pb1. Hence, the former can acquire a partial p_z character. The p_z orbital component can strongly interact with the substrate continuum through hybridization with the surface state [151]. For this reason we propose that the strength of the interaction between the substrate s state and the Pb p_{xy} states is stronger in the case of Pb2 and weaker for Pb3.

The last point to be addressed is the different band intensity for k values smaller or larger than the Au sp crossing. Before crossing with the Au band, the spectral weight of the Pb1 and Pb2 states is small compared to the intensity of the Pb3 band and the branch of Pb2 outside the Au sp state (see Fig. 4.5 a-c-d). This is another consequence of a different degree of interaction between the Pb derived bands and the substrate continuum. For larger k values, in fact, the bands enter in the projected bulk gap of the substrate indicated in Fig. 4.4 b [170], hence the absence of bulk continuum makes impossible for the Pb3 states to hybridize and delocalize according to the mechanism discussed above. The interaction strength, as well as and the penetration depth of the Pb2 wave-function in the Au bulk continuum, are smaller than for Pb1. Pb1 is so strongly interacting with the bulk continuum that the resulting energy spread blurs the constant energy contour. On the other hand, for Pb2 the longer penetration in the Au bulk continuum manifest itself as a change in the band structure. The Pb2 state feels more strongly the substrate symmetry, while Pb3 is more localized in the Pb overlayer and displays its two-domains symmetry.

4.2.5 V. Conclusions

We performed STM and ARPES measurements on the Pb ML on Au(111). Our observations show a peculiar orbital selective interaction of three Pb derived bands with the bulk continuum of the substrate.

Interestingly, the two p_{xy} derived bands have distinctively different symmetries; while the first (Pb2) follows the substrate symmetry, the second (Pb3) is linked to the symmetry of the overlayer. As captured by a model tight binding calculation, the Pb2 state has a mixed p_{xy} and p_z character due to the interaction with Pb1. The p_z component can hybridize with the s band and the Au surface state, thus increasing the penetration depth of the state in the bulk continuum. The intermixing of the Pb p orbital with the substrate s state may also explain the hybridization gap between the Pb2 and Pb3 band. For the Pb1 band the selective hybridization broadens the state in such a strong way that the blurred Fermi level contour does not allow for a unique identification of the underlying symmetry. While the broadening effect is weaker for Pb2, one can still observe the effect of delocalization in the bulk as a change in the band structure itself, which follows the substrate symmetry. A similar interaction mechanism is impossible for Pb3 because it lies entirely within the projected band gap of the Au substrate.

4.2.6 Appendix

The different hybridization strengths used in the tight binding model presented in Fig. 4.6 are summarized in the following Table.

Table 4.1: Hybridization parameters following the notation of Ref. [171] and corresponding absolute energy values in units of $(pp\sigma)$.

Parameters	Fig. 4.6 a	Fig. 4.6 b	Fig. 4.6 c
$(pp\sigma)$	1	1	1
$(pp\pi)$	0.3	0.3	0.3
$(ss\sigma)$	N/A	N/A	0.5
$(sp\sigma)$	N/A	N/A	0.5
z -asymmetry	0	0.1	0

4.3 Combined ARPES and XPD study of the Pb/Ag(100) $c(6 \times 2)$ interface

In the ARPES experiments previously discussed, the large lattice mismatch between the Pb ML and the various metallic substrates (Cu(111) [147, 150], Ag(111) [151] and Au(111)) gives origin to a complex moiré super-periodicity. These interfaces are characterized by a large buckling of the adsorbed atoms, and simultaneously by an inverse corrugation of the topmost substrate layer [149, 151]. In the case of Pb/Au(111), our results suggest that the incommensurability between the Pb ML and the substrate favors the hybridization between the different Pb p states. We have investigated also the electronic properties of the Pb ML grown on Ag(100), in order to elucidate the influence of the surface structure onto this hybridization mechanism.

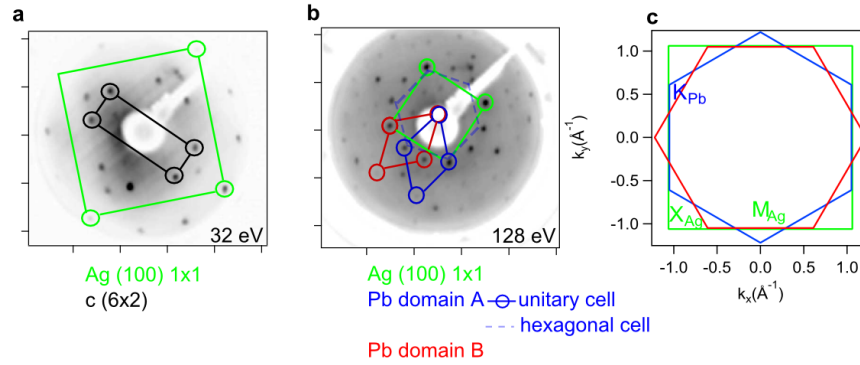


Figure 4.8: **a** and **b** show two LEED images at 32 eV and 128 eV respectively of the Pb ML on Ag(100). Green lines indicate the square Ag(100) unit cell. Black lines indicate one $c(6 \times 2)$ domain of the surface reconstruction. In panel **b**, the Pb extra spots clearly display a quasi-hexagonal symmetry, which is interpreted as the periodicity of the Pb ML. Blue and red continuous lines trace the unit cells of the two rotational domains of Pb. Blue dashed line instead delineates the pseudo-hexagonal cell of one of the rotational domains. In panel **c** the Brillouin zone (BZ) for the proposed model of the interface is sketched, with all the high symmetry points. A green square traces the substrate BZ, while blue and red hexagons trace the BZ of the two Pb domains.

A coverage of approximately 1ML of Pb on Ag(100) yields a $c(6 \times 2)$ reconstruction, with two possible domains rotated by 90° . Fig. 4.8 a shows a LEED image of the interface acquired at 32 eV. Green and black lines indicate respectively the substrate (1×1) spots and the $c(6 \times 2)$. The $c(6 \times 2)$ periodicity results as the correspondence cell between the four-fold Ag(100) lattice and the pseudo-hexagonal Pb ML, whose periodicity is clearly resolved at higher energy in the LEED image of panel b. Two Pb rotational domains exist, with an angle of 30° between them. Figure 4.8 c shows a schematic drawing of the associated Brillouin zones. Surprisingly, despite the two different symmetries, the Pb/Ag(100) interface results commensurate. The matching between the two symmetries is obtained by a small variation of the Pb-Pb bond length. The precise in-plane position and the vertical displacement of the adsorbed atoms were investigated by means of X-ray photoelectron diffraction (XPD). The results are briefly summarized in the next section.

4.3.1 Structural determination by means of XPD

The XPD experiments were performed at the VUV beamline (Elletra, Trieste) in collaboration with Dr. Rong Rong Zhan, from the Surface Science group of Dr. Alessandro Baraldi (University of Trieste). The XPD patterns of the $\text{Ag}_{3d_{5/2}}$ core level were collected at four different excitation energies between 450 eV and 580 eV. These photon energies were chosen in order to maximize the photoionization cross-section and to gain different multiple scattering contributions by varying the electron kinetic energies. The low kinetic energies (in the range between 85 eV and 212 eV) enabled us to extract mainly the backward scattering features, thus largely enhancing the sensitivity to the inter-layer distances, as well as to the atomic bonding distances.

The core-level XPS spectra were decomposed by using a line shape obtained by the convolution of a Doniach-Šunjić function and a gaussian. The former accounts for the core-hole lifetime broadening and the asymmetric tail due to the electron-hole pair creation typical of the metals. The second includes experimental resolution, surface inhomogeneity and vibrational broadening. Once the $\text{Ag}_{3d_{5/2}}$ core level spectra were fitted for all collection angles (θ, ϕ) , the angular dependence of the peak intensity was expressed in term of a modulation function $\chi_{exp}(\theta, \phi) = [I(\theta, \phi) - I_0(\theta)]/I_0(\theta)$. $I_0(\theta)$ is the average intensity over all the azimuthal angles ϕ at a given polar angle θ . The subscript *exp* is adopted to distinguish the experimental modulations from the theoretical ones.

The subsequent XPD analysis consists in a quantitative comparison between the experimental χ -function and a theoretical χ -function (χ_{th}) obtained by multiple-scattering calculations based on trial structures. In this study the Multiple Scattering Calculation of Diffraction (MSCD) package was used [172]. The goodness of the simulated pattern was evaluated by means of a Pendry's Reliability factor (R-factor): $R = \sum_{[i]} (\chi_{exp,i} - \chi_{th,i})^2 / (\chi_{exp,i}^2 + \chi_{th,i}^2)$, where the sum index runs over all experimental data points (all the angular positions for all the photon energies) [173]. The structural analysis, aimed at the research of the best theoretical structure with the lowest R-factor, was accomplished by means of iterative simulation-experiment comparisons accompanied by the implementation of the steepest-descent algorithm.

The stereographic projections of the XPD modulation functions are presented in Fig-

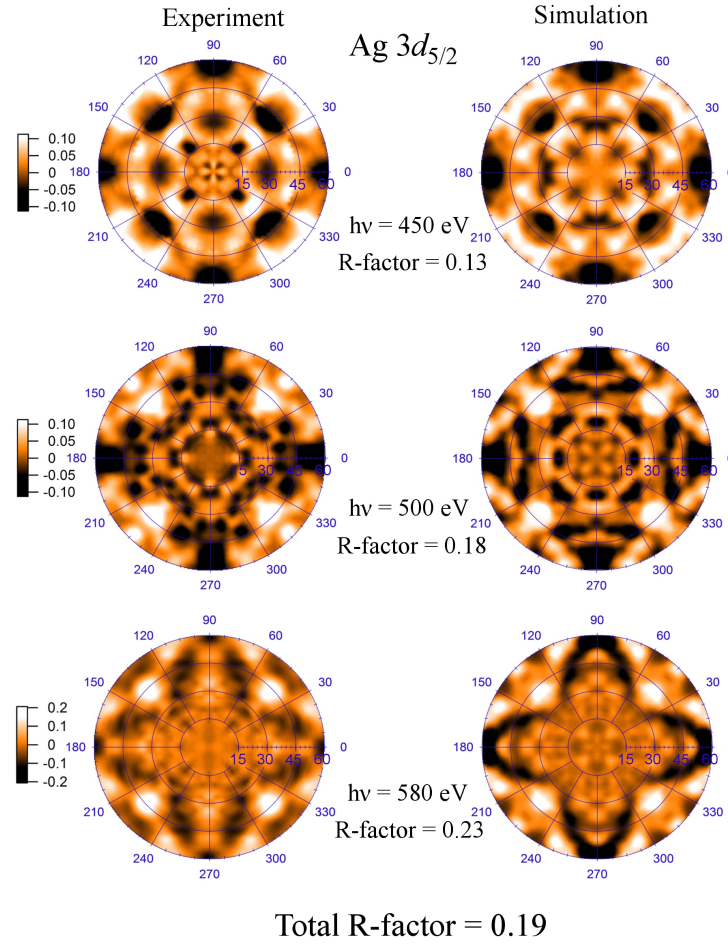


Figure 4.9: Experimental (left) and simulated (right) diffraction patterns for the $\text{Ag}3d_{5/2}$ core level. The photon energies and the partial R-factors are reported in the middle, while the global reliability factor, including the whole data set, is given in the bottom.

ure 4.9, where the experimental data are displayed according to the photon energy. In these representations, the polar angle increases radially, as marked on the horizontal axis, while the value of the azimuthal angle is indicated on the circular scale around each stereographic projection. The experimental patterns of the $\text{Ag}3d_{5/2}$ core level are shown on the left and the corresponding best simulated patterns are presented on the right side of the figure. The amplitude of the modulation is indicated by the reported color scale. The photon energy increases from the top to the bottom of the figure, and the partial R-factor for each photon energy is reported in the middle. The total R-factor for the entire experimental data set is reported in the bottom of the figure.

The good agreement between experiments and simulations is qualitatively confirmed by the fact that all the main diffraction spots, as well as many of the higher order diffraction features, are correctly reproduced by the simulations. Furthermore, the reliability of the structural model is quantitatively confirmed by the low final R-factor of 0.19. The mod-

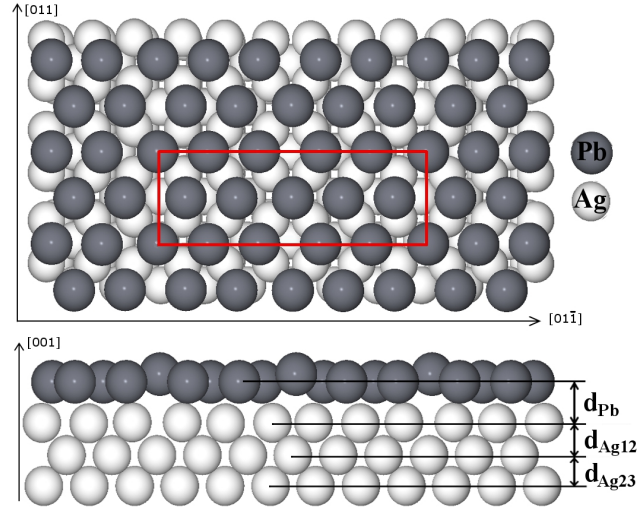


Figure 4.10: Top (upper part) and side (lower part) view of the structural model for the Pb/Ag(100) surface proposed by means of XPD investigations. The interlayer distances discussed in the text are label on the right side of the picture in the bottom. And the red colored rectangle indicates the $c(6 \times 2)$ supercell.

ulation patterns display a fourfold azimuthal symmetry, as expected for the $[100]$ -oriented Ag surface. Indeed, this symmetry reflects the square geometry characteristic of the arrangement of both the emitter atoms (Ag) and of the large part of the scatterers. However, many of the diffraction features are originated by the scattering events occurring on Pb atoms. These contributions become particularly significant at low kinetic energies, where the XPD technique is extremely surface sensitive.

The structural model inferred from the XPD investigation is shown in Figure 4.10. The dark gray spheres represent the Pb ML and the bright gray ones represent the Ag(100) substrate. The $c(6 \times 2)$ correspondence cell is marked by a red rectangle. Figure 4.10 indicates that the Pb atoms form a pseudo-hexagonal ML with the in-plane primitive vectors of slightly different lengths (4%). The lattice matching between the ad-layer and the substrate gives rise to a commensurate superlattice. Within the $c(6 \times 2)$ correspondence cell, there are 10 Pb atoms and 12 Ag atoms belonging to the first Ag layer; hence the Pb coverage is close to 0.83 ML.

In the first step of the structural relaxation, all the (x,y) positions of the atoms in the first three Ag layers, and those of the Pb ML are held fixed, while the three interlayer distances are free to relax. As shown on the bottom of Fig. 4.10, very small interlayer relaxation is found for the Ag substrate: $d_{Ag12} = 2.04 \pm 0.10 \text{ \AA}$ and $d_{Ag23} = 1.90 \pm 0.10 \text{ \AA}$. The spacing between the first Ag layer and Pb overlayer, d_{Pb} , is equal to $2.55 \pm 0.05 \text{ \AA}$: which is close to the average between the interlayer distances of bulk Ag(100) (2.04 \AA [174]) and Pb(111) (2.86 \AA [175]). Once the optimum interlayer distances are achieved, all the non-equivalent atoms of the Pb layer and of the first Ag layer are relaxed (these two layers have the predominant effects on the diffraction patterns). The final result shows atomic in-plane displacements for both the Ag and Pb atoms. Along the surface normal direction,

the most significant effect is the buckling of the Pb atoms at the center and at the corner of the cell ($0.4 \pm 0.1 \text{ \AA}$). This buckling arises as a consequence of the strong lattice stress induced by the matching between layers of different symmetries to form the $c(6 \times 2)$ phase. In fact, the Pb atoms preferentially adsorb in hollow sites, but owing to the geometrical differences, some Pb atoms are placed in quasi-bridge positions. Interestingly, during the local atomic relaxations, some of the Pb atoms are shifted from the quasi-bridge sites to quasi-hollow positions along the $[01\bar{1}]$ direction, thus getting closer to the central Pb atom. These in-plane movements have two main consequences. The first is the outward buckling of the central Pb atom, as discussed above. The second is the expansion of the Ag lattice underneath the buckled Pb atom along the $[011]$ direction. This movement is forced by the Coulomb repulsion from the larger electron cloud surrounding the bucked Pb atom.

In summary the Pb thin film deviates only weakly from an ideal flat-freestanding ML. Besides, also the subsurface Ag layer presents mainly in plane displacements, but negligible inverse corrugation, in contrast to what is reported for example for Pb/Cu(111) [146] and to what is expected from calculations in the case of Pb/Ag(111) [151]. The structural difference between the Pb ML grown on (111) terminated surfaces and on the Ag(100) surface is reflected in the electronic properties of the interface, which is the subject of the next section.

4.3.2 Electronic properties of Pb/Ag(100)

The band structure of the Pb/Ag(100) $c(6 \times 2)$ was investigated at the LSE laboratory (with the HeI α line at 21.2 eV) and at the VUV beamline at Elettra (at a photon energy of 76 eV). Figures 4.11 a and b report the band dispersion acquired at 76 eV along the two $\bar{\Gamma}\bar{K}_{Pb}$ directions, of the two Pb rotational domains. The high symmetry direction of panel a coincides also with the substrate $\bar{\Gamma}\bar{M}_{Ag}$ direction ($\bar{\Gamma}\bar{K}_{Pb} = 1.13 \text{ \AA}^{-1}$, $\bar{\Gamma}\bar{M}_{Ag} = 1.03 \text{ \AA}^{-1}$). Panels c-d are a schematization of the experimental data.

The first Pb induced band, labelled Pb1 (indicated by green lines in panel c-d), has a broad line shape. Besides, two free-electron like parabola disperse reaching their minimum at the \bar{M}_{Ag} point, and blue lines trace their dispersion in c and d. They result from the two rotational domains contribution of a second Pb2 state. At lower binding energies two further parabola are found crossing each other at \bar{M}_{Ag} (indicated by red lines in c and d). Actually, the doubling of this band is due to the folding of a single Pb3 at the boundary of substrate BZ. The Pb3 band reaches its minimum at the \bar{K}_{Pb} point. This is clearly seen along the inequivalent $\bar{\Gamma}\bar{K}_{Pb}$ direction of panel b, where the Umklapp replica is absent.

Figure 4.12 a displays a constant energy map collected at a binding energy of -0.6 eV. The image results from the second derivative of the four-fold symmetrized sum of three data sets acquired along the $\bar{\Gamma}\bar{M}_{Ag}$, $\bar{\Gamma}\bar{X}_{Ag}$ and $\bar{\Gamma}\bar{K}_{Pb}$ directions at $\hbar\omega = 21.2 \text{ eV}$. The BZs of the substrate and of the two rotational Pb domains are indicated by green, and blue/red lines respectively. The symmetry of the contours associated to Pb2 and to Pb3 are well resolved. Pb2 lies close to the $\bar{\Gamma}$ point and displays a hexagonal flower-like shape. Pb3 gives origin to small electron pockets centered at the six \bar{K} point of the Pb ML. The presence of two rotational domains doubles the number of pockets. Moreover the four pockets in proximity of \bar{M}_{Ag} are doubled owing to the periodicity of the substrate. At

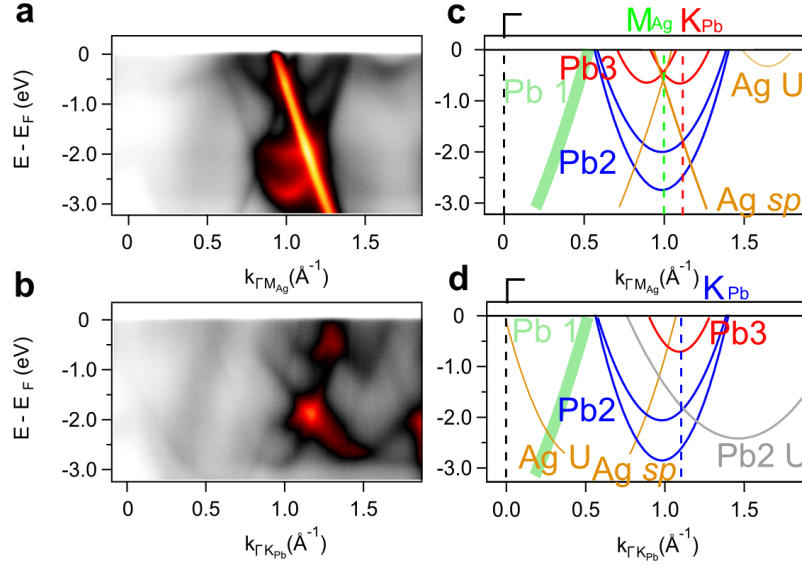


Figure 4.11: **a** and **b** show band dispersions along the $\overline{\Gamma K}_{Pb}$ directions of the two rotation Pb domains (the first one coincides with $\overline{\Gamma M}_{Ag}$). **c** and **d** display cartoon models of the band dispersion of panels **a** and **b**. The preeminent spectral features of the band dispersions are indicated by color lines.

this particular photon energy the intensity of the Pb1 band is very low: hence, the contour associated to this state is not visible in the CE map. Figure 4.12 **b** reports a close up of the region around \overline{M}_{Ag} , which is highlighted by a yellow dashed rectangle in **a**. The Ag *sp* state is visible in between the pockets as a line parallel to k_y . Panel **c** displays the CE map at the Fermi level for the same region of the BZ of panel **b**. Both the CE map and the band dispersion evidence the fact that both the Pb2 and the Pb3 show the six-fold symmetries and the two domains contribution of the Pb ML.

4.3.3 Discussion and comparison between the Pb/Au(111) and Pb/Ag(100) results

The electronic structure of the Pb/ Ag(100) interface closely resembles that of Pb/ Au(111) interface describe in 4.2. Despite the complexity introduced by several Umklapp replicas of the Ag *sp* state and of the Pb bands, the band structure of the Pb ML is simply formed by three bands. Pb1 is broader and its relative intensity is weak. This band, which has p_z orbital character [150] [151], strongly interact with the Ag continuum, hence acquiring three-dimensional character, as discussed also in the case of Pb/Au(111).

As previously noticed, Pb2 and Pb3 display the symmetry and the double contribution of the two Pb domains. For a perfectly flat Pb ML, tight binding calculation attributes to Pb2 and Pb3 p_{xy} character. In the case of Pb/Au(111) (and Pb/Ag(111) [151]) a moiré patterns is observed accompanied by a large buckling of the Pb atoms. In that case the incommensurability was proposed to introduce a mixing of the p_x , p_y and p_z characters

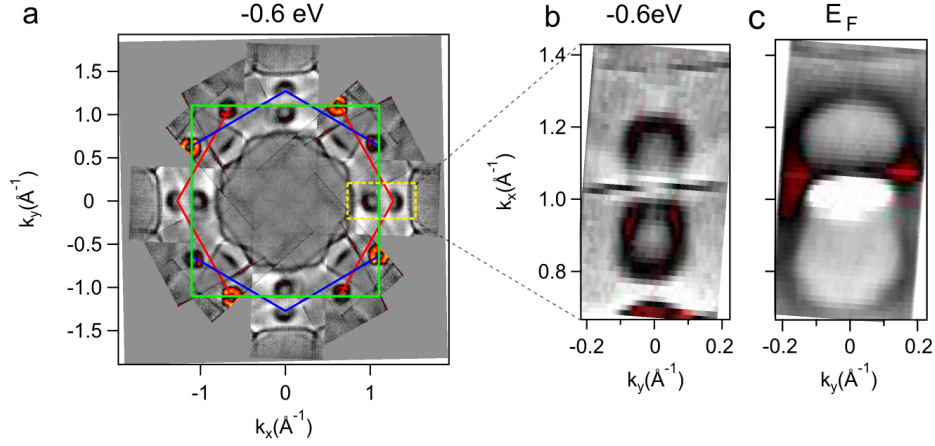


Figure 4.12: **a-c** constant energy maps at -0.6 eV (**a** and **b**) and at E_F (**c**), acquired with photon energy equal to 21.218 eV. The image in **a** results from the second derivative of the four-fold symmetrized sum of three data sets along $\bar{\Gamma}\bar{M}_{Ag}$, $\bar{\Gamma}\bar{X}_{Ag}$ and $\bar{\Gamma}\bar{K}_{Pb}$. The inner branch of Pb2 gives rise to the flower shape close to the $\bar{\Gamma}$ point. The Pb3 state originates the pocket at the \bar{K}_{Pb} points. All the states clearly displayed the doubled signal due to the two Pb rotational domains. **b** and **c** are close-ups of the region near to \bar{M}_{Ag} , enlightened by a yellow dashed line.

within the Pb bands. The consequence of this hybridization is primarily, the opening of a gap between Pb2 and Pb3 close to the K point of the substrate. Moreover, Pb2 gains the possibility to interact with the substrate continuum, similarly to Pb1, thus displaying the symmetry of the substrate.

In the case of Ag(100) both Pb2 and Pb3 show the symmetry of the two rotational domains, thus reflecting a complete delocalization in the ad-layer and a weak interaction with the substrate. The absence of the hybridization gap between Pb2 and Pb3 is another remarkable difference between the valence band of the two Pb ML grown on Ag(100) and on Au(111).

We propose that these differences in the electronic properties of the Pb ML grown on Ag and Au reflect the difference in the hybridization of their p orbitals. Our tight-binding calculations suggest that such diversity may arise from the two distinct surface structures. The calculations, in fact, indicate that only in the case of broken in-plane symmetry a gap is opened at the \bar{K}_{Pb} point. In the case of Pb/Ag(100) the commensurability and the flatness of the Pb film contribute to preserve the hexagonal symmetry of the Pb ML, in contrast to the Pb/Au(111) case.

Large Spin Splitting in One-Dimensional Surface Alloys

Contents

5.1	One dimensional surface states at stepped Si(111) surface	84
5.2	One dimensional spin-split states at the Cu(110) surface	87
5.2.1	Surface characterization of the Bi/Cu(110) interface	87
5.2.2	Spin-split surface states with one-dimensional character in the Bi/Cu(110) $p(4 \times 1)$ surface alloy	88
5.2.3	Surface characterization of the Pb/Cu(110) interface	93
5.2.4	Evolution of the spin splitting in Pb/Cu(110) $p(5 \times 1)$ and in the mixed alloy	94

The physical properties of a solid, such as the electronic band structure or the phonon dispersion, are often discussed in a simplified form starting from a one-dimensional chain toy-model [26, 25]. This approximation is useful because it neglects most of the *real* complications of the three-dimensional system, but still retains most of the important physical concepts. Nonetheless, surprisingly, one-dimensional chain model fails in predicting the electronic properties of *real* one-dimensional systems. One-dimensional materials are sensitive to several kinds of instabilities (namely charge density wave (CDW), spin density wave (SDW) or Peierls instability), which lead the system to a broken symmetry ground state [176].

Several theoretical models have been developed to describe the complex ground state of one-dimensional systems. Even if one disregards the existence of strong correlation between the electrons and the various boson modes, in fact, the elementary excitation in a 1D system cannot be described in the frame of the Fermi liquid model based on coherent quasiparticles and incoherent dressing. A detailed theoretical description of the *non-Fermi liquid* ground state is beyond the aim of this thesis. A basic introduction to this physics, accompanied with the most recent ARPES results on several 1D compounds, can be found in ref. [177].

The subject of this thesis is the investigation of the *generalized* Rashba-Bychkov model in different materials. In recent years, several one-dimensional systems have been artificially grown using anisotropic (110) surfaces [Pt(110) [178, 179], Cu(110) [180, 181]] or stepped surfaces as template for the self-assembling of nanowires [182, 183, 184, 185, 186, 187, 188, 189, 190, 191]. The possibility to transfer the giant spin-splitting to one-dimensional systems motivated the study of stepped Si(111) surface and of metallic (110)

surfaces. In particular this chapter reports the complete ARPES study of 1D-like surface alloy, grown on the surface of Cu(110) by evaporation of heavy elements (Pb and Bi). I experimentally observed spin-split surface states with reduced dimensionality. These results are supported by *ab initio* calculations.

5.1 One dimensional surface states at stepped Si(111) surface

Si surfaces slightly tilted out of the [111] direction constitute a family of stepped surfaces, in which terraces with (111) symmetry are separated by atomic steps. The average lateral dimension of the terraces depends on the angle of misalignment (ranging between 1.26 nm for 14.4° up to 2.13 nm for 8.5° , see ref [187]). The well ordered steps become part of the surface reconstruction, whose periodicity is reflected in its electronic properties. Therefore, if one considers the step periodicity, and not the pristine (111), miscut surfaces are very anisotropic with almost no interaction between different steps, resulting in one-dimensional like structures.

Several stepped surfaces ((335), (553), (775) and (557)) have been used as template for the self-organization of nanowires and nanoribbons of evaporated high Z materials (Au [182, 183, 184, 185, 186, 187, 188, 189], Pb [190, 191]). In all cases the 1D wires show no band dispersion in the direction orthogonal to the chain. Open Fermi surfaces are observed, indicating one-dimensional character. In particular, Au/Si(557) has been subject of intense ARPES studies [182, 183, 185, 186, 188, 189]. A nominal Au coverage of 0.18 ML [187] yields chains with a single Au atom per (111) terrace. The interest in this reconstruction arose from the observation of a pair of bands, crossing each other at the Fermi level, where their spectral weight is strongly suppressed. Such behavior was interpreted by Segovia *et al.* as a signature of deviation from the Fermi liquid model, with the formation of two bands associated to the charge (holon) and to the spin (spinon) excitations [182].

The Luttinger liquid scenario was later discarded: high resolution measurements, in fact, showed that the two bands effectively do not merge at E_F , and the spectral weight is also mostly conserved [183, 184], as it is displayed in Fig. 5.1 a. The doubling of the bands was ascribed to the existence of two chains per unit cell, or to one single chain of step atoms with two broken bonds, and hence two free orbitals. The geometrical structure of the chains was defined more clearly with the combined use of STM and x ray diffraction [185]. A schematization of the crystal structure is displayed in Fig. 5.1 b. Contrary to the mentioned two proximal bands model only one Au chain is present, lying in the middle of the (111) terrace.

The hypothesis which attributes the metallic bands to the Si atom at the step, is rejected on the basis of DFT calculations [188]. Fig. 5.1 c shows the results of non spin-polarized calculations. The dangling bond at the Si step-atom gives rise to an instability which leads to a buckling of the step edge and to a doubling of the unit cell ((2×1) superlattice). Actually, two bands result from inequivalent atoms B and A : they are weakly dispersing and they are indicated by square symbols (with the band associated to B fully occupied and the one related to A only partially filled). The metallic dispersing band, the only one consistent with the ARPES data of Fig. 5.1 a, is denoted by dark circles and it arises from

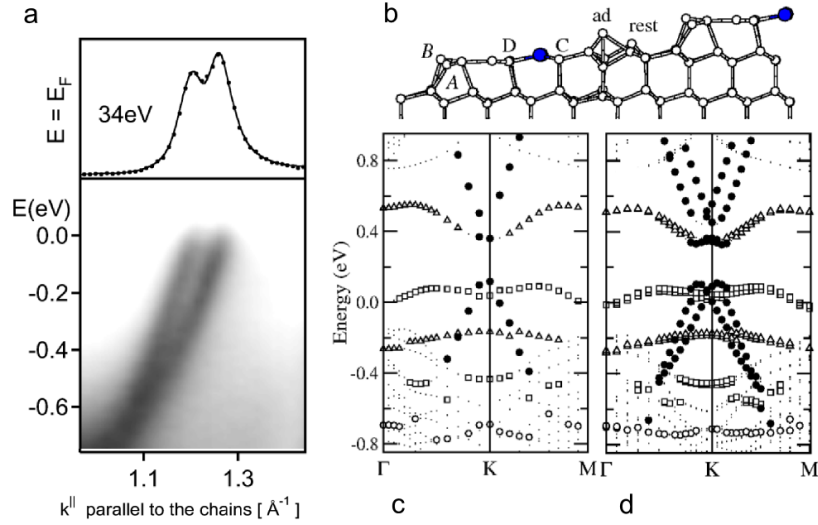


Figure 5.1: **a** band dispersion of Au/Si(557) parallel to the chain direction [183]. The two bands do not merge at E_F and no gap is opened. The schematic side view of the surface reconstruction is displayed in **b**, as obtained by STM study [187]. Panel **c** and **d** show respectively *ab initio* calculations without and with the spin orbit interaction. The doubling of the Au induced metallic state (indicated by black circles) is a direct consequence of the spin orbit interaction [188].

the hybridization of $3p$ state of Si with the $6p$ orbital of Au.

In the calculation of Fig. 5.1 **c** the metallic band is single-degenerate. The experimental doubling is well reproduced by taking adequately into account the spin orbit interaction, and the results of fully relativistic calculation are shown in Fig. 5.1 **d**. Similarly to what described in chapter 2 for Au(111), the large atomic SO interaction of gold gives origin to spin polarized surface states, with large spin splitting. To the best of my knowledge no spin-resolved ARPES experiment has been performed to verify this hypothesis. An indirect confirmation has been provided by the observation of mini gaps close to the \bar{K}' point where the spin-split bands cross their Umklapp replica originated by the (2×1) superlattice periodicity. The bands carrying the same spin avoid crossing by opening interaction gaps which have been experimentally resolved by means of ARPES [189].

The results obtained on Au/Si(557) suggest that asymmetric surfaces can host spin-split states with reduced dimensionality. This reconstruction is characterized by a large structural anisotropy, which is reflected in the electronic properties of the interface. The possibility to transfer such anisotropy also to the wave-functions (or equivalently to the in-plane gradient potential) represented an ideal playground for testing the *generalized* Rashba-Bychkov model.

Pb/Si(557) has been already subject of combined STM and ARPES study [190, 191]. Contrary to the Au case, Pb forms a dense phase constituted by nanoribbons confined in the (111) terraces, and interrupted by the atomic steps. Several Pb-induced bands cross E_F and form open Fermi contours. Despite the high atomic SOC of Pb (for the $6p$ orbital ξ_{SO}

is twice as large as the one of Au) no signature of spin splitting was reported by Su Kim et al. [190, 191].

At the early stage of this thesis, several attempts to grow ordered Bi nanowires were performed. Si(557) and Si(553) surfaces were used as templates for the self-assembling. Even though several ordered phases have been identified by means of LEED ((4×3) , (6×6) or $(\sqrt{3} \times \sqrt{3})R30^\circ$), none of them displayed one-dimensional behavior or signature of spin splitting in the band structure. Therefore a completely different route has been explored, by exploiting very asymmetric, namely $p(n \times 1)$, reconstructions on the (110) surface termination of noble metals. The most important ARPES results of those studies are presented in the next sections.

5.2 One dimensional spin-split states at the Cu(110) surface

5.2.1 Surface characterization of the Bi/Cu(110) interface

A detailed surface X-ray diffraction study reported the formation of two possible ordered superstructures after deposition of Bi onto Cu(110) [192]. A coverage of approximately 0.5 ML yields a $c(2 \times 2)$ reconstruction, which is interpreted as a quasi-hexagonal structure. When the Bi coverage reaches 0.75 ML a $p(4 \times 1)$ reconstruction is formed.

Interestingly, the latter can be described as a missing row reconstruction in which every fourth Cu row in the [001] direction is replaced by bismuth. This Bi atoms occupy substitutional sites and form a surface alloy, similarly to the case of BiAg₂ [87]. Figure 5.2 displays schematic top and side views of the Bi/Cu(110) $p(4 \times 1)$ structure. Besides the substitutional Bi atom, two further inequivalent Bi atoms in the unit cell occupy fourfold hollow adsorption sites [192].

The surface alloy forms quasi-one dimensional chains, with a spatial separation (1.02 nm) large enough to make the direct overlap of the wave-functions very small. Nonetheless, a strong interaction with the substrate is expected, which may result in the coexistence of bands with 1D and 2D character. All the structural parameters obtained by the surface XRD study constituted the starting point for the *ab initio* calculations of the electronic band structure of the surface alloy.

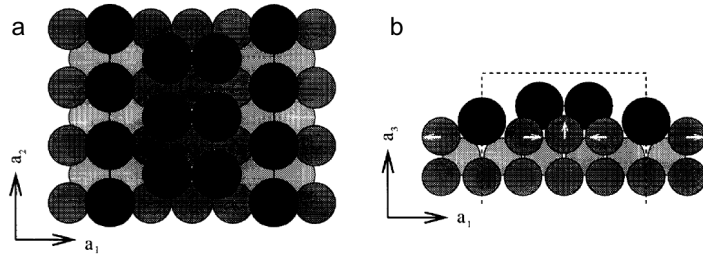


Figure 5.2: Top (a) and side view (b) of the substitutional model of the Bi/Cu(110) $p(4 \times 1)$ surface structure. The large dark circles are Bi atoms and smaller and lighter circles are Cu atoms. The directions of the sub-surface displacements of the Cu atoms are indicated by arrows. The dashed lines indicate a $p(4 \times 1)$ unit cell [192].

5.2.2 Spin-split surface states with one-dimensional character in the Bi/Cu(110) $p(4 \times 1)$ surface alloy

In this section I discuss the observation of one-dimensional spin-split surface states in the BiAg(110) $p(4 \times 1)$ surface alloy.

Figure 5.3 **a** shows a LEED image of the $p(4 \times 1)$ surface reconstruction. Black squares indicate the (0,1) and (1,1) spots of the substrate. Figure 5.3 **b** displays a schematic model of the Bi/Cu(110) interface, as obtained by a previous surface x-ray diffraction study (and shown in Figure 5.2) [192]. The unit cell is delineated with a white rectangle in the top panel of Figure 5.3 **b**. It contains two inequivalent Bi atoms: the one at the corner of the cell occupies substitutional site in the first Cu layer, as shown in the bottom panel of Figure 5.3 **b**. By analogy with the BiAg(111) $\sqrt{3} \times \sqrt{3}$ R30° system we refer to this atom as the one forming the surface alloy [87]. Interestingly, there is a buckling $\Delta z = 0.2 \pm 0.01 \text{ \AA}$ of this Bi atom with respect to the neighboring Cu atoms [192]. This value is approximately half of the correspondent one for heavy elements (Bi, Pb) surface alloys grown on the (111)-terminated surface of Ag and Cu [105]. The alloyed Bi atoms form rows with quasi one-dimensional character, as observed in a previous STM study on similar surface reconstruction (Pb/Cu(110) $p(n \times 1)$ [193]), hereafter we refer to them as Bi chains. The distance between neighboring chains is equal to 1.02 nm .

Figure 5.3 **c** shows an ARPES image map of the band dispersion parallel to the Bi

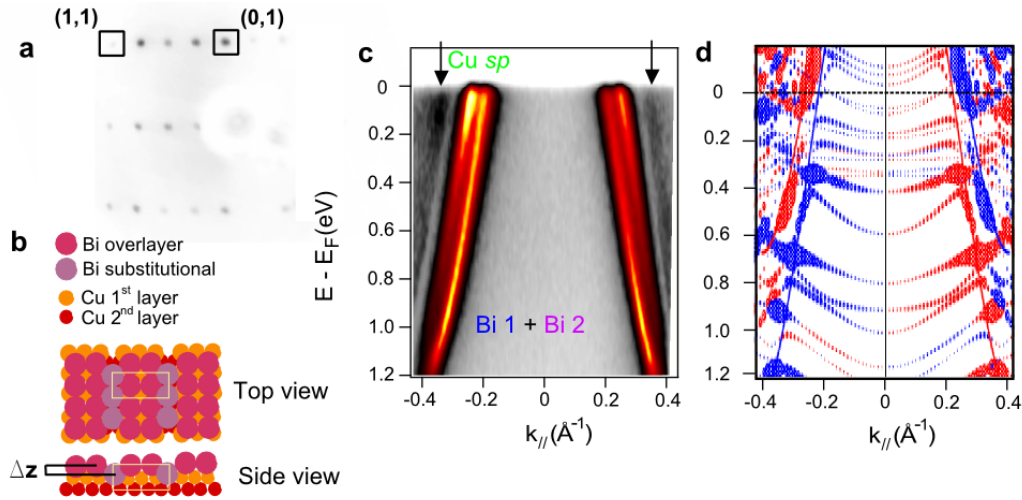


Figure 5.3: **a** LEED image of the Bi/Cu(110) $p(4 \times 1)$ reconstruction. Black squares enclosed the (0,1) and (1,1) substrate spots. **b** schematization of the surface structure as reported in a previous X-ray diffraction study [192]. The Bi atoms in substitutional site form chains, and they are characterized by a large buckling ($\Delta z = 0.2 \pm 0.01 \text{ \AA}$) with respect to the neighboring Cu atoms. **c** and **d** measured and calculated band dispersion parallel to the chain ($\overline{\Gamma Y}$). A pair of spin-split surface states (labelled Bi1 and Bi2) disperse with negative effective mass.

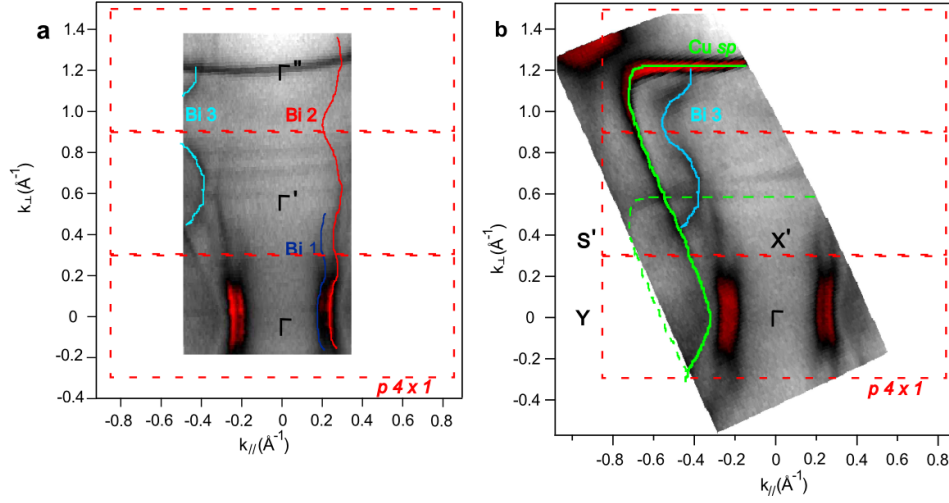


Figure 5.4: **a** and **b** Fermi surface measured respectively along the $\overline{\Gamma X}$ and $\overline{\Gamma S}$ high symmetry directions. Red dashed lines delimit the $p(4 \times 1)$ BZ. Remarkably the Bi1 and Bi2 bands present open contours, fingerprint of strong one-dimensional character. A further one dimensional Bi derived state is observed (Bi3) in the second and third BZ of the reconstruction.

chain, for $k_{\perp} = 0 \text{ \AA}^{-1}$. Three bands are visible: the two most intense, labelled Bi1 and Bi2, are interpreted as a pair of spin split surface states. The third band, dispersing with larger k_F value (indicated by black arrows), is the Cu *sp* state. The Bi1 and Bi2 bands disperse with negative effective mass, with their crossing lying above the Fermi level. The spin splitting, as obtained from the fit to the momentum distribution curve (MDC) at the Fermi level, is equal to $\Delta k = 2k_0 = 0.048 \pm 0.005 \text{ \AA}^{-1}$, where k_0 is the momentum offset of the band maximum. From the parabolic fit of the spin-split bands we obtain an effective mass $m^* = -0.26 \pm 0.05 m_e$.

Figure 5.3 **d** shows the results of *ab initio* calculations, which well reproduce the experimental dispersion of the Bi induced states [194]. Moreover, the calculations confirm the spin polarization of the Bi states. Blue and red markers indicate the two possible spin directions. The size of the markers evidence the degree of spin polarization of the states. In the calculations several further states, forming the Cu(110) bulk continuum, disperse and hybridize with the Bi bands.

Figure 5.4 **a** and **b** show two constant energy maps at the Fermi level (with $\overline{\Gamma X} = 1.22 \text{ \AA}^{-1}$, $\overline{\Gamma Y} = 0.86 \text{ \AA}^{-1}$ and $\overline{\Gamma S} = 1.49 \text{ \AA}^{-1}$). The most striking feature is the open character of the Fermi surface sheets associated to the Bi1 and Bi2 states. This experimental finding represents a novelty for the study of spin-split surface states in surface alloys. Spin-split states with one dimensional character were previously reported only for Au chains grown on stepped Si surfaces [189, 188]. In Figure 5.4 **a** red dashed lines delimit the border of the $p(4 \times 1)$ Brillouin zone. The Fermi contour associated to Bi1 loses drastically intensity when entering in the second BZ. The spectral weight of Bi2 also similarly reduced, but this state is still visible in higher order BZs. A red line guides the eye on the right branch of Bi2.

The warping of the band denotes an interaction with a two-dimensional potential, similarly to what reported by ARPES investigations of bulk quasi one-dimensional systems [177]. A third Bi induced state is observed in the second and third BZ. It is labelled Bi3, and a light blue line delineates its Fermi contour, whose behavior is fully captured in Fig. 5.4 b. The warping of this state is much stronger than for Bi1 and Bi2, even though the state presents still an open Fermi contour.

Panel b displays the well-known dog-bone shape of the Cu *sp* state. Noticeably, the spectral weight of this state has an inverted behavior with respect to the spin-split surface states, and its intensity decreases when approaching the $\bar{\Gamma}$ point. We interpret such effect as a transfer of spectral weight between the substrate *sp* band and the Bi induced states. The interaction of the Cu *sp* state with the spin-split bands has a second dramatic consequence. A comparison of the Fermi contour of Bi2 in the first and second BZ reveals that the 4×1 periodicity is broken. Owing to the interaction with the Cu *sp* state near the $\bar{\Gamma}$ point, the Bi1 and Bi2 states shrink and deviate from their expected wiggling.

Figure 5.5 a and b show the band dispersion parallel to the Bi chain in proximity of the high symmetry points $\bar{\Gamma}$ and $\bar{\Gamma}'$ (respectively at $k_{\perp} = -0.07 \text{ \AA}^{-1}$ and $k_{\perp} = +0.54 \text{ \AA}^{-1}$). The Bi1 and Bi2 bands (dashed blue and red lines) have different k_F values in the first BZ (a) and in the second BZ (b). The most prominent consequence of such periodicity breaking is the improper numerical evaluation of the spin splitting obtained in the first BZ. From a thorough survey of Fig. 5.5 a and b, in fact, we observe that the Bi1 and Bi2 bands do not undergo a rigid shift toward smaller k values, but their splitting is also affected. Hence, the k splitting in the second BZ (and similarly in third BZ) is $\Delta k = 2k_0 = 0.067 \pm 0.05 \text{ \AA}^{-1}$. This value is larger than the one found in the first BZ, and it is larger than the spin splitting reported in the Bi(111) surface state [81, 87]. Such value is comparable with the spin splitting in the surface alloy PbAg_2 and in the mixed alloy $\text{Bi}_x\text{Pb}_{1-x}\text{Ag}_2$ [90]. Furthermore, in Figure 5.5 a, Bi1 shows a reduction of its spectral weight and a broadening of its line shape, for binding energies larger than 1 eV in the region enclosed by a black rectangle. This effect may arise from the hybridization of the one dimensional spin-split states with the Cu(110) bulk continuum, as suggested by the gaps observed in the *ab initio* calculations of Figure 5.3 d. These experimental findings reveal that the hybridization of the surface state wave-function with the substrate continuum plays an important role in defining the value of the splitting.

Figure 5.5 c displays a cut in the electronic band dispersion orthogonal to the Bi chain direction taken at $k_{//} = -0.33 \text{ \AA}^{-1}$. Two rectangles enclose the region of the band dispersion associated to the Bi induced states, with the same color coding used in Figure 5.3 c. A strictly one-dimensional band would not disperse in the direction orthogonal to the chain, while Bi1 and Bi2 wiggle over an energy range of several hundreds of meV. This observation is consistent with the two-dimensional warping already observed for the Fermi contours in Fig. 5.4 a and b. Figure 5.5 c clearly displays also the large transfer of spectral weight due to the hybridization of the one dimensional surface states with the Cu bulk continuum, in the region close to $\bar{\Gamma}$ ($k_{\perp} = 0 \text{ \AA}^{-1}$). Figure 5.5d shows the calculated band structure along the $\bar{\Gamma}\bar{X}$ high symmetry direction $k_{//} = 0 \text{ \AA}^{-1}$ [194].

Figure 5.6 displays a stack of energy distribution curves (EDCs) extracted from Fig. 5.3c in the range between $k = -0.332 \text{ \AA}^{-1}$ and $k = -0.194 \text{ \AA}^{-1}$, vertically offset from the

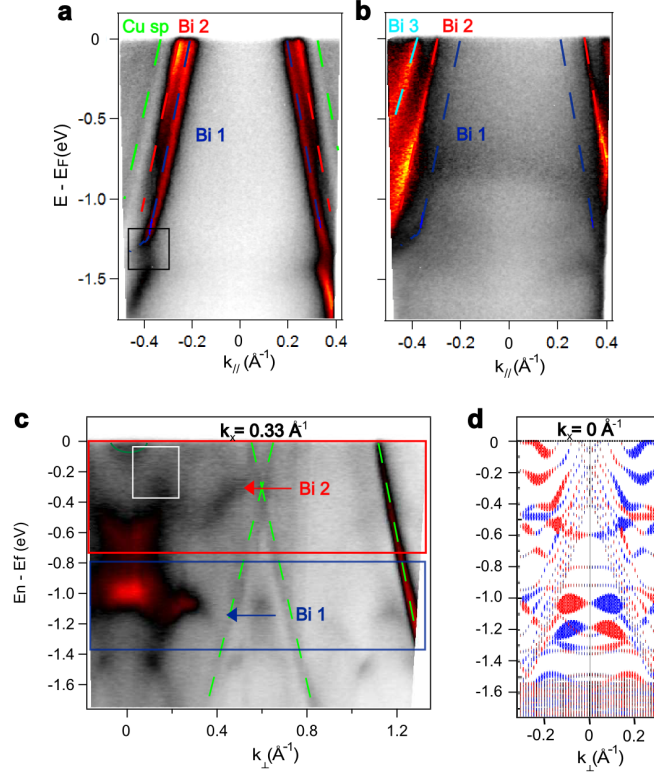


Figure 5.5: **a** and **b** band dispersion along the Bi chain direction at -0.07 \AA^{-1} and $+0.54 \text{ \AA}^{-1}$, in proximity of the high symmetry points $\bar{\Gamma}$ and $\bar{\Gamma}'$. The interaction with the bulk *sp* breaks the $p(4 \times 1)$ periodicity. The k_F values of Bi1 and Bi2 are smaller in the first BZ (**a**) than in the second BZ (**b**). The splitting is affected as well, and it is reduced by a factor 1.5 in the first BZ. **c** displays the measure band dispersion in the direction orthogonal to the Bi chain (taken at $k_{||} = -0.33 \text{ \AA}^{-1}$). Bi1 and Bi2 weakly disperse also along this direction. Green dashed lines indicate the Cu *sp* state and its Umklapp on the $p(4 \times 1)$ periodicity. **d** calculated band structure along the $\bar{\Gamma}\bar{X}$ high symmetry direction $k_{||} = 0 \text{ \AA}^{-1}$.

lowest k value to the largest. The green, red and blue spectra correspond respectively the Fermi level crossing of the Cu *sp*, Bi2 and Bi1 states. Interestingly, the lineshape of Bi2 broadens when approaching the Fermi level; on the contrary Bi1 gets sharper and more intense when dispersing towards the Fermi energy. This may indicate a deviation from a purely Fermi-liquid behavior, as a consequence of the reduced dimensionality.

In summary, ARPES shows the existence of one dimensional spin-split surface states at the Bi/Cu(110) $p(4 \times 1)$ surface reconstruction. The experimental findings are supported by *ab initio* fully relativistic calculations [194]. The one dimensional behavior is originated by the reduced dimensionality of the Bi atoms in substitutional site forming atomic chains. The large buckling of the Bi atoms in the substitutional site represents a strong analogy with the alloys grown on the (111)-terminated surface of Ag and Cu [105]. The k splitting is larger than the values reported for the surface states of Au(111) [10] and Bi(111) [81],

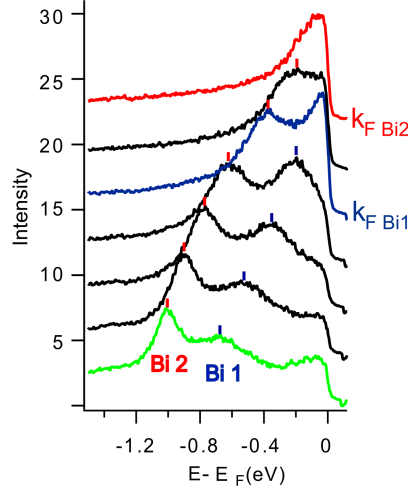


Figure 5.6: Stack of EDCs, positively shifted when going from $k_{//} = -0.332 \text{ \AA}^{-1}$ to $k_{//} = -0.194 \text{ \AA}^{-1}$. The green red and blue spectra show respectively the Fermi level crossing of the for the Cu *sp*, Bi2 and Bi1 states. Bi2 peak broadens when dispersing toward the Fermi level. An opposite trend characterizes the Bi1 peak.

and it is comparable with the giant spin splitting observed in the Ag(111) surface alloys [87, 90, 97, 102]. Furthermore, we observe a difference in the spin splitting between the first and the higher orders Brillouin zones. This is interpreted as a consequence of the hybridization between the one dimensional state and the bulk continuum, and it suggests that the large spin splitting strongly depends on the properties of the surface state wave-functions, as proposed for the giant spin splitting in BiAg₂ [89].

Furthermore, the one-dimensional character of these states represents a novelty in the study of giant Rashba-Bychkov systems, and one dimensional surface alloys may become a prototype for the investigation of non Fermi liquid behavior.

5.2.3 Surface characterization of the Pb/Cu(110) interface

The discovery of 1D surface states with large spin splitting stimulated further studies, with the aim to selectively quantify the role played by the adsorbate and by the substrate in defining the strength parameter α_R in the extended RB model. Lead is the best candidate to replace bismuth, due to the large atomic SOC and to the similar atomic radius. Several studies investigated the sub-monolayer coverage of Pb on Cu(110) [195, 196, 197] revealing a very complex phase diagram. Scanning tunnelling microscopy succeeded in resolving the surface structure of the interface [193].

Similarly to the Bi case, the lowest coverage phase is a $c(2 \times 2)$ superstructure, at approximately 0.5 ML. While larger amount of Bi yields a single 1D-like surface reconstruction, in the case of Pb several 1D phases exist with different separation between the chains. These $p(n \times 1)$ superstructures are interpreted as linear combination of two building blocks: the $p(4 \times 1)$ reconstruction at 0.75 ML and the $p(5 \times 1)$ reconstruction at 0.8 ML. The coexistence, in the same sample, of several phases is possible owing to the very small differences in the coverage. Figure 5.7 a shows an STM topographic map of an inhomogeneous sample, in which various phases with $n = 4, 8$ and 12 are visible [193]. These superstructures are interpreted as arising from the substitution of every n th row of Cu with Pb atoms. Figure 5.7 b displays a model of the $p(5 \times 1)$ reconstruction, and it closely resembles the structure of Bi/Cu(110) $p(4 \times 1)$ [192]. Unfortunately, while the indicated in-plane distances are calculated by reconsidering previous XRD data [195, 196], in the literature there are no rod profile study. Hence, no precise value for the buckling of the Pb atom in the substitutional site is available.

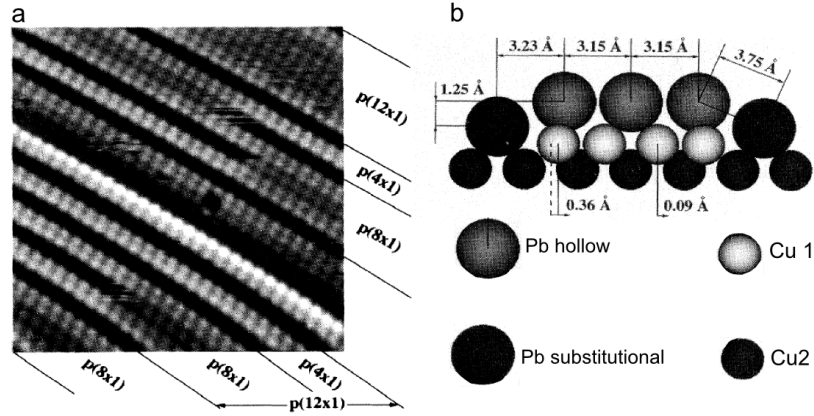


Figure 5.7: **a** STM topographic map of an inhomogeneous Pb/Cu(110) surface, hosting several different $p(n \times 1)$ domains ($n = 4, 8, 12$). **b** schematic model for the $p(5 \times 1)$ reconstruction, investigated in our ARPES study. The structure closely resemble the one of Bi/Cu(110) $p(4 \times 1)$ with a larger separation between the 1D chains: 1.27 nm for Pb and 1.02 nm for Bi [193].

5.2.4 Evolution of the spin splitting in Pb/Cu(110) $p(5 \times 1)$ and in the mixed alloy

Only the highest coverage $p(5 \times 1)$ phase was subject of a detailed ARPES investigation. LEED experiments were carefully performed over the whole sample surface in order to evidence the presence of extra spots associated to different $p(n \times 1)$ domains.

Figure 5.8 **a** displays the band dispersion parallel to the direction of the Pb chain. The measurement was performed at liquid nitrogen temperature, with angular resolution set equal to 0.2° and energy resolution better than 10 meV. Two intense and sharp states are resolved, crossing the Fermi level at approximately $k_{F1} = \pm 0.31 \text{ \AA}^{-1}$ and $k_{F2} = \pm 0.28 \text{ \AA}^{-1}$, and the resulting splitting in the FBZ is equal to $\Delta k = 2k_0 = 0.029 \text{ \AA}^{-1}$. The k_F values are larger than in the case of Bi/Cu(110) $p(4 \times 1)$, and this is explained as a consequence of the different atomic electronic configurations: $[Xe]4f^{14}5d^{10}6s^26p^3$ for Bi and $[Xe]4f^{14}5d^{10}6s^26p^2$ in the case of Pb. The reduced $6p$ occupation translates in a rigid shift of the surface states.

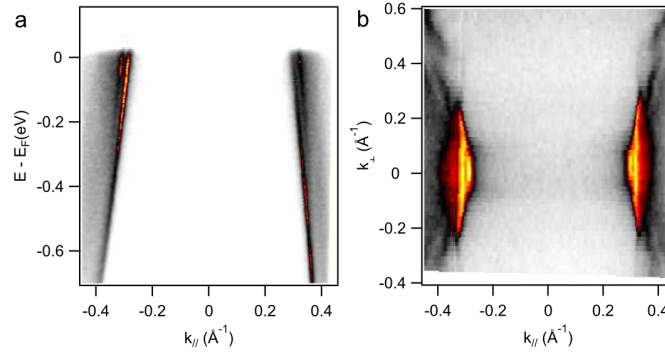


Figure 5.8: **a** band dispersion of the Pb/Cu(110) $p(5 \times 1)$ reconstruction parallel to the Pb chain. A small but not negligible spin splitting is resolved ($\Delta k = 0.029 \text{ \AA}^{-1}$). **b** Fermi surface in the FBZ, the spin-split states form an open Fermi surface. The expected periodicity is hidden by the interaction with the Cu sp state, as previously observed in the case of Bi/Cu(110) $p(4 \times 1)$. The hybridization results in a strong transfer of spectral weight between the Cu and the Pb derived state, which appears particularly intense in the FBZ.

The spin-splitting is reduced by a factor 1.66 when replacing Bi with Pb, and such effect cannot be ascribed only to the different atomic SOC (the ratio between the two is, in fact, 1.37). A similar reduction is observed for the BiAg₂ and PbAg₂ surface alloys already discussed (see chapter 2) [90, 198].

The large spin splitting in the 1D surface alloys is hence probably the result of a complex interplay between atomic properties and structural parameters, similarly to the case of the (111) terminated surfaces. A future structural investigation of the vertical displacement of the Pb atoms is required in order to place this system in the $(\alpha_R, \Delta z)$ phase space proposed by Gierz *et al.* [105].

The influence of the substrate on the 1D surface states is manifest in the two-dimensional

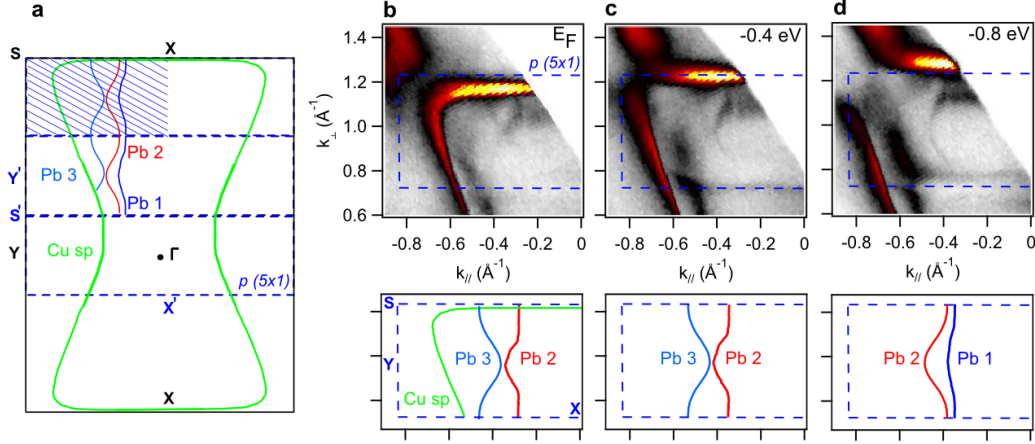


Figure 5.9: **a** cartoon of the reciprocal space of the Pb/Cu(110) interface. The high symmetry points of the Cu(110) substrate (black) and of the $p(5 \times 1)$ reconstruction (blue) are shown. The contours of the Cu sp band and of the Pb induced states are traced by color lines. The dashed area corresponds to the region of the reciprocal space displayed in panel **b-d**. **b-d** three constant energy maps (E_F , -0.4 eV and -0.8 eV) of Pb/Cu(110) in the third BZ. The contours associated to the different Pb related states are visible, and clear signature of 2D warping is present. The bottom part of panel **b-d** is a schematization of the band contours to guide the eyes of the reader.

warping of the constant energy contours in the direction orthogonal to the chain, and in the deviation from the expected $p(5 \times 1)$ periodicity. Figure 5.8 **b** shows the Fermi Surface in the FBZ with $\Gamma\bar{X}' = 0.25 \text{ \AA}^{-1}$ and $\Gamma\bar{Y} = 0.87 \text{ \AA}^{-1}$. For $k_{\perp} = 0 \text{ \AA}^{-1}$ the two spin-split states are distinguishable, whereas close to the zone boundary the intensity of the inner components is strongly reduced. Similarly to the case of Bi/Cu(110) the surface states interact with the Cu sp band, which is barely recognizable in Fig. 5.8 due to the transfer of spectral weight to the 1D states. The actual symmetry of the 1D states is investigated in the third BZ of the reconstruction ($\Gamma^{3rd} = 0.98 \text{ \AA}^{-1}$). Figure 5.9 **a** is a sketch of the Cu(110) BZ, and the high symmetry points of the substrate (black) and of the reconstruction (blue) are indicated. Color lines trace the Fermi surface contours of the Cu sp band and of the 1D surface states. Figure 5.9 **b-d** show three constant energy maps respectively at E_F , -0.4 eV and -0.8 eV, in the reciprocal space region indicated by the dashed blue area in panel **a**. A blue rectangle indicates half of the $p(5 \times 1)$ cell, for $k_{||} < 0 \text{ \AA}^{-1}$.

The most intense state is the Cu sp state, while the Pb states are faint and visible only in the upper part of the unit cell. For all three maps a cartoon of the contours is shown in the bottom panels. The one-dimensional character of the Pb states is confirmed by the open Fermi surface. The contour associated to the inner spin branch (labelled Pb1) is visible only at higher binding energies. Similarly to the case of Bi/Cu(110) additional extra states are visible in the higher order BZ, namely Pb3, and its concavity is opposite to the one of the spin-split states (in agreement with the case of Bi/Cu(110), see Figure 5.4).

The contour of the external spin branch, Pb2, is more clearly resolved, and the associated 2D warping at the Fermi level is equal to $\pm 0.05 \text{ \AA}^{-1}$. This is equivalent to a variation of 15% with respect to the k_F value, and larger than for the Bi case, where we report a modulation of $\pm 0.03 \text{ \AA}^{-1}$ corresponding to 10% of k_F . Surprisingly, in the $p(5 \times 1)$ reconstruction the distance between the chains is 1.27 nm , therefore 25% larger than in the case of Bi/Cu(110) $p(4 \times 1)$ (1.02 nm). The larger 2D warping in the Pb states suggests that the interaction between the chains is not direct but mediated by the substrate.

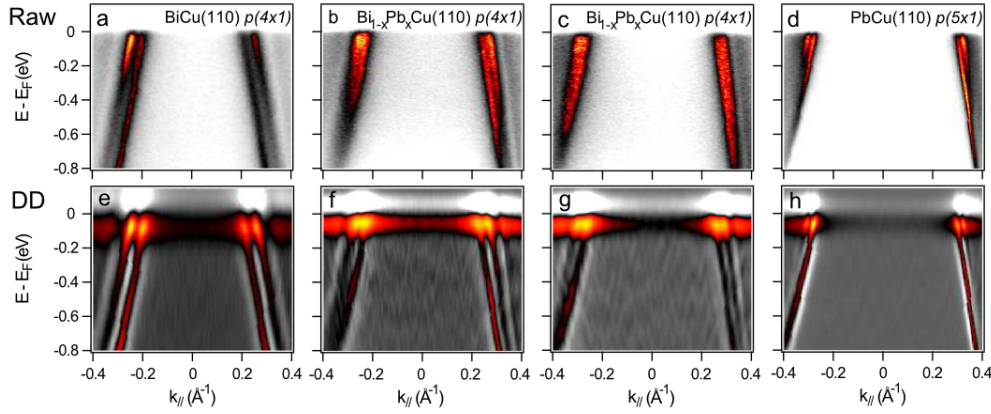


Figure 5.10: Band dispersion parallel to the chain direction for the mixed alloy $\text{Bi}_{1-x}\text{Pb}_x/\text{Cu}(110)$. Top panels show the raw data, while bottom panels display the second derivative, in order to enhance the spin splitting. The left (right) panels are related to the pristine Bi/Cu(110) (Pb/Cu(110)) surface, while the central panels (b, c, f, g) report the results for two different stoichiometries.

This experimental finding is of importance for two reasons. Firstly, the Rashba parameter α_R results from the surface state wave-functions which are formed by the orbitals of both the substrate and the adatoms. Understanding in detail the mixing of these states may help in assessing the relative effective contribution of the different elements to the large spin-splitting. Secondly, the interaction with the substrate endows the 1D states with a non-negligible 2D character. Understanding precisely the mechanism of hybridization may provide indications on how to tailor the interface in order to grow ideal 1D chain systems, which may exhibit (in extreme cases) deviations from the Fermi liquid model.

The possibility to manipulate the electronic properties of the $p(n \times 1)$ was explored by growing mixed $\text{Bi}_{1-x}\text{Pb}_x/\text{Cu}(110)$ surface alloy. The similar atomic radii and the comparable surface free energies (resulting in comparable surface reconstructions) enabled us to mix the two atomic species with a wide range of possible x values. The ordering of the $p(4 \times 1)$ reconstruction was ensured by LEED. Figure 5.10 shows the band dispersion parallel to the chain for two selected stoichiometries, compared to the pristine Bi/Cu(110) and Pb/Cu(110). The top panels a-d display the raw data; in b and c the splitting is less resolved due to the intrinsic disorder of the mixed alloy. Similar band broadening was previously reported also for the $\text{Bi}_{1-x}\text{Pb}_x/\text{Ag}(111)$ surface alloys [90]. The second derivative images, in the bottom panels e-f, clearly show the splitting in the mixed alloys.

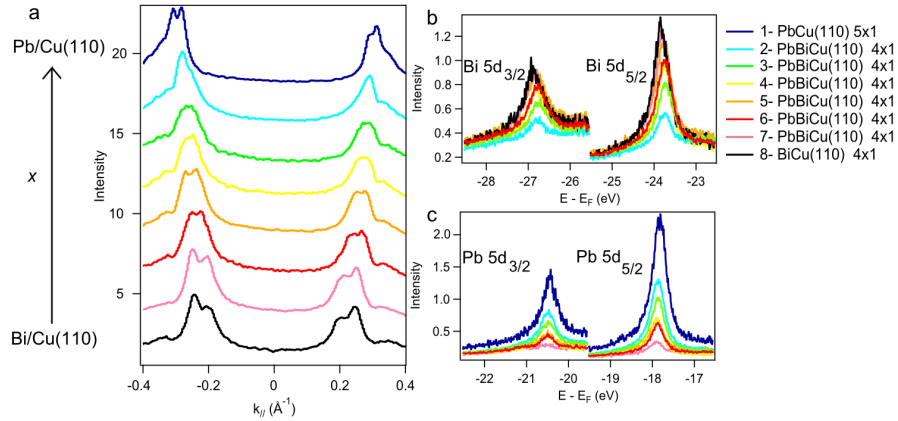


Figure 5.11: **a** stack of MDCs taken at E_F for the various $\text{Bi}_{1-x}\text{Pb}_x/\text{Cu}(110)$ samples, and vertically offset. The stoichiometry is evaluated from the area of $5d$ the core levels, displayed in panel **c**. **b** $5d$ core levels of Bi.

Pb concentration induces a continuous shift of the surface states, and a reduction of the splitting. These two effects are clearly discerned in Figure 5.11 **a**, displaying MDCs at E_F for all the measured samples. The spectra are vertically offset for clarity, with the pure Bi/Cu(110) (Pb/Cu(110)) at the bottom (top). Figure 5.11 **b** and **c** show the $5d$ core level spectra of Bi and Pb, the latter is used for defining the stoichiometry.

Each MDC is fit with a multi-components function, describing the two spin branches and a background due to the Cu sp band. The positions of the maxima of the two peaks, corresponding to k_{F1} (outer branch) and k_{F2} (inner branch), are shown in Figure 5.12 **b** as a function of x and two dashed lines indicate qualitatively the trend. The difference between each pair of k_F values defines the spin-splitting, shown in panel **a**. A clear decrease of $\Delta k = 2k_0$ is observed when increasing the Pb content.

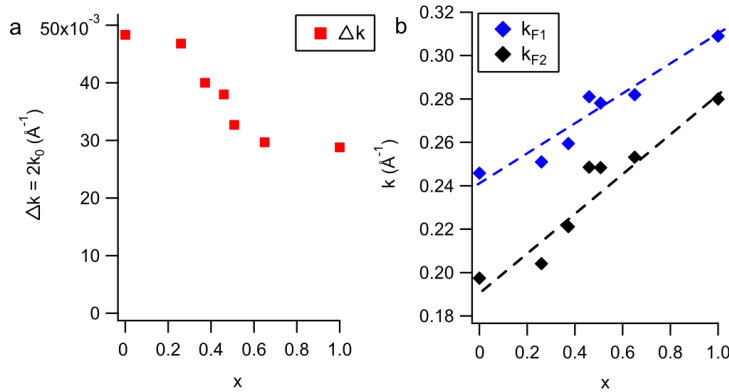


Figure 5.12: **a** spin splitting Δk of $\text{Bi}_{1-x}\text{Pb}_x/\text{Cu}(110)$ for various stoichiometries. **b** Fermi wave-vectors for the inner spin branch k_{K1} and for the outer component k_{K1} as a function of x .

It is important to notice that for all the mixed alloys the surface reconstruction is $p(4 \times 1)$. In this way the atomic substitution on the splitting is decoupled from the structural influence of the reconstruction. A complementary point of view would consist in measuring the evolution of the spin splitting for the different Pb $p(n \times 1)$ reconstructions, in order to quantify the role played by the surface structure. Unfortunately such important investigation is very difficult due to the very small separation in coverage between the various phases.

In summary, I believe that the Pb/Cu(110) system might play an important role in isolating the structural influence (namely the buckling Δz) on the spin splitting, without need to change the adsorbed atom but simply by modifying n . A systematic combined high resolution ARPES and structural (XRD, or XPD or IV-LEED) investigation would be desirable.

Large Dresselhaus and Rashba Spin Splitting at BiTeI Surfaces

Contents

6.1	The Crystal structure of Bismuth Tellurohalide BiTeI	100
6.2	Giant Rashba-type spin splitting in bulk BiTeI	101
6.3	Giant Ambipolar Rashba Effect in the Semiconductor BiTeI	103
6.4	Supplemental Material: Giant Ambipolar Rashba Effect in the Semiconductor BiTeI	109
6.4.1	Surface Terminations	109
6.4.2	Bulk conduction and valence bands	111
6.4.3	Surface potential manipulation by K dosing	112
6.4.4	Spin resolved constant energy contours	113
6.5	Two independent XARPES studies of the three-dimensional band dispersion of BiTeI	115

The formation of a conducting two-dimensional electron gas (2DEG) in bulk insulators, or in semiconductors, is a fundamental condition for technological applications. Moreover, the combination of the high charge mobility of the 2DEG with large spin splitting is desirable for the advent of spintronics devices. With this motivation transition metal oxides (TMOs) based on large Z elements, such as KTaO_3 , have been recently investigated by ARPES, but despite the strong atomic spin-orbit coupling, the observed 2DEG does not display a measurable spin splitting [125].

The formation of large spin split 2DEG was reported, instead, at the surface of the topological insulator Bi_2Se_3 , due to the strong surface band bending and the formation of a charge accumulation layer [199]. A similar mechanism was proposed also to explain the formation of spin split states in the non centro-symmetric polar BiTeI [48]. The broken inversion symmetry in its crystal structure makes BiTeI a prototype for giant bulk Rashba spin splitting [46]. Our work contributes to shed light on the bulk and surface origin of the spin split states. Moreover, we have shown that due the polar nature of the BiTeI surface it is possible to tune the position of the Fermi level over a broad energy range. In particular both hole and electron charge carriers can be obtained by a precise control of the surface termination.

6.1 The Crystal structure of Bismuth Tellurohalide BiTeI

Figure 6.1 shows schematically the crystal structure of BiTeI (left panel) along with a summary of the most important structural parameters (right table) [200]. BiTeI crystallizes in a hexagonal structure with $P3m1$ space group, and with lattice constants $a = 4.339 \text{ \AA}$ and $c = 6.854 \text{ \AA}$. The crystal structure is a deformed variant of the $2H - \text{CdI}_2$ structure type, with a precise ordering of Te and I in separated layers alternating with Bi, which occupy octahedral interstices sites. Bismuth and tellurium atoms are covalently bonded to form a positively charged bilayer. The characteristic bond length ($\text{Bi-Te} = 3.039 \text{ \AA}$) is similar to those of binary compounds, for example the topological insulator Bi_2Te_3 ($\text{Bi-Te} = 3.027 \text{ \AA}$).

Because of the non neutral character of the Bi-Te subcell, the crystal structure is described in term of a semi-ionic model, in which the positively charged bilayer interacts with the negatively charged iodine atoms, resulting in an ionic contact between Bi and I. This model succeeds in explaining the longer Bi-I bond length ($\text{Bi-I} = 3.272 \text{ \AA}$), similar to bismuth thiohalides [200]. The positive charge of the BiTe^+ bilayer is mainly localized on the Bi atoms, and therefore the Bi-Te and Bi-I are chemical bonds with respectively covalent and ionic nature. The interaction between Te and I is weaker and defines the cleavage plane. It is interesting to notice that the precise alternating packing of Te and I along the c -axes introduces a three-fold rotational symmetry in the material, which should be reflected in the corresponding electronic properties.

Finally, the BiTe^+ bilayer is corrugated and closely resembles the geometry of a metallic bismuth bilayer, which has been recently proposed to host a quantum spin Hall phase [201]. The BiTe^+ bilayer and the bismuth bilayer are isoelectronic, with five electrons and with a lone pair ns^2 per atom. BiTe^+ and Bi^0 layers are analogues, and the concept of cluster, typical of the Bi system, is substituted by the concept of BiTe^+ heterocluster.

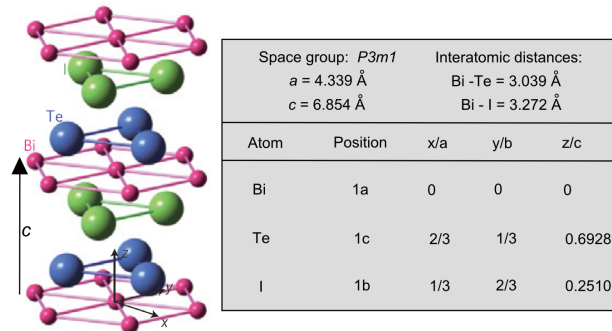


Figure 6.1: Schematic representation of the crystal structure of BiTeI (left) (from [48]) and most relevant information about the lattice symmetry, bond lengths and atomic positions in the unitary cell, as obtained from X-ray powder diffraction study [200].

6.2 Giant Rashba-type spin splitting in bulk BiTeI

The interest in the origin of the large spin splitting in the band structure of the polar BiTeI was initiated by the pioneering work of Ishizaka *et al.*. A combined ARPES and spin resolved ARPES study, supported by *ab initio* calculation, offered a first insight in the electronic properties of this material. Figure 6.2 **a** and **b** shows respectively the three dimensional Brillouin zone and the energy dispersion of the bands obtained by relativistic first principle calculations [48, 202]. Despite the layered nature of the crystal, the band structure presents a non negligible dispersion along the $\bar{\Gamma}\bar{A}$ high symmetry direction (parallel to the k_z axis, orthogonal to the surface). The existence of a small gap is reported, whose magnitude is underestimated by the DFT model. Optical measurements provide a direct experimental view of the gap, which is found to be equal to ~ 0.4 eV [203]. In-plane electric resistivity indicates a metallic behavior down to liquid He temperature, which is interpreted in term of a small deviation from stoichiometry, and for this reason BiTeI is described as a degenerate small gap semiconductor. The bands at the Fermi level are derived from the Bi 6*p* states, while the valence band is constituted mainly by the Te and I 5*p* orbitals.

By comparing the results of the calculated electronic structures with and without spin orbit (not shown) a drastic change is observed close to the \bar{A} point. The spin degeneracy is resolved and the maximum (minimum) of the valence (conduction) band is shifted away from the high symmetry point by approximately $\pm k_{VB} = \pm 0.05 \text{ \AA}$ ($\pm k_{CB} = \pm 0.05 \text{ \AA}$). The band dispersion resembles the Rashba-like dispersion characteristic of surface states, but in this case the large spin splitting affects bulk bands, making BiTeI the largest bulk Rashba spin split material.

These theoretical findings called for detailed ARPES measurements, whose results are briefly shown in Figure 6.2 **c**. High energy and momentum resolution were achieved by the use of laser based ARPES. Surprisingly two sets of spin split states are observed crossing the Fermi level, with binding energy respectively equal to 0.33 eV and 0.17 eV. The bottom of the conduction band is therefore considerably shifted downward with respect to the *ab initio* calculation (0.14 eV), and this indicates the presence of a strong near-surface band bending. To simulate this effect the authors used the Poisson-Schrödinger equation method, developed for the study of InN surface [204] and successfully applied to the topological insulator Bi₂Se₃ [199]. The results of this simulation are shown in Figure 6.2 **d**, where the potential energy $V(z)$ is displayed as a function of the depth from the surface z . There exists a band-bending layer with thickness equal to $\sim 20 \text{ \AA}$ with an electron accumulation 10 times larger than in the bare bulk conduction band.

The pair of spin states of Figure 6.2 **c** was interpreted as two distinct quantum well subbands arising from the spatial confinement of the conduction band wave-functions in the sub-surface accumulation layer. The quantization mechanism conveys a dispersionless character to the bulk derived states, and this was partially confirmed by measurements at two different photon energies (21.2 eV and 40.8 eV, respectively the HeI α and HeII α lines). At higher photon energies only one pair of spin split state is resolved, and this was ascribed to the higher momentum resolution of the laser-ARPES and the deeper probing depth of the low energy photoemitted electron.

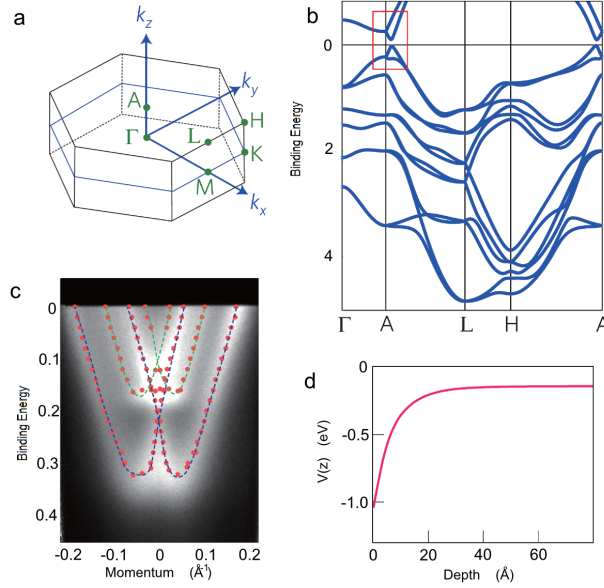


Figure 6.2: **a** three dimensional Brillouin zone of BiTeI. **b** shows the energy dispersion of the bands obtained by relativistic first principle calculation [48, 202]. **c** displays laser-ARPES measurement of the band dispersion, two set of spin split states are observed, and they are interpreted as two distinct quantum well subbands arisen from the quantization of the conduction band in the sub-surface accumulation layer. The surface band bending is simulated by solving a Poisson-Schrödinger equation, and panel **d** shows the calculated potential energy $V(z)$ as a function of the depth from the surface z [48].

Spin resolved ARPES confirmed the spin polarization of the states at the Fermi level, but the origin of such splitting remains still unclear. The authors discarded the origin of the splitting as an effect of the band bending, because the magnitude of the splitting introduced by the surface potential gradient results small. However, as it was discussed in Chapter 2, the simple Rashba - Bychkov model is never capable to reproduce quantitatively the large splitting in surface states. King *et al.* were able to capture the spin splitting of the quantum wells states in Bi_2Se_3 , but similarly their model fails at a numerical level [199]. In order to shed light on the surface contribution to the large spin separation and to investigate the k_z dispersion of the conduction and valence band states, we carried out a detailed ARPES study of BiTeI, which is subject of the next section. This article has been published as Physical Review Letters [205], and highlighted with a synopsis in Physics [206].

6.3 Giant Ambipolar Rashba Effect in the Semiconductor BiTeI

We observe a giant spin-orbit splitting in bulk and surface states of the non-centrosymmetric semiconductor BiTeI. We show that the Fermi level can be placed in the valence or in the conduction band by controlling the surface termination. In both cases it intersects spin-polarized bands, in the corresponding surface depletion and accumulation layers. The momentum splitting of these bands is not affected by adsorbate-induced changes in the surface potential. These findings demonstrate that two properties crucial for enabling semiconductor-based spin electronics – a large, robust spin splitting and ambipolar conduction – are present in this material.

The relativistic spin-orbit interaction (SOI) lifts the usual Kramers spin degeneracy in electron systems that lack inversion symmetry. It lies at the origin of many subtle and interesting effects in the electronic structure of materials such as the emergence of topological insulators (TI), a new quantum state of matter. In the bulk of materials with non-centrosymmetric structures, such as the zincblende and wurzite structures, it gives rise to the Dresselhaus [47] and Rashba [46] effects. An analogous effect, the Rashba-Bychkov effect, describes the lifting of the spin degeneracy at surfaces and at asymmetric interfaces, where inversion symmetry is also broken [45]. The SOI is a general phenomenon, but it is especially relevant in solids containing high-Z elements because of their large atomic spin-orbit parameter. The characteristic splitting in energy and momentum was first directly observed by angle-resolved photoelectron spectroscopy (ARPES) on the Au(111) surface [10]. The predicted polarization of the electronic states was confirmed by spin-polarized ARPES [58, 60], and the Rashba scenario has been extended to other surfaces and interfaces [67, 81, 207, 51, 189, 87, 123, 114, 111].

The vision of an all-electric control of spin transport in new device concepts explains the strong current interest for materials with large Rashba or Dresselhaus effects. Future devices operating at room temperature will require a large separation between the spin-polarized bands and the ability to tune the position of the chemical potential over a broad energy range. Whereas the former have been reported in surface alloys with high-Z elements such as Pb or Bi, only limited tunability has been achieved so far.

BiTeI is a non-centrosymmetric semiconductor for which theory predicts a large bulk Rashba effect, and the emergence of a topological insulating phase under pressure [208]. Ishizaka *et al.* [48] used spin-resolved ARPES to reveal spin-polarized states with a large momentum splitting. They assigned them to a quantum-well state (QWS) confined in the accumulation layer that appears because of band bending in the surface region. This interpretation has been questioned in part by more recent ARPES data and theory that show the coexistence of surface and bulk bands near the Fermi level [209].

In this Letter, we show that in BiTeI the chemical potential can be moved well into the conduction band or the valence band by controlling the surface termination. Remarkably, a giant spin splitting at the Fermi surface is observed in both cases. First-principles relativistic calculations indicate that both the surface and the bulk bands are split by the SOI. We also prove that the size of the Rashba effect is largely insensitive to changes in the sur-

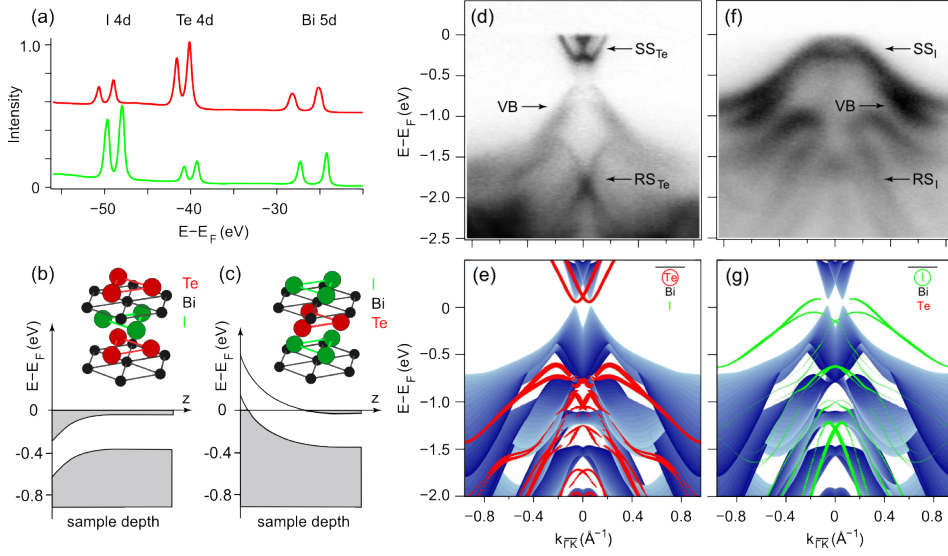


Figure 6.3: (a) I 4*d*, Te 4*d* and Bi 5*d* core level spectra measured at $h\nu = 120$ eV on Te-terminated (red, top) and I-terminated (green, bottom) surfaces. (b,c) Schemes of surface band bending for the two surface terminations. The thickness of the accumulation layer was estimated to be ~ 3 nm in Ref. [48]. (d) ARPES dispersion along the $\overline{\Gamma K}$ direction measured at 93 eV and $T = 40$ K, for a Te-terminated surface, compared to (e) the projected slab band structure calculated from first principles. The size of red symbols is proportional to the magnitude of projection onto the surface Te atoms. The continuum of bulk states is shown in blue. (f,g) Corresponding plots for the I-terminated surface. The size of the green symbols is proportional to the contribution of the surface I atoms. In (e) and (g) only projection amplitudes larger than 0.1 are shown.

face potential. Therefore, the splitting has mainly an atomic origin. These results establish BiTeI as a versatile material, characterized by the coexistence of very large ambipolar bulk and surface Rashba effects.

We performed ARPES experiments at the Electronic Structure Factory, beam line 7.0.1 of the Advanced Light Source. The energy and momentum resolution of the hemispherical Scienta R4000 analyzer were 30 meV and 0.1° . High quality single crystals of BiTeI, in the form of platelets, were grown by chemical vapor transport and by the Bridgman technique, and characterized by x-ray diffraction and transport. They shown a metallic conduction due to a small ($<2\%$) deviation from stoichiometry. The samples were mounted on a He cryostat and cleaved in UHV to expose flat, shiny surfaces.

First-principles electronic structure calculations were performed within the density functional theory (DFT) framework employing the generalized gradient approximation (GGA) as implemented in the QUANTUM-ESPRESSO package [210]. Spin-orbit effects were accounted for using the fully relativistic norm-conserving pseudopotentials acting on valence electron wave-functions represented in the two-component spinor form [211]. The surface band structures were obtained using a slab model consisting of 39 atomic layers. Since the BiTeI crystal has no inversion symmetry, the surfaces of the slab are necessar-

ily different. The slab model considered here includes two unpassivated experimentally relevant terminations (Te and I). The surface bands at the two different surfaces were disentangled by projecting the Kohn-Sham wave functions onto atomic wave functions at the surface layer. The bulk and the slab band structures were aligned by matching the potential in the middle of the slab with the bulk potential.

BiTeI has a trigonal layered structure, with Bi, Te and I planes alternating along the c axis. The Bi and Te planes are covalently bonded to form a positively charged $(\text{BiTe})^+$ bilayer. The ionic coupling between the bilayer and the adjacent I^- plane defines the natural cleavage plane [200]. The topmost layer – Te or I – is identified by the relative intensities of the Te and I $4d$ core levels, as in Fig. 6.3 (a). Ideally, due to the lack of inversion symmetry, the surface termination is uniquely determined by the direction of the c -axis. However, repeated cleaves of the same crystal randomly expose both terminations due to the occurrence of stacking faults, which also explains the observation of 6-fold symmetry in the Laue patterns (not shown). We have measured ‘pure’ surfaces and also ‘mixed’ surfaces that presented areas with both terminations (see supplementary information). Data for the former are illustrated in Fig. 6.3. The surface charges – positive for Te, negative for I – induce band bending in opposite directions for the two terminations. The Fermi level lies into either the conduction or the valence band, giving rise to a charge accumulation or, respectively, depletion layer. This is schematically illustrated in Fig. 6.3 (b,c) and substantiated by the ARPES data. It should be noted that our DFT calculations reproduce qualitatively the observed band bending. The surface bands of the Te(I)-terminated surface appear below (above) the bulk conduction (valence) bands (Fig. 6.3 (e,g)).

Figure 6.3 (d) illustrates the ARPES dispersion of the Te-terminated surface, measured along the $\bar{\Gamma}\text{K}$ high-symmetry direction ($\bar{\Gamma}\text{K} = 0.96 \text{ \AA}^{-1}$) of the Brillouin zone. The most prominent feature is the split parabolic band (SS_{Te}) straddling the Fermi level E_{F} . The two subbands have minima at -0.32 eV and are offset by $\pm 0.055 \text{ \AA}^{-1}$ around $\bar{\Gamma}$. This is consistent with previous data, and with a Rashba interaction one order of magnitude stronger than for the Au(111) benchmark case [48]. This feature is well reproduced in the first-principles band structure of Fig. 6.3 (e). It shows that the spin-split state is localized in the topmost bilayer, and partially overlaps with conduction band states that exhibit a smaller momentum offset. The bulk signal is too weak to be identified in Fig. 6.3 (d), but it can be discerned between SS_{Te} and E_{F} at closer inspection (see the supplementary material). The projected bulk valence band exhibits gaps supporting other surface states. These states exhibit an even larger, but previously unnoticed, splitting. Their spin polarization has non negligible radial and out-of-plane components (see the supplementary material), at variance with the simple Rashba scenario, and similar to recent observations on topological insulators [212]. The complex manifold cannot be easily disentangled in the ARPES map, which shows a prominent state, labelled RS_{Te} , symmetrically split around $\bar{\Gamma}$. The maxima of RS_{Te} are at $\pm 0.2 \text{ \AA}^{-1}$ and -1.3 eV , corresponding to a very large and previously unnoticed momentum splitting. The bulk valence band (VB), with a maximum 0.37 eV below the bottom of SS_{Te} also exhibits a large spin-orbit splitting, reproduced by the calculation.

The picture from the I-terminated surface (Fig. 6.3 (f,g)) is quite different. The electron pockets around $\bar{\Gamma}$ are replaced by hole pockets from a spin-split state (SS_{I}) with a strong projection on the surface I atoms. The momentum offset is again quite large, of the order

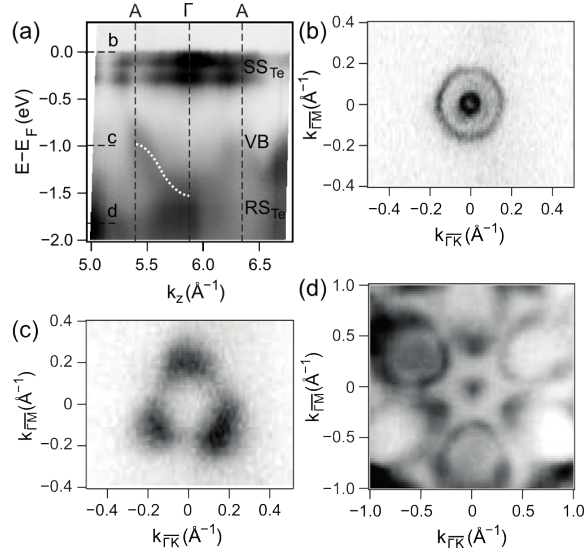


Figure 6.4: (a) ARPES intensity from a Te-terminated surface, measured at $\sim 0.3^\circ$ off normal emission, in a photon energy scan between 84 eV and 162 eV, plotted as a function of k_z , the wave vector along the c -axis. Both the upper and the lower branch of SS_{Te} are visible. The white dashed curve is the calculated dispersion of the corresponding bulk valence state. (b-d) Constant energy contours measured at the energies marked by the corresponding (b,c,d) horizontal lines in panel (a).

of $\pm 0.2 \text{ \AA}^{-1}$. A precise determination is difficult because the top of the band lies above E_F . The top of VB is also located above E_F . There is a complete change from electron to hole carriers with respect to Fig. 6.3 (d), which demonstrates ambipolar conduction in BiTeI. The total change in band bending between the Te- and I-terminated surfaces, estimated from core level spectra (see supplementary information), is $\Delta E_{BB} = 0.9 \text{ eV}$, to be compared with the estimated energy gap $\Delta E_g \sim 0.38 \text{ eV}$ [48]. Additional features (RS_I) symmetrically split around $\bar{\Gamma}$, can again be identified at higher energy in the ARPES map.

We stress the importance of the ambipolar nature of the low-energy states in view of possible applications. Achieving control of the Fermi level position in Rashba systems or topological insulators has proved a challenging task. Previous strategies based on surface doping by chemi- or physisorbed species, or on alloying, have obvious drawbacks. The former faces the problem of chemical stability, the latter that of disorder leading to a reduced mobility. By contrast, switching between electron and hole conduction is achieved in BiTeI without modifying the ideal crystal structure or the stoichiometry.

The assignment of the spectral features of Fig. 6.3 to surface or bulk states is further supported by the data shown in Fig. 6.4 (a). It illustrates the photoelectron intensity measured at near-normal emission from a Te-terminated surface as a function of k_z , the wave vector along the c -axis. SS_{Te} exhibits an intensity modulation but no dispersion, as expected for true surface states. By contrast, state VB exhibits a $\sim 0.7 \text{ eV}$ dispersion along ΓA , consistent with its bulk character, and well reproduced by the calculation (dashed line).

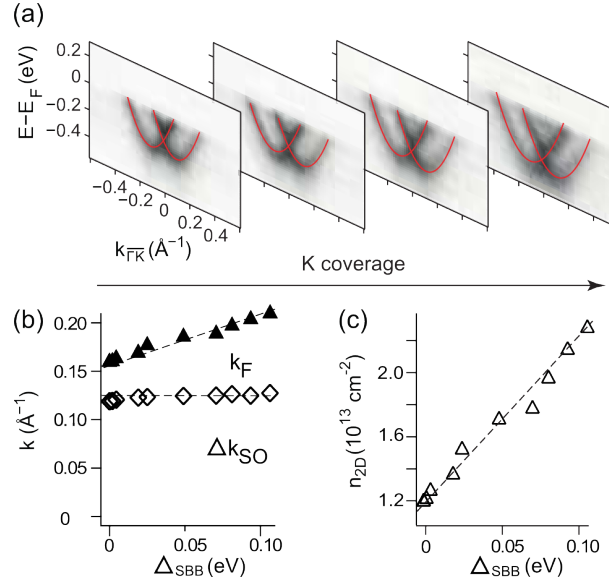


Figure 6.5: (a) Evolution of the spin-split SS_{Te} surface state band as a function of K coverage. The red parabolas are the result of a fit to the band dispersion along $\bar{\Gamma}\bar{K}$. (b) The Fermi wave vector k_F of the outer branch (solid symbols) and the Rashba splitting Δk_{SO} (empty symbols) are plotted as a function of the measured change in surface band bending Δ_{SBB} . (c) The corresponding surface electron density.

This is confirmed by constant energy maps (CEM) of these states. The CEM measured at E_F for SS_{Te} (Fig. 6.4 (b)) has two concentric contours typical of the Rashba scenario. The external contour, warped by the interaction with the lattice potential, has a 6-fold symmetry, as required by time-reversal symmetry for a surface state [141]. In the CEM measured at the crossing point of RS_{Te} (Fig 6.4 (d)), the inner contour has collapsed to a point at $\bar{\Gamma}$. The outer contour again exhibits a 6-fold symmetry. Interestingly, it is not closed around $\bar{\Gamma}$, but it is broken into 6 disconnected pockets aligned along the 6 equivalent $\bar{\Gamma}\bar{M}$ directions. This can be seen as the limit of strong warping, reflecting a large in-plane asymmetry of the surface potential [144]. Conversely, the CEM through VB (Fig. 6.4 (c)) shows a single 3-fold contour. This symmetry reduction is not due to partial extinction of a 6-fold contour induced by ARPES matrix-elements, because the pattern remained locked to the crystallographic directions when the crystal was rotated around the surface normal. Therefore, the 3-fold pattern of VB reflects the 3-fold symmetry of the bulk potential, and confirms the bulk character of this state (see the supplementary material).

We now turn our attention to the origin of the very large Rashba splitting. Competing models beyond the standard Rashba scenario have been proposed. They alternatively stress atomic contributions [44], the in-plane anisotropy of the surface potential [56], the asymmetry of the wave-functions [89], or the local orbital angular momentum [63]. A bulk origin has been invoked for BiTeI [48], but this conflicts with the surface nature of the relevant states.

In the standard Rashba scenario the size of the splitting is controlled by the gradient of

the surface potential, and this prediction was found to be consistent with the properties of QWS formed in an accumulation layer at the surface of the TI Bi_2Se_3 [199]. In order to test this hypothesis for BiTeI we have changed in a controlled way the surface band bending, and hence the gradient of the potential in the surface region. This was achieved by depositing increasing amounts of potassium on a Te-terminated surface. Adsorbed K atoms donate electrons to the CB, leaving a positively charged surface layer which enhances the downward surface band bending. Figure 6.5 (a) illustrates the evolution of SS_{Te} as a function of K coverage.

As expected, SS_{Te} and all core levels (see the supplementary information) shift to lower energies, following the change in band bending. The total shift at saturation K coverage is 0.12 eV, bringing the bottom of SS_{Te} 0.44 eV below E_{F} . A closer inspection shows that the energy shift of SS_{Te} is rigid. Figure 6.5 (b) shows the Fermi wave vector k_{F} of the outer branch and the momentum offset Δk_{SO} . They were estimated from a parabolic fit of the dispersion, keeping the effective mass unchanged. Within error bars Δk_{SO} remains constant. The bottom of SS_{Te} gives an upper limit for band bending. Therefore a $>40\%$ change in the surface band bending has no measurable effect on the strength of the Rashba effect. The SO-split surface state at the Ir(111) surface covered by graphene was recently found to be similarly insensitive to the surface potential gradient [66]. This experimental observation strongly suggests that other parameters, namely the atomic spin-orbit parameter of the heavy elements, determine the large spin splitting. Figure 6.5 (c) shows that the surface carrier density, estimated from the area of the electron pockets, varies linearly with the downward shift of the split bands. This is again consistent with a constant Δk_{SO} . By contrast, deviations from linearity have been observed for the QWS at the Bi_2Se_3 surface [199].

In summary, we have shown that large ambipolar bulk and surface Rashba effects co-exist in the non-centrosymmetric semiconductor BiTeI. The Fermi level at the surface lies either into the valence or the conduction band, depending on the nature of the topmost layer. Achieving ambipolar conduction in a semiconductor with a large Rashba splitting is an important step towards practical applications. In our bulk crystals the surface termination was randomly chosen by cleavage due to stacking faults, but a definite improvement is possible in thin film samples. Molecular beam epitaxy and chemical vapor deposition – a technique compatible with large-scale thin films production – can in fact be exploited to gain control on the nature of the topmost layer. It is therefore realistic to consider that regions with opposite band bending – a “Rashba p-n junction” – could be patterned on a substrate, opening new perspectives for the manipulation of spin-polarized states.

6.4 Supplemental Material: Giant Ambipolar Rashba Effect in the Semiconductor BiTeI

6.4.1 Surface Terminations

All cleaved surfaces we measured exhibited domains of both the Te- or I- terminated surfaces, with no significant differences between the two crystal growth methods (vapor transport or Bridgman). The typical lateral size of these domains was $\sim 150 \mu\text{m}$. With a beam spot size of $\sim 100 \mu\text{m} \times 40 \mu\text{m}$ (H \times V) it was often possible to probe a region with a single termination. Occasionally domains as large as 0.5 mm were obtained. This enabled broad angular scans such as the one shown in Fig. 6.9 (e) below. The atomic termination can be determined from the relative intensities of the shallow I $4d$, Te $4d$ and Bi $5d$ core levels, which can all be measured in a single spectrum collected over a narrow energy range. When spectra are normalized to the same Bi $5d$ integrated intensity as in Fig. 6.6 (e), the ratio of

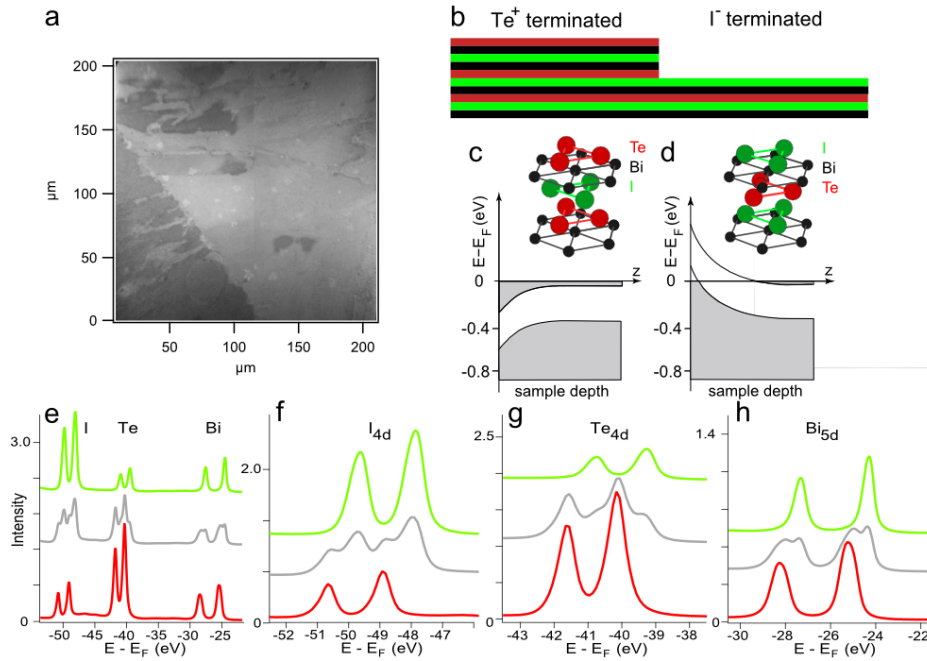


Figure 6.6: **(a)** Photoemission ($h\nu = 21.2\text{eV}$) electron microscope (PEEM) image of a typical cleaved surface, showing domains of the two surface terminations. Contrast is provided by the different work functions. Both Te-terminated and I-terminated surfaces can be exposed by cleavage in BiTeI due to stacking faults. The two terminations can also coexist on the same cleaved surface in the presence of steps, as in **(b)**. **(c)(d)** Schematic view of band bending for the two terminations. **(e)** I $4d$, Te $4d$ and Bi $5d$ core levels measured at $h\nu = 120$ eV and $T = 40$ K on an I-terminated (top, green line), a Te-terminated (bottom, red line) and a mixed (middle, grey) surface. **(f-h)** Close-ups of the three core levels showing a common $\Delta E = 0.9$ eV energy shift between the two surface terminations. The width of the accumulation layer was estimated to be ~ 3 nm in Ref. [48].

the integrated Te 4*d* and I 4*d* intensities corrected for the respective photoionization cross sections [213], $\mathcal{I}(\text{Te } 4d)$ and $\mathcal{I}(\text{I } 4d)$, is reversed between the two surfaces. Specifically, we obtain $\mathcal{I}(\text{Te } 4d)/\mathcal{I}(\text{I } 4d) = 0.35$ for the I-terminated surface, and $\mathcal{I}(\text{I } 4d)/\mathcal{I}(\text{Te } 4d) = 0.32$ for the Te-termination.

All core levels exhibit the same energy shift $\Delta E_{\text{BB}} = 0.9$ eV towards lower binding energy between the Te-terminated and the I-terminated surfaces. This shift reflects the change in surface band bending, schematically illustrated in panels (b,c). The same energy shift is observed in the valence band spectra (see below).

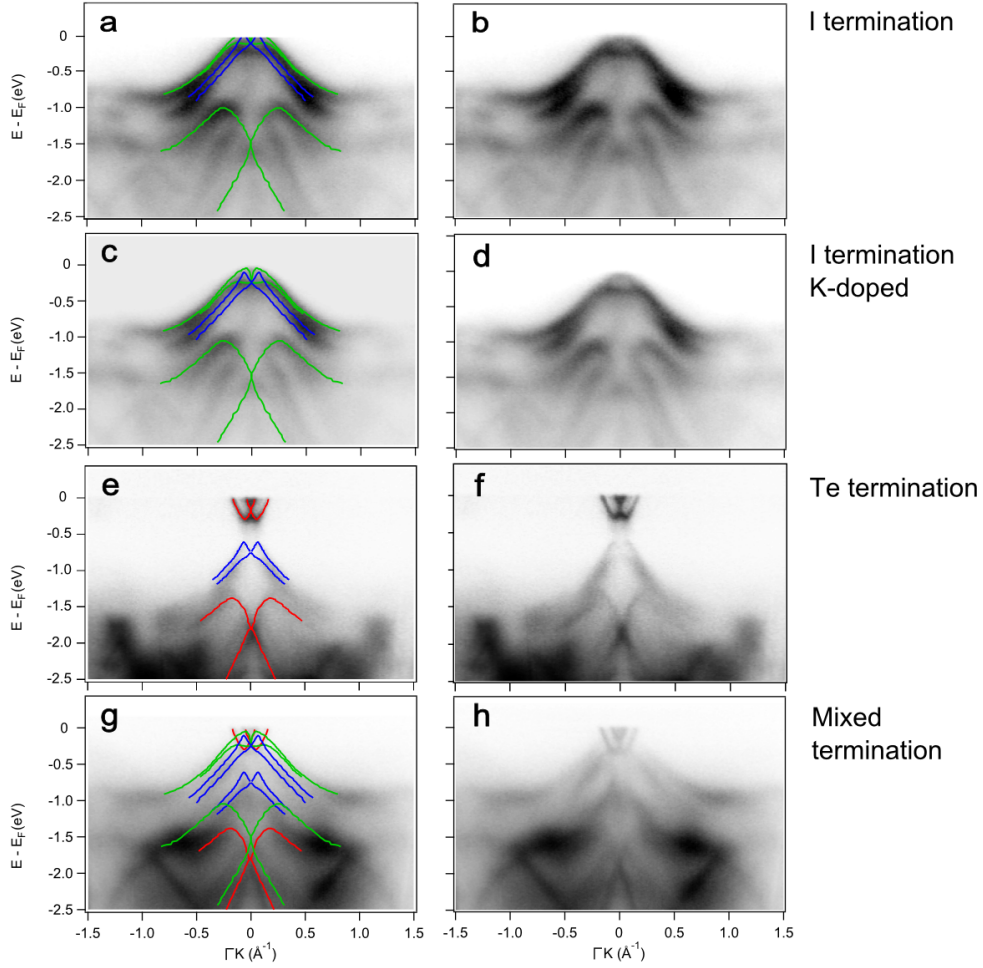


Figure 6.7: ARPES dispersion along the $\overline{\Gamma K}$ high symmetry direction measured at $h\nu = 93$ eV and $T = 40$ K. In the left column red (Te-related states), green (I-related states) and blue (bulk valence states) lines have been superimposed to the raw images of the right column to highlight the main band features. (a,b) I-terminated surface; (c,d) I-terminated surface after a short K deposition; (e,f) Te-terminated surface; (g,h) a mixed surface.

We have also observed cleaved surfaces showing the spectral signatures of both termi-

nations. This indicates that terraces with different terminations, and separated by steps, are present at the surface, as in Fig. 6.6 (a,b). The middle lines of panels (e)-(h) illustrate the case of such a mixed surface. The (Te 4d)/(I 4d) ratio is intermediate between those of the two pure terminations. Moreover, all core levels are split into two partially overlapping doublets, corresponding to the Te- and, respectively, the I-terminated terraces.

Figure 6.7 illustrates the band dispersion along the $\bar{\Gamma}\bar{K}$ high symmetry direction for various surfaces. Panels (a,b) correspond to an I-terminated surface, characterized by a positive band bending. The Fermi level cuts the top of the I-derived surface state SS_I and of the bulk valence band. A short K evaporation reduces the band bending and brings the top of these bands below E_F (c,d). Panels (e,f) are for a Te-terminated surface. The case of a cleaved surface where both terminations are present is shown in (g,h). The ARPES map is essentially a superposition of the I- and Te-terminated cases. The upward shift of the I-derived bands is slightly smaller than for a pure I termination, reflecting a more complex in-plane surface potential landscape in the presence of terraces.

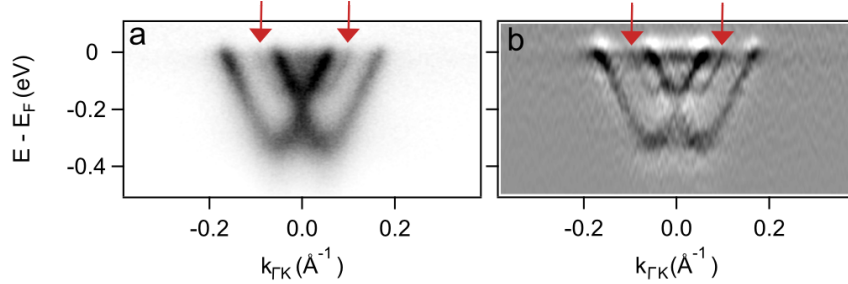


Figure 6.8: ARPES intensity map near $\bar{\Gamma}$ for a Te-terminated surface ($h\nu = 93$ eV). (a) Raw data; (b) second derivative. Red arrows mark the Fermi level crossings of the outer branch of spin-split conduction band states.

6.4.2 Bulk conduction and valence bands

Our first-principles calculations for the Te-terminated surface predict that surface state SS_{Te} overlaps with bulk conduction states. This is indeed confirmed by Fig. 6.8. Besides SS_{Te} a weak feature is visible at lower binding energy. One can recognize a second set of spin-split parabolas with minima at -0.13 eV. The E_F crossing of the outer branches of these states is marked by red arrows.

The bulk nature of the valence band state VB is supported by the 3-fold symmetry of its constant energy maps (CEM), in contrast with the 6-fold symmetry of the Te- and I-derived surface states. Figure 6.9 (a)-(c) shows three CEM measured at $E = -0.95$ eV for a Te-terminated surface and three different sample orientations. The measured ARPES intensity is proportional to matrix elements of the form: $|\langle \psi_f | \mathbf{A} \cdot \mathbf{p} | \psi_i \rangle|^2$, where ψ_i and ψ_f are the wave-functions of the initial and final states, \mathbf{A} is the vector potential of the e-m wave and \mathbf{p} is the momentum of the electron. Matrix elements can strongly affect and even suppress the signal for specific scattering geometries [214]. Namely, if the wave vectors of both the photon and the photoelectron lie in a mirror plane of the crystal, emission from odd (even)

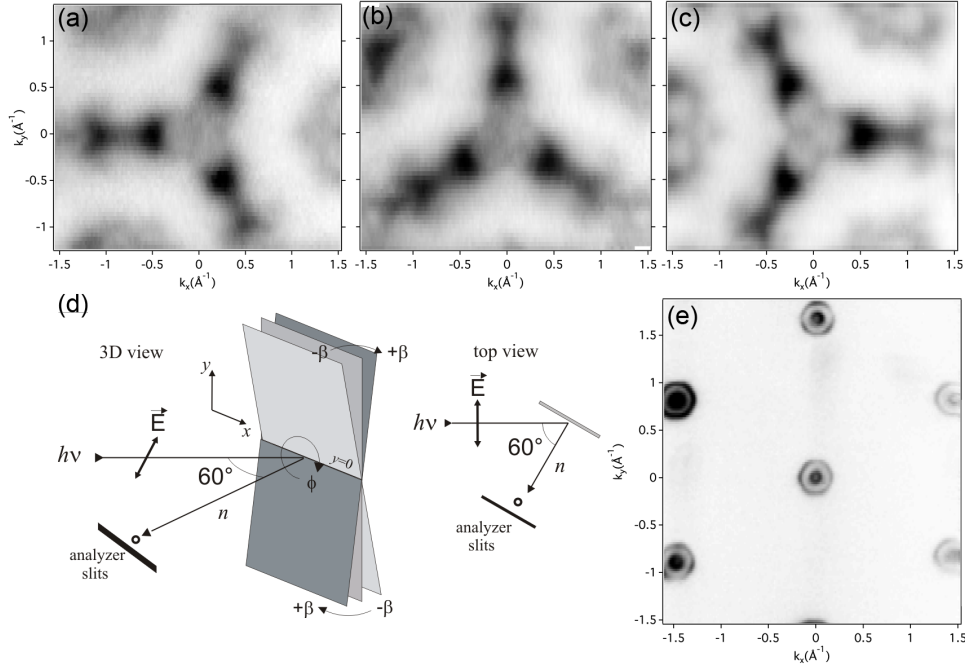


Figure 6.9: (a-c) Constant energy maps at $E = -0.95$ eV through the valence band state VB, for three different azimuthal orientations of the sample around the surface normal. (d) Experimental geometry. (e) Constant energy map at E_F over several Brillouin zones showing the 6-fold symmetry of surface state SS_{Te} .

initial states wave-functions is suppressed for light linearly polarized in (perpendicular to) the plane. Intensity is nevertheless smoothly recovered outside the mirror plane, where the parity of the states is ill-defined. In our experiment the horizontal scattering plane is fixed and contains the polarization vector (Fig. 6.9 (d)). The data of panels (a)-(c) were measured for three different azimuthal orientations (0° ; 30° ; 60°) around the surface normal. Each horizontal line (k_x direction) is measured in one shot, while the k_y range is spanned by a rotation of the β angle around the x axis of the sample. The intensity suppression is clearly not linked to the horizontal ($k_y = 0$) plane, and the 3-fold pattern is instead locked to the crystallographic directions, reflecting the 3-fold symmetry of the bulk crystal potential. This sharply contrasts with the constant energy map of the SS_{Te} surface state (panel (e)), which exhibits a clear 6-fold symmetry.

The dependence of the ARPES spectra on the wave vector k_z perpendicular to the crystal surface is shown in Fig. 6.10, extracted from Fig. 6.4 of the main text. Here, the dispersive VB and the essentially dispersionless RS_{Te} states are readily identified.

6.4.3 Surface potential manipulation by K dosing

We have modified the surface band bending by repeated evaporations of K from an effusion cell onto the cleaved surfaces at $T = 60$ K. Figure 6.11 shows the corresponding changes in the energies of the $I_{4d_{5/2}}$, $Te_{4d_{5/2}}$ and $Bi_{5d_{5/2}}$ core levels, and of the surface states for both

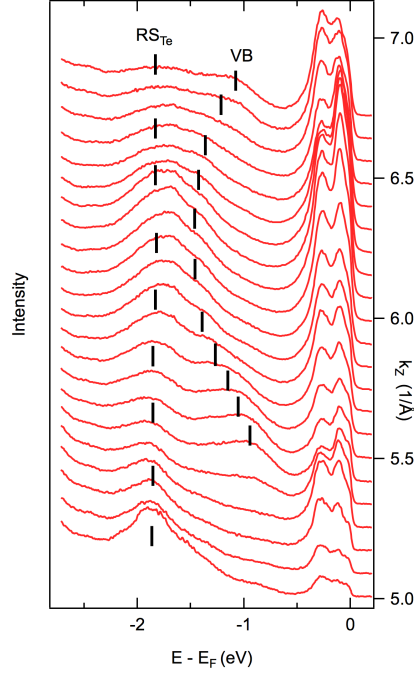


Figure 6.10: The k_z dependence of the ARPES spectra.

I-terminated and Te-terminated surfaces. For the I-terminated surface all core levels and surface state SS_I shift together by the same amount to lower energy. The initial positive band bending is reversed, and a negative one is established. The total shift is $\Delta E_I = -0.75$ eV, which almost equals the difference in band bending between the I- and Te-terminated surfaces. For the Te-terminated surface all core levels and surface state SS_{Te} again shift together to lower energy, but the total shift is only $\Delta E_{Te} = -0.12$ eV. This shows that, as expected, it is more and more difficult to push the Fermi level deep into the conduction band. The determination of the structure of the K-covered surfaces, an interesting subject in itself, is beyond the scope of the present paper and left for future work.

6.4.4 Spin resolved constant energy contours

From our slab DFT calculation, we extracted spin-resolved constant energy contours for the Te surface states by calculating the spin-polarized k -resolved density of states at various energies. In Fig. 6.12 we show the spin helicity of these contours, defined as the projection of the spin on the direction normal to the wave vector $\mathbf{k}_{||}$ in the xy plane. A positive value of helicity indicates that the sense of rotation of the electron spin along the constant energy contour is counterclockwise. The conduction band (state SS_{Te}) exhibits the typical spin texture of a Rashba split state. Above the band crossing at $\bar{\Gamma}$ two contours with opposite helicity can be observed. In the valence band (state RS_{Te}) the picture is slightly more complicated since two spin-split bands are present. Below the crossing point of these bands at $\bar{\Gamma}$ two contours with opposite spin helicity can be seen for each of these bands. These contours confirm that BiTeI exhibits a strong Rashba splitting both in its valence and

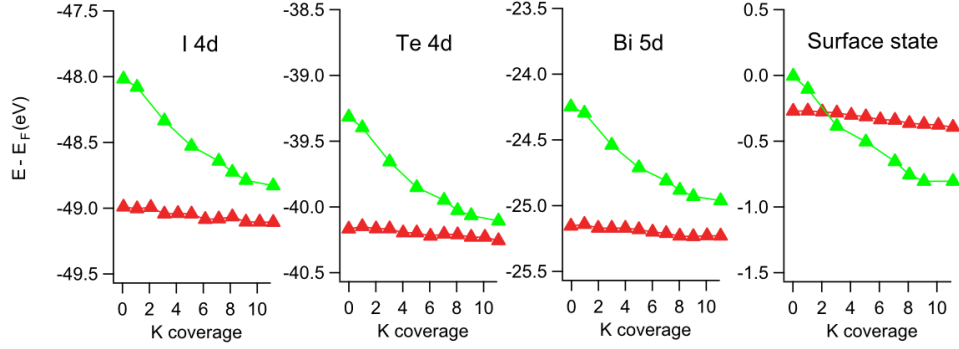


Figure 6.11: **(a-c)** Peak energies of the $I_{4d_{5/2}}$, $Te_{4d_{5/2}}$ and $Bi_{5d_{5/2}}$ core levels as a function of the number of K evaporation steps. Green symbols refer to the I-termination surface, red symbols to the Te-termination. **(d)** Energy of the top of SS_I (solid green symbols) and of the bottom of SS_{Te} (solid red symbols).

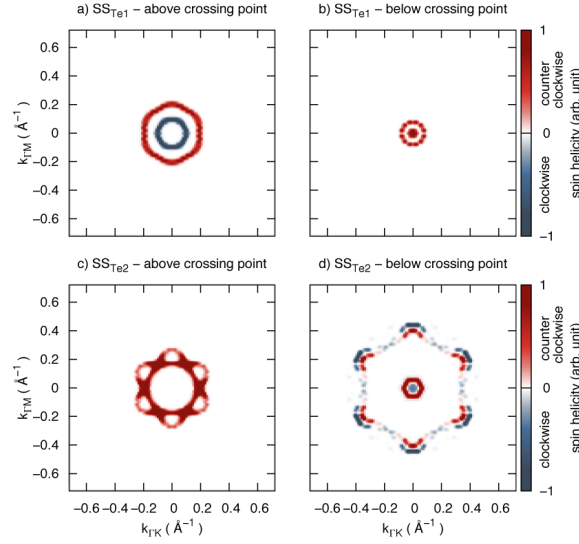


Figure 6.12: **(a-d)** Spin resolved constant energy contours for SS_{Te} **(a)** above and **(b)** below the crossing of the SS_{Te} bands at $\bar{\Gamma}$, and for RS_{Te} **(c)** above and **(d)** below the crossing of the RS_{Te} bands at $\bar{\Gamma}$. The color indicates the spin helicity of the states (see text).

conduction bands.

6.5 Two independent XARPES studies of the three-dimensional band dispersion of BiTeI

A parallel study performed by G. Landolt and coworkers confirmed the experimental findings of our work [209]. The combined use of UV light (24 eV) and soft X-rays (760 eV) provided the capability to disentangle the surface and the bulk contributions to the electronic properties of BiTeI. Several efforts have been recently spent to develop high-resolution ARPES at high photon energies (XARPES) in order to exploit the longer escape depth of photoemitted electrons for greater bulk sensibility. Moreover, the larger radius of the associated Ewald sphere makes the cut at constant photon energy very close to a cut at constant k_z , overcoming one of the complications of photon energy scans in the UV spectral region.

Figure 6.13 shows the experimental band dispersion along $\overline{\Gamma M}$ at two distinct photon energies (24 eV and 760 eV respectively in panel **a** and **b**) along with the results of *ab initio* calculations (**c**). At low photon energy the cross section of the surface states dominates the photoemission process, the conduction and valence bands are barely recognizable and the spin split states crossing the Fermi level well resemble the results of our work. At higher photon energy the signal from the bulk is strongly enhanced, and the magnitude of the measured band gap is close to the value obtained by optical experiments [203]. The calculation of panel **c** confirms our interpretation of the existence of two distinct families of surface states arisen from the two possible surface terminations.

In Figure 6.13 **a** the sample surface presents clearly both the terminations. No measurement is reported for the purely Te^+ and I^- terminated surfaces, probably due to the larger spot size of the light, or to the higher density of stacking faults. The complexity of the mixed surface makes it impossible to recognize the existence of a large and opposite band bending for the I^- termination. At first sight, a comparison with the calculated band structure is quite satisfactory. Nevertheless, this agreement is due to the underestimation of the band gap typical of DFT calculation, and only core level spectra can unambiguously resolve the two opposite band bendings at the base of the ambipolar character of the charge carriers in BiTeI.

The identification of the bulk signal in the XARPES spectra offered the possibility to

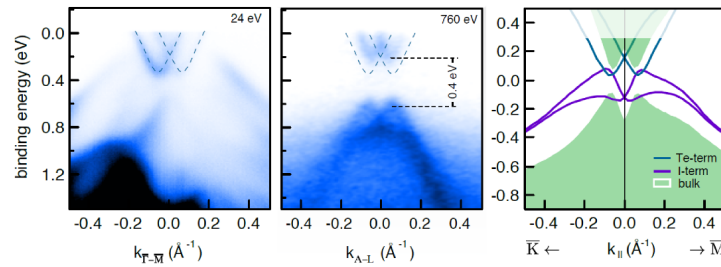


Figure 6.13: Experimental band dispersion along $\overline{\Gamma M}$ at two distinct photon energies (24 eV and 760 eV respectively in panel **a** and **b**) along with the calculated band structure **c** [209].

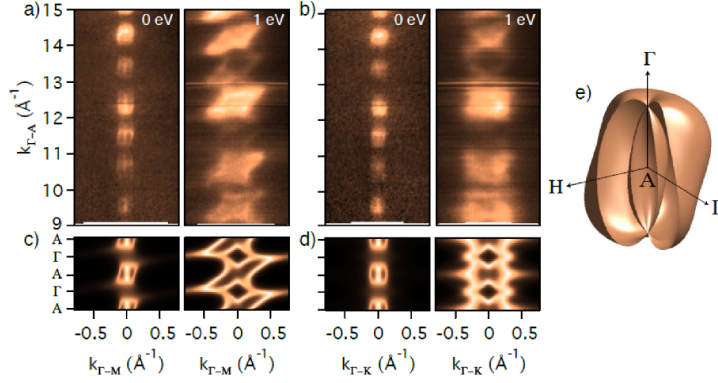


Figure 6.14: Experimental (**a** and **b**) and calculated (**c** and **d**) constant energy maps, respectively at the Fermi energy (left panel) and -1eV (right panel), for the $\langle \bar{\Gamma}M \bar{\Gamma}A \rangle$ plane (**a** and **c**) and the $\langle \bar{\Gamma}K \bar{\Gamma}A \rangle$ plane (**b** and **d**). The three dimensional Fermi surface is a torus distorted according to the trigonal crystal structure, as displayed in panel **e** [209].

study in detail the properties of the three dimensional band structure. Figure 6.14 **a** and **b** shows constant energy maps, respectively at the Fermi energy (left panel) and -1eV (right panel), for the $\langle \bar{\Gamma}M \bar{\Gamma}A \rangle$. The symmetry of the contours is well reproduced by DFT

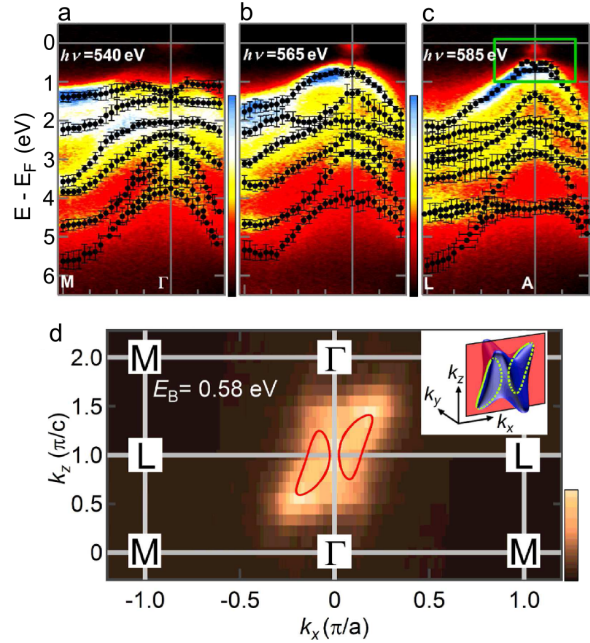


Figure 6.15: **a-c** bulk band dispersion obtained with the use of soft X-ray (540-585 eV), corresponding to $k_z = 0; 0.56\pi/c; \pi/c$. The three dimensional dispersion of the bulk conduction and valence band is resolved. The resulting three dimensional constant energy surface for the valence band (-0.58eV) is shown in panel **d** [215].

calculation, shown in panel (c) and (d). The three-dimensional Fermi surface, displayed in Figure 6.14 e, can be described as a spindle torus distorted according to the crystal structure.

A similar XARPES study was performed by Sakano *et al.* and the results are shown in Figure 6.15 a-c for three photon energies [215]. The three maps correspond respectively to $k_z = 0$; $0.56\pi/c$; π/c . The k_z dependence of the electronic properties of the material is well captured, and the spin splitting of the valence band, as well. Figure 6.15 d shows a constant energy map in the valence band (-0.58 eV) and the symmetry is in good agreement with the data displayed in Figure 6.14 a. The three-dimensional topology of an energy constant surface is schematized in the inset of panel d and it confirms the results of Landolt *et al.* [209].

These data support our picture of the simultaneous presence of bulk and surface contributions. On the other hand the hypothesis of quantized sub-bands of the conduction band due to surface band bending is in poor agreement with the measurements in the soft x-ray.

In summary we have proven the existence of two distinct families of surface states and two opposite band bendings for the two possible cleavage terminations. This offers the possibility to tune the position of the Fermi level alternatively in the conduction and valence band, offering for the first time a large Rashba spin split system with ambipolar character of the charge carriers. The possibility to grow in a controlled manner interfaces between the two terminations opens new perspective for future applications in n - p junction with spin polarized current.

Time- and Angle-Resolved Photoemission Study of the Topological Insulators Bi_2Se_3

Contents

7.1	Time- and angle-resolved photoemission	120
7.1.1	Introduction	120
7.1.2	The time dependent spectral function and Fermi-Dirac distribution .	122
7.1.3	Hot electrons and time dependent Fermi-Dirac distribution	123
7.1.4	Two-temperatures model and its extension	125
7.2	Tr-ARPES investigation of the topological insulator state	127
7.2.1	The role of topological invariants in solid state physics: the rise of topological insulators	127
7.2.2	The ground state electronic properties of bismuth chalcogenides Bi_2X_3 X = Te, Se	130
7.2.3	Previous tr-ARPES investigation of p doped Bi_2Se_3	132
7.2.4	Previous tr-ARPES investigation of Bi_2Te_3	133
7.3	Ultrafast photo-doping and effective Fermi-Dirac distribution of the Dirac particles in Bi_2Se_3	135
7.4	Supplemental Material: Ultrafast photo-doping and effective Fermi- Dirac distribution of the Dirac particles in Bi_2Se_3	141
7.4.1	1. Extracting the Fermi-Dirac distribution term from the EDC fit . .	141

Angle resolved photoemission spectroscopy represents a powerful investigation tool on the frontier of condensed matter physics, due to its unique capability to access the electronic band structure of solids. Even though this technique is anything but new, and it is well established both from the experimental and theoretical point of views, it offers still several unexplored potentialities. For example, large efforts were made, recently, to provide ARPES with larger bulk sensibility with the use of soft X-rays (400 eV- 1 keV), as briefly discussed in chapter 6. The possibility to confine gas at atmospheric pressure in a small region close to the sample opened the way to the investigation of chemical reactions and catalytical properties [216]. The study of inhomogeneous materials called for the advent of light sources with micro- and nano- metric spot size [217].

ARPES based on tabletop UV laser light, as produced by higher order harmonics of the infrared laser fundamental, constitutes an important direction of development. The low energy light (between 5.5 eV and 7 eV) translates into ultrahigh energy and angular resolutions (below 1 meV) [12] [5]. At the same time the low energy of the photo-emitted electrons offers larger bulk sensitivity [218] [219]. Moreover, at this photon energy, light can propagate through glass-based optical elements (lenses), which easily focus the UV light down to few micrometers. For our purposes, the most important characteristic of a Ti:Sapphire laser source is the possibility to generate light pulses on the femtosecond time scale (50 - 200 fs). The ultrashort pulses can be used to investigate the out-of-equilibrium electronic properties not only in the *frequency* but also in the *time* domain.

Part of my thesis project has been devoted to the development and characterization of a novel time- and angle- resolved photoemission setup, in collaboration with the T-ReX group held by Professor Fulvio Parmigiani (University of Trieste, Italy). In this chapter a very brief introduction to this novel technique is given, accompanied by our first experimental results. Owing to our interest in the electronic properties of strongly spin-orbit coupled systems, which constitute the core of this thesis, we investigated the three-dimensional topological insulator (TI), Bi_2Se_3 .

7.1 Time- and angle-resolved photoemission

7.1.1 Introduction

The working principle of tr-ARPES is that of a pump-probe stroboscope. A first femtosecond infra-red (IR) laser pulse (pump) excites the sample, while a second UV pulse (probe) extracts photoelectrons from the sample at variable delay times after the excitation. The difference in time arrival between the two beams is modified by the precise micro-metric control of the optical path of the pump (or probe) pulse. Each delay represents a snapshot on the evolution of the excitation and relaxation dynamics of the out-of-equilibrium electronic properties triggered by the pump.

The dynamical response of the material provides rich information on the interaction of the electrons with the other degrees of freedom. An ideal gas of non-interacting particles would recover the ground state after optical perturbation only in an infinite time. In reality several processes cooperate in order to restore the initial equilibrium conditions. The core of any time resolved techniques is the fact that each of this relaxation processes acts on a specific time-scale, and a sufficiently high temporal resolution allows the various processes to be disentangled.

While the advent of tr-ARPES is quite recent, time resolved optical techniques have been developed since the 1970s with the use of pico- and later femto-second lasers. Optical investigations (*i.e.* transmittivity, reflectivity, raman, photoluminescence) of materials driven out-of-equilibrium provide us with a first subdivision of the relaxation dynamics in few "regions" of the time-domain, according to the underlying physics. Figure 7.1 summarizes the excitation and relaxation processes according to their characteristic times [220].

The fastest process is the carrier excitation, which is realized within the pump pulse duration. Electrons adsorb IR photons and are excited to higher states in the conduction

band, leaving behind holes in the valence band and in the partially occupied conduction band (in the case of a metal). Absorption can be assisted by phonons, and multi-photons absorption is possible, as well. Inter-band and intra-band excitation play different roles in the case of material displaying large bandgap and this will be addressed more specifically in the study of the topological insulator Bi_2Se_3 .

The pump pulse leaves the excited electrons in a non-equilibrium state, described by a nascent electron distribution. Carrier-carrier scattering causes rapid dephasing of the coherence between excited particles, for both electrons and holes. The overall extra energy introduced in the system by the laser light is not dissipated during this second step, but electron-electron scattering only redistributes the energy among the excited particles. Therefore the electrons thermalize on a time scale of few fs, and a *hot* thermal distribution function is approached. Owing to the larger mean energy, the electronic temperature (T_e) is thus larger than the lattice temperature (T_L). The third process consists in the transfer of energy from the electronic system to the lattice via electron-phonon coupling. Depending on the magnitude of the electron-phonon coupling constant λ , this interaction has characteristic time ranging from fraction of ps up to several ps [221].

In the case of semiconductors and insulators, the fourth process is the recombination of the excited electrons with the remaining holes. Several mechanisms contribute to remove the extra charges from the conduction band: radiative processes, Auger recombination or diffusion of the excited particles out of the investigated region.

The last relaxation step involves anharmonic phonon interactions and thermal/structural effects. The system after thermalization of electrons and phonons, and after carrier equilibration, is left in a *heated* state, as achieved by conventional means. The difference, with

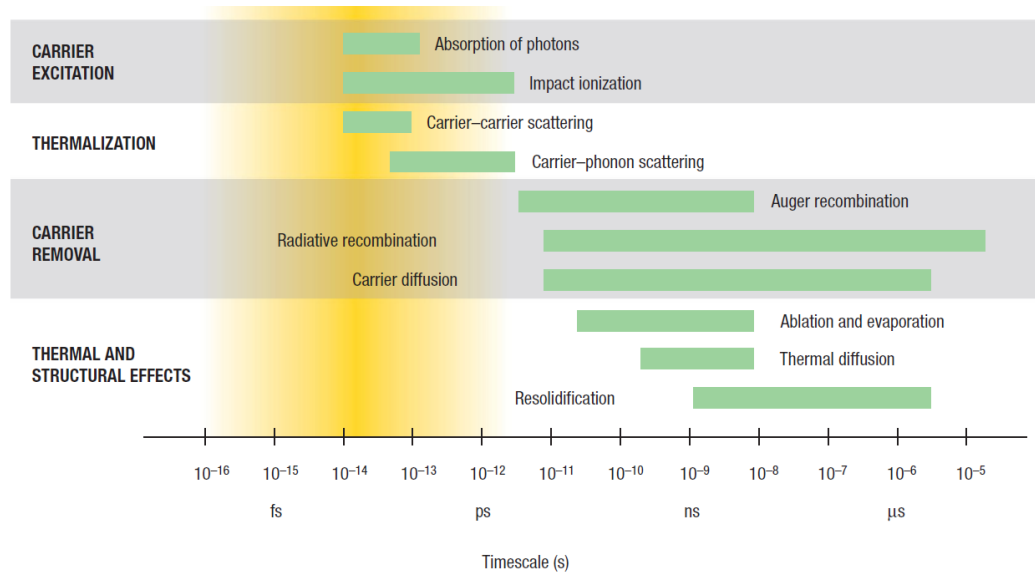


Figure 7.1: Timescales of various electron and lattice processes in laser-excited solids [220].

conventional heating, is that such high temperature is obtained in few picosecond, and the temperature can be locally higher than the melting (boiling) point: the sample may be *superheated*, and ions or clusters can leave the surface leading to ablation.

We are particularly interested in the fast dynamics [below 10 ps], involving electron-electron and electron-phonon interactions. Tr-ARPES offers, in fact, a direct insight in many-body interactions. Seminal works investigated correlations in charge density wave (CDW) materials (1T TaS₂ [222, 6], TbTe₃ [223]) and in high temperature superconductors (HTSCs) based on cuprates (BISCO [224, 225, 226, 227]) and pnictides [228] [229]. Metals constitute another large class of materials which was subject of intense tr-ARPES studies [230, 231, 232]. They represent the case study to elucidate how excited electrons thermalize, and to investigate the interplay between electron-electron and electron-phonon interactions.

In the next section a formalism is introduced to interpret tr-ARPES experiments. Then a simple introduction to the experiments performed on correlated materials is given, to show the potentiality of the technique. Larger space is devoted to the studies of metals (and semiconductors) which provide the basic tools to understand our recent results on topological insulators.

7.1.2 The time dependent spectral function and Fermi-Dirac distribution

It is of great importance to establish a direct connection between time resolved and static ARPES, in order to benefit from the theoretical models already developed for the latter. At a deep theoretical level, the ARPES spectra are interpreted in terms of the one-particle spectral function $A(E, \vec{k})$, as briefly discussed in chapter 1. In general, a photo-excited state should be described in terms of many body density matrix, where the off-diagonal terms describe optical coherence. Since coherence is lost in the first few tens of fs (below the actual time resolution of our setup), the density matrix can be assumed diagonal [233] [234]. As a consequence, the out-of-equilibrium electronic properties are described by a non-equilibrium distribution function which accounts for the evolution of the diagonal elements at the different delay times [6, 219]. In this approximation, time and energy are disentangled and the electronic states are described in the energy domains, whereas the relaxation of these distributions, due for example to electron-phonon coupling, is described in the time domain.

The tr-APRES spectra are proportional to $A(E, \vec{k}, t) \cdot f(E, t)$, where A is the one particle spectral function, t is the delay time and f is an effective *hot* thermal distribution function. The transient spectral function contains many fine details about the modification of the photo-hole lifetime and about the change in the many-body correlations during the relaxation processes. Unfortunately the low energy and angular resolution of conventional tr-ARPES setups based on time-of-flight spectrometers forbade such thorough investigation [224]. Only the recent use of high resolution hemispherical analyzers in pump-probe experiments opened the way to this kind of study, as shown in Figure 7.2 for the case of the HTSC $\text{Bi}_2\text{Sr}_2\text{CaCu}_2\text{O}_{8+\delta}$ [226, 227]). Panel **a** and **b** show the modification of the spectral weight of the nodal quasiparticle (QP) peak respectively below and above the critical temperature $T_c = 91\text{K}$. The suppression of spectral weight after optical excitation is strongly

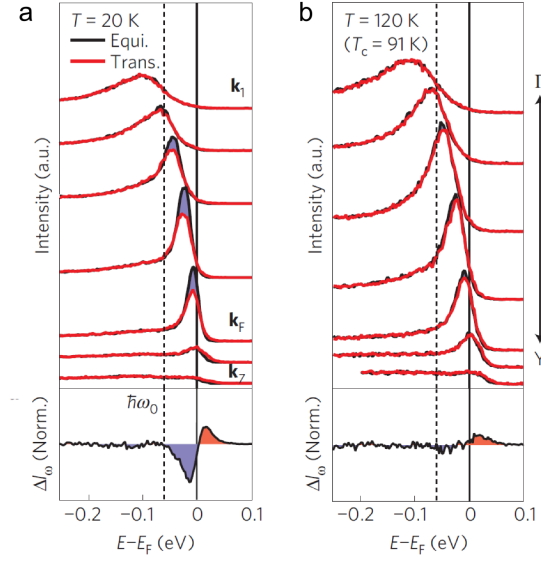


Figure 7.2: Stack of EDCs below (a) and above (b) transition temperature in $\text{Bi}_2\text{Sr}_2\text{CaCu}_2\text{O}_{8+\delta}$ at the nodal quasiparticle peak. Black (red) lines display the behavior of the system before (after) optical perturbation. The suppression of spectral weight is strongly enhanced in the superconducting state, thus evidencing a connection between the nodal QP and superconductivity [226].

enhanced in the superconducting state. This strongly modifies the static ARPES picture of nodal QP almost indifferent to superconductivity [226].

Apart from these correlation effects, the one-particle spectral function contains the information on the bare band structure of the compound, and ultrashort laser pulses are found to strongly modify also the band dispersion. In the case of correlated insulators, such as CDW materials [223] and Mott-Hubbard insulators [222, 6, 235], the gap can be partially filled and an insulator-to-metal phase transition is photoinduced. Photoinduced bandgap collapse occurs also in GaAs [236], even though no tr-ARPES investigation are available.

For what concerns the occupation function, most of the experimental studies investigated the modification of the Fermi-Dirac (FD) distribution in simple and correlated metals [230, 231, 232, 224]. In particular, if the electron-electron scattering which mediates the electron thermalization is fast, a *hot* FD distribution may be built before electrons transfer their excess energy to the lattice. Such approximation is at the base of the two-temperatures model [221], which is the subject of the next section.

7.1.3 Hot electrons and time dependent Fermi-Dirac distribution

In a metal the phase space available for an electron to adsorb a photon and being promoted to the empty states in the conduction band is large. Also in the de-excitation, several scattering channels are accessible and the absence of a bandgap makes the relaxation much faster with respect to insulators. In the following we describe the application of tr-ARPES

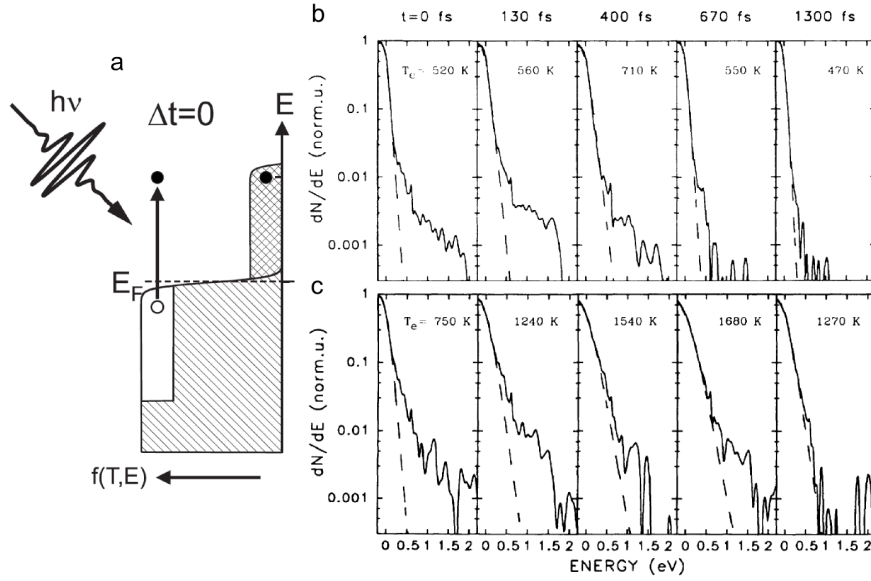


Figure 7.3: **a** Illustration of the nascent electron distribution directly after optical excitation of a metal with an ultra-short laser pulse ($t = 0 \text{ fs}$) [231]. **b** and **c** show the evolution of the electronic distribution in polycrystalline gold, after optical excitation at two different pump fluences ($120 \mu\text{J}/\text{cm}^2$ and $300 \mu\text{J}/\text{cm}^2$). Dashed lines represent the best fit with a Fermi-Dirac distribution, whose effective temperature is reported above. The fraction of electron above FD constitutes the non-thermal electrons, which redistribute their energy among the electronic bath through electron-electron scattering. The complete thermalization of the electrons required several hundreds of fs and the characteristic time depends inversely on the pump fluence [230].

to the study of simple metals.

Polycrystalline thin gold films were among the first systems investigated by tr-ARPES [230]. After optical excitation the electrons above the Fermi level are described by a nascent electron distribution which deviates from a thermal FD function, as schematically illustrated in Figure 7.3 **a**. Figure 7.3 **b** and **c** show the evolution of the electron distribution at different delay times for two pump fluences ($120 \mu\text{J}/\text{cm}^2$ and $300 \mu\text{J}/\text{cm}^2$). A logarithmic scale is adopted and dashed lines indicated the best FD fit. At time $t = 0 \text{ fs}$ a flat distribution is observed up to 1.84 eV above E_F , corresponding to the energy of the pump pulse. As time increases, the fraction of non-thermal electrons above the FD distribution decreases and the effective temperature increases. It reaches a maximum of 710 K (1680 K) after 400 fs in the low (high) perturbation regime [230].

The time required to reach a complete thermalization of the photo-excited electrons is shorter at larger pump fluences. This depends on the fact that thermalization is built up by electron-electron scattering, and the larger extra- energy (at $300 \mu\text{J}/\text{cm}^2$) makes available more hot-electrons at higher energies for scattering. The energy relaxation in metals is described by the Fermi liquid theory and it scales as $(E - E_F)^2$. In particular, in the

random-phase approximation (RPA) the lifetime τ of an excited electron is

$$\tau = \tau_0 \frac{E_F^2}{\delta E^2} \quad (7.1)$$

where τ_0 is a constant inversely proportional to the plasma frequency, and δE indicates the phase space of available initial and final states [230]. Within this simple model a characteristic life time of almost 1 ps is obtained for the case of Au, in good agreement with the experimental data.

Thermalization on the timescale of 1 ps is signature of weak electronic correlation, and it requires to deal with electron-electron and electro-phonon couplings at the same level of approximation. To some extents, simple metals represent a complicate case in which the energy thermalization within the electronic bath is not complete before the energy relaxation to the lattice starts. Therefore the simple two-temperatures model does not provide always a complete description of the non-equilibrium system. Despite the limitation of the model, several studies on metals (Gd(0001) [232], Ru(001) [231]) successfully interpreted the data in the framework of the two-temperatures model.

7.1.4 Two-temperatures model and its extension

The two-temperatures model is based on the assumption that the electron-electron scattering which mediates the electron thermalization is fast, and a *hot* FD distribution is built before electrons transfer their excess energy to the lattice. The electrons reach an effective temperature T_e much higher than the lattice one, T_L [221].

A set of rate equations can be introduced to described the transfer of energy among electrons and phonons, and the rate depends on the electron-phonon coupling constant λ , which can be expressed as the second moment of the Eliashberg function $\alpha^2 F(\omega)$, $\lambda \langle \omega^2 \rangle = 2 \int_0^\infty (\alpha^2 F(\omega) \omega) d\omega$ [221]. Several other physical quantities are present in the model, such as the specific heat of the electrons and of the lattice. If some guesses are possible for these values, or if complementary experiments can provide this information, the system of rate equations gives direct access to the momentum averaged electron-phonon coupling.

The quantity $\lambda \langle \omega^2 \rangle$ is of great importance in the study of superconductors, because it plays an important role in defining the transition temperature T_c . No other experimental technique can directly probe $\lambda \langle \omega^2 \rangle$, and few experiments are capable to separate electron-phonon coupling from other effects. For this reason tr-ARPES, and more in general time-resolved techniques, were used to examine the formation and successive relaxation of hot electrons in high temperature superconductors, where the role played by phonons in the formation of the Cooper pair is still questioned [237, 9]. In particular, the analysis of the one-particle spectral function in ARPES provides a measure of the coupling between electrons and all the boson modes, without the possibility to disentangle the phonon contribution from the magnetic one (spin excitation) [5]. The direct access to the evolution of the time-dependent electronic temperature $T_e(t)$ makes tr-ARPES the ideal tool to solve this controversy [224]. Moreover the momentum resolution of tr-ARPES provides a precise evaluation of the relaxation mechanism at different position in the Brillouin Zone, thus enabling to explore the difference between nodal and anti-nodal quasi particles, as well [225, 227].

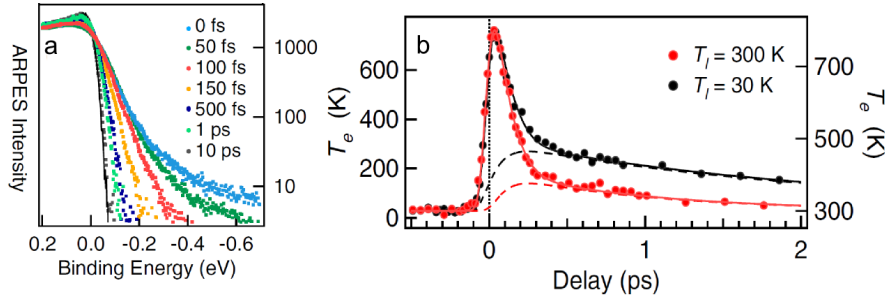


Figure 7.4: **a** set of EDCs of the nodal QP at different delays after optical perturbation of the cuprate HTSC $\text{Bi}_2\text{Sr}_2\text{CaCu}_2\text{O}_{8+\delta}$. The effective temperature obtained from the FD fit is reported in panel **a**, for two sample temperatures. The fast decay of T_e is followed by a very slow relaxation. Such bottleneck is interpreted by enlarging the two-temperature model to account for strongly and weakly coupled phonon modes [224].

Figure 7.4 **a** displays a set of EDCs of the nodal QP at different delays after optical perturbation of the cuprate HTSC $\text{Bi}_2\text{Sr}_2\text{CaCu}_2\text{O}_{8+\delta}$ [224]. After 100 fs the fraction of electrons non-thermalized has approached zero, thus confirming that in the case of strong electronic correlation the two temperatures model is a good starting point to describe the excited system. Panel **b** shows the evolution of T_e as obtained from the FD fit. Its relaxation cannot be described with the use of one single decaying exponential, because after a fast drop within the first 100 fs , T_e reaches a plateau, signature of a bottleneck in the de-excitation process. Two distinct timescales are found, which are interpreted in the frame of an extended two temperatures model, called three temperature model. The phonon contribution is split into two parts. Some phonon modes are strongly coupled to the electronic bath, thus resulting in a fast reduction in the electronic energy. The coupling to the remaining phonons is weaker, and it explains the bottleneck in the T_e relaxation. The three-temperature model was recently adopted also to interpret the evolution of the effective temperature in a different family of high temperature superconductors, the 122 pnictides ($\text{Ba}/\text{EuFe}_2\text{As}_2$) [229].

7.2 Tr-ARPES investigation of the topological insulator state

7.2.1 The role of topological invariants in solid state physics: the rise of topological insulators

The concept of 3-dimensional topological insulator was briefly introduced in chapter 2, where the band inversion mechanism is described in the case of $\text{Bi}_{1-x}\text{Sb}_x$. Hereafter, the origins of this novel state of quantum matter are discussed more in detail.

The definition of topological insulators has deep roots in theoretical physics. Commonly the symmetry of the Hamiltonian defines the ground state properties. This assumption is not consistent with the observation of the Quantum Hall effect (QH), proposed theoretically in the 1974 [238] and successively verified in the 1980 by Klaus von Klitzing [239], who was awarded the 1985 Nobel prize. The QH state consists in a two-dimensional insulating system in which, at low temperature under the effect of high magnetic fields, the Hall conductivity assumes only value multiple of the quanta $\sigma = \nu e^2/h$. The origin of the quantization was described in term of gauge invariance by Laughlin [240]. Halperin successively generalized the annular model proposed by Laughlin and found that under strong magnetic field the Landau levels form delocalized extended states at the perimeter of the sample [241]. These edge-states carry current with opposite chiralities, and they cannot be localized by disorder.

In general, we are used to describe an insulator as a material with an energy bandgap, but such definition is not satisfactory in the case of the QH conductance at the edge states. As proposed by Fu and Kane, following the model of Kohn [242], an insulator can be defined as a system in which the electronic properties are *local* and not affected by boundary effects [78]. Following this definition, in a closed system, such as the annulus modelled by Laughlin, the sensitivity to the magnetic field threading the hole should be exponentially small. This is true in the simple atomic insulator, and similarly in the ionic and covalent insulators, whose Hamiltonians can be transformed adiabatically into each other without any modification of the ground state (*i.e.* a phase transition). The QH state does not share

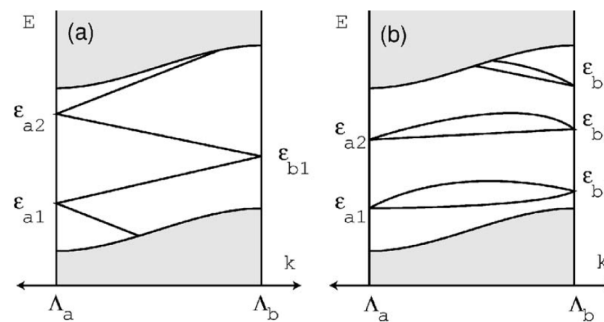


Figure 7.5: Effect of the Kramers theorem in trivial and topological insulator with spin split surface states. At the TRIM two states with opposite spins are degenerate, but in the first case when moving between two TRIM the couple is modified. In the second case it is conserved [78].

the same property of *locality* and it belongs to a different class of insulators.

The concept of adiabatic transformation of the Hamiltonian $\hat{H}(t)$ is connected to the concept of Berry's phase [243]. The atomic insulator and the QH state are topologically distinct, because their Hamiltonians cannot be connected by an adiabatic transformation. The QH state is thus identified by an integer number, the TKNN number [244], which represents the topological invariant which distinguishes this state of matter from conventional insulators. The concept of QH state can be also generalized to higher dimension (3) where the topology is described by a set of three integer numbers [245].

The stability of the edge states in the presence of disorder motivated several studies, with the aim to "free" the QH state from the constraints of low temperature and high magnetic field. A special state of matter was proposed to exist preserving the time-reversal symmetry but with the special requirement of strong spin-orbit coupling [246], the Quantum Spin Hall state (QSH). The QSH state was later experimentally confirmed in HgTe/HgCdTe quantum wells [247]. QSH insulators have similar, although distinct, non trivial topological properties as the QH insulators. QSH insulators are invariant under time-reversal symmetry, they show a bulk gap, but gapless edge states are found in the bulk gap. Owing to strong spin-orbit coupling the edge states are not spin-degenerate, and the edge chirality is substituted by the spin helicity: two states with opposite spin counterpropagate at a given edge [248, 249, 250]. For this reason back-scattering on a non-magnetic impurity is forbidden and perfect one-dimensional transport is observed [247]. Therefore, in the QSH insulator the edge states are spin filtered, and QSH systems are the ideal candidates for spintronics and quantum computing.

This quantum phase of matter is distinguished from a trivial insulator by a single Z_2 topological invariant [248]. The Kramers' doublets constituted by the helical edge states must cross at some special points of the Brillouin zone, the so-called time-reversal invariant momenta (TRIM), similarly to the case of the surface states described by the Rashba-Bychkov model (see chapter 2).

Topological insulators are the 3-dimensional analogous of the 2-dimensional QSH insulator. In topological insulators the 1-dimensional gapless edge states are substituted by metallic spin-polarized surface states lying in the bulk bandgap. The single Z_2 invariant is replaced by four distinct Z_2 numbers [78]. Three of these ($\nu_{1,2,3}$) rely on the translational symmetry and only the fourth (ν_0) is robust in the presence of disorder and it characterizes the "strong topological insulator phase" [77].

Under inversion symmetry, the evaluation of the Z_2 invariants can be simplified by introducing the parity invariants $\delta(\Gamma_i)$ defined as

$$\delta(\Gamma_i) = \prod_n \xi_{2n}(\Gamma_i) \quad (7.2)$$

where ξ is the parity of the occupied bands at Γ_i , one of the eight *bulk* TRIM [251]. Each of this parity invariants is a topological invariant, and the only way to modify the value of $\delta(\Gamma_i)$ is to close the gap at that TRIM (with ν_0 defined as the product of all the $\delta(\Gamma_i)$). Similarly a second important class of topological invariants can be introduced, the surface fermion parity $\pi(\Lambda_a)$

$$\pi(\Lambda_a) = (-1)^n \delta(\Gamma_{a1}) \delta(\Gamma_{a2}) \quad (7.3)$$

where Λ_a is a *surface* TRIM, which results from the projection of the two Γ_{a1} and Γ_{a2} *bulk* TRIM, and n accounts for the number of Kramers pairs. The product between $\pi(\Lambda_a)$ and $\pi(\Lambda_b)$ defines the parity of the number of crossing at E_F when moving along the $\Lambda_a\Lambda_b$ direction. In the case of trivial insulators this product is always equal to $+1$, indicating an even number of crossing. Whereas, in TIs this product assumes (somewhere) -1 value, thus guaranteeing an odd number of gapless surface states [251].

Such difference between trivial and topological insulators is illustrated in Figure 7.5. At each *surface* TRIM (Λ_a and Λ_b) two states with opposite spin must be degenerate to fulfil the Kramers theorem. But in the case of a TI, when moving from the first TRI point to the second, the couple of states is modified, while in the trivial case it is conserved. Such effect is called band parter switching and it originates from the change in surface fermion parity between the two TRIM [78]. Therefore the existence of the metallic states at the surface is required by the bulk band structure and by the parity invariants. Finally, the surface states result topologically protected by time reversal symmetry when a topological

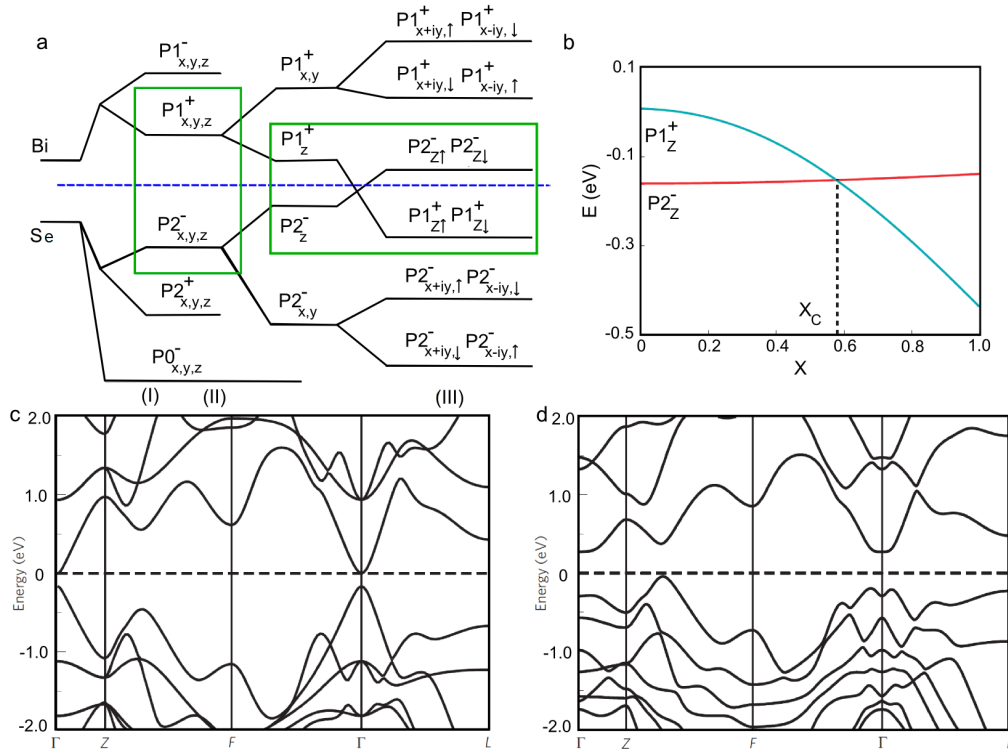


Figure 7.6: **a** energy ordering of the p orbitals for Bi and Se, after formation of the chemical bonds (I), crystal potential (II) and finally spin-orbit coupling (III). SOC is responsible for the band inversion at the Γ point, and the behavior of the gap is studied as a function of the rescaled SOC (x) in **b**. **c** and **d** show the calculated bulk band structure without and with SOC. In the latter a clear evidence of anti-crossing behavior is visible between the valence and conduction band at Γ [252].

insulator with $Z_2 = -1$ is joined to a trivial insulator with $Z_2 = 1$, namely at the interface normally provided by *vacuum* [253].

7.2.2 The ground state electronic properties of bismuth chalcogenides Bi_2X_3 $\text{X} = \text{Te}, \text{Se}$

The criteria developed by Fu and Kane to evaluate the topological class under inversion symmetry suggests some simple principles to identify potential TIs [78]. A good candidate is an insulator, or a semiconductor, in which the conduction and the valence band have opposite parities and a band inversion is introduced at some TRIM because of the large spin-orbit coupling, thus requiring atoms with large atomic number Z . The search for materials with these properties brought to the discover of the second generation of topological insulators, constituted by the bismuth chalcogenides Bi_2X_3 $\text{X} = \text{Te}, \text{Se}$ and by Sb_2Te_3 [252].

The important role played by the atomic spin-orbit coupling is evidenced in Figure 7.6 a [252], reporting the energy ordering of the p orbitals for Bi and Se. The scheme is constituted by three parts. In (I) the levels are modified by the formation of chemical bonds. Successively (II) the presence of the crystal field separates the components according to the x, y, z character. Only the SOC (III) inverts the ordering of the $P2^-$ and $P1^+$ states at the Fermi level. In particular, such band inversion is studied as a function of the rescaled

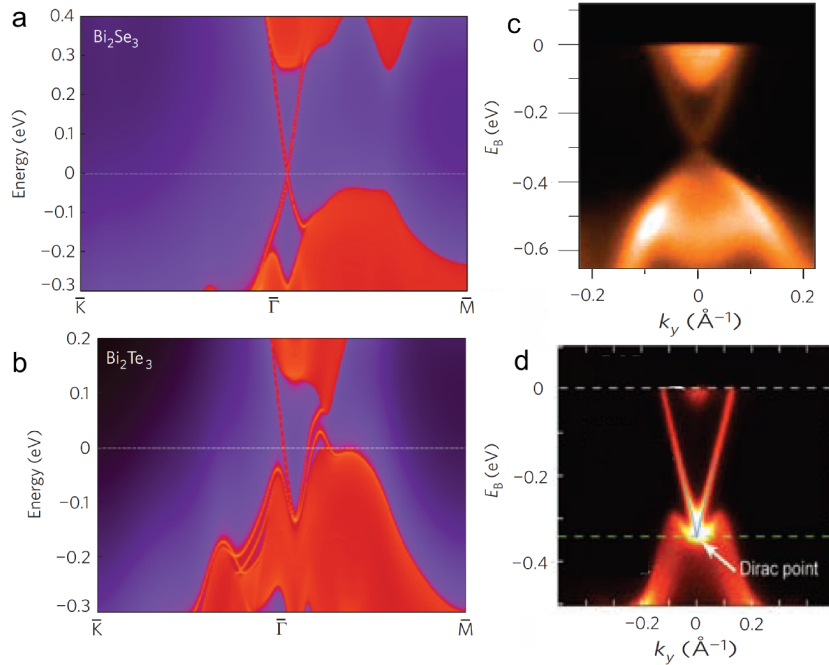


Figure 7.7: **a** and **b** calculated band structure in slab approximation revealing the nature of the surface states of two different topological insulators: Bi_2Se_3 and Bi_2Te_3 [252]. Panel **c** and **d** report the respective measured band dispersion from [254] and [255].

atomic SOC of Bi $\lambda = x\lambda_0$, Figure 7.6 **b** shows that the crossing of the states with opposite parities occurs for $x = 0.6$. In the case of $\text{Bi}_{1-x}\text{Sb}_x$ the parity inversion is instead studied as a function of the x concentration (see Figure 2.13) [11].

Figure 7.6 **c** and **d** show the calculated bulk band structure without and with the effect of SOC. In particular the m -like shape of the valence band at the $\bar{\Gamma}$ point in the presence of SOC reflects the anti-crossing between the inverted bands. In particular the parity is *only* changed at $\bar{\Gamma}$ thus resulting in the transition from trivial to non-trivial topology, with $Z_2 = -1$ [252].

The existence of surface states in Bi_2Se_3 is confirmed by *ab initio* slab calculations, whose results are shown in Figure 7.7 **a** along with the results for Bi_2Te_3 (**b**), for which a similar analysis is also valid. In these materials the surface states form a single Dirac cone, *i. e.* a band with linear dispersion, connecting the valence and the conduction bands [252]. Nowadays, the Dirac states are subject of intense tr-ARPES studies. Therefore, it is of particular importance to give a reference for the low energy electronic properties, as measured with high resolution conventional ARPES setup. Figure 7.7 **c** and **d** show the experimental band dispersion of the Dirac particle respectively in Bi_2Se_3 and in Bi_2Te_3 along the $\bar{\Gamma}\bar{K}$ high symmetry directions [254, 255]. The broad unstructured intensity within the Dirac cone is the projected bulk conduction band. At the surface all these materials are slightly n -doped due to vacancies and to Se (Te) excess, and only chemical doping (by substitution with Sn, for example, [255]) reestablishes the insulating phase. ARPES photon energy dependent studies evidenced the k_z dispersion of the valence and conduction bands, whereas the Dirac particle is found to be only modulated in intensity, due to strong matrix element effect [254, 257].

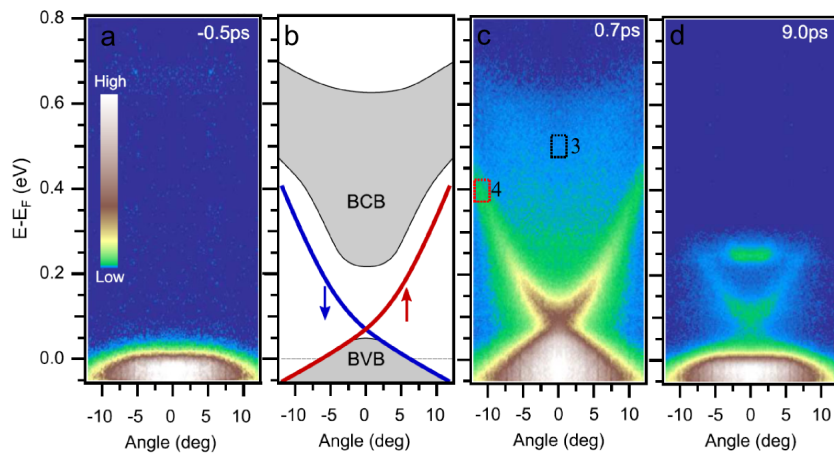


Figure 7.8: **b** cartoon of the band structure of p doped Bi_2Se_3 . **a**, **c** and **d** show the measured band dispersion at three time delays, both before perturbation (-200fs) and after (0.7ps and 9ps) [256].

7.2.3 Previous tr-ARPES investigation of p doped Bi_2Se_3

Single crystals of slightly p doped Bi_2Se_3 (Mg doped) were investigated by time- and angle- resolved photoemission spectroscopy [256]. The first harmonic (1.5 eV) of a high-repetition amplifier (80 MHz) was used to excite the system (fluence = $26 \mu\text{J}/\text{cm}^2$), which was subsequently probed by the fourth harmonic at 6 eV.

The band dispersion before the arrival of the pump pulse is shown in Figure 7.8 **a** along with a schematic of the band structure (**b**). A Fermi-Dirac distribution describes the step at E_F , and the large intensity observed at negative energy is related to the occupied valence band. At positive delay times (**c** and **d**) the Dirac state and the conduction band are populated, and for both the maximum population is reached after 0.7 ps. This delay suggests that electrons are not directly excited in these states, which are rather filled by electrons scattered from higher energy states [256].

This model is schematized in Figure 7.9 **a-d**. An optical inter-band transition excites electrons from the valence band to high energy branches of the unoccupied conduction

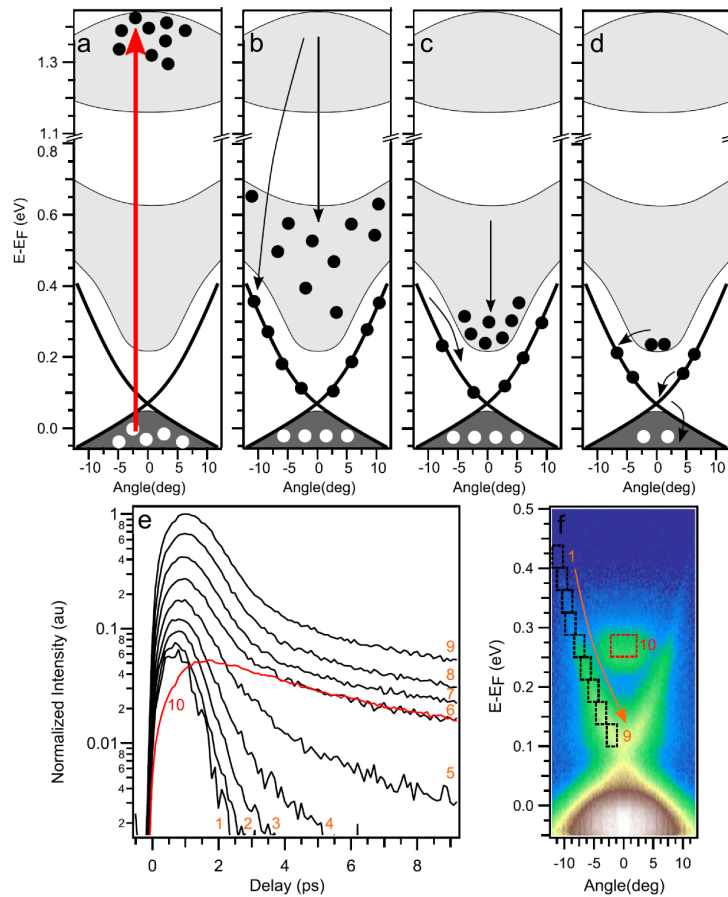


Figure 7.9: **a-d** sketch of the excitation-relaxation mechanism proposed for p doped Bi_2Se_3 . A cascade process explains the delayed population of the bottom part of the conduction band. This is proposed to act as a charge reservoir for the surface state [256].

band. Intra-band scattering accounts for the finite time required to populate the bottom of the lower branch. At the same time, electrons from the conduction band can recombine with the holes in the valence band via the Dirac state [256]. The magnitude of the gap (200 meV) prevents electron-hole recombination via phonons, since the largest energy mode has approximately 23 meV [256]. The recombination is thus proposed to be realized via diffusion, and partially via dissipation along the surface state. The small phase space available for scattering slows down the latter process. The slow relaxation across the gap, which is typical of semiconductors [258], leaves the sample with a modified electron density in the conduction band.

The conduction band is proposed to act as a charge reservoir for the Dirac state. This is described in Figure 7.9 e, which shows the intensity as a function of the delay times, as obtained from the integral over small (E, \vec{k}) regions (as shown in panel f) [256]. The dynamics is fast at large binding energy, and it slows down when approaching the Fermi level. Such effect is proposed to be solely due to the photodoping of the conduction band. The cascade mechanism succeeds in explaining the delayed population in the surface state, but it cannot account for the variation in relaxation times for the various regions below the conduction band, which should all present the same dynamics.

7.2.4 Previous tr-ARPES investigation of Bi_2Te_3

The dependence between the relaxation time and the position in the electronic band structure was independently verified also in a different TI, Bi_2Te_3 [259]. Figure 7.10 a and b show a schematization of the low energy electronic properties, along with the measured unperturbed band structure at negative delay times (-200 fs). Four regions are outlined: two correspond to the surface state above (S^*) and below (S) the Fermi level. The remaining two contain large part of the conduction band, divided in the low branch (B_2^*) and in the upper branch (B_1^*) [259]. Contrary to the previous study, this compound is slightly *n* doped and the bottom of the conduction band lie below E_F .

Figure 7.10 c shows the temporal evolution of the four populations (S , S^* , B_1^* and B_2^*), after optical excitation with the laser fundamental at 1.58 eV with fluence equal to $150 \mu\text{J}/\text{cm}^2$. The upper part of the conduction band has a fast dynamics, while the intensity persists much longer in the surface state. It was proposed that this effect is due to the charge reservoir role played by the bottom of the conduction band (B_2^*), which is also found to relax slowly [259].

In order to be more quantitative, a complex system of rate equations is introduced to described the de-excitation. Several channels are considered: B_1^* is directly populated by the pulse and the excess electrons decay in B_2^* and in S^* (in approximately 0.34 ps). Successively, the electrons in these two states relax with similar characteristic times (1.8 ps for B_2^* and 2.1 ps for S^*). The photo-holes in S recombine both with the conduction band and with the excited surface states, with two distinct relaxation times (0.14 ps and 5.7 ps). The model provides the functions used in the fitting routine, whose best results are shown in Figure 7.10 c as continuous line [259]. Different terms account for the direct population of B_2^* and S^* , besides the cascade mechanism proposed in the case of *p* doped Bi_2Se_3 . Even though the model provides remarkable agreement with the data, it contains

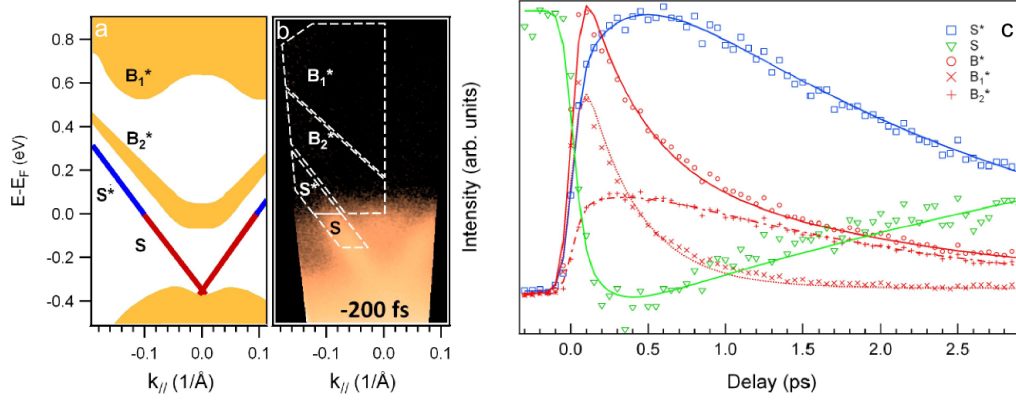


Figure 7.10: schematization (a) of the band structure of Bi_2Te_3 along the $\Gamma\bar{K}$ direction, and measured dispersion at 6.32 eV (b). Four regions are enlightened and the behavior of the associated intensity is shown in c as a function of the time delay. The fits (continuous lines) are performed with a functions obtained from a system of rate equation [259].

several independent parameters, and no connection is established, for example, between the relaxation time of the excited electrons and holes, thus suggesting that the recombination is due to physically different processes. In addition, the surface state and the two branches of the conduction band are treated as a unique. Hence, the excited electrons in each band should have similar relaxation dynamics, since no term in the model takes into account their energy position. On the contrary, we observed experimentally that the dynamics strongly depends on the energy position. In the next section I present our recent tr-ARPES data as published in Physical Review B [260].

7.3 Ultrafast photo-doping and effective Fermi-Dirac distribution of the Dirac particles in Bi_2Se_3

We exploit time- and angle- resolved photoemission spectroscopy to determine the evolution of the out-of-equilibrium electronic structure of the topological insulator Bi_2Se_3 . The response of the Fermi-Dirac distribution to ultrashort IR laser pulses has been studied by modelling the dynamics of the *hot* electrons after optical excitation. We disentangle a large increase of the effective temperature (T^*) from a shift of the chemical potential (μ^*), which is consequence of the ultrafast photodoping of the conduction band. The relaxation dynamics of T^* and μ^* are k -independent and these two quantities uniquely define the evolution of the excited charge population. We observe that the energy dependence of the non-equilibrium charge population is solely determined by the analytical form of the effective Fermi-Dirac distribution.

The recent discovery of topological insulators (TIs) is renewing the attention on the effects of spin orbit interactions (SOI) in solids, paving the road for the emergence of new quantum states of matter [11, 254, 255, 261, 262, 257, 263, 77, 252]. The SOI acquires particular relevance in the case of systems containing high-Z elements, leading to the lifting of the Kramers spin-degeneracy in broken inversion symmetry systems, as described by Rashba [46, 48, 205], Dresselhaus [47] and Rashba-Bychkov [45, 10]. Therefore, understanding the consequence of SOI is of primary importance also for future technological applications in spintronics.

TIs are band insulators (semiconductors) where the conduction and the valence band states have opposite parities and their energy ordering is inverted by the SOI [77, 78]. The most prominent feature of their electronic structure is the odd number of spin polarized Dirac cones at the surface, connecting the opposite sides of the bulk band gap, resulting in topological protection from backscattering [263]. Several classes of TIs ($\text{Bi}_x\text{Sb}_{1-x}$ [11], Bi_2Se_3 [254], Bi_2Te_3 [255], TlBiSe_2 [264, 265], Ternary Heusler compounds [261] and Pb based TIs [262, 266]) have been discovered. Among these, Bi_2Se_3 represents a paradigmatic case, owing to the simplicity of its band structure characterized by a single Dirac cone [254, 252].

In this Letter we report on the study of the out-of-equilibrium electronic properties of Bi_2Se_3 , investigated by time- and angle- resolved photoemission spectroscopy (tr-ARPES). Although conventional ARPES, with its surface sensitivity, has proven to be effective and rich of information [11, 255, 257], the combined use of ultrashort laser pulses and angle-resolved photoemission experiments offers the unique possibility to explore the dynamical evolution of the charge carriers after an optical excitation, opening the door to the investigation of mechanisms and states hidden to experiments in the frequency domain. After optical excitation, electrons thermalize on a short timescale owing to the fast electron-electron interaction. The resulting *hot* electron gas is described by a Fermi-Dirac distribution with an effective electronic temperature $T^*(t)$ and an effective chemical potential $\mu^*(t)$ [221, 224]. From the analysis of the temporal evolution of the Fermi-Dirac function at the Fermi wave-vector k_F , we succeed in disentangling the large increase of T^* from the ultrafast shift in the chemical potential, $\Delta\mu^*$.

Our experiment reveals that the dynamics of the non-equilibrium excited electron and hole populations strongly varies with the kinetic energy and the wave-vector (E , k). We develop a model based on the exponential relaxation of $T^*(t)$ and $\mu^*(t)$ in the Fermi-Dirac function to quantitatively fit the measured dynamics. We find that the relaxation times of $T^*(t)$ and $\mu^*(t)$ are k -independent. The energy dependence of the charge population is then uniquely determined by the analytical form of the Fermi-Dirac distribution. Our model, owing to the universal properties of the Fermi-Dirac function, is more generally applicable to other tr-ARPES experiments on similar materials.

High quality single crystals of Bi_2Se_3 , in the form of platelets, were grown by the Bridgman technique. The Bi_2Se_3 samples are n-doped due to atomic vacancies and excess selenium [254]. The tr-ARPES experiments were performed at the T-ReX laboratory, Elettra (Trieste), with the use of a commercial Ti:Sa regenerative amplifier (Coherent RegA 9050), producing 800 nm (1.55 eV) laser pulses at 250 kHz repetition rate, with temporal duration of 60 fs. The samples were mounted on a He cryostat held at 100 K, and cleaved *in situ* in ultrahigh vacuum ($2 \cdot 10^{-10}$ mbar) at room temperature. The pump laser light was p -polarized, and the absorbed pump fluence was equal to $210 \mu\text{J}/\text{cm}^2$. The delay between pump and probe was introduced by modifying the optical path of the pump. Electrons were photoemitted by the s -polarized fourth harmonic at 6.2 eV, obtained by harmonic genera-

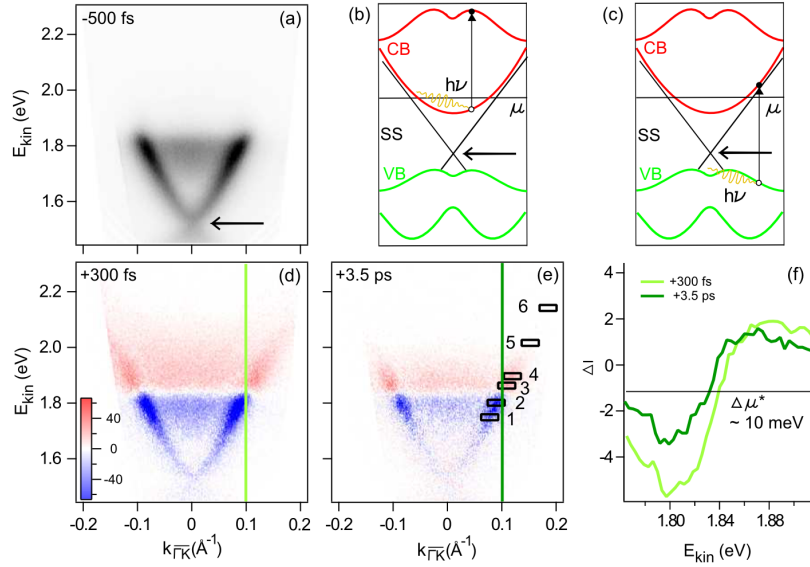


Figure 7.11: (a) ARPES band dispersion of Bi_2Se_3 at negative delay time along the ΓK high symmetry direction. (b) and (c) schematization of inter-band excitation channels between the conduction-conduction band (CB-CB) (b), and between the valence-conduction bands (VB-CB) (c). (d) and (e) Pump-probe tr-ARPES signal obtained as the difference between the images at positive delays (300 fs and 3.5 ps) and negative delay (-500 fs). Red (blue) represents an increase (decrease) of the spectral weight. (f) Pump-probe difference EDCs at the Fermi wave-vector $k_F = 0.1 \text{ \AA}^{-1}$, cut from panels (d) and (e). A shift of the chemical potential, $\Delta\mu^*$, is experimentally resolved.

tion in phase-matched BBO crystals. The photo-electrons were analyzed and detected by a SPECS Phoibos 225 hemispherical spectrometer, with energy and angular resolution set respectively equal to 10 meV and 0.3°, equivalent to 0.005 Å⁻¹. The overall temporal resolution was set to 300 fs, thus preserving the very high energy resolution required by the present experiment.

Figure 7.11 (a) illustrates the band dispersion of Bi₂Se₃ at negative delay time, *i.e.* before the arrival of the pump pulse (-500 fs), along the $\bar{\Gamma}\bar{K}$ high symmetry direction. The energy scale reports the measured kinetic energy, since the chemical potential μ does not represent a good reference for the energy scale in the present experiment, as will be discussed in detail in the following. The linearly-dispersing topological surface state is clearly resolved. A black arrow points towards its apex, *i.e.* the Dirac point. The weaker signal within the Dirac cone at 1.7 - 1.84 eV corresponds to the bottom of the conduction band. These observations are consistent with previous ARPES results from conventional UV sources [254, 257].

The intense pump pulses cause charge excitations between the occupied and unoccupied parts of the conduction band (Fig. 7.11 (b)), similarly to what observed in metals (CB-CB transitions) [230, 231]. In the present case, the photon energy is larger than the band gap and this enables also inter-band excitations across the gap, from the fully occupied valence band (VB) to the partially unoccupied conduction band (CB) (VB-CB transitions) (Fig. 7.11 (c)). Figure 7.11 (d) and (e) show the pump-probe signal obtained as the difference between the ARPES images after and before the optical perturbation. Red (blue) represents an increase (decrease) of the spectral weight. At short delay time (+300 fs) a large density of electrons populates the surface state and the conduction band above the chemical potential. Such electrons result from intra- and inter- band transitions across the bandgap. However, the temporal resolution in this experiment is not sufficient to capture the formation of the nascent non-equilibrium electron distribution, which is expected to thermalize into a *hot* Fermi-Dirac distribution via electron-electron interaction, with a characteristic time shorter than 40 fs [267]. Figure 7.11 (e) illustrates the reduction in the pump-probe signal at larger delay times (+3.5 ps). The density of excited charge carriers is reduced, as normally observed in metals [230, 231].

Despite this similarity, we also observe a deviation from a purely metallic response. Such difference is well captured by a close inspection in the pump-probe difference energy distribution curves (dEDCs) at the Fermi wave-vector $k_F = 0.1 \text{ Å}^{-1}$ for various delay times. Figure 7.11 (f) shows the two pump-probe dEDCs at +300 fs and +3.5 ps. We focus our attention on the zero-crossing point, which separates the charge-depletion and the charge-accumulation regions. The zero-crossing point clearly shifts more than 10 meV. We propose that the modification of the zero-crossing energy can be explained by an ultrafast shift of the chemical potential, as recently reported in Bi₂Se₃ also by Wang *et al.* [268]. We interpret such an effect as the consequence of the photo-doping resulting from the inter-band excitations across the gap. In the case of a non-degenerate semiconductor (*i.e.* μ lying in the band gap) the optically excited electrons and holes must be considered as separated systems, each with a distinct thermal distribution, and with a different chemical potential depending on the charge density [258]. The thermalized electron and hole distributions relax towards equilibrium via radiative processes, Auger recombination

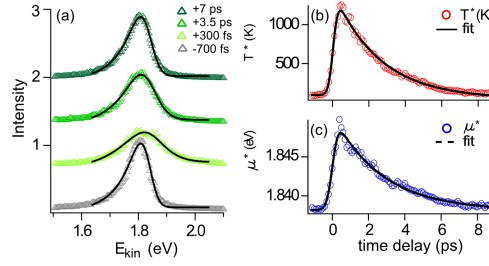


Figure 7.12: (a) EDCs at the Fermi wave-vector $k_F = 0.1 \text{ \AA}^{-1}$ at four different delay times (-700 fs, +300 fs, +3.5 ps and +7 ps). The fitting curves, in black lines, contain the FD distribution, multiplied with a lorentzian which accounts for the surface state peak. The temporal evolution of the effective temperature T^* and of the effective chemical potential μ^* , as obtained from the the fit, are shown respectively in panel (b) and (c). A single decay exponential function well fits the temporal dynamics, with characteristic relaxation time equal to $\tau_T \sim 2.5 \text{ ps}$ and $\tau_\mu \sim 2.7 \text{ ps}$, respectively.

or diffusion. A simpler relaxation via diffusion was also proposed for p-doped Bi_2Se_3 [256]. The electron-phonon scattering is unsuitable for recombining the excited electrons with holes, because the value of the gap is larger than the highest phonon energy (23 meV) [269, 256]. Furthermore, for n-doped Bi_2Se_3 , the band gap is acting as a bottleneck slowing down the relaxation of the photo-excited holes at high binding energies (in VB) and of the low energy holes (in CB). This results in a transient excess of charge carriers in the conduction band, which is at the origin of the proposed ultrafast shift of the chemical potential.

The emergence of the ultrafast chemical shift is further supported by a quantitative analysis of the temporal evolution of the FD distribution function at k_F . Figure 7.12 (a) displays the EDCs at some selected delay times (-700 fs, +300 fs, +3.5 ps and +7 ps). The product of the FD distribution with a lorentzian, describing the surface state peak, is used as model function to fit the spectra (see suppl. information). The values of the effective temperature T^* and of the effective chemical potential μ^* , as obtained from the *hot* FD, are shown as a function of the delay time in Figure 7.12 (b) and (c) respectively. Their temporal evolution is fitted with a single decay exponential, with a proper rise-time (modelled by a step-function), convoluted with a gaussian to account for the temporal resolution. The characteristic relaxation times are $\tau_T \sim 2.5 \text{ ps}$ and $\tau_\mu \sim 2.7 \text{ ps}$. The T^* relaxation is slightly slower than previously reported for p-doped Bi_2Se_3 (1.67 ps) [256]. This discrepancy might be ascribed to the different doping, but it could also be related to the larger pump fluence used in the present case. The maximum value of $\Delta\mu^*$ is 12 meV, in agreement with the pump-probe dEDCs data.

The creation of a long-lived population in the conduction band has been proposed to be the key-mechanism responsible for the slow relaxation time in the topological insulators Bi_2Se_3 [256] and Bi_2Te_3 [259]. In these models, the conduction band acts as a charge reservoir for the topological surface state at lower binding energies. Such an effect was inferred from the difference in the temporal evolution of the tr-ARPES intensity at different

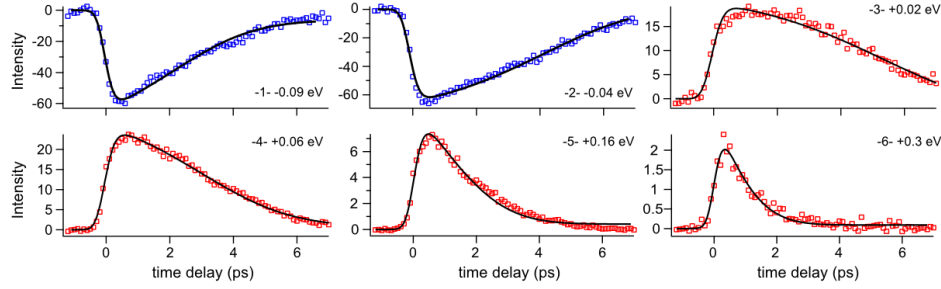


Figure 7.13: Ultrafast evolution of the non-equilibrium charge population in the topological surface state at six energies, along its linear dispersion, as indicated in Figure 1 (e). The results of the fitting routine are displayed as black lines. The model function results from the intensity of the Fermi Dirac distribution at that energy at an effective temperature T^* and with an effective chemical potential μ^* , which relax exponentially in time as shown respectively in Figure 7.12 (b) and (c).

positions in the band structure, $I(E, k, t)$. Also in our investigation, the evolution of the surface state population at different binding energies along its linear dispersion shows a peculiar energy dependent relaxation. However, a detailed analysis of the data suggests a different interpretation.

Figure 7.13 displays the $I(E, k, t)$ signal, for six selected (E, k) positions below and above the chemical potential, as indicated in Figure 7.11 (e). We focus on the topological surface state and on the evolution of its out-of-equilibrium population. Similar trends are observed in the conduction band, as well. We average the intensity over a narrow energy window (less than 20 meV), and this provides us with a precise information on the *energy dependent* temporal evolution of the excited electrons. This constitutes an important difference to a previous study on Bi_2Te_3 , in which large energy windows were selected, enclosing distinct bands [259]. The dynamics is fast for $E \gg \mu$ (-6-), and *apparently* slows down when approaching μ (-4- and -3-). The behavior is opposite in sign but symmetric around μ (-1- and -2-). A similar observation was reported in previous studies of p-doped Bi_2Se_3 , but the dynamics was analyzed only at a qualitative level [256]. In the following, a simple but effective model is proposed to account for this peculiar energy dependence of $I(E, k, t)$. The spectra at the various kinetic energies are fit with the model function $\zeta(E, t)$, given by the following relation:

$$\zeta(E, t) = \int_{-\infty}^{+\infty} \Theta(t' - t_0) \cdot \frac{C}{1 + \exp(E - \mu^*(t')/k_B T^*(t'))} \cdot G(t - t') dt' + \phi. \quad (7.4)$$

At time t the intensity $\zeta(E, t)$ is the result of the convolution of a gaussian G , describing the temporal resolution, with a Fermi-Dirac distribution. The latter is defined by a time-dependent effective temperature $T^*(t)$ and an effective chemical potential $\mu^*(t)$, which relax in time as discussed previously. Θ is a step function which accounts for the

rise-time. The intensity C has a weak dependence on the kinetic energy E , which we attributed to matrix element effect. C accounts for the variation in sign in the signal between accumulation and depletion, when moving from above to below the chemical potential. Finally, ϕ represents a background. In our model the relaxation time is uniquely determined by τ_T and τ_μ , and the apparent energy dependence is conveyed by the Fermi-Dirac distribution. The $\zeta(E, t)$ function is used to fit all the spectra (from -1- to -6-). The results of the fit are reported as black lines in Figure 7.13, showing a remarkably good agreement with the experimental data. A microscopic description of the charge population evolution is complex, since several de-excitation mechanisms must be considered, especially for the recombination of the holes across the band gap. Moreover, the cascade relaxation of electrons excited in high branches of the conduction band should also be taken into account, as suggested in Refs. [256, 259]. This may explain the better agreement between the data and the model at larger delay time, when this fast process is over. Nevertheless the analysis of Figure 7.13 proves that the observed non-equilibrium electronic dynamics of the ultrafast photodoped Bi_2Se_3 is controlled by the evolution of the Fermi-Dirac distribution. The temporal evolution of the tr-ARPES intensity $I(E, k, t)$ is properly fit by the value of the time-dependent effective Fermi-Dirac function, which is uniquely determined by the characteristic relaxation time of the effective electronic temperature T^* and of the effective chemical potential μ^* .

In summary, we investigated in detail the time-dependent electronic thermal distribution after optical excitation in Bi_2Se_3 . We find that, at all the delay times, the electrons in the surface states are thermalized. Their distribution can be approximated by an effective Fermi-Dirac function, whose temperature T^* and chemical potential μ^* relax in time with a decaying exponential behavior. The fast electronic thermalization, below the experimental resolution (300 fs), is ensured by the characteristic time of the electron-electron interaction (< 40 fs [267]). The variation in the effective chemical potential is interpreted as the result of the ultrafast photodoping of the conduction band, similarly to what recently reported by Wang *et al.* [268]. The relaxation time of T^* and μ^* are respectively equal to $\tau_T \sim 2.5$ ps and $\tau_\mu \sim 2.7$ ps. The former is compatible with a mechanism of energy relaxation to the lattice mediated by the electron-phonon interaction. The latter is related to the relaxation of the excess charge in the conduction band via diffusion.

We propose a model which relies only on the inherent properties of the Fermi-Dirac distribution function, therefore it provides a viable interpretation for similar energy dependence of the electronic dynamics in a different material [259] or in p-doped Bi_2Se_3 [256]. Finally, for the universal character of the Fermi-Dirac function it may provide a reference for future tr-ARPES on similar systems.

7.4 Supplemental Material: Ultrafast photo-doping and effective Fermi-Dirac distribution of the Dirac particles in Bi_2Se_3

7.4.1 1. Extracting the Fermi-Dirac distribution term from the EDC fit

In order to investigate the evolution of both the effective electronic temperature T^* and the effective chemical potential μ^* we analyze in details the temporal evolution of the EDCs integrated over a narrow k window (0.01 \AA^{-1}) centered at the Fermi wave-vector $k_F = 0.1 \text{ \AA}^{-1}$.

The time-dependent model function is the result of a Fermi-Dirac (FD) distribution function $f_{FD}(t, T^*, E - \mu^*)$ multiplied with a lorentzian, which describes the quasi-particle spectral function $A(t, E, k_F)$. This function is successively convolved with a gaussian G which accounts for the energy resolution of the setup.

The FD function describes the thermal distribution of electrons, while A describes the band structure and it accounts for the modification in the average number of quasi-particle in the region probed by the laser light.

Figure 7.14 (a) shows four EDCs at different delay times (-700 fs, +300 fs, +3.5 ps and +7 ps). The large decrease in intensity below the chemical potential is determined *both* by the thermal broadening of the FD distribution *and* by the depletion of the band by photo-excitation. In order to improve the quality of the fit we disentangle the two contributions, by symmetrization of the EDCs. Similar analysis was recently carried out in the tr-ARPES study of the spectral weight suppression in the cuprate compound $\text{Bi}_2\text{Sr}_2\text{CaCu}_2\text{O}_{7+\delta}$ [226, 227].

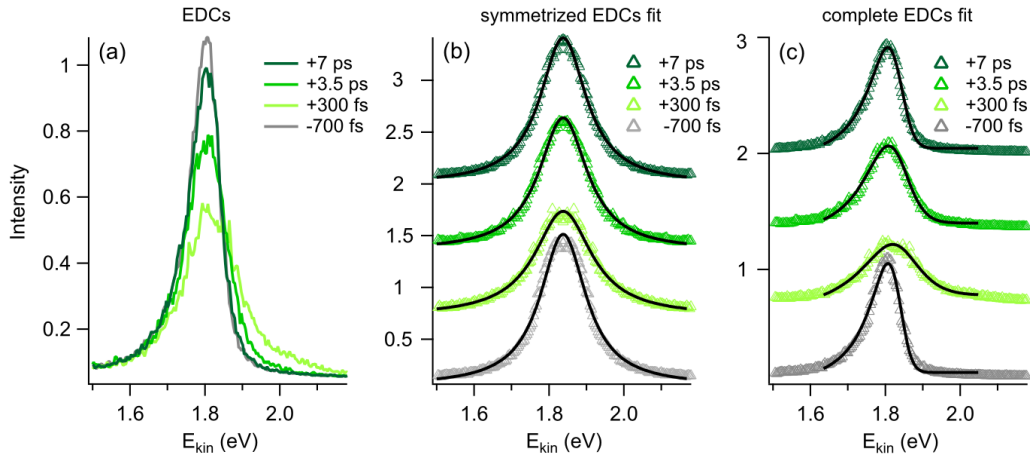


Figure 7.14: (a) Stack of EDCs at $k_F = 0.1 \text{ \AA}^{-1}$ for various delay times (-700 fs, +300 fs, +3.5 ps and +7 ps). (b) Symmetrized EDCs with corresponding lorentzian fit (indicated by black lines). (c) The best-fit parameters are then used to fit the EDCs, with a function obtained as the product of a Fermi-Dirac distribution with a lorentzian, convoluted with a gaussian, which accounts for the experimental energy resolution.

The symmetrization is performed by using the well established sum rule [270]:

$$I(t, E + \mu, k_f) + I(t, -E + \mu, k_f) = \int_{-\infty}^{+\infty} A(t, E, k_f) \cdot G(E - \varepsilon) d\varepsilon. \quad (7.5)$$

This removes the thermal effect by cancelling out the FD function. Moreover, this procedure does not require any *a priori* knowledge of the effective temperature.

Figure 7.14 (b) shows the corresponding symmetrized EDCs, with a vertical offset. The convolution of a lorentzian with a gaussian is fit to each peak, and the best-fit functions are displayed with black lines. All the parameters of the lorentzian (intensity, position and FWHM) are then introduced in the fit of the EDCs, as discussed above, whose results are shown in Figure 7.14 (c).

From the FD term we extract the effective temperature T^* and the effective chemical potential μ^* , whose evolution with time is described in Figure 7.12 of the main article. Successively, we repeat the analysis by symmetrizing at slightly different values of the chemical potential, within the experimentally resolved shift (10 meV). We find that the results of our EDCs fit are unsensitive to weak modification of chemical potential in the EDC symmetrization, thus confirming that the value of $\Delta\mu^*$ is not affected by our analysis.

Concluding Remarks

This thesis work consisted in the investigation of the electronic properties of several different systems which are all characterized by a sizeable spin orbit interaction. I summarize here the main results.

The spin orbit interaction lifts the spin degeneracy of electronic states in the absence of inversion symmetry, for example at crystal surfaces, where this effect was firstly described by Rashba and Bychkov. The study of spin-split surface states has recently gathered the attention of the scientific community both from a theoretical and experimental point of view. For the first time I have reported the existence of spin-split surface states in one-dimensional surface alloys grown by the deposition of large Z atoms (Bi and Pb) on the surface of Cu(110). The magnitude of the splitting is comparable to the one of the BiAg₂ surface alloy. Interestingly all these surface reconstructions are characterized by a large buckling of the heavy atoms in substitutional sites, thus confirming the key role played by the Bi (Pb) atomic positions in defining the asymmetry of the surface state wave-function and consequently the *effective* spin-orbit coupling.

Semiconductors hosting spin-split states represent appealing candidates for spintronics devices. Therefore, I have studied in detail the symmetry of the spin-gaps in the tri-layer BiAg₂/Ag/Si(111). I reported the six-fold modulation of the gaps, whose energy position can be controlled continuously by deposition of alkali metal. For the case of two-dimensional systems, I also investigated the existence of spin-split states in the Pb monolayer grown on Au(111). I resolved a peculiar hybridization of the Pb orbitals, which I attributed to the broken in-plane hexagonal symmetry arising from the incommensurate moiré superstructure. This hypothesis has been tested and verified by investigating the electronic properties of a Pb ML grown on Ag(100). In this case, in fact, the interface is commensurate, thus resulting in the absence of hybridization gaps between the Pb states.

Non-centrosymmetric bulk crystal can host spin-split *bulk* states, as described by Dresselhaus and Rashba, and recently proposed for BiTeI. My ARPES results, supported by *ab initio* calculations, show that the band structure of this bulk compound is more complex than what was recently proposed. Besides the three-dimensional *bulk* spin-split states, I observed two distinct families of spin-split surface states, resulting from the two possible crystal terminations (Te⁺ and I⁻). Furthermore, I report on the opposite surface band bending of the two terminations: the charge carriers in the Te⁺ surface are electrons, while holes are responsible for the conduction at the I⁻ surface. BiTeI is therefore an ambipolar semiconductor with spin-split surface and bulk states.

Finally, during my PhD I contributed to the development and characterization of a novel time and angle resolved photoemission setup. I have studied the out-of-equilibrium electronic properties of the topological insulator Bi₂Se₃, after optical perturbation with laser light in a pump-probe experiment. I have observed an ultrafast shift of the chemical potential, and a modification of the effective electronic temperature. A model based on

the modification of the effective Fermi Dirac distribution has been developed in order to quantitatively describe the relaxation dynamics of the *hot* electrons in the Dirac cone.

Bibliography

- [1] S. Hüfner, *Photoelectron Spectroscopy: Principles and Applications*. Springer-Verlag, 1995. (Cited on pages [1](#), [3](#), [4](#) and [9](#).)
- [2] J. J. Thompson *Phil. Mag.*, vol. 48, p. 547, 1899. (Cited on page [1](#).)
- [3] P. Lenard *Ann. Physik*, vol. 2, p. 359, 1900. (Cited on page [1](#).)
- [4] D. Roy and D. Tremblay, “Design of electron spectrometer,” *Rep. Prog. Phys.*, vol. 53, p. 1621, 1990. (Cited on page [2](#).)
- [5] J. D. Koralek, J. F. Douglas, N. C. Plumb, Z. Sun, A. V. Federov, M. M. Murnane, H. C. Kapteyn, S. R. Cundiff, Y. Aiura, K. Oka, H. Eisaki, and D. S. Dessau, “Laser based angle-resolved photoemission, the sudden approximation and quasiparticle-like spectral peaks in $Bi_2Sr_2CaCu_2O_8$,” *Phys. Rev. Lett.*, vol. 96, p. 017005, 2006. (Cited on pages [2](#), [120](#) and [125](#).)
- [6] L. Perfetti, P. A. Loukakos, M. Lisowski, U. Bovensiepen, M. Wolf, H. Berger, S. Biermann, and A. Georges, “Femtosecond dynamics of electronic states in the Mott insulator $1T - TaS_2$ by time resolved photoelectron spectroscopy,” *New Journal of Phys.*, vol. 10, p. 053019, 2008. (Cited on pages [2](#), [122](#) and [123](#).)
- [7] T. Koopman *Physica*, vol. 1, p. 104, 1934. (Cited on page [2](#).)
- [8] A. Damascelli, “Probing the electronic structure of complex systems by arpes,” *Physica Scripta*, vol. 109, pp. 61–74, 2004. (Cited on pages [3](#), [5](#), [6](#) and [9](#).)
- [9] A. Damascelli, Z. Hussain, and Z.-X. Shen, “Angle-resolved photoemission studies of the cuprate superconductors,” *Rev. Mod. Phys.*, vol. 75, p. 473, 2003. (Cited on pages [3](#), [5](#), [6](#), [9](#), [66](#) and [125](#).)
- [10] S. LaShell, B. A. McDougall, and E. Jensen, “Spin splitting of an Au(111) surface state band observed with angle resolved photoelectron spectroscopy,” *Phys. Rev. Lett.*, vol. 77, pp. 3419–3422, Oct 1996. (Cited on pages [4](#), [16](#), [17](#), [25](#), [91](#), [103](#) and [135](#).)
- [11] D. Hsieh, D. Qian, L. Wray, Y. Xia, Y. S. Hor, R. J. Cava, and M. Z. Hasan, “A topological dirac insulator in a quantum spin hall phase,” *Nature*, vol. 452, p. 970, 2008. (Cited on pages [4](#), [30](#), [47](#), [131](#) and [135](#).)
- [12] M. Okawa, K. ishizaka, H. Uchiyama, H. Tadatomo, T. Masui, S. Tajima, X.-Y. Wang, C.-T. Chen, S. Watanabe, A. Chainani, T. Saitoh, and S. Shin, “Superconducting electronic state in optimally doped $YBa_2Cu_3O_7$ observed with laser-excited angle-resolved photoemission spectroscopy,” *Phys. Rev. B*, vol. 79, p. 144528, 2009. (Cited on pages [4](#) and [120](#).)

- [13] D. Pines and P. Nozières, *The theory of Quantum Liquid- Normal Fermi Liquid*. Addison- Wesley, 1966. (Cited on page 9.)
- [14] L. Perfetti, H. Berger, A. Reggiani, L. Degiorgi, H. Höchst, J. Voit, G. Margaritondo, and M. Grioni, “Spectroscopic indications of polaronic carriers in the quasi-one-dimensional conductor $(\text{TaSe}_4)_2\text{I}$,” *Phys. Rev. Lett.*, vol. 87, p. 216404, Nov 2001. (Cited on page 9.)
- [15] J. M. Luttinger, “Fermi surface and some simple equilibrium properties of a system of interacting fermions,” *Phys. Rev.*, vol. 119, pp. 1153–1163, Aug 1960. (Cited on page 9.)
- [16] R. Claessen, R. O. Anderson, J. W. Allen, C. G. Olson, C. Janowitz, W. P. Ellis, S. Harm, M. Kalning, R. Manzke, and M. Skibowski, “Fermi-liquid line shapes measured by angle-resolved photoemission spectroscopy on $1T - \text{TiTe}_2$,” *Phys. Rev. Lett.*, vol. 69, pp. 808–811, Aug 1992. (Cited on page 9.)
- [17] J. D. Denlinger, G.-H. Gweon, J. W. Allen, C. G. Olson, J. Marcus, C. Schlenker, and L.-S. Hsu, “Non-Fermi-liquid single particle line shape of the quasi-one-dimensional non-CDW metal $\text{Li}_{0.9}\text{Mo}_6\text{O}_{17}$: Comparison to the Luttinger liquid,” *Phys. Rev. Lett.*, vol. 82, pp. 2540–2543, Mar 1999. (Cited on page 9.)
- [18] V. Vescovi, F. Zwick, W. Henderson, L. Degiorgi, M. Grioni, G. Gruner, and L. K. Montgomery, “Optical and photoemission evidence for a Tomonaga-Luttinger liquid in the Bechgaard salts,” *Eur. Phys. J. B.*, vol. 13, p. 503, 2000. (Cited on page 9.)
- [19] L. Perfetti, C. Rojas, A. Reggiani, L. Gavioli, H. Berger, G. Margaritondo, M. Grioni, R. Gaál, L. Forró, and F. Rullier Albenque, “High-resolution angle-resolved photoemission investigation of the quasiparticle scattering processes in a model fermi liquid: $1T - \text{TiTe}_2$,” *Phys. Rev. B*, vol. 64, p. 115102, Aug 2001. (Cited on page 9.)
- [20] G. A. Sawatzky, “Testing fermi-liquid models,” *Nature*, vol. 342, p. 480, 1989. (Cited on page 9.)
- [21] V. Brouet, W. L. Yang, X. J. Zhou, Z. Hussain, R. G. Moore, R. He, D. H. Lu, Z. X. Shen, J. Laverock, S. B. Dugdale, N. Ru, and I. R. Fisher, “Angle-resolved photoemission study of the evolution of band structure and charge density wave properties in RTe_3 (R = Y, La, Ce, Sm, Gd, Tb, and Dy),” *Phys. Rev. B*, vol. 77, p. 235104, Jun 2008. (Cited on page 9.)
- [22] E. D. Hansen, T. Miller, and T.-C. Chiang, “Observation of photoemission line widths narrower than the inverse lifetime,” *Phys. Rev. Lett.*, vol. 80, pp. 1766–1769, Feb 1998. (Cited on page 10.)
- [23] N. V. Smith, P. Thiry, and Y. Petroff, “Photoemission linewidths and quasiparticle lifetimes,” *Phys. Rev. B*, vol. 47, pp. 15476–15481, Jun 1993. (Cited on page 10.)

- [24] M. Lindroos and A. Bansil, “A novel direct method of fermi surface determination using constant initial energy angle-scanned photoemission spectroscopy,” *Phys. Rev. Lett.*, vol. 77, p. 2985, 1996. (Cited on pages 10, 11 and 73.)
- [25] N. W. Ashcroft and I. Mermin, *Solid State Physics*. Harcourt College, 1976. (Cited on pages 13 and 83.)
- [26] C. Kittel, *Quantum Theory of Solids*. J. Wiles, 1963. (Cited on pages 13 and 83.)
- [27] H. Cercellier, *Etude par photoémission et microscopie à effet tunnel des relations entre propriétés structurales et électronique des interface Ce / Sc(0001) et Ag / Au(111)*. PhD thesis, Université Henri Poincaré, Nancy I, 2004. (Cited on pages 13 and 18.)
- [28] A. Zangwill, *Physics at the Surfaces*. Cambridge University Press, 2001. (Cited on page 13.)
- [29] I. Tamn, “Über eine mögliche Art der Elektronenbindung an Kristalloberflächen,” *Zeitschrift für Physics A Hadrons and Nuclei*, vol. 76, p. 849, 1932. (Cited on page 13.)
- [30] A. W. Maue, “Die Oberflächenwellen in der Elektronentheorie del Metalle,” *Z. Physik*, vol. 94, p. 717, 1935. (Cited on pages 13 and 14.)
- [31] E. T. Goodwin, “Electronic states at the surfaces of crystals,” *Proc. Camb. Phil. Soc.*, vol. 35, p. 474, 1939. (Cited on pages 13 and 14.)
- [32] W. Shockley, “On the surface states associated with periodic potential,” *Phys. Rew.*, vol. 56, p. 317, 1939. (Cited on pages 13 and 14.)
- [33] F. Forstmann, “On the theory of surface states in nearly free electron systems,” *Z. Physik*, vol. 235, p. 69, 1970. (Cited on page 14.)
- [34] E. Antoncik, “On the theory of surface states,” *J. Phys. Chem. Solids*, vol. 21, p. 137, 1961. (Cited on page 14.)
- [35] V. Heine, “Theory of surface states,” *Phys. Rew.*, vol. 138, p. 1689, 1965. (Cited on page 14.)
- [36] N. V. Smith, “Phase analysis of image states and surface states associated with nearly-free-electron band gaps,” *Phys. Rew. B*, vol. 32, p. 3549, 1985. (Cited on page 14.)
- [37] J. Heinrichs, “Tight-binding surface states in infinite crystals,” *J. Phys.: Condens. Matter*, vol. 12, p. 5565, 2000. (Cited on page 14.)
- [38] G. Chiarotti, G. Del Signore, and S. Nannarone, “Optical detection of surface states on cleaved (111) surfaces of Ge,” *Phys. Rev. Lett.*, vol. 21, pp. 1170–1172, Oct 1968. (Cited on page 14.)

- [39] G. Chiarotti, S. Nannarone, R. Pastore, and P. Chiaradia, “Optical absorption of surface states in ultrahigh vacuum cleaved (111) surfaces of Ge and Si,” *Phys. Rev. B*, vol. 4, pp. 3398–3402, Nov 1971. (Cited on page 14.)
- [40] J. Li, W.-D. Schneider, R. Berndt, O. R. Bryant, and S. Crampin, “Surface-state lifetime measured by scanning tunneling spectroscopy,” *Phys. Rev. Lett.*, vol. 81, pp. 4464–4467, Nov 1998. (Cited on page 15.)
- [41] J. Kliewer, R. Berndt, E. V. Chulkov, V. M. Silkin, P. M. Echenique, and S. Crampin, “Dimensionality effects in the lifetime of surface states,” *Science*, vol. 288, p. 1399, 2000. (Cited on page 15.)
- [42] G. Nicolay, F. Reinert, S. Hufner, and P. Blaha, “Spin-orbit splitting of the L-gap surface state on Au(111) and Ag(111),” *Phys. Rev. B*, vol. 65, p. 033407, Dec 2001. (Cited on pages 15, 16 and 19.)
- [43] F. Reinert, G. Nicolay, S. Schmidt, D. Ehm, and S. Hufner, “Direct measurements of the L-gap surface states on the (111) face of noble metals by photoelectron spectroscopy,” *Phys. Rev. B*, vol. 63, p. 115415, Mar 2001. (Cited on pages 15 and 16.)
- [44] L. Petersen and P. Hodegard, “A simple tight-binding model of spin-orbit splitting sp-derived surface states,” *Surf. Sci.*, vol. 459, p. 49, 2000. (Cited on pages 16, 19, 21, 72 and 107.)
- [45] Y. A. Bychokov and E. I. Rashba, “Properties of a 2d electron gas with lifted spectral degeneracy,” *JETP Lett.*, vol. 39, p. 278, 1984. (Cited on pages 16, 51, 53, 54, 103 and 135.)
- [46] E. I. Rashba *Sov. Phys. Solid state*, vol. 2, p. 1109, 1960. (Cited on pages 17, 99, 103 and 135.)
- [47] G. Dresselhaus, “Spin-orbit coupling effectc in zinc blende structures,” *Phys. Rev. Lett.*, vol. 100, p. 580, 1955. (Cited on pages 17, 103 and 135.)
- [48] K. Ishizaka, M. S. Bahramy, H. Murakawa, M. Sakano, T. Shimojima, T. Sonobe, K. Koizumi, S. Shin, H. Miyahara, A. Kimura, K. Miyamoto, T. Okuda, H. Namatame, M. Taniguchi, R. Arita, N. Nagaosa, K. Kobayashi, Y. Murakami, R. Kumai, Y. Kaneko, Y. Onose, and Y. Tokura., “Giant Rashba-type spin splitting in bulk BiTeI,” *Nat. Material*, vol. 10, p. 521, 2011. (Cited on pages 17, 47, 99, 100, 101, 102, 103, 104, 105, 106, 107, 109 and 135.)
- [49] H. Cercellier, Y. Fagot-Revurat, B. Kierren, F. Reinert, D. Popovic, and D. Malterre, “Spin-orbit splitting of the Shockley state in the Ag / Au(111) interface,” *Phys. Rev. B*, vol. 70, p. 193412, Nov 2004. (Cited on pages 17, 18 and 31.)
- [50] D. Popovic, F. Reinert, S. Hufner, V. G. Grigoryan, M. Springborg, H. Cercellier, Y. Fagot-Revurat, B. Kierren, and D. Malterre, “High-resolution photoemission on Ag / Au(111): Spin-orbit splitting and electronic localization of the surface state,” *Phys. Rev. B*, vol. 72, p. 045419, Jul 2005. (Cited on pages 17, 18 and 31.)

- [51] H. Cercellier, C. Didiot, Y. Fagot-Revurat, B. Kierren, L. Moreau, D. Malterre, and F. Reinert, "Interplay between structural, chemical, and spectroscopic properties of Ag / Au(111) epitaxial ultrathin films: A way to tune the Rashba coupling," *Phys. Rev. B*, vol. 73, p. 195413, May 2006. (Cited on pages 17, 18, 31 and 103.)
- [52] F. Baumberger, "St. andrews laboratory web page," <http://www.st-andrews.ac.uk/physics/condmat/arpes/index.html>. (Cited on page 18.)
- [53] F. Forster, S. Hüfner, and F. Reinert, "Rare gas on noble-metal surfaces: an angle-resolved photoemission study with high energy resolution," *J. Phys. Chem. B*, vol. 108, p. 14692, 2004. (Cited on pages 18 and 19.)
- [54] T. Andreev, I. Barke, and H. Hövel, "Adsorbed rare-gas layers on au(111): Shift of the shockley surface state studied with ultraviolet photoelectron spectroscopy and scanning tunneling spectroscopy," *Phys. Rev. B*, vol. 70, p. 205426, Nov 2004. (Cited on page 19.)
- [55] M. Nagano, A. Kodama, T. Shishidou, and T. Oguchi, "A first-principles study on the rashba effect in surface systems," *J. Phys.: Condens. Matter*, vol. 21, p. 064239, 2009. (Cited on page 19.)
- [56] J. Premper, M. Trautmann, J. Henk, and P. Bruno, "Spin-orbit splitting in an anisotropic two-dimensional electron gas," *Phys. Rev. B*, vol. 76, p. 073310, Aug 2007. (Cited on pages 19, 21, 31, 32, 53, 55 and 107.)
- [57] J. Henk, M. Hoesch, J. Osterwalder, A. Ernst, and P. Bruno, "Spin-orbit coupling in the L-gap surface states of Au(111): Spin-resolved photoemission experiments and first-principles calculations," *J. Phys.: Condens. Matter*, vol. 16, p. 7581, 2004. (Cited on pages 19 and 20.)
- [58] M. Hochstrasser, J. G. Tobin, E. Rotenberg, and S. D. Kevan, "Spin-resolved photoemission of surface states of W(110)-(1x1)H," *Phys. Rev. Lett.*, vol. 89, p. 216802, Nov 2002. (Cited on pages 19, 25 and 103.)
- [59] J. Henk, A. Ernst, and P. Bruno, "Spin polarization of the L-gap surface states on Au(111)," *Phys. Rev. B*, vol. 68, p. 165416, Oct 2003. (Cited on page 19.)
- [60] M. Hoesch, M. Muntwiler, V. N. Petrov, M. Hengsberger, L. Patthey, M. Shi, M. Falub, T. Greber, and J. Osterwalder, "Spin structure of the Shockley surface state on Au(111)," *Phys. Rev. B*, vol. 69, p. 241401, Jun 2004. (Cited on pages 19 and 103.)
- [61] G. Bihlmayer, Y. M. Koroteev, P. M. Echenique, E. V. Chulkova, and S. Blügel, "The rashba-effect at metallic surfaces," *Surf. Sci.*, vol. 600, p. 3888, 2006. (Cited on pages 19, 21 and 42.)
- [62] C. R. Ast and I. Gierz, "*sp*-band tight-binding model for the bychkov-rashba effect in a two-dimensional electron system including nearest-neighbor contributions from an electric field," *Phys. Rev. B*, vol. 86, p. 085105, Aug 2012. (Cited on page 20.)

- [63] S. R. Park, C. H. Kim, J. Yu, J. H. Han, and C. Kim, “Orbital-angular-momentum based origin of rashba-type surface band splitting,” *Phys. Rev. Lett.*, vol. 107, p. 156803, Oct 2011. (Cited on pages 21, 22, 23, 55 and 107.)
- [64] B. Kim, C. H. Kim, P. Kim, W. Jung, Y. Kim, Y. Koh, M. Arita, K. Shimada, H. Namatame, M. Taniguchi, J. Yu, and C. Kim, “Spin and orbital angular momentum structure of Cu(111) and Au(111) surface states,” *Phys. Rev. B*, vol. 85, p. 195402, May 2012. (Cited on pages 22, 24 and 25.)
- [65] J.-H. Park, C. H. Kim, J.-W. Rhim, and J. H. Han, “Orbital rashba effect and its detection by circular dichroism angle-resolved photoemission spectroscopy,” *Phys. Rev. B*, vol. 85, p. 195401, May 2012. (Cited on page 22.)
- [66] A. Varykhalov, D. Marchenko, M. R. Scholz, E. D. L. Rienks, T. K. Kim, G. Bihlmayer, J. Sánchez-Barriga, and O. Rader, “Ir(111) surface state with giant rashba splitting persists under graphene in air,” *Phys. Rev. Lett.*, vol. 108, p. 066804, Feb 2012. (Cited on pages 26 and 108.)
- [67] E. Rotenberg, J. W. Chung, and S. D. Kevan, “Spin-orbit coupling induced surface band splitting in Li / W(110) and Li / Mo(110),” *Phys. Rev. Lett.*, vol. 82, pp. 4066–4069, May 1999. (Cited on pages 25 and 103.)
- [68] A. M. Shikin, A. Varykhalov, G. V. Prudnikova, D. Usachov, V. K. Adamchuk, Y. Yamada, J. D. Riley, and O. Rader, “Origin of spin-orbit splitting for monolayers of Au and Ag on W(110) and Mo(110),” *Phys. Rev. Lett.*, vol. 100, p. 057601, Feb 2008. (Cited on pages 25, 26 and 43.)
- [69] E. Simon, A. Szilva, B. Ujfalussy, B. Lazarovits, G. Zarand, and L. Szunyogh, “Anisotropic rashba splitting of surface states from the admixture of bulk states: Relativistic ab initio calculations and kp perturbation theory,” *Phys. Rev. B*, vol. 81, p. 235438, Jun 2010. (Cited on page 27.)
- [70] A. Nuber, M. Higashiguchi, F. Forster, P. Blaha, K. Shimada, and F. Reinert, “Influence of reconstruction on the surface state of Au(110),” *Phys. Rev. B*, vol. 78, p. 195412, Nov 2008. (Cited on page 27.)
- [71] S. L. Hulbert, P. D. Johnson, and M. Weinert, “High-resolution inverse-photoemission study of the Pd(111) surface,” *Phys. Rev. B*, vol. 34, pp. 3670–3673, Sep 1986. (Cited on page 26.)
- [72] J. Wiebe, F. Meier, K. Hashimoto, G. Bihlmayer, S. Blügel, P. Ferriani, S. Heinze, and R. Wiesendanger, “Unoccupied surface state on Pt(111) revealed by scanning tunneling spectroscopy,” *Phys. Rev. B*, vol. 72, p. 193406, Nov 2005. (Cited on page 26.)
- [73] A. Bendounan, K. Aï-Mansour, J. Braun, J. Minár, S. Bornemann, R. Fasel, O. Grönig, F. Sirotti, and H. Ebert, “Evolution of the rashba spin-orbit-split shockley state

- on ag/pt(111),” *Phys. Rev. B*, vol. 83, p. 195427, May 2011. (Cited on pages 26 and 27.)
- [74] E. Frantzeskakis, S. Pons, A. Crepaldi, H. Brune, K. Kern, and M. Grioni, “Ag-coverage-dependent symmetry of the electronic states of the Pt(111)-Ag-Bi interface: The ARPES view of a structural transition,” *Phys. Rev. B*, vol. 84, p. 245443, Dec 2011. (Cited on page 26.)
- [75] P. Heimann, H. Miosga, and H. Neddermeyer, “Occupied surface-state bands in sp gaps of Au(112), Au(110), and Au(100) faces,” *Phys. Rev. Lett.*, vol. 42, pp. 801–804, Mar 1979. (Cited on page 27.)
- [76] P. Heimann, J. Hermanson, and H. Miosga, “Photoemission observation of a new surface state band on Cu(110),” *Surf. Sci.*, vol. 85, p. 263, 1979. (Cited on page 27.)
- [77] L. Fu, C. L. Kane, and E. J. Mele, “Topological insulators in three dimensions,” *Phys. Rev. Lett.*, vol. 98, p. 106803, 2007. (Cited on pages 28, 29, 47, 128 and 135.)
- [78] L. Fu and C. L. Kane, “Topological insulators with inversion symmetry,” *Phys. Rev. B*, vol. 76, p. 045302, 2007. (Cited on pages 28, 29, 127, 128, 129, 130 and 135.)
- [79] D. Hsieh, Y. Xia, L. Wray, D. Qian, A. Pal, J. H. Dil, J. Osterwalder, F. Meier, G. Bihlmayer, C. L. Kane, Y. S. Hor, R. J. Cava, and M. Z. Hasan, “Observation of unconventional quantum spin textures in topological insulator,” *Science*, vol. 323, p. 919, 2009. (Cited on pages 28, 29 and 30.)
- [80] M. Z. Hasan and C. L. Kane, “Colloquium: Topological insulators,” *Rev. Mod. Phys.*, vol. 82, p. 3046, 2010. (Cited on page 28.)
- [81] Y. M. Koroteev, G. Bihlmayer, J. E. Gayone, E. V. Chulkov, S. Blügel, P. M. Echenique, and P. Hofmann, “Strong spin-orbit splitting on Bi surfaces,” *Phys. Rev. Lett.*, vol. 93, p. 046403, Jul 2004. (Cited on pages 30, 90, 91 and 103.)
- [82] T. Hirahara, K. Miyamoto, I. Matsuda, T. Kadono, A. Kimura, T. Nagao, G. Bihlmayer, E. V. Chulkov, S. Qiao, K. Shimada, H. Namatame, M. Taniguchi, and S. Hasegawa, “Direct observation of spin splitting in bismuth surface states,” *Phys. Rev. B*, vol. 76, p. 153305, Oct 2007. (Cited on page 30.)
- [83] K. Sugawara, T. Sato, S. Souma, T. Takahashi, M. Arai, and T. Sasaki, “Fermi surface and anisotropic spin-orbit coupling of Sb(111) studied by angle-resolved photoemission spectroscopy,” *Phys. Rev. Lett.*, vol. 96, p. 046411, Feb 2006. (Cited on page 30.)
- [84] S.-Y. Xu, Y. Xia, L. A. Wray, S. Jia, F. Meier, J. H. Dil, J. Osterwalder, B. Slomski, A. Bansil, H. Lin, R. J. Cava, and M. Z. Hasan, “Topological phase transition and texture inversion in a tunable topological insulator,” *Science*, vol. 332, p. 560, 2011. (Cited on page 30.)

- [85] J. Dalmas, H. Oughaddou, C. Léandri, J.-M. Gay, G. Le Lay, G. Tréglia, B. Aufray, O. Bunk, and R. L. Johnson, “Ordered surface alloy formation of immiscible metals: The case of Pb deposited on Ag(111),” *Phys. Rev. B*, vol. 72, p. 155424, Oct 2005. (Cited on page 31.)
- [86] I. M. McLeod, V. R. Dhanak, A. Matilainen, M. Lahti, K. Pussi, and K. Zhang, “Structure determination of the $p(\sqrt{3}x\sqrt{3})R30^\circ Bi - Ag(111)$ surface alloys using LEED I-V and DFT analysis,” *Surf. Sci.*, vol. 604, p. 1395, 2010. (Cited on page 31.)
- [87] C. R. Ast, J. Henk, A. Ernst, L. Moreschini, M. C. Falub, D. Pacilé, P. Bruno, K. Kern, and M. Grioni, “Giant spin splitting through surface alloying,” *Phys. Rev. Lett.*, vol. 98, p. 186807, May 2007. (Cited on pages 31, 32, 33, 44, 51, 53, 55, 57, 87, 88, 90, 92 and 103.)
- [88] F. Meier, H. Dil, J. Lobo-Checa, L. Patthey, and J. Osterwalder, “Quantitative vectorial spin analysis in angle-resolved photoemission: Bi / Ag(111) and Pb / Ag(111),” *Phys. Rev. B*, vol. 77, p. 165431, Apr 2008. (Cited on pages 32 and 33.)
- [89] G. Bihlmayer, S. Blügel, and E. V. Chulkov, “Enhanced Rashba spin-orbit splitting in Bi / Ag(111) and Pb / Ag(111) surface alloys from first principles,” *Phys. Rev. B*, vol. 75, p. 195414, May 2007. (Cited on pages 32, 33, 42, 53, 92 and 107.)
- [90] C. R. Ast, D. Pacilé, L. Moreschini, M. C. Falub, M. Papagno, K. Kern, M. Grioni, J. Henk, A. Ernst, S. Ostanin, and P. Bruno, “Spin-orbit split two-dimensional electron gas with tunable Rashba and Fermi energy,” *Phys. Rev. B*, vol. 77, p. 081407, Feb 2008. (Cited on pages 33, 34, 53, 90, 92, 94 and 96.)
- [91] F. Meier, V. Petrov, S. Guerrero, C. Mudry, L. Patthey, J. Osterwalder, and J. H. Dil, “Unconventional Fermi surface spin textures in the Bi_xPb_{1-x} / Ag(111) surface alloy,” *Phys. Rev. B*, vol. 79, p. 241408, Jun 2009. (Cited on pages 33, 35, 36 and 37.)
- [92] E. Cappelluti, C. Grimaldi, and F. Marsiglio, “Topological change of the Fermi surface in low-density Rashba gases: Application to superconductivity,” *Phys. Rev. Lett.*, vol. 98, p. 167002, Apr 2007. (Cited on page 34.)
- [93] E. Cappelluti, C. Grimaldi, and F. Marsiglio, “Electron-phonon effects on spin-orbit split bands of two-dimensional systems,” *Phys. Rev. B*, vol. 76, p. 085334, Aug 2007. (Cited on page 34.)
- [94] L. Covaci and M. Berciu, “Polaron formation in the presence of rashba spin-orbit coupling: Implications for spintronics,” *Phys. Rev. Lett.*, vol. 102, p. 186403, May 2009. (Cited on page 34.)
- [95] C. R. Ast, G. Wittich, P. Wahl, R. Vogelgesang, D. Pacilé, M. C. Falub, L. Moreschini, M. Papagno, M. Grioni, and K. Kern, “Local detection of spin-orbit splitting by scanning tunneling spectroscopy,” *Phys. Rev. B*, vol. 75, p. 201401, May 2007. (Cited on page 34.)

- [96] L. Moreschini, *Spin-Orbit Coupling effects in the Band structure of surface alloys*. PhD thesis, École Polytechnique Fédérale de Lausanne, 2009. (Cited on page 35.)
- [97] L. Moreschini, A. Bendounan, I. Gierz, C. R. Ast, H. Mirhosseini, H. Höchst, K. Kern, J. Henk, A. Ernst, S. Ostanin, F. Reinert, and M. Grioni, “Assessing the atomic contribution to the Rashba spin-orbit splitting in surface alloys: Sb/Ag(111),” *Phys. Rev. B*, vol. 79, p. 075424, Feb 2009. (Cited on pages 35 and 92.)
- [98] F. Meier, V. Petrov, H. Mirhosseini, L. Patthey, J. Henk, J. Osterwalder, and J. H. Dil, “Interference of spin states in photoemission from Sb / Ag(111) surface alloy,” *J. Phys.: Condens. Matter*, vol. 23, p. 072207, 2011. (Cited on page 35.)
- [99] H. Mirhosseini, A. Ernst, S. Ostanin, and J. Henk, “Tuning indipendently the Fermi energy and the spin splitting in Rashba systems: Ternary surface alloys on Ag(111),” *J. Phys.: Condens. Matter*, vol. 22, p. 385501, 2010. (Cited on page 35.)
- [100] I. Gierz, F. Meier, J. H. Dil, K. Kern, and C. R. Ast, “Tuning the spin texture in binary and ternary surface alloys on Ag(111),” *Phys. Rev. B*, vol. 83, p. 195122, May 2011. (Cited on page 35.)
- [101] L. Moreschini, A. Bendounan, C. R. Ast, F. Reinert, M. Falub, and M. Grioni, “Effect of rare-gas adsorption on the spin-orbit split bands of a surface alloy: Xe on Ag(111)-($\sqrt{3}x\sqrt{3}$)R30°-Bi,” *Phys. Rev. B*, vol. 77, p. 115407, Mar 2008. (Cited on page 35.)
- [102] H. Bentmann, F. Forster, G. Bihlmayer, E. V. Chulkov, L. Moreschini, M. Grioni, and F. Reinert, “Origin and manipulation of the Rashba splitting in surface alloys,” *Europhys. Lett.*, vol. 87, p. 37003, 2009. (Cited on pages 36, 37, 55, 57 and 92.)
- [103] H. Bentmann, T. Kuzumaki, G. Bihlmayer, S. Blügel, E. V. Chulkov, F. Reinert, and K. Sakamoto, “Spin orientation and sign of the Rashba splitting in Bi/Cu(111),” *Phys. Rev. B*, vol. 84, p. 115426, Sep 2011. (Cited on pages 36 and 37.)
- [104] L. Moreschini, A. Bendounan, H. Bentmann, M. Assig, K. Kern, F. Reinert, J. Henk, C. R. Ast, and M. Grioni, “Influence of the substrate on the spin-orbit splitting in surface alloys on (111) noble-metal surfaces,” *Phys. Rev. B*, vol. 80, p. 035438, Jul 2009. (Cited on page 35.)
- [105] I. Gierz, B. Stadtmüller, J. Vuorinen, M. Lindroos, F. Meier, J. H. Dil, K. Kern, and C. R. Ast, “Structural influence on the rashba-type spin splitting in surface alloys,” *Phys. Rev. B*, vol. 81, p. 245430, Jun 2010. (Cited on pages 38, 88, 91 and 94.)
- [106] H. Mirhosseini, J. Henk, A. Ernst, S. Ostanin, C.-T. Chiang, P. Yu, A. Winkelmann, and J. Kirschner, “Unconventional spin topology in surface alloys with Rashba-type spin splitting,” *Phys. Rev. B*, vol. 79, p. 245428, Jun 2009. (Cited on pages 37, 38 and 55.)
- [107] S. Datta and B. Das, “Electronic analog of the electro-optic modulator,” *Appl. Phys. Lett.*, vol. 56, p. 665, 1990. (Cited on pages 39 and 51.)

- [108] K. J. Wan, T. Guo, W. K. Ford, and J. C. Hermanson, “Initial growth of Bi films on a Si(111) substrate: Two phases of $(\sqrt{3}x\sqrt{3})$ low-energy-electron-diffraction pattern and their geometric structures,” *Phys. Rev. B*, vol. 44, pp. 3471–3474, Aug 1991. (Cited on page 39.)
- [109] K. J. Wan, T. Guo, W. K. Ford, and J. C. Hermanson, “Low energy electron diffraction studies of $Si(111) - (\sqrt{3}x\sqrt{3})R30^\circ - Bi$ system: Observation and structural determination of two phases,” *Surf. Sci.*, vol. 261, p. 69, 1992. (Cited on page 39.)
- [110] S. Nakatani, T. Takahashi, Y. Kuwahara, and M. Aono, “Use of X-ray reflectivity for determining the $Si(111) (\sqrt{3}x\sqrt{3}) - Bi$ surface structures,” *Phys. Rev. B*, vol. 52, pp. R8711–R8714, Sep 1995. (Cited on page 39.)
- [111] I. Gierz, T. Suzuki, E. Frantzeskakis, S. Pons, S. Ostanin, A. Ernst, J. Henk, M. Grioni, K. Kern, and C. R. Ast, “Silicon surface with giant spin splitting,” *Phys. Rev. Lett.*, vol. 103, p. 046803, Jul 2009. (Cited on pages 39, 40, 47, 51 and 103.)
- [112] E. Frantzeskakis, S. Pons, and M. Grioni, “Band structure scenario for the giant spin-orbit splitting observed at the Bi/Si(111) interface,” *Phys. Rev. B*, vol. 82, p. 085440, Aug 2010. (Cited on pages 39, 40 and 55.)
- [113] K. Sakamoto, H. Kakuta, K. Sugawara, K. Miyamoto, A. Kimura, T. Kuzumaki, N. Ueno, E. Annese, J. Fujii, A. Kodama, T. Shishidou, H. Namatame, M. Taniguchi, T. Sato, T. Takahashi, and T. Oguchi, “Peculiar Rashba splitting originating from the two-dimensional symmetry of the surface,” *Phys. Rev. Lett.*, vol. 103, p. 156801, Oct 2009. (Cited on pages 39, 40 and 41.)
- [114] K. Sakamoto, T. Oda, A. Kimura, K. Miyamoto, M. Tsujikawa, A. Imai, N. Ueno, H. Namatame, M. Taniguchi, P. E. J. Eriksson, and R. I. G. Uhrberg, “Abrupt rotation of the Rashba spin to the direction perpendicular to the surface,” *Phys. Rev. Lett.*, vol. 102, p. 096805, Mar 2009. (Cited on pages 41, 51, 52 and 103.)
- [115] S. Hatta, T. Aruga, Y. Ohtsubo, and H. Okuyama, “Large rashba spin splitting of surface resonance bands on semiconductor surface,” *Phys. Rev. B*, vol. 80, p. 113309, Sep 2009. (Cited on page 42.)
- [116] K. Yaji, Y. Ohtsubo, S. Hatta, H. Okuyama, K. Miyamoto, T. Okuda, A. Kimura, H. Namatame, M. Taniguchi, and T. Aruga, “Large rashba spin splitting of a metallic surface-state band on a semiconducting surface,” *Nat. Commun.*, vol. 1, p. 17, 2010. (Cited on pages 42, 43 and 51.)
- [117] T.-C.-Chiang, “Photoemission studies of quantum well states in thin films,” *Surface Science Reports*, vol. 39, p. 181, 2000. (Cited on page 43.)
- [118] N. J. Speer, S.-J. Tang, T. Miller, and T.-C. Chiang, “Coherent electronic fringe structure in incommensurate silver-silicon quantum wells,” *Science*, vol. 314, p. 804, 2006. (Cited on pages 43 and 44.)

- [119] K. He, Y. Takeichi, M. Ogawa, T. Okuda, P. Moras, D. Topwal, A. Harasawa, T. Hirahara, C. Carbone, A. Kakizaki, and I. Matsuda, “Direct spectroscopic evidence of spin-dependent hybridization between rashba-split surface states and quantum-well states,” *Phys. Rev. Lett.*, vol. 104, p. 156805, Apr 2010. (Cited on pages 43, 44, 45, 48, 52 and 53.)
- [120] J. H. Dil, F. Meier, J. Lobo-Checa, L. Patthey, G. Bihlmayer, and J. Osterwalder, “Rashba-type spin-orbit splitting of quantum well states in ultrathin Pb films,” *Phys. Rev. Lett.*, vol. 101, p. 266802, Dec 2008. (Cited on pages 43 and 55.)
- [121] A. G. Rybkin, A. M. Shikin, V. K. Adamchuk, D. Marchenko, C. Biswas, A. Varykhalov, and O. Rader, “Large spin-orbit splitting in light quantum films: Al/W(110),” *Phys. Rev. B*, vol. 82, p. 233403, Dec 2010. (Cited on page 43.)
- [122] J. F. Sánchez-Royo, J. Avila, V. Pérez-Dieste, M. De Seta, and M. C. Asensio, “Two-domains bulklike Fermi surface of Ag films deposited onto Si(111)-(7 x 7),” *Phys. Rev. B*, vol. 66, p. 035401, Jun 2002. (Cited on page 43.)
- [123] K. He, T. Hirahara, T. Okuda, S. Hasegawa, A. Kakizaki, and I. Matsuda, “Spin polarization of quantum well states in Ag films induced by the Rashba effect at the surface,” *Phys. Rev. Lett.*, vol. 101, p. 107604, Sep 2008. (Cited on pages 43, 44, 48, 51, 53, 55, 57 and 103.)
- [124] E. Frantzeskakis, S. Pons, H. Mirhosseini, J. Henk, C. R. Ast, and M. Grioni, “Tunable spin gaps in a quantum-confined geometry,” *Phys. Rev. Lett.*, vol. 101, p. 196805, Nov 2008. (Cited on pages 43, 44, 47, 48, 50, 51, 52, 53, 54, 55, 56 and 57.)
- [125] P. D. C. King, R. H. He, T. Eknapakul, P. Buaphet, S.-K. Mo, Y. Kaneko, S. Harashima, Y. Hikita, M. S. Bahramy, C. Bell, Z. Hussain, Y. Tokura, Z.-X. Shen, H. Y. Hwang, F. Baumberger, and W. Meevasana, “Subband structure of a two-dimensional electron gas formed at the polar surface of the strong spin-orbit perovskite KTaO_3 ,” *Phys. Rev. Lett.*, vol. 108, p. 117602, Mar 2012. (Cited on pages 47 and 99.)
- [126] N. J. Speer, S.-J. Tang, T. Miller, and T.-C. Chiang, “Coherent electronic fringe structure in incommensurate silver-silicon quantum wells,” *Science*, vol. 314, p. 804, 2006. (Cited on pages 47, 51 and 53.)
- [127] T. Hirahara, T. Komorida, A. Sato, G. Bihlmayer, E. V. Chulkov, K. He, I. Matsuda, and S. Hasegawa, “Manipulating quantum-well states by surface alloying: Pb on ultrathin Ag films,” *Phys. Rev. B*, vol. 78, p. 035408, Jul 2008. (Cited on pages 47, 52 and 53.)
- [128] E. Frantzeskakis, A. Crepaldi, S. Pons, K. Kern, and M. Grioni, “Tuning the giant rashba effect on a BiAg_2 surface alloy: Two different approaches,” *Journal of Electron Spectroscopy and Related Phenomena*, vol. 181, no. 1, pp. 88 – 95, 2010. (Cited on pages 47, 48, 52, 53 and 57.)

- [129] B. Srisongmuang, P. Pairor, and M. Berciu, “Tunneling conductance of a two-dimensional electron gas with Rashba spin-orbit coupling,” *Phys. Rev. B*, vol. 78, p. 155317, Oct 2008. (Cited on pages 48 and 51.)
- [130] L. Gen-Hua and Z. Guang-Hui, “Conductance for a quantum wire with weak Rashba spin-orbit coupling,” *Chinese Phys. Lett.*, vol. 22, p. 3159, 2005. (Cited on page 48.)
- [131] M. Lee and M.-S. Choi, “Ballistic spin currents in mesoscopic metal/In(Ga)As/metal junctions,” *Phys. Rev. B*, vol. 71, p. 153306, Apr 2005. (Cited on page 48.)
- [132] N. Miyata, H. Narita, M. Ogawa, A. Harasawa, R. Hobara, T. Hirahara, P. Moras, D. Topwal, C. Carbone, S. Hasegawa, and I. Matsuda, “Enhanced spin relaxation in an ultrathin metal film by the rashba-type surface,” *Phys. Rev. B*, vol. 83, p. 195305, May 2011. (Cited on pages 48, 49, 50 and 51.)
- [133] M. Ogawa, P. M. Sheverdyaeva, P. Moras, D. Topwal, A. Harasawa, K. Kobayashi, C. Carbone, and I. Matsuda, “Electronic structure study of ultrathin Ag(111) films modified by a Si(111) substrate and $\sqrt{3}x\sqrt{3}Ag_2Bi$ surface,” *J. Phys.: Condens. Matter*, vol. 24, p. 115501, 2012. (Cited on pages 48 and 60.)
- [134] S. Hikami, A. I. Larkin, and Y. Nagaoka, “Spin-orbit interaction and magnetoresistance in the two dimensional random system,” *Progress of Theoretical Physics*, vol. 63, no. 2, pp. 707–710, 1980. (Cited on page 49.)
- [135] A. Crepaldi, S. Pons, E. Frantzeskakis, K. Kern, and M. Grioni, “Anisotropic spin gaps in BiAg₂-Ag/Si(111),” *Phys. Rev. B*, vol. 85, p. 075411, 2012. (Cited on page 50.)
- [136] I. Zutíc, J. Fabian, and S. D. Sama, “Spintronics: Fundamentals and applications,” *Rev. Mod. Phys.*, vol. 76, p. 323, 2004. (Cited on page 51.)
- [137] Q.-F. Sun and X. C. Xie, “Spontaneous spin-polarized current in a nonuniform rashba interaction system,” *Phys. Rev. B*, vol. 71, p. 155321, 2005. (Cited on page 51.)
- [138] T. Koga, J. Nitta, and H. Takayanagi, “Spin-filter device based on the rashba effect using a nonmagnetic resonant tunneling diode,” *Phys. Rev. Lett.*, vol. 88, p. 126601, 2002. (Cited on page 51.)
- [139] S. Hatta, T. Aruga, Y. Ohtsubo, and H. Okuyama, “Large rashba spin splitting of surface resonance bands on semiconductor surface,” *Phys. Rev. B*, vol. 80, p. 113309, Sep 2009. (Cited on page 51.)
- [140] C. Didiot, Y. Fagot-Revurat, S. Pons, B. Kierren, C. Chatelain, and D. Malterre, “Reconstruction-induced multiple gaps in the weak coupling limit: The surface bands of Au(111) vicinal surfaces,” *Phys. Rev. B*, vol. 74, p. 081404, Aug 2006. (Cited on page 53.)

- [141] L. Fu, “Hexagonal warping effects in the surface states of the topological insulator Bi_2Te_3 ,” *Phys. Rev. Lett.*, vol. 103, p. 266801, Dec 2009. (Cited on pages 55 and 107.)
- [142] S. Basak, H. Lin, L. A. Wray, S.-Y. Xu, L. Fu, M. Z. Hasan, and A. Bansil, “Spin texture on the warped dirac-cone surface states in topological insulators,” *Phys. Rev. B*, vol. 84, p. 121401, Sep 2011. (Cited on page 55.)
- [143] E. Frantzeskakis, *Spectroscopic Studies on Semiconducting Systems with Giant Spin Splitting*. PhD thesis, Ecole Polytechnique Fédérale de Lausanne, 2010. (Cited on page 55.)
- [144] E. Frantzeskakis and M. Grioni, “Anisotropy effects on rashba and topological insulator spin-polarized surface states: A unified phenomenological description,” *Phys. Rev. B*, vol. 84, p. 155453, Oct 2011. (Cited on pages 55 and 107.)
- [145] S. Vajna, E. Simon, A. Szilva, K. Palotas, B. Ujfalussy, and L. Szunyogh, “Higher-order contributions to the Rashba-Bychkov effect with application to the Bi/Ag(111) surface alloy,” *Phys. Rev. B*, vol. 85, p. 075404, Feb 2012. (Cited on page 55.)
- [146] I.-P. Hong, C. Brun, F. Patthey, I. Y. Sklyadneva, X. Zubizarreta, R. Heid, V. M. Silkin, P. M. Echenique, K. P. Bohnen, E. V. Chulkov, and W.-D. Schneider, “Decay mechanisms of excited electrons in quantum-well states of ultrathin Pb islands grown on Si(111): Scanning tunneling spectroscopy and theory,” *Phys. Rev. B*, vol. 80, p. 081409, Aug 2009. (Cited on pages 63 and 79.)
- [147] F. Baumberger, A. Tamai, M. Muntwiller, T. Greber, and J. Osterwalder, “The electronic structure of a surfactant layer: Pb / Cu(111),” *Surf. Sci.*, vol. 532, no. 0, p. 82, 2003. (Cited on pages 63, 64, 66, 67, 69, 71, 72 and 75.)
- [148] B. H. Müller, T. Schmidt, and M. Henzler, “Growth and melting of a Pb monolayer on Cu(111),” *Surf. Sci.*, vol. 376, p. 123, 1997. (Cited on page 64.)
- [149] S. Müller, J. E. Prieto, C. Rath, L. Hammer, R. Miranda, and K. Heinz, “Surfactant-induced surface reconstructing: (4x4) - Pb/Cu(111),” *J. of Phys. Condens. Matter*, vol. 13, no. 9, p. 1793, 2001. (Cited on pages 64 and 75.)
- [150] F. Baumberger, W. Auwärte, T. Greber, and J. Osterwalder, “Electron coherence in a melting lead monolayer,” *Science*, vol. 306, p. 2221, 2004. (Cited on pages 64, 66, 69, 71, 75 and 80.)
- [151] C. R. Ast, D. Pacilé, M. Papagno, T. Gloor, F. Mila, S. Fedrigo, G. Wittich, K. Kern, H. Brune, and M. Grioni, “Orbital selective overlayer-substrate hybridization in a Pb monolayer on Ag(111),” *Phys. Rev. B*, vol. 73, p. 245428, Jun 2006. (Cited on pages 64, 65, 66, 67, 69, 70, 71, 72, 73, 74, 75, 79 and 80.)
- [152] M. Grioni, C. R. Ast, D. Pacilé, M. Papagno, H. Berger, and L. Perfetti, “Photoemission as a probe of coexisting and conflicting periodicities in low-dimensional solids,” *New J. Phys.*, vol. 7, p. 106, 2005. (Cited on page 66.)

- [153] J. Voit, L. Perfetti, F. Zwick, H. Berger, G. Margaritondo, G. Grüner, H. Höchst, and M. Grioni, “Electronic structure of solids with competing periodic potentials,” *Science*, vol. 290, p. 501, 2000. (Cited on page 66.)
- [154] J. Schäfer, E. Rotenberg, G. Meigs, S. D. Kevan, P. Blaha, and S. Hüfner, “Direct spectroscopic observation of the energy gap formation in the spin density wave phase transition at the Cr(110) surface,” *Phys. Rev. Lett.*, vol. 83, pp. 2069–2072, Sep 1999. (Cited on page 66.)
- [155] L. X. Yang, Y. Zhang, H. W. Ou, J. F. Zhao, D. W. Shen, B. Zhou, J. Wei, F. Chen, M. Xu, C. He, Y. Chen, Z. D. Wang, X. F. Wang, T. Wu, G. Wu, X. H. Chen, M. Arita, K. Shimada, M. Taniguchi, Z. Y. Lu, T. Xiang, and D. L. Feng, “Electronic structure and unusual exchange splitting in the spin-density-wave state of the BaFe₂As₂ parent compound of iron-based superconductors,” *Phys. Rev. Lett.*, vol. 102, p. 107002, Mar 2009. (Cited on page 66.)
- [156] T. Brugger, S. Günther, B. Wang, J. H. Dil, M.-L. Bocquet, J. Osterwalder, J. Wintterlin, and T. Greber, “Comparison of electronic structure and template function of single-layer graphene and a hexagonal boron nitride nanomesh on Ru(0001),” *Phys. Rev. B*, vol. 79, p. 045407, Jan 2009. (Cited on page 66.)
- [157] M. Corso, W. Auwärter, M. Muntwiler, A. Tamai, T. Greber, and J. Osterwalder, “Boron nitride nanomesh,” *Science*, vol. 303, p. 217, 2004. (Cited on page 66.)
- [158] R. Laskowski, P. Blaha, T. Gallauner, and K. Schwarz, “Single-layer model of the hexagonal boron nitride nanomesh on the Rh(111) surface,” *Phys. Rev. Lett.*, vol. 98, p. 106802, Mar 2007. (Cited on page 66.)
- [159] A. T. N’Diaye, S. Bleikamp, P. J. Feibelman, and T. Michely, “Two-dimensional Ir cluster lattice on a graphene moiré on Ir(111),” *Phys. Rev. Lett.*, vol. 97, p. 215501, Nov 2006. (Cited on page 66.)
- [160] S. Marchini, S. Günther, and J. Wintterlin, “Scanning tunneling microscopy of graphene on Ru(0001),” *Phys. Rev. B*, vol. 76, p. 075429, Aug 2007. (Cited on page 66.)
- [161] T. Land, T. Michely, R. Behm, J. Hemminger, and G. Comsa, “STM investigation of single layer graphite structures produced on Pt(111) by hydrocarbon decomposition,” *Surf. Sci.*, vol. 264, no. 3, pp. 261 – 270, 1992. (Cited on page 66.)
- [162] I. Pletikoscic, M. Kralj, P. Pervan, R. Brako, J. Coraux, A. T. N’Diaye, C. Busse, and T. Michely, “Dirac cones and minigaps for graphene on Ir(111),” *Phys. Rev. Lett.*, vol. 102, p. 056808, Feb 2009. (Cited on pages 66 and 71.)
- [163] S. Rusponi, M. Papagno, P. Moras, S. Vlaic, M. Etzkorn, P. M. Sheverdyayeva, D. Pacilé, H. Brune, and C. Carbone, “Highly anisotropic Dirac cones in epitaxial graphene modulated by an island superlattice,” *Phys. Rev. Lett.*, vol. 105, p. 246803, Dec 2010. (Cited on pages 66 and 71.)

- [164] J. Camarero, J. Ferrón, V. Cros, L. Gómez, A. L. Vázquez de Parga, J. M. Gallego, J. E. Prieto, J. J. de Miguel, and R. Miranda, “Atomistic mechanism of surfactant-assisted epitaxial growth,” *Phys. Rev. Lett.*, vol. 81, pp. 850–853, Jul 1998. (Cited on page 66.)
- [165] N. Tsud, S. Fabík, V. Dudr, M. Vondracek, V. Cháb, V. Matolín, and K. C. Prince, “Interfacial reconstruction in the system Pb/Ag(110),” *Surf. Sci.*, vol. 542, p. 112, 2003. (Cited on page 66.)
- [166] S. Qin, J. Kim, Q. Niu, and C.-K. Shih, “Superconductivity at the two-dimensional limit,” *Science*, vol. 324, p. 1314, 2009. (Cited on page 66.)
- [167] T. Zhang, P. Cheng, W.-J. Li, Y.-J. Sun, G. Wang, X.-G. Zhu, K. He, L. Wang, X. Ma, X. Chen, Y. Wang, Y. Liu, H.-Q. Lin, J.-F. Jia, and Q.-K. Xue, “Superconductivity in one-atomic-layer metal films grown on Si(111),” *Nat. Phys.*, vol. 6, p. 104, 2010. (Cited on page 66.)
- [168] I. Horcas, R. Fernández, J. M. G. Rodríguez, J. Colchero, J. Gómez-herrero, and A. M. Baro, “Wsxm: a software for scanning probe microscopy and a tool for nanotechnology,” *Rev. Sci. Instrum.*, vol. 78, p. 013705, 2007. (Cited on page 69.)
- [169] T. Wiederholt, H. Brune, J. Winterlin, R. J. Behm, and G. Ertl, “Formation of the two-dimensional sulfide phases on Al(111): an STM study,” *Surf. Sci.*, vol. 324, p. 91, 1995. (Cited on page 69.)
- [170] R. Mazzarello, A. D. Corso, and E. Tosatti, “Spin-orbit modifications and splittings of deep surface states on clean Au(111),” *Surf. Sci.*, vol. 602, no. 4, pp. 893 – 905, 2008. (Cited on pages 70 and 74.)
- [171] J. C. Slater and G. F. Koster, “Simplified LCAO method for the periodic potential problem,” *Phys. Rev.*, vol. 94, pp. 1498–1524, Jun 1954. (Cited on pages 72 and 75.)
- [172] Y. Chen, F. J. García de Abajo, A. Chassé, R. X. Ynzunza, A. P. Kaduwela, M. A. Van Hove, and C. S. Fadley, “Convergence and reliability of the Rehr-Albers formalism in multiple-scattering calculations of photoelectron diffraction,” *Phys. Rev. B*, vol. 58, pp. 13121–13131, Nov 1998. (Cited on page 76.)
- [173] J. B. Pendry, “Reliability factors for leed calculations,” *J. Phys.C: Solid St. Phys.*, vol. 13, p. 937, 1980. (Cited on page 76.)
- [174] H. Li, J. Quinn, Y. S. Li, D. Tian, F. Jona, and P. M. Marcus, “Multilayer relaxation of clean Ag001,” *Phys. Rev. B*, vol. 43, pp. 7305–7307, Mar 1991. (Cited on page 78.)
- [175] G. Q. Huang, “Surface lattice vibration and electron phonon interaction in pb(111) ultrathin superconducting films from first principles: both with and without si substrate,” *New J. Phys.*, vol. 13, p. 093023, 2011. (Cited on page 78.)
- [176] G. Grüner, *Density waves in solids*. Addison-Wesley, 1994. (Cited on page 83.)

- [177] M. Grioni, S. Pons, and E. Frantkeskakis, “Recent ARPES experiments on quasi-1D bulk materials and artificial structures,” *J. Phys.: Condens. Matter*, vol. 21, p. 023201, 2009. (Cited on pages 83 and 90.)
- [178] C. Deisl, K. Swamy, N. Memmel, E. Bertel, C. Franchini, G. Schneider, J. Redinger, S. Walter, L. Hammer, and K. Heinz, “(3x1)-Br/Pt(110) structure and the charge-density-wave-assisted (2x2) to (3x1) phase transition,” *Phys. Rev. B*, vol. 69, p. 195405, May 2004. (Cited on page 83.)
- [179] M. Minca, S. Penner, E. Dona, A. Menzel, E. Bertel, V. Brouet, and J. Redinger, “Surface resonance on transition metals as low-dimensional model systems,” *New J. Phys.*, vol. 9, p. 386, 2007. (Cited on page 83.)
- [180] K. Kern, H. Niehus, A. Schatz, P. Zeppenfeld, J. Goerge, and G. Comsa, “Long-range spatial self-organization in the adsorbate-induced restructuring of surfaces: Cu(110) (2x1)-O,” *Phys. Rev. Lett.*, vol. 67, pp. 855–858, Aug 1991. (Cited on page 83.)
- [181] A. Menzel, Z. Zhang, M. Minca, T. Loerting, C. Deisl, and E. Bertel, “Correlation in low dimensional electronic states on metal surfaces,” *New J. Phys.*, vol. 7, p. 102, 2005. (Cited on page 83.)
- [182] P. Segovia, D. Purdie, M. Hengsberger, and Y. Baer, “Observation of spin and charge collective modes in one-dimensional metallic chains,” *Nature*, vol. 402, p. 504, 1999. (Cited on pages 83 and 84.)
- [183] R. Losio, K. N. Altmann, A. Kirakosian, J.-L. Lin, D. Y. Petrovykh, and F. J. Himpsel, “Band splitting for Si(557)-Au: Is it spin-charge separation?,” *Phys. Rev. Lett.*, vol. 86, pp. 4632–4635, May 2001. (Cited on pages 83, 84 and 85.)
- [184] K. N. Altmann, J. N. Crain, A. Kirakosian, J.-L. Lin, D. Y. Petrovykh, F. J. Himpsel, and R. Losio, “Electronic structure of atomic chains on vicinal Si(111)-Au,” *Phys. Rev. B*, vol. 64, p. 035406, Jun 2001. (Cited on pages 83 and 84.)
- [185] I. K. Robinson, P. A. Bennett, and F. J. Himpsel, “Structure of quantum wires in Au/Si(557),” *Phys. Rev. Lett.*, vol. 88, p. 096104, Feb 2002. (Cited on pages 83 and 84.)
- [186] J. R. Ahn, H. W. Yeom, H. S. Yoon, and I.-W. Lyo, “Metal-insulator transition in au atomic chains on Si with two proximal bands,” *Phys. Rev. Lett.*, vol. 91, p. 196403, Nov 2003. (Cited on pages 83 and 84.)
- [187] J. N. Crain, J. L. McChesney, F. Zheng, M. C. Gallagher, P. C. Snijders, M. Bissen, C. Gundelach, S. C. Erwin, and F. J. Himpsel, “Chains of gold atoms with tailored electronic states,” *Phys. Rev. B*, vol. 69, p. 125401, Mar 2004. (Cited on pages 83, 84 and 85.)

- [188] D. Sánchez-Portal, S. Riikonen, and R. M. Martin, “Role of spin-orbit splitting and dynamical fluctuations in the Si(557)-Au surface,” *Phys. Rev. Lett.*, vol. 93, p. 146803, Sep 2004. (Cited on pages 83, 84, 85 and 89.)
- [189] I. Barke, F. Zheng, T. K. Rügheimer, and F. J. Himpsel, “Experimental evidence for spin-split bands in a one-dimensional chain structure,” *Phys. Rev. Lett.*, vol. 97, p. 226405, Dec 2006. (Cited on pages 83, 84, 85, 89 and 103.)
- [190] K. S. Kim, H. Morikawa, W. H. Choi, and H. W. Yeom, “Strong lateral electron coupling of Pb nanowires on stepped Si(111): Angle-resolved photoemission studies,” *Phys. Rev. Lett.*, vol. 99, p. 196804, Nov 2007. (Cited on pages 83, 84, 85 and 86.)
- [191] K. S. Kim and H. W. Yeom, “Giant kink in electron dispersion of strongly coupled lead nanowires,” *Nano Letters*, vol. 9, p. 1916, 2009. (Cited on pages 83, 84, 85 and 86.)
- [192] L. Lottermoser, T. Buslaps, R. L. Johnson, R. Feidenhans'l, M. Nielsen, D. Smilgies, E. Landemark, and H. L. Meyerheim, “Bismuth on copper (110): Analysis of the $c(2 \times 2)$ and $p(4 \times 1)$ structures by surface X-ray diffraction,” *Surf. Sci.*, vol. 373, p. 11, 1996. (Cited on pages 87, 88 and 93.)
- [193] C. Nagl, M. Pinczolits, M. Schmid, P. Varga, and I. K. Robinson, “ $p(n \times 1)$ superstructures of Pb on Cu(110),” *Phys. Rev. B*, vol. 52, pp. 16796–16802, Dec 1995. (Cited on pages 88 and 93.)
- [194] G. Bihlmayer, “Private comm..”. (Cited on pages 89, 90 and 91.)
- [195] W. C. Marra, P. H. Fuoss, and P. E. Eisenberger, “X-ray diffraction studies: Melting of Pb monolayers on Cu(110) surfaces,” *Phys. Rev. Lett.*, vol. 49, pp. 1169–1172, Oct 1982. (Cited on page 93.)
- [196] S. Brennan, P. H. Fuoss, and P. Eisenberger, “X-ray crystallographic studies of Pb monolayers on Cu(110) surfaces,” *Phys. Rev. B*, vol. 33, pp. 3678–3683, Mar 1986. (Cited on page 93.)
- [197] C. de Beauvais, D. Rouxel, B. Bigeard, and B. Mutaftschiev, “Thermal-energy atom-scattering study of Pb submonolayers on Cu(110),” *Phys. Rev. B*, vol. 44, pp. 4024–4027, Aug 1991. (Cited on page 93.)
- [198] D. Pacilé, C. R. Ast, M. Papagno, C. Da Silva, L. Moreschini, M. Falub, A. P. Seitsonen, and M. Grioni, “Electronic structure of an ordered Pb/Ag(111) surface alloy: Theory and experiment,” *Phys. Rev. B*, vol. 73, p. 245429, Jun 2006. (Cited on page 94.)
- [199] P. D. C. King, R. C. Hatch, M. Bianchi, R. Ovsyannikov, C. Lupulescu, G. Landolt, B. Slomski, J. H. Dil, D. Guan, J. L. Mi, E. D. L. Rienks, J. Fink, A. Lindblad, S. Svensson, S. Bao, G. Balakrishnan, B. B. Iversen, J. Osterwalder, W. Eberhardt,

- F. Baumberger, and P. Hofmann, “Large tunable Rashba spin splitting of a two-dimensional electron gas in Bi_2Se_3 ,” *Phys. Rev. Lett.*, vol. 107, p. 096802, Aug 2011. (Cited on pages 99, 101, 102 and 108.)
- [200] A. V. Shelkov, E. V. Dikarev, R. V. Shpanchenko, and B. A. Popovkin, “Crystal structures of bismuth tellurohalides $BiTeX$ ($X = Cl, Br, I$) from X-ray powder diffraction data,” *J. Solid. State Chem.*, vol. 114, p. 379, 1995. (Cited on pages 100 and 105.)
- [201] S. Murakami, “Quantum spin hall effect and enhanced magnetic response by spin-orbit coupling,” *Phys. Rev. Lett.*, vol. 97, p. 236805, Dec 2006. (Cited on page 100.)
- [202] M. S. Bahramy, R. Arita, and N. Nagaosa, “Origin of giant bulk Rashba splitting: Application to $BiTeI$,” *Phys. Rev. B*, vol. 84, p. 041202, Jul 2011. (Cited on pages 101 and 102.)
- [203] J. S. Lee, G. A. H. Schober, M. S. Bahramy, H. Murakawa, Y. Onose, R. Arita, N. Nagaosa, and Y. Tokura, “Optical response of relativistic electrons in the polar $BiTeI$ semiconductor,” *Phys. Rev. Lett.*, vol. 107, p. 117401, Sep 2011. (Cited on pages 101 and 115.)
- [204] P. D. C. King, T. D. Veal, and C. F. McConville, “Nonparabolic coupled Poisson-Schrödinger solutions for quantized electron accumulation layers: Band bending, charge profile, and subbands at InN surfaces,” *Phys. Rev. B*, vol. 77, p. 125305, Mar 2008. (Cited on page 101.)
- [205] A. Crepaldi, L. Moreschini, G. Autès, C. T.-Colletta, S. Moser, N. Virk, H. Berger, P. Bugnon, Y. J. Chang, K. Kern, A. Bostwick, E. Rotenberg, O. V. Yazyev, and M. Grioni, “Giant ambipolar rashab effect in the semiconductors bitei,” *Phys. Rev. Lett.*, vol. 109, p. 096803, 2012. (Cited on pages 102 and 135.)
- [206] “Synopsis: skin-deep spintronics,” <http://physics.aps.org/synopsis-for/10.1103/PhysRevLett.109.096803>. (Cited on page 102.)
- [207] O. Krupin, G. Bihlmayer, K. Starke, S. Gorovikov, J. E. Prieto, K. Döbrich, S. Blügel, and G. Kaindl, “Rashba effect at magnetic metal surfaces,” *Phys. Rev. B*, vol. 71, p. 201403, May 2005. (Cited on page 103.)
- [208] M. S. Bahramy, B.-Y. Yang, R. Arita, and N. Nagaosa, “Emergence of non-centrosymmetric topological insulating phase in $BiTeI$ under pressure,” *Nature Commun.*, vol. 3, p. 679, 2012. (Cited on page 103.)
- [209] G. Landolt, S. V. Ereameev, Y. M. Koroteev, B. Slomski, S. Muff, M. Kobayashi, V. N. Strocov, T. Schmitt, Z. S. Aliev, M. B. Babnly, I. R. Amirasanov, E. V. Chulkov, J. Osterwalder, and J. H. Dil, “Surface and bulk fermiology and band dispersion in non-centrosymmetric $BiTeI$,” *Phys. Rev. Lett.*, vol. 109, p. 116403, 2012. (Cited on pages 103, 115, 116 and 117.)

- [210] P. Giannozzo, S. Baroni, N. Bonini, M. Calandra, R. Car, and C. C. et al., “QUANTUM ESPRESSO: a modular and open-source software project for quantum simulations of materials,” *J. Phys.: Condens. Matter*, vol. 21, p. 395502, 2009. (Cited on page 104.)
- [211] A. D. Corso and A. M. Conte, “Spin-orbit coupling with ultrasoft pseudopotentials: Application to Au and Pt,” *Phys. Rev. B*, vol. 71, p. 115106, Mar 2005. (Cited on page 104.)
- [212] S.-Y. Xu, Y. Xia, L. A. Wray, S. Jia, F. Meier, J. H. Dil, J. Osterwalder, B. Slomski, A. Bansil, H. Lin, R. J. Cava, and M. Z. Hasan, “Topological phase transition and texture inversion in a tunable topological insulator,” *Science*, vol. 332, p. 560, 2011. (Cited on page 105.)
- [213] J. Yeh and I. Lindau, “Atomic data and nuclear data tables,” vol. 1, 1985. (Cited on page 110.)
- [214] J. Mesot, M. Randeria, M. R. Norman, A. Kaminski, H. M. Fretwell, J. C. Campuzano, H. Ding, T. Takeuchi, T. Sato, T. Yokoya, T. Takahashi, I. Chong, T. Terashima, M. Takano, T. Mochiku, and K. Kadowaki, “Determination of the Fermi surface in high T_c superconductors by angle-resolved photoemission spectroscopy,” *Phys. Rev. B*, vol. 63, p. 224516, May 2001. (Cited on page 111.)
- [215] M. Sakano, J. Miyawaki, A. Chainani, Y. Takata, T. Sonobe, T. Shimojima, M. Oura, S. Shin, M. S. Bahramy, R. Arita, N. Nagaosa, H. Murakawa, Y. Kaneko, Y. Tokura, and K. Ishizaka, “Three-dimensional bulk band dispersion in polar BiTeI with giant Rashba-type spin splitting,” *Phys. Rev. B*, vol. 86, p. 085204, Aug 2012. (Cited on pages 116 and 117.)
- [216] M. Salmeron and R. Schlögl, “Ambient pressure photoelectron spectroscopy: A new tool for surface science and nanotechnology,” *Surf. Sci. Reports*, vol. 63, p. 169, 2008. (Cited on page 119.)
- [217] P. Sutter, M. S. Hybertsen, J. T. Sadowski, and E. Sutter, “Electronic structure of few-layer epitaxial graphene on Ru(0001),” *NanoLett.*, vol. 9, p. 2654, 2009. (Cited on page 119.)
- [218] T. Kiss, T. Shimojima, K. Ishizaka, A. Chainani, and T. Togashi, “A versatile system for ultrahigh resolution, low temperature and polarization dependent laser-angle-resolved photoemission spectroscopy,” *Rev. Sci. Instrum.*, vol. 79, p. 023106, 2008. (Cited on page 120.)
- [219] U. Bovensiepen, H. Petek, and M. Wolf, *Dynamics At Solid State Surfaces and Interfaces. Volume1*. Wiley-VCH. (Cited on pages 120 and 122.)
- [220] S. K. Sundaram and E. Mazur, “Inducing and probing non-thermal transitions in semiconductors using femtosecond laser pulse,” *Nature Mat.*, vol. 1, p. 217, 2002. (Cited on pages 120 and 121.)

- [221] P. B. Allen, “Theory of thermal relaxation of electrons in metals,” *Phys. Rev. Lett.*, vol. 59, p. 1460, 1987. (Cited on pages 121, 123, 125 and 135.)
- [222] L. Perfetti, P. A. Loukakos, M. Lisowski, U. Bovensiepen, H. Berger, S. Biermann, P. Cornaglia, A. Georges, and M. Wolf, “Time evolution of the electronic structure of $1T - TaS_2$ through the insulator-metal transition,” *Phys. Rev. Lett.*, vol. 97, p. 067402, 2006. (Cited on pages 122 and 123.)
- [223] F. Schmitt, P. S. Kirchmann, U. Bovensiepen, R. G. Moore, L. Retting, M. Krenz, J.-H. Chu, N. Ru, L. Perfetti, D. H. Lu, M. Wolf, I. R. Fisher, and Z.-X. Shen, “Transient electronic structure and melting of a charge density wave in $TbTe_3$,” *Science*, vol. 321, p. 1649, 2008. (Cited on pages 122 and 123.)
- [224] L. Perfetti, P.A.Loukakos, M. Lisowski, U. Bovensiepen, H. Eisaki, and M. Wolf, “Ultrafast electron relaxation in superconducting $Bi_2Sr_2CaCu_2O_8$ by time-resolved photoelectron spectroscopy,” *Phys. Rev. Lett.*, vol. 99, p. 197001, 2007. (Cited on pages 122, 123, 125, 126 and 135.)
- [225] R. Cortés, L. Retting, Y. Yoshida, H. Eisaki, M. Wolf, and U. Bovensiepen, “Momentum-resolved ultrafast electron dynamics in superconducting $Bi_2Sr_2CaCu_2O_8$,” *Phys. Rev. Lett.*, vol. 107, p. 097002, 2011. (Cited on pages 122 and 125.)
- [226] J. Graf, C. Jozwiak, C. Smallwood, H. Eisaki, R. A. Kaindl, D.-H. Lee, and A. Lanzara, “Nodal quasiparticle meltdown in ultrahigh-resolution pump-probe angle-resolved photoemission,” *Nature Phys.*, vol. 7, p. 805, 2011. (Cited on pages 122, 123 and 141.)
- [227] C. L. Smallwood, J. P. Hilton, C. Jozwiak, W. Zhang, J. D. Koralek, H. Eisaki, D.-H. Lee, J. Orenstei, and A. Lanzara, “Tracking Cooper pairs in a cuprate superconductor by ultrafast angle-resolved photoemission,” *Science*, vol. 336, p. 1137, 2012. (Cited on pages 122, 125 and 141.)
- [228] L. Retting, R. Cortés, S. Thirupathaiah, P. Gegenwart, H. S. Jeevan, M. Wolf, J. Fink, and U. Bovensiepen, “Ultrafast momentum-dependent response of electrons in antiferromagnetic $EuFe_2As_2$ driven by optical excitation,” *Phys. Rev. Lett.*, vol. 108, p. 097002, 2012. (Cited on page 122.)
- [229] I. Avigo, R. Cortés, L. Retting, S. Thirupathaiah, H. S. Jeevan, P. Gegenwart, T. Wolf, M. Ligges, M. Wolf, J. Fink, and U. Bovensiepen, “Coherent excitation and electron phonon coupling in $Ba/EuFe_2As_2$ compounds investigated by femtosecond time- and angle-resolved photoemission spectroscopy,” *arxiv*, p. 12044069, 2012. (Cited on pages 122 and 126.)
- [230] W. S. Fann, R. Storz, H. W. K. Tom, and J. Bokor, “Electron thermalization in gold,” *Phys. Rev. B*, vol. 46, p. 13592, 1992. (Cited on pages 122, 123, 124, 125 and 137.)

- [231] M. Lisowski, P. Loukakos, U. Bovensiepen, J. Stähler, C. Gahl, and M. Wolf, “Ultrafast dynamics of electron thermalization cooling and transport effects in Ru(001),” *App. Phys. A*, vol. 78, pp. 165–176, 2004. (Cited on pages [122](#), [123](#), [124](#), [125](#) and [137](#).)
- [232] M. Lisowski, P. A. Loukakos, A. Melnikov, I. Radu, L. Ungureanu, M. Wolf, and U. Bovensiepen, “Femtosecond electron and spin dynamics in Gd(0001) studied by time-resolved photoemission and magneto-optics,” *Phys. Rev. Lett.*, vol. 95, p. 137402, 2005. (Cited on pages [122](#), [123](#) and [125](#).)
- [233] M. Wagner, “Expansions of nonequilibrium green’s function,” *Phys. Rev. B*, vol. 44, p. 6105, 1991. (Cited on page [122](#).)
- [234] W. Nessler, S. Ogawa, H. Nagano, H. Petek, J. Shimoyama, Y. Nakayama, and K. Kishio, “Femtosecond time-resolved study of the energy and temperature dependence of hot-electron lifetimes in $Bi_2Sr_2CaCu_2O_8$,” *Phys. Rev. Lett.*, vol. 81, pp. 4480–4483, Nov 1998. (Cited on page [122](#).)
- [235] J. C. Petersen, S. Kaiser, N. Dean, A. Simoncig, H. Y. Liu, A. L-Cavalieri, C. Cacho, I. C. E. Turcu, E. Springate, F. Frassetto, L. Poletto, S. S. Dhesi, H. Berger, and A. Cavalleri, “Clocking the melting transition of charge and lattice order in $1T - TaS_2$ with ultrafast extreme-ultraviolet angle-resolved photoemission spectroscopy,” *Phys. Rev. Lett.*, vol. 107, p. 177402, 2011. (Cited on page [123](#).)
- [236] J. P. Callan, A. M.-T. Kim, C. A. D. Roeser, and E. Mazur, “Universal dynamics during and after ultrafast laser-induced semiconductor-to-metal transition,” *Phys. Rev. B*, vol. 64, p. 073201, 2001. (Cited on page [123](#).)
- [237] B. Batlogg, R. Cava, A. Jayaraman, R. B. van Dover, G. A. Kourouklis, S. Sunshine, D. W. Murphy, L. W. Rupp, H. S. Chen, A. White, K. T. Short, A. M. Mujesce, and E. A. Rietman, “Isotope effect in the high temperature superconductors $Ba_2YCu_3O_7$ and $Ba_2EuCu_3O_7$,” *Phys. Rev. Lett.*, vol. 58, p. 2333, 1987. (Cited on page [125](#).)
- [238] T. Ando, “Theory of quantum transport in a two-dimensional electron system under magnetic fields,” *J. Phys. Soc. Jpn*, vol. 37, p. 622, 1974. (Cited on page [127](#).)
- [239] K. v. Klitzing, G. Dorda, and M. Pepper, “New method for high-accuracy determination of the fine structure constant based on quantized hall resistance,” *Phys. Rev. Lett.*, vol. 45, p. 494, 1980. (Cited on page [127](#).)
- [240] R. B. Laughlin, “Quantized hall conductivity in two dimensions,” *Phys. Rev. B*, vol. 23, p. 5632, 1981. (Cited on page [127](#).)
- [241] B. I. Halperin, “Quantized hall conductance, current-carrying edge states, and the existence of extended states in a two-dimensional disordered potential,” *Phys. Rev. B*, vol. 25, p. 2185, 1982. (Cited on page [127](#).)

- [242] W. Kohn, "Theory of insulating state," *Phys. Rev.*, vol. 133, p. A171, 1964. (Cited on page 127.)
- [243] M. V. Berry, "Quantal phase factors accompanying adiabatic changes," *Proc. R. Soc. Lond. A*, vol. 392, p. 45, 1984. (Cited on page 128.)
- [244] D. J. Thouless, M. Kohomoto, M. P. Nightingale, and M. den Nijs, "Quantized hall conductance in a two-dimensional periodic potential," *Phys. Rev. Lett.*, vol. 49, p. 405, 1982. (Cited on page 128.)
- [245] J. E. Avron, R. Seiler, and B. Simon, "Homotopy and quantization in condensed matter physics," *Phys. Rev. Lett.*, vol. 51, p. 51, 1983. (Cited on page 128.)
- [246] S. Murakami, N. Nagaosa, and S.-C. Zhang, "Dissipationless quantum spin current at room temperature," *Science*, vol. 301, p. 1348, 2003. (Cited on page 128.)
- [247] M. Köning, S. Wiedmann, C. Brüne, A. Roth, H. Buhmann, L. W. Molenkamp, X.-L. Qi, and S.-C. Zhang, "Quantum spin hall insulator state in HgTe quantum wells," *Science*, vol. 318, p. 766, 2007. (Cited on page 128.)
- [248] C. L. Kane and E. J. Mele, "Quantum spin hall effect in graphene," *Phys. Rev. Lett.*, vol. 95, p. 226801, 2005. (Cited on page 128.)
- [249] C. L. Kane and E. J. Mele, " z_2 topological order and the quantum spin hall effect," *Phys. Rev. Lett.*, vol. 95, p. 146802, 2005. (Cited on page 128.)
- [250] B. A. Bernevig and S.-C. Zhang, "Quantum spin hall effect," *Phys. Rev. Lett.*, vol. 96, p. 106802, 2006. (Cited on page 128.)
- [251] J. C. Y. Teo, L. Fu, and C. L. Kane, "Surface states and topological invariants in three-dimensional topological insulators: Application to $Bi_{1-x}Sb_x$," *Phys. Rev. B*, vol. 78, p. 045426, 2008. (Cited on pages 128 and 129.)
- [252] H. Zhang, C.-X. Liu, X.-L. Qi, X. Dai, Z. Fang, and S.-C. Zhang, "Topological insulators in Bi_2Se_3 , Bi_2Te_3 and Sb_2Te_3 with a single Dirac cone on the surface," *Nature Phys.*, vol. 5, p. 438, 2009. (Cited on pages 129, 130, 131 and 135.)
- [253] F. Zhang, C. L. Kane, and E. J. Mele, "Surface states of topological insulators," *Phys. Rev. B*, vol. 86, p. 081303, 2012. (Cited on page 130.)
- [254] Y. Xia, D. Qian, D. Hsieh, L. Wray, A. Pal, H. Lin, A. Bansil, D. Grauer, Y. S. Hor, R. J. Cava, and M. Z. Hasan, "Observation of a large-gap topological-insulator class with a single dirac cone on the surface," *Nature Phys.*, vol. 5, p. 398, 2009. (Cited on pages 130, 131, 135, 136 and 137.)
- [255] Y. L. Chen, J. G. Analytis, J.-H. Chu, Z. K. Liu, S.-K. Mo, X. L. Qi, H. J. Zhang, D. H. Lu, X. Dai, Z. Fang, S. C. Zhang, I. R. Fisher, Z. Hussain, and Z.-X. Shen, "Experimental realization of a three-dimensional topological insulator, Bi_2Te_3 ," *Science*, vol. 325, p. 178, 2009. (Cited on pages 130, 131 and 135.)

- [256] J. A. Sobota, S. Yang, J. G. Analytis, Y. L. Chen, I. R. Fisher, and P. S. K. Z.-X. Shen, “Ultrafast optical excitation of a persistent surface-state population in the topological insulator Bi_2Se_3 ,” *Phys. Rev. Lett.*, vol. 108, p. 117403, 2012. (Cited on pages 131, 132, 133, 138, 139 and 140.)
- [257] M. Bianchi, D. Guan, S. Bao, J. Mi, B. B. Iversen, P. D. C. King, and P. Hofmann, “Coexistence of the topological state and a two-dimensional electron gas on the surface of Bi_2Se_3 ,” *Nature comm.*, vol. 1, p. 1, 2010. (Cited on pages 131, 135 and 137.)
- [258] A. Othonos, “Probing ultrafast carrier and phonon dynamics in semiconductors,” *J. Appl. Phys.*, vol. 83, p. 1789, 1998. (Cited on pages 133 and 137.)
- [259] M. Hajlaoui, E. Papalazarou, J. Mauchain, G. Lantz, N. Moisan, D. Boschetto, Z. Jiang, I. Miotkowski, Y. P. Chen, A. Taleb-Ibrahimi, L. Perfetti, and M. Marsi, “Ultrafast surface carrier dynamics in the topological insulator Bi_2Te_3 ,” *NanoLett.*, vol. 12, pp. 3532–3536, 2012. (Cited on pages 133, 134, 138, 139 and 140.)
- [260] A. Crepaldi, B. Ressel, F. Cilento, M. Zacchigna, C. Grazioli, H. Berger, P. Bugnon, K. Kern, M. Grioni, and F. Parmigiani, “Ultrafast photodoping and effective fermi-dirac distribution of the dirac particles in bi_2se_3 ,” *Phys. Rev. B*, vol. 86, p. 205133, Nov 2012. (Cited on page 134.)
- [261] S. Chadov, X. Qi, J. Kübler, G. H. Fecher, C. Felser, and S. C. Zhang, “Tunable multifunctional topological insulators in ternary heusler compounds,” *Nature mat.*, vol. 9, p. 541, 2010. (Cited on page 135.)
- [262] S. V. Eremeev, G. Landolt, T. V. Menshchikova, B. Slomski, Y. M. Koroteev, Z. S. Aliev, M. B. Babanly, J. Henk, A. Ernst, L. Patthey, A. Eich, A. A. Khajetoorians, J. Hagemester, O. Pietzsch, J. Wiebe, R. Wiesendanger, P. M. Echenique, S. S. Tsirkin, I. R. Amiraslanov, J. H. Dil, and E. V. Chulkov, “Atom-specific spin mapping and buried topological states in a homologous series of topological insulators,” *Nature comm.*, vol. 3, p. 1, 2012. (Cited on page 135.)
- [263] P. Roushan, J. Seo, C. V. Parker, Y. S. Hor, D. Hsieh, D. Qian, A. Richardella, M. Z. Hasan, R. J. Cava, and A. Yazdani, “Topological surface states protected from backscattering by chiral spin texture,” *Nature*, vol. 460, p. 1106, 2009. (Cited on page 135.)
- [264] Y. L. Chen, Z. Liu, J. G. A. and J.-H. Chu, H. J. Zhang, B. H. Yan, S.-K. Mo, R. G. Moore, D. H. Lu, I. R. Fisher, S. C. Zhang, Z. Hussain, and Z.-X. Shen, “Single Dirac cone topological surface state and unusual thermoelectric property of compounds from a new topological insulator family,” *Phys. Rev. Lett.*, vol. 105, p. 266401, 2010. (Cited on page 135.)
- [265] K. Kuroda, M. Ye, A. Kimura, S. V. Eremeev, E. E. Krasovskii, E. V. Chulkov, Y. Ueda, K. Miyamoto, T. Okuda, K. Shimada, H. Namatame, and M. Taniguchi,

- “Experimental realization of a three-dimensional topological insulator phase in a ternary chalcogenide $TlBiSe_2$,” *Phys. Rev. Lett.*, vol. 105, p. 146801, 2010. (Cited on page 135.)
- [266] S.-Y. Xu, A. Wray, Y. Xia, R. Shankar, A. Petersen, A. Fedorov, H. Lin, A. Bansil, Y. S. Hor, D. Grauer, R. J. Cava, and M. Z. Hasan, “Discovery of several large families of topological insulator classes with backscattering-suppressed spin-polarized single Dirac cone on the surface,” *arxiv*, p. 10075111, 2010. (Cited on page 135.)
- [267] S. R. Park, W. S. Jung, C. Kim, D. J. Song, C. Kim, S. Kimura, K. D. Lee, and N. Hur, “Quasiparticle scattering and the protected nature of the topological states in a parent topological insulator Bi_2Se_3 ,” *Phys. Rev. B*, vol. 81, p. 041405, Jan 2010. (Cited on pages 137 and 140.)
- [268] Y. H. Wang, D. Hsieh, E. J. Sie, H. Steinberg, D. R. Gardner, Y. S. Lee, P. Jarillo-Herrero, and N. Gedik, “Measurement of intrinsic Dirac fermion cooling on the surface of a topological insulator Bi_2Se_3 using time- and angle-resolved photoemission spectroscopy,” *arXiv*, vol. 1208.4782v1, p. accepted on *Phys. Rev. Lett.*, 2012. (Cited on pages 137 and 140.)
- [269] W. Richter and C. R. Becker *Phys. Status Solidi (b)*, vol. 84, p. 619, 1977. (Cited on page 138.)
- [270] M. R. Norman, H. Ding, M. Randeria, J. C. Campuzano, T. Yokoya, T. Takeuchi, T. Takahashi, T. Mochiku, K. Kadowaki, P. Guptasarma, and D. G. Hinks, “Destruction of the Fermi surface in underdoped high- T_c superconductors,” *Nature*, vol. 392, p. 157, 1998. (Cited on page 142.)

Curriculum Vitae

Personal Information

Alberto Crepaldi
Nationality: Italian
Born on the 19th of April 1985

Education - Professional experience

Ph.D. in Physics at the Ecole Polytechnique Fédérale de Lausanne (EPFL) Switzerland. (2008-today)

Thesis advisors: Professor Klaus Kern (MPI Stuttgart, EPFL) and Professor Marco Grioni (EPFL)

Thesis title: *High resolution spectroscopy of complex interfaces*

Main experimental technique: Angle-Resolved Photoemission Spectroscopy, Low-Energy Electron Diffraction, Ultra-High Vacuum, liquid Nitrogen and liquid Helium Cryogeny, Synchrotron Radiation experiments (ELETTRA, Trieste), Laser Angle-Resolved Photoemission Spectroscopy and Time-resolved ARPES (tr-ARPES) in collaboration with the T-ReX Research group at ELETTRA

Other tasks: Teaching Assistant in General Physics (Electro-Magnetism and Quantum Mechanics)

Masters degree in Physics, curriculum Condensed Matter, at the University of Trieste, Italy (2006-2008)

Thesis advisor: Professor Fulvio Parmigiani (UNITS)

Thesis title: *Time dependent dielectric function of photo-excited CuGeO₃*

Main experimental technique: non linear optics with ultra-fast amplified Ti:Sa laser, super-continuum generation and pump probe optical spectroscopy

Internship in the laboratory of non-linear optics at ELETTRA, Trieste, Italy (2007-2008)

Project title: *Installation and characterization of a hollow fiber for the temporal compression of a laser pulse below 10fs*

Main experimental technique: non linear optics with ultra-fast amplified Ti:Sa laser

Bachelor degree in physics at the University of Trieste, Italy (2003-2006)

Thesis advisor: Professor Fulvio Parmigiani (UNITS)

Thesis title: *Fermi surface mapping of Cobaltates by means of Angle-Resolved Photoemission Spectroscopy*

Main experimental technique: Angle-Resolved Photoemission Spectroscopy on strongly correlated electron systems

Teaching

Teaching assistant at the EPFL (2006-today) in the subjects General Physics III and IV for the 2nd year B.Sc. students of electrical engineering and material science.

Topics covered: fluid-statics, fluid-dynamics, Bernoulli equation, Euler equation, viscosity, electrostatics, dielectrics, magnetostatics, electromagnetic induction, Maxwell equations, electromagnetic radiation, interference and diffraction of waves, wave-particle duality, Schrödinger's equation, basic principles of quantum mechanics, the hydrogen atom, Pauli exclusion principle, the chemical bond, solids

Main Tasks: preparation of the exercises, interaction with the students (2h/week) about the solution of the exercises, correction of the tests and final exams

Distinctions- Prizes

UNITS and ELETTRA: *Luciano Fonda* scholarship (2006-2008)

Interests

Scientific: Strong Spin-Orbit Coupling and Topological Insulator. Static and Time-Resolved Spectroscopies (tr-ARPES and optical pump probe experiment)

Hobbies: Natural Science, Science-Fiction literature, Comics.

Conferences and Doctoral School

- *MaNEP meeting*, Les Diablerets (Switzerland), August 2009
- *X School on Synchrotron Radiation on Fundamentals, Methods and Applications*, Trieste (Italy), September 2009
- *Quantum Nanoscience*, winter school in Crans Montana (Switzerland), March 2011
- *MaNEP Topical meeting: Topological properties of Electronic Material*, Geneve (Switzerland), May 2011
- *Joint Annual Meeting of the Swiss and Austrian Physical Societies: Topical Sessions on Surfaces, Interfaces and Thin Films* Lausanne (Switzerland), June 2011
- *CECAM meeting: Topological Insulator and non-perturbative Spin-Orbit Coupling*, Lausanne (Switzerland), January 2012

Language skills

Italian: mother language

English: fluent oral and written

French: good comprehension and basic oral and written

Publications

- 1 *Disentangling thermal and nonthermal excited states in a charge-transfer insulator by time- and frequency-resolved pump-probe spectroscopy*
Claudio Giannetti, Goran Zgrablic, Cristina Consani, Alberto Crepaldi, Damiano Nardi, Gabriele Ferrini, G. Dhalenne, A. Revcolevschi and Fulvio Parmigiani
Phys. Rev. B **80**, 235129 (2009)
- 2 *Tuning the giant Rashba effect on a BiAg₂ surface alloy: Two different approaches*
E. Frantzeskakis, A. Crepaldi, S. Pons, K. Kern, M. Grioni
J. Electron Spectr. Rel. Phenom. **181** 88 (2010)
- 3 *Ag-coverage-dependent symmetry of the electronic states of the Pt(111)-Ag-Bi interface: The ARPES view of a structural transition*
E. Frantzeskakis, S. Pons, A. Crepaldi, H. Brune, K. Kern, and M. Grioni
Phys. Rev. B **84**, 245443 (2011)
- 4 *Anisotropic spin gaps in BiAg₂-Ag/Si(111)*
Alberto Crepaldi, Stéphane Pons, Emmanouil Frantzeskakis, Klaus Kern and Marco Grioni
Phys. Rev. B **85** 075411 (2012)
- 5 *Giant Ambipolar Rashba Effect in the Semiconductor BiTeI*
A. Crepaldi, L. Moreschini, G. Autès, C. T.-Colletta, S. Moser, N. Virk, H. Berger, Ph. Bugnon, Y. J. Chang, K. Kern, A. Bostwick, E. Rotenberg, O. V. Yazyev and M. Grioni
Phys. Rev. Lett. **109** 096803 (2012)
- 6 *Ultrafast photodoping and effective Fermi-Dirac distribution of the Dirac particle in Bi₂Se₃*
A. Crepaldi, B. Ressel, F. Cilento, M. Zacchigna, C. Grazioli, H. Berger, Ph. Bugnon, K. Kern and M. Grioni
Phys. Rev. B **86** 205133 (2012)
- 7 *Combined ARPES and STM study of Pb/Au(111) moiré: one overlayer, two symmetries*
Alberto Crepaldi, Stéphane Pons, Emmanouil Frantzeskakis, Fabian Calleja, Markus Etzkorn, Klaus Kern, Harald Brune and Marco Grioni
to be submitted to Phys. Rev. B
- 8 *ARPES and XPD study of PbAg(100) c(6×2): role of the structural commensurability in the band structure of a Pb monolayer*
Alberto Crepaldi, Rong Rong Zhan, Simon Moser, Alessandro Baraldi, Klaus Kern,

Carlo Carbone, and Marco Grioni

In preparation

9 *One dimensional spin split surface states in BiCu(110) $p(4\times 1)$ surface alloy*

Alberto Crepaldi, Klaus Kern and Marco Grioni

In preparation